

Femtosecond laser-based optomechanical processes for permanent and high-precision fine alignment of optical systems

Présentée le 20 décembre 2021

Faculté des sciences et techniques de l'ingénieur
Laboratoire Galatea
Programme doctoral en photonique

pour l'obtention du grade de Docteur ès Sciences

par

Saood Ibni NAZIR

Acceptée sur proposition du jury

Prof. C. Moser, président du jury
Prof. Y. Bellouard, directeur de thèse
Prof. R. R. Thomson, rapporteur
Prof. M. Withford, rapporteur
Prof. S. Henein, rapporteur

To my father, who by patiently answering all my questions became the greatest teacher of my life;

And to my mother, who taught me everything else.

Acknowledgements

Although at the forefront of the work reported in this thesis, I owe a great deal of gratitude to many people whose support has been instrumental in its fulfillment. Yves placed a bet and hired me to work on a multi-disciplinary problem despite much proof of my abilities to navigate this arduous journey. I am deeply indebted to him for placing his faith in me. Over the years, his continuous support, intensive scientific guidance, and strive towards fostering a positive work environment made that path easier. Merci beaucoup Yves.

This thesis would be incomplete with the assistance from my colleagues – Andrea Kraxner, Antoine M. Delgoffe, Arunkrishnan Radhakrishnan, Enrico Casamenti, Gözden Torun, Julien G. E. Gateau, Margarita Lesik, Olivier Bernard, Pieter Vlugter, Ruben Ricca, Samuel P. Rey, Samuel Y. Benketaf, and Vinod Parmar. Their support, in and out of the workspace has pushed me past some of the toughest times during the years. I have benefited immensely from the knowledge of Pieter, with whom I shared my office for the past four-plus years. His advice, suggestions, and hands-on help have been a part of my entire journey thus far. I would also like to acknowledge Antoine, who was altruistic in offering his help to proofread the initial manuscript. Besides, I have regularly fed off his knowledge on optics. A special thanks to Julien for maintaining the laser platforms used in this work; to Gözden for her constant motivation during the writing of this manuscript.

I would also like to thank the past members of our research group – Alessandro Pontearso, Ben McMillen, Christos E. Athanasiou, David Lambelet, Erica Block, Manon Tardif, Sacha Pollonghini, Sargis Hakobyan, Tao Yang, and Vladimir Bourquin, alongside whom I spent a very fruitful time. I am especially grateful to Christos who bequeathed his stress-relaxation know-how which I have aimed to fulfill in this work. I would also like to acknowledge the help of Vladimir, who did his semester project as part of this thesis.

I must also thank people who have worked behind the scenes to make this possible. To Josiane Pachoud, our lab secretary, who kept me free of administrative and bureaucratic workloads, and organized our lab outings; to Joël Currit, our expert in the machine shop, who machined countless support structures used in my experiments. Although Joël speaks French, he picked up very quickly on my wild gesticulations.

The pursuit of science is only possible through the obscured sacrifices of many people. My family back home has relinquished many privileges, surrendered, and curtailed their pleasures for the sake of my perpetual scientific pursuit. My perennial absence in their affairs borders on the ad nauseam and no amount of words can describe their contributions.

Long before science allured me, I was charmed by someone else and I am lucky to have married her. Her unflinching support has nullified the lows and magnified the highs of this journey.

Thank you, everyone!

Saood I. Nazir

Neuchâtel, September 29th, 2021

Abstract

Miniaturization has been at the forefront of scientific research in the past decade covering diverse areas such as electronics, mechanics, and optics. While ‘small is beautiful’ may be a vast generalization, the true benefits of miniaturization are especially evident in terms of performance, robustness, packaging density, and manufacturing cost.

In this context, femtosecond laser processing of transparent dielectric materials has emerged as a versatile tool for designing complex shapes at the micro-scale. Its three-dimensional (3D) capability, single-step maskless fabrication approach, and material-independent nature bypass many limitations of traditional lithographic methods, thereby enabling the fabrication of micro-mechanical and micro-optical components in glass substrates, as well as their monolithic integration for optomechanical, optofluidic, and other such applications.

The subject of this thesis is permanent high-precision alignment of micro-optical components. Here, we explore the use of femtosecond laser processing to fabricate pseudo-monolithic optical assemblies. Specifically, we integrate complex optomechanical functions on a single glass substrate and investigate novel non-contact alignment methods based on complex morphological events that occur within a laser-irradiated region. Due to the non-linear nature of laser absorption, the alignment method distinguishes itself from existing methods by its ability to introduce permanent and controlled sub-nanometer deformations in 3D glass micro-positioners, thereby forming a single monolith on which optical components are placed.

First, we discuss some general design principles for micro-positioning elements. Although a plethora of examples can be found in literature, we establish certain constraints, based on which, some designs are chosen for further investigation. Next, we carry out component-level demonstrations by actuating the chosen designs using non-ablative femtosecond laser exposure. The laser exposure strategy, which is a crucial part of the alignment process, is also investigated and optimized. Later on, system-level integration is demonstrated in a fiber-coupling device by combining two alignment functions on a single substrate. Inside a compact design footprint, we achieve a near-theoretical coupling efficiency.

Alignment sensitivity requirements vary from case to case and can range between sub- μm down to sub-nm levels. To investigate the resolution capability of femtosecond laser-enabled fine-alignment methods, we test this approach on a Fabry–Pérot cavity, typically designed for atom trapping applications, and that illustrates an application with extreme resolution requirements.

Finally, as an essential parameter for sustainable packaging, we report on the long-term stability of laser-aligned optical systems. There, using a novel micro-tensile testing method, the room-temperature relaxation dynamics of fused silica under static stress conditions are explored for stress levels approaching 2 GPa.

This work holds promise for both research and industrial applications. It enhances the potential of femtosecond laser micromachining by adding alignment functions, thereby enabling the fabrication of an ‘all-glass optical motherboard’, onto which optical components are added. The potential resolution of this method, combined with the intrinsic material properties of fused silica, are particularly interesting for the packaging of high-precision instruments, such as those for space applications.

Keywords: Femtosecond laser microfabrication, non-contact manipulation, permanent repositioning, optical packaging, integrated optics, monolithic, stress relaxation in glass, optical cavities.

Résumé

Depuis plusieurs décennies, la miniaturisation de systèmes se retrouve au cœur même des développements scientifiques, dans des domaines aussi variés tels que l'électronique, la mécanique et l'optique. L'expression "small is beautiful" ne justifie pas à elle seule cette orientation technologique, mais car la miniaturisation présente véritablement des avantages indéniables et attrayants, aussi bien en termes de performance, que de robustesse, de compacité, de densité d'intégration de composants et coût de fabrication.

Dans un tel contexte, le traitement de matériaux diélectriques transparents par laser femtoseconde s'est établi comme un outil polyvalent, de premier choix, pour concevoir des formes complexes à l'échelle micro. Sa capacité à adresser les trois dimensions de l'espace, sans masque et en une seule étape d'écriture, indépendamment du choix du matériau, permet de contourner de nombreuses limitations auxquelles les méthodes lithographiques traditionnelles sont confrontées. Rendant ainsi possible la fabrication monolithique de systèmes optomécaniques, optofluidiques, etc. associants des composants micromécaniques et micro-optiques gravés directement dans des substrats de verre.

Cette thèse se focalise sur l'établissement d'une technique qui permet un alignement permanent et de haute précision de composants micro-optiques. Nous y explorons l'utilisation du traitement laser femtoseconde pour fabriquer des assemblages optiques pseudo-monolithiques. Plus précisément, nous intégrons des fonctions optomécaniques complexes sur un substrat de verre unique, et nous étudions une nouvelle méthode d'alignement basées sur des modifications locales et complexes du matériau par irradiation laser. En raison de la nature non linéaire de l'absorption laser, la méthode d'alignement, ici explorée, se distingue des méthodes existantes par sa capacité à générer, sans contact, des déformations sub-nanométriques contrôlées et permanentes dans des micro-positionneurs fabriqués directement en 3D dans le substrat de verre, sur lesquels sont fixés les composants optiques.

Tout d'abord, nous discutons de certains principes généraux de conception des éléments de micro-positionnement. Bien qu'une pléthore d'exemples puisse être trouvée dans la littérature, nous établissons certaines contraintes, sur la base desquelles, certains modèles sont retenus pour une étude plus approfondie. Ensuite, nous effectuons diverses démonstrations expérimentales au niveau des composants, pris isolés, en les actionnant à l'aide d'une exposition non ablative avec un laser femtoseconde. La stratégie d'exposition au laser, qui est un élément crucial du processus d'alignement, est également étudiée et optimisée. Ensuite, la preuve de concept est poussée au stade d'un système, avec un dispositif de couplage de fibres qui combine deux fonctions d'alignement intégrées sur un seul et même substrat. De manière très compacte, nous obtenons une efficacité de couplage très proche de la valeur théorique.

Les exigences en matière de précision d'alignement varient d'un cas à l'autre, pouvant aller d'un niveau sous-micrométrique (sub- μm) à sous-nanométrique (sub-nm). Pour étudier la capacité de résolution des méthodes d'alignement fin par laser femtoseconde, nous mettons à l'épreuve cette approche avec une cavité Fabry Péro, typiquement conçue pour une capture d'atomes par piège optique, et qui illustre une application aux exigences de résolution extrêmes.

Enfin, en tant que paramètre essentiel pour la réalisation de produits finis, déployés industriellement, qui se doivent d'être fiables et qui perdurent dans le temps, nous analysons la stabilité à long terme des systèmes optiques alignés par notre méthode laser femtoseconde. La dynamique de relaxation du verre de silice produit par fusion est étudiée à température ambiante, à l'aide d'une nouvelle méthode d'essai, qui permet de générer par microtraction des contraintes statiques dont les niveaux peuvent avoisiner jusqu'à 2 GPa.

Ces travaux sont prometteurs tant pour la recherche que pour des applications industrielles. Ils améliorent le potentiel du micro-usinage par laser femtoseconde en y ajoutant des fonctions d'alignement, permettant ainsi la fabrication d'une "carte mère optique entièrement en verre", sur laquelle des composants optiques externes peuvent être ajoutés et interfacés à des parties déjà gravées de façon monolithique. Le potentiel de cette méthode, pour corriger des déplacements et rotations avec une résolution extrêmement fine, associé aux propriétés intrinsèques de la silice fondue, rend cette approche particulièrement intéressante pour la réalisation d'instruments de haute précision et fiables, tels que ceux destinés à des applications spatiales.

Mots-clés: Microfabrication par laser femtoseconde, manipulation sans contact, repositionnement permanent, packaging optique, optique intégrée, monolithique, relaxation des contraintes dans les verres, cavités optiques.

Contents

Acknowledgements	v
Abstract	vii
Résumé	ix
Contents	xi
Chapter 1 Introduction	13
1.1 Assembly and fine-positioning at the micro-scale	13
1.2 Short pulse laser-matter interaction	16
1.2.1 Femtosecond laser manufacturing in fused silica	18
1.3 Stress-engineered functional devices	20
1.4 Thesis objectives and outline	24
Chapter 2 Design Methodology	27
2.1 Towards pseudo-monolithic optical assemblies	27
2.2 Femtosecond laser-enabled actuation – general concepts	30
2.3 A brief overview of the main design constraints	32
2.3.1 Range of motion	32
2.3.2 Dynamics	32
2.3.3 Real estate	33
2.3.4 Fabrication and exposure constraints	34
2.3.5 Fatigue	34
2.4 Taxonomy of mechanisms	34
2.4.1 Class A: Actuators coupled to a guidance	35
2.4.2 Class B: Integrated solution – combined actuating and guiding elements	38
2.5 Topology optimization	40
2.6 Analytical description of compliant mechanisms	42
2.7 Summary	46
Chapter 3 One degree of freedom repositioning using femtosecond lasers	47
3.1 Measurement setup	47
3.2 In-plane actuation	48
3.2.1 Working principle	48
3.2.2 Device kinematics	49
3.2.3 Fabrication process	50
3.3 Experiments	50
3.3.1 Exposure setup	50
3.3.2 Identification of optimal writing parameters using micro-cantilevers	51
3.3.3 Effect of short pulses (50 fs)	53
3.3.4 Effect of long pulses (300 fs)	55
3.3.5 Stability analysis	56
3.4 Out-of-plane actuation	57

3.4.1 Part 1: Actuator separated from flexures	58
3.4.2 Part 2: Flexures as actuators.....	64
3.5 Summary.....	67
Chapter 4 Femtosecond laser-assisted optical packaging	69
4.1 Introduction.....	69
4.2 Coupling device	70
4.2.1 Motion kinematics.....	73
4.3 Volumetric distribution of stressors.....	74
4.3.1 Horizontal writing vertical stacking.....	74
4.3.2 Vertical writing horizontal stacking.....	75
4.3.3 Point writing.....	77
4.4 Monolithic fiber coupler	79
4.4.1 Fabrication and assembly	79
4.4.2 Fiber injection experiment	80
4.4.3 Loss analysis	83
4.5 Summary and discussion	83
Chapter 5 An all-glass fiber Fabry–Pérot cavity	85
5.1 Fabry–Pérot resonator.....	85
5.2 Design and experiment	87
5.2.1 Design	87
5.2.2 Experiment	89
5.2.3 Towards a laser-aligned FFPC.....	94
5.3 Summary.....	98
Chapter 6 The behavior of fused silica under high stress at room temperature	99
6.1 Introduction.....	99
6.1.1 Water in glass.....	99
6.2 Stress optimization within stressors.....	100
6.3 Device mechanism.....	104
6.4 Experimental procedure.....	106
6.4.1 Fabrication and re-exposure.....	106
6.4.2 Retardance measurements.....	109
6.4.3 Stress measurements over time	111
6.4.4 Stressed micro-tensile beam profile	115
6.5 Discussion and interpretation.....	116
6.6 Summary.....	120
Chapter 7 Epilogue	121
7.1 Summary.....	121
7.2 Outlook	123
Annex A: Bimorph strain validation	125
Bibliography	126
Curriculum Vitae	137

Chapter 1 Introduction

Our motivation in this thesis is to provide a framework for developing monolithic or pseudo-monolithic free-space optical systems. Conventionally, any optical system or device is an assembly of multiple components and with different material properties, all assembled on the same bench. A given attachment method is used to feed an input into the system, which propagates through the assembly and results in the desired output. This work aims at circumventing such conventional approaches of assembly and proposes methods where a functional system is constructed from a single monolith, or assembled into a monolithic design block with pre-aligned markers. Such methods hold promise for the development of high-precision integrated optical systems that demand stringent alignment tolerances and high thermal and mechanical stability. To facilitate this, femtosecond laser processing is used as a manufacturing tool to fabricate such systems, and afterward, the same tool is also used to reposition the constituent elements into a permanent and well-defined orientation.

Under this purview, we start by reviewing some commonly used methods to align micro-systems.

1.1 Assembly and fine-positioning at the micro-scale

The increasing strive towards miniaturization of optical systems puts extremely stringent requirements on the spatial and angular positioning accuracy between various components. At the macro-scale, such demands can be fulfilled relatively easily since the functional elements can be handled using conventional pick-and-place techniques. However, as size of the objects scales down, physical manipulation becomes increasingly difficult. Forces such as surface adhesion, friction, and Van der Waals interaction, which are insignificant in the macro-world become dominant at the micro-scale. Although sometimes possible, fulfilling positioning requirements in optical assemblies during the manufacturing step itself is technologically challenging and economically impractical. Instead, a commonly used approach relies on coarsely aligned systems, that are further fine-adjusted in a post-processing step, thereby offering more flexibility and lower manufacturing cost.

A simple example of high precision positioning is best illustrated in optical fiber connectors. Such connectors use a re-mateable physical connection between two optical fibers, which are epoxy-glued into cylindrical ferrules with a precision hole at the center. A high-performance connector, i.e. low insertion loss at the mating point, requires a near-perfect concentricity between the optical axis of the fiber and the ferrule axis. Imperfections can stem from various sources, such as cladding-to-core or ferrule-hole to ferrule-outer-diameter eccentricities or a mismatch between hole and cladding diameters. This inherent manufacturing tolerance directly affects the performance of these connectors. In high-end connectors, to position the fiber core at the center of the ferrule, a mechanical method using an indenter-like tool (Figure 1.1) is used to plastically deform the metallic region surrounding the fiber [1]. As the tool is pressed into the fiber end face, the ferrule is rotated and at the same time, light propagating through the fiber is monitored on a camera. In this manner, eccentricities upto $0.25\text{ }\mu\text{m}$ can be achieved.

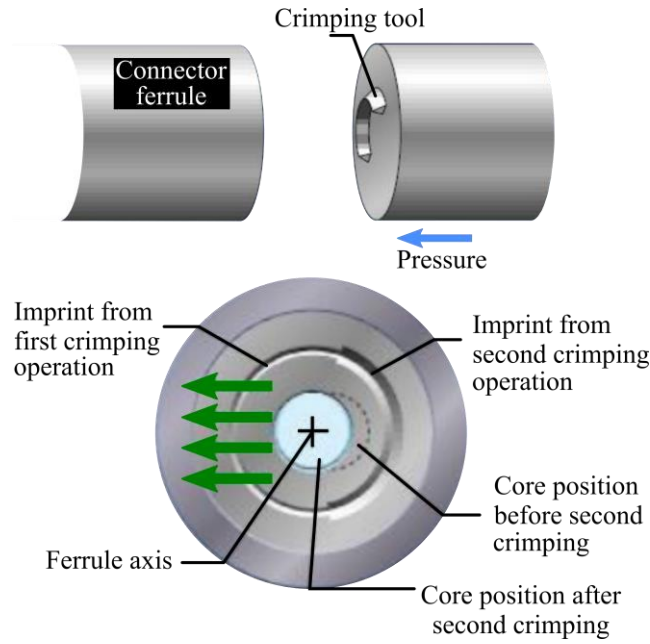


Figure 1.1 – Active alignment of optical fiber connectors using mechanical indentation [1], [2].

More complex examples are found in a variety of optical assemblies. Specifically, optical systems designed for space applications need to sustain extreme climatic conditions and therefore need to be robust, thermally as well as mechanically, and maintain alignment over long experimental durations. As post-launch adjustment is seldom possible, most such systems are aligned and permanently fixed into place before launch. Figure 1.2 shows some relevant examples where, in Figure 1.2a [3], optical elements are first glued into place while being held by a high-precision six-axis manipulator. Alignment is actively controlled during the fixation step, resulting in a permanently aligned system. In Figure 1.2b [4], resistance soldering technique is used to thermally melt a thin layer of solder deposited on the base plate. While the solder solidifies, the optical component is continuously aligned using a similar approach. The example of Figure 1.2c [5] uses a pre-defined template fabricated on a Zerodur baseplate, into which optics are assembled and fixed using hydroxide-catalysis bonding [6], [7]. Since these methods sandwich a filler (glue, solder, hydroxide solution, etc.) between two surfaces, the assembly is cumbersome and requires control over various process parameters for perfect bonding. To achieve uniform filler thickness across the interface, perfect parallelism between surfaces, and long curing times are some of the common challenges. The active alignment step is challenging too, often requiring multiple alignment lasers and position sensing detectors (PSDs) to obtain positional and angular metrology information. More such examples can be found in [8]–[11].

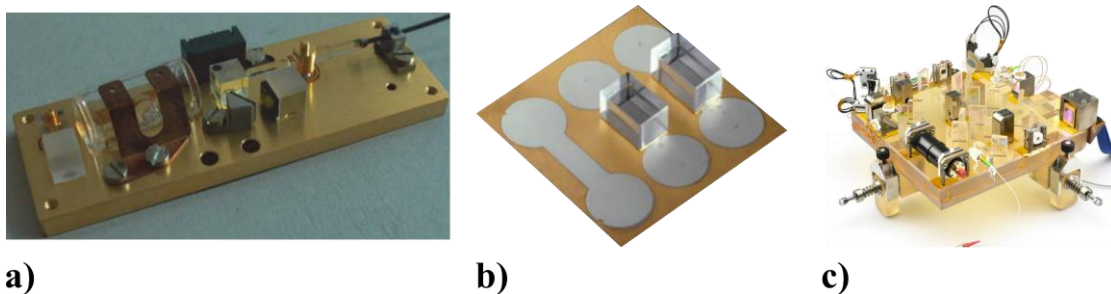


Figure 1.2 – Some examples of permanently aligned high-precision optical systems. a) A miniature optical system designed for space qualification [3], and fixed using adhesive bonding. b) Fixation of optical components using resistive soldering [4]. c) A complex optical assembly designed for light interferometer space antenna (LISA) [5], and fixed using hydroxide catalysis bonding.

Due to the limited access to components of a fully assembled system, mechanical deformation or repositioning through physical contact is not always possible. The forces therewith can also introduce perturbations in other parts of a multi-component assembly. As such, laser-based non-contact positioning methods are common in numerous applications involving precision assembly. Unlike their mechanical counterparts, these methods offer more flexibility, cleaner process conditions, long-term reliability, and do not require a work-piece-dependent tool but can be easily adapted to different conditions by simply changing the laser parameters. Below, we review some of these methods.

A common method of laser-based adjustment originates from the flame bending technique. Through laser-induced non-uniform thermal stress [12], [13], a localized deformation is created in a selected location acting as a deformable element. As the laser is focussed on the surface of such element, a temperature gradient builds up near the surface gradually decreasing along the laser propagation direction (Figure 1.3a). As the temperature rises, the material begins to expand, gradually introducing stress in the laser-affected zone and the surrounding volume. If the temperature and consequently the stress are high enough, the region deforms in a non-reversible manner. When the laser is switched off, the temperature gradient reduces slowly, and as the material starts to cool down and shrink, permanent deformation occurs towards the modified surface. Due to its thermal nature and the presence of a heat-affected zone, permanent residual stresses remain in the laser-exposed element. Furthermore, the deformation occurs through linear absorption of the laser energy and is thus limited to the surface of materials. Furthermore, this principle only applies to materials that can be plastically deformed, typically metals, and as such, excludes brittle materials which often have the best thermal stability behavior. Inherent to its working principle, mostly bending motion can be produced or one-axis expansion in thin elements. Although motion along two axes has also been shown [14], in the context of optical devices where translations and rotations are necessary functions, the process has limited applicability.

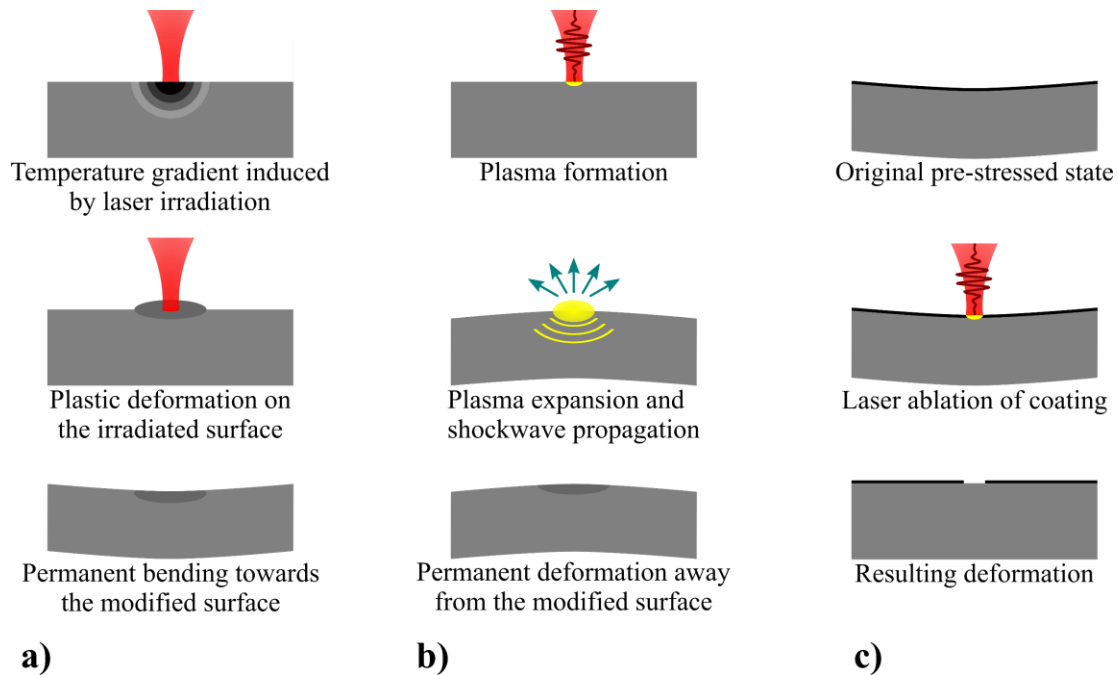


Figure 1.3 – Non-contact adjustment processes using lasers. a) Temperature gradient mechanism uses laser energy to create a surface thermal expansion. b) Laser-shock adjustment uses shorter pulses between nanoseconds and picoseconds to generate a plasma shockwave in the material. c) By using a pre-stressed coating and short pulse lasers, local ablation of the coating causes stress relaxation and subsequent deformation.

To circumvent the heat-related effects, adjustment using short pulse lasers offers a non-thermal interaction zone as will be discussed in more detail in the next section. While still relying on linear absorption events, the use of shorter pulses lowers the interaction timescale and minimizes thermal diffusion effects. The ad-

justment process, known as laser-shock adjustment (Figure 1.3b), uses a sacrificial layer that is locally ablated by tightly focussing a high-intensity laser pulse [15]–[18]. During this process, material from the sacrificial layer is vaporized and a recoiling shock-wave propagates through the sample resulting in a permanent plastic deformation away from the irradiated surface. Unlike the thermal deformation described above, adjustment is almost instantaneous, and according to [18], bending accuracies approaching few tens of nanoradians can be achieved, and that too in a wide variety of materials such as copper, silicon, glass, etc.

A technique similar to laser-shock adjustment makes use of a coating to pre-stress the substrate [19], resulting in a curved starting position (Figure 1.3c). After laser exposure, the coating is locally ablated thus relaxing the initial stress. This results in a change in curvature of the actuator. In terms of applications, short-pulse laser adjustment is mostly used for curvature adjustment of micro-cantilevers. Furthermore, as it remains a surface interaction effect, the process has limited applicability.

Although the above methods fulfill adjustment requirements at the micro-scale, they have certain limitations in the case of optical systems, which require more complex adjustments such as rotations or pure translations along certain specific axes than simple bending. Furthermore, and as mentioned earlier, the presence of a heat-affected zone and requirements of specific substrate material further limit their use in such cases.

In what follows, we build our case for non-contact alignment using femtosecond laser-induced non-linear absorption in transparent dielectric materials such as fused silica. At first, laser-matter interaction is discussed for short pulses, followed by a state-of-the-art of ultrafast laser manufacturing process. Next, through some examples, we discuss the potential of the process for fabricating high-precision functional devices. Finally, the concept of adding stress-induced functionalities is introduced followed by the thesis objectives and outline.

1.2 Short pulse laser-matter interaction

The field of optics in general, and lasers in particular, has come a long way since their first experimental description in 1960 by Theodore H. Maiman [20]. More than two decades later, Donna Strickland and Gerard Mourou evidenced Chirped Pulse Amplification (CPA) [21], which made it possible to achieve extremely narrow pulses down to a few femtoseconds together with high peak powers of the order of terawatts. Two years later in 1987, the first reports about material modification using ultrafast lasers were published separately by Srinivasan *et al.* [22], and Küper and Stuke [23]. In the last three decades, significant advances have been made in the area of ultrafast laser-based manufacturing, which has paved the way towards optical re-wiring in transparent materials and manufacturing completely monolithic circuitry.

Laser-matter interaction can be radically different depending on the temporal width of the irradiating pulse. For shorter pulses of the order of a few hundred femtoseconds, and under tight focusing conditions, ultra-high intensities of tens of gigawatts per millimeter square are attained inside the focal volume. These high intensities trigger *non-linear* absorption events in an otherwise transparent material leading to effects such as multiphoton, avalanche, and tunneling ionization [24], [25]. For a certain exposure dose exceeding the threshold of the material for a permanent modification, an irreversible structural change occurs inside the material. What makes ultrafast laser processing so versatile is the confinement of the modifications *within* the focal volume. In other words, the interior of the laser-transparent material gets modified with no change occurring on the surface, which is otherwise impossible to achieve using mechanical tooling processes.

Longer pulses of the order of a picosecond to tens of picoseconds can cause material breakdown too, however, larger pulse energies are required to surpass the modification threshold of the material. Another primary difference is the size of the heat-affected zone, which extends beyond the focal volume due to comparable timescales of thermal and excitation effects [26]–[30]. On the contrary, for pulses in the femtosecond regime, the heat-affected zone is suppressed. Even though local heating of electrons in the irradiated region can oc-

cur, the timescale for thermal diffusion events to start is orders of magnitude higher than the electron excitation time. Such de-coupling ensures a very small damage region, which is limited to the focal volume.

As a material, fused silica is one of the most commonly used materials for ultrashort pulsed laser processing. A wide array of parameters such as laser wavelength, pulse width, pulse energy, repetition rate, net fluence or deposited energy, writing speed, and focal spot size can induce different types of modifications in fused silica [30]. In the existing nomenclature, such modifications are commonly classified into three types of morphologies as shown in Figure 1.4 and elaborated below.

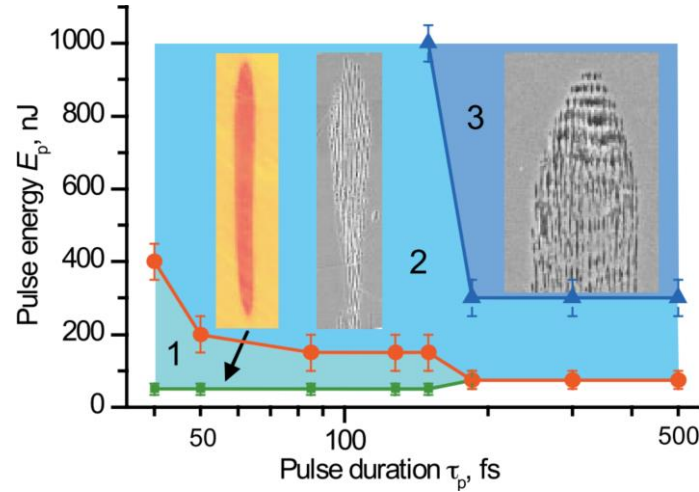


Figure 1.4 – Different types of modifications that can be generated in fused silica using femtosecond laser exposure [31]. In the inset, pictures are shown for three different morphologies, nicknamed Type I (left, smooth modification), Type II (middle, nanograting regime), and Type III (right, chaotic patterns). In this thesis, the same nomenclature will be used to refer to these modifications.

Type I modifications occur for shorter pulse widths (< 200 fs) and at lower pulse energies just above the modification threshold. In the irradiated region, a smooth modification is observed accompanied by an optically isotropic and positive change in the refractive index in comparison to the surrounding pristine material [32], [33], and generation of localized defects [34]. The increase in refractive index is believed to occur mainly due to a localized increase in material density, which has been experimentally verified by various means, such as through scanning thermal microscopy [35], [36], Raman spectroscopy [35], [37], and nanoindentation combined with birefringence measurements [38]. Since the pioneering work at Kyoto University in Japan in the mid-nineties [32], [33], who first demonstrated that such modifications can confine and guide light, many researchers around the world [39]–[47], including companies such as Translume Inc. [48], Optoscribe, Modular Photonics, and FEMTOprint to name a few, have demonstrated index contrast waveguides with $\Delta n \sim 10^{-3}$ on average. Other applications for photonics lanterns [49], [50], photonic quantum circuits [51]–[56], fluidic devices [57], [58] for lab-on-a-chip applications [59], [60], and micro-molding and beyond [61]–[63] have also been showcased. The work in [32] marks a seminal event in the processing of materials using femtosecond laser pulses, and the field of direct-write optical components has seen an explosive growth since then.

Type II modifications occur at similar pulse widths or longer but with higher pulse energies. The modified region exhibits an optical anisotropy characterized by the formation of sub-wavelength periodic structures within the focal volume. These structures, popularly called ‘nanogratings’, show a $\lambda/2n$ periodicity, strong form birefringence [64] and polarization-dependent scattering [65], and reflection [66]. An average negative refractive index change is observed within the periodic structures. Using backscattered electron imaging, Shimotsuma *et al.* [67] showed that nanogratings consist of periodically distributed oxygen-deficient regions. Bricchi *et al.* [68] correlated the negative index change and form birefringence to the existence of periodic

modulation of refractive index within the nanogratings themselves. According to them, nanogratings consist of alternating regions of higher and lower refractive indices, thus leading to a polarization-dependent response, and hence this form birefringence effect.

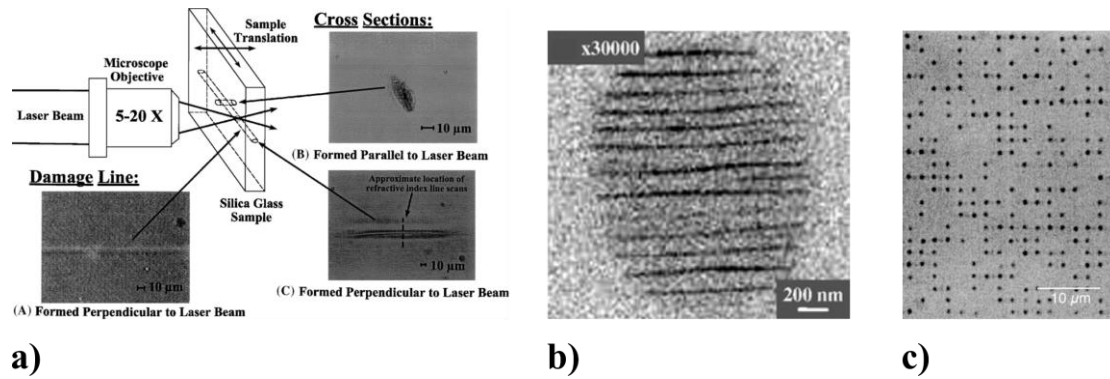


Figure 1.5 – Seminal events in the field of femtosecond laser processing. a) The first demonstration of waveguide writing in a variety of glasses as shown in [32]. b) A scanning electron microscope (SEM) image of nanogratings that form inside the irradiated volume [67]. c) A transmitted light photograph of a binary data pattern stored inside fused silica [69].

Type III modifications occur for longer pulse widths and have a larger modification threshold (approaching micro-joule). The modified region consists of disruptive void-like defects [70].

The above two regimes are being actively researched for high-density optical data storage applications [69], [71], and are at the core of microfabrication processes based on femtosecond laser exposure combined with wet chemical etching [72]–[74]. For the latter, considering its importance for the current work, we elaborate on it further in the next section.

1.2.1 Femtosecond laser manufacturing in fused silica

Fused silica, with its wide transparency window extending to mid-IR, is one of the most widely exploited materials for three-dimensional (3D) manufacturing using femtosecond lasers. Among its useful properties, it is chemically inert and does not react with most chemical compounds. Such inertness is useful in a laboratory environment when used as a tool in contact with caustic chemicals in biological or microfluidic applications. It has a high glass transition temperature (T_g) and therefore, it is suitable for laboratory equipment and high-temperature applications. Fused silica is also one of the most thermally stable materials with the lowest known coefficient of thermal expansion ($CTE \sim 10^{-7}/^{\circ}C$) among non-engineered materials, making it thermal shock resistant.

Together with its excellent material properties, the ability to modify fused silica using femtosecond laser processing has diversified its use in various applications covering optical, electronics, biological, and chemical engineering. Particularly for Type II modifications, an enhanced etching rate is observed for laser exposed regions compared to pristine material in chemical etchants such as dilute hydrofluoric acid (HF) [73]–[75], potassium hydroxide (KOH) [76], [77], and recently, NaOH [78]. The etching rate can be controlled by adjusting the polarization of the laser [79], thus allowing 3D fabrication of arbitrarily shaped structures on the surface as well as in the bulk of the material. A typical setup for laser processing of a fused silica wafer is shown in Figure 1.6.

The ability to modify bulk material properties in combination with wet chemical etching offers a powerful tool for the 3D structuring of dielectric materials. For example, Cheng *et al.* [80] fabricated a micro-mirror and an embedded mini-optical circuit in photosensitive glass with superior optical quality. Tielen *et al.* [81] reported a 3D cross pivot with overlapping notch hinges fabricated in fused silica using the same process. At

the micrometer scale, fabrication of such a pivot is not possible using conventional fabrication techniques including lithographic approaches. In [74], Bellouard *et al.* demonstrated high aspect ratio microfluidic channels paving the way towards monolithic μ -total analysis systems and lab-on-chip devices [82]. In [83], the same authors demonstrated a merger of optical and mechanical functions by fabricating an array of waveguides on a flexure-based motion stage, movable with respect to a stationary waveguide for embedded displacement sensing applications. A remarkable thing about this optomechanical device is its monolithic nature and the unusual combination of functions offered by femtosecond laser processing. Similarly, integration of electro-mechanical functions has also been reported [84].

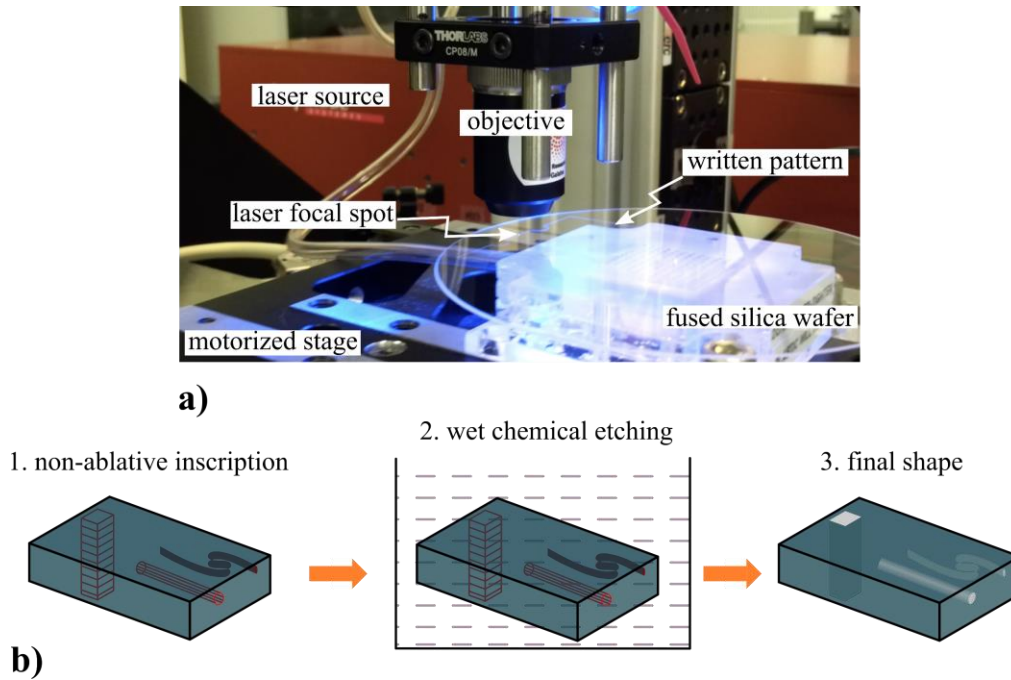


Figure 1.6 – Overview of the femtosecond laser manufacturing process. a) Using a high magnification objective, a low-energy femtosecond pulse is focussed on the substrate, and the material is modified layer by layer through a combined motion along X, Y, and Z axes. b) In a second step, the modified material is removed by wet chemical etching in a dilute solution of hydrofluoric acid.

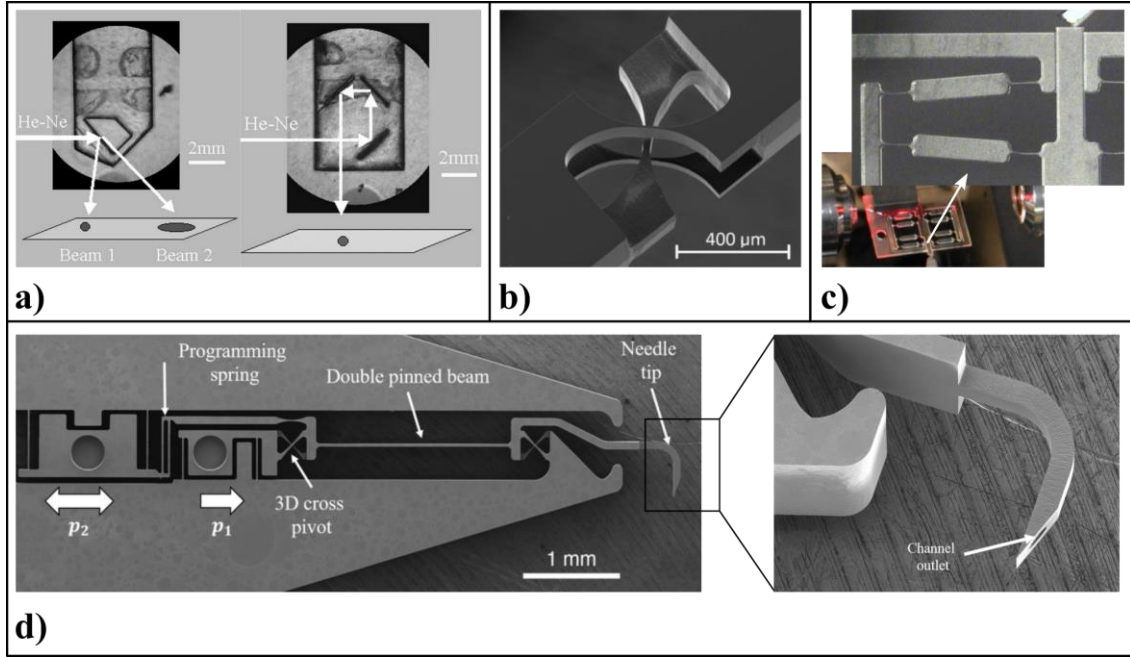


Figure 1.7 – Some illustrations demonstrating the applications of femtosecond laser fabrication process. a) A micro-optical circuit embedded in Foturan [80]. b) a 3D cross-pivot [81]. c) An all-glass optomechanical device with onboard waveguides for sensing applications [83]. d) A miniature high-precision medical device made in glass to inject medicine into retinal veins [85]. The device consists of integrated fluidic channels for drug delivery and a bi-stable flexure mechanism that produces a rotational motion of the needle tip when actuated.

1.3 Stress-engineered functional devices

Beyond the manufacturing of 3D shapes and devices discussed in the previous section, femtosecond laser processing has been extensively used to embed functional elements in bulk glass. This is made possible by the formation of nanogratings during the exposure step. Unlike normal birefringence which occurs due to optical anisotropy and is found in crystalline materials such as calcite and quartz, the internal structure of nanogratings consists of isotropic nanopores organized anisotropically in nanoplanes [68], [86]. This creates a strong form birefringence localized in the modified volume. The organization of nanogratings have a dual periodicity [87], one along the direction of polarization and the second along the direction of light propagation, leading to two different refractive indices along these directions. Therefore, a beam of light passing through these structures experiences phase retardation depending upon its polarization with respect to the interface.

Exploiting this phenomenon, it is possible to fabricate polarization-sensitive elements such as waveplates [88], [89], diffractive optical elements [90], [91], and polarization converters [92] inside an otherwise isotropic material. In [93], the authors used a laser imprinted half-wave plate matrix to simultaneously achieve more than four polarization states for fast high-density data storage in glass. To do so conventionally would require rotating a half-wave plate for achieving different polarizations, thus slowing down the process. Some examples are shown in Figure 1.8.

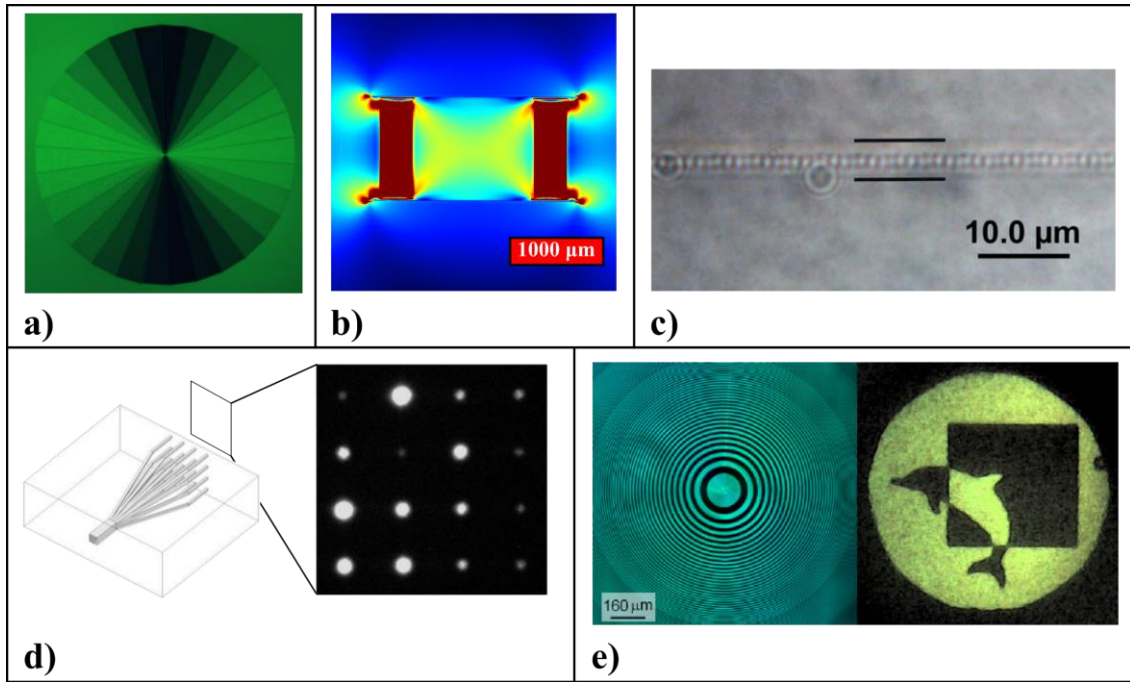


Figure 1.8 – Some examples of optical functionalities embedded inside glass using femtosecond laser processing. a) A vortex converter with varying retardation achieved through a spatially variant distribution of nanogratings [92]. b) A waveplate embedded in glass employing stress-induced birefringence [94]. c) A waveguide Bragg grating (WBG) written inside a femtosecond laser inscribed waveguide (shown by black lines) [95]. d) Schematic of a photonic lantern connecting multiple single-mode fibers into a multimode fiber [49], [50]. A white light transmission micrograph is shown on the right. e) A birefringent Fresnel zone plate inscribed in fused silica [88]. On the right, the University of Southampton logo is imaged.

Femtosecond laser exposure using low-energy non-ablative pulses also leads to a volume change in the modified zone [96], [97] – material densification in Type I modifications causes a reduction (compressive stress), whereas porosity of the nanoplanes leads to an increase in volume (tensile stress) in Type II modifications. The change in glass volume induces a permanent elastic strain, and therefore stress in-and-around the modified region. Interestingly, the stress field can be changed not only in direction, i.e. compressive to tensile, but also in magnitude by changing the laser polarization [98], [99], and is therefore a powerful tool to embed optical functions devoid of scattering effects caused by the nanogratings. For example, the waveplate shown in Figure 1.8b [94] uses volume expansion of the nanogratings to create stress-induced birefringence inside an optically clear aperture. In [96], Champion *et al.* used a micro-mechanical approach to measure these changes, which we will re-use later in Chapter 3. The same method was also used in [97] to demonstrate the stress-state inversion by varying the deposited energy (Figure 1.9) and was further expanded recently to investigate the temperature-dependant mechanical properties of laser-written patterns [100]–[102].

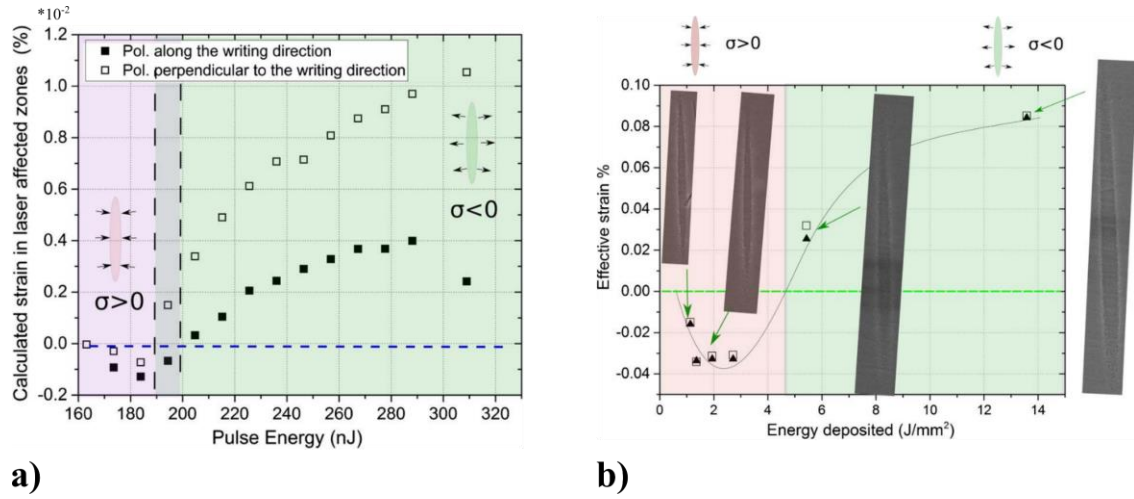


Figure 1.9 – Transition from Type I to Type II modifications as a function of laser parameters [97]. Using a micro-mechanical method, the authors demonstrated opposite bending behavior of a cantilever beam when exposed near its surface. a) Strain inside the modified zone as a function of pulse energy. Above a certain threshold (190 – 200 nJ), negative strain (indicative of compressive stress in Type I modifications) gives way to positive strain (indicative of tensile stress in Type II modifications). This transition can be traced to a similar trend observed in Figure 1.4. b) The transition from negative to positive strain can also be observed for Type I at a fixed pulse energy, by gradually increasing the deposited energy, and this, despite the absence of nanogratings. The cause of this particular stress-state inversion is assumed to be related to the gradual appearance of pores in the laser-affected zones as the exposure dose is increased.

Earlier we discussed the integration of mechanical and optical functions in a glass-based device [83]. Although such addition of localized functionalization is not new and has been earlier demonstrated for other materials [103], utilizing glass for mechanical functions sounds very counter-intuitive due to its low toughness and brittle nature. However, fused silica flexures fabricated by femtosecond laser processing (Figure 1.10a) have been shown to sustain extraordinary stress levels reaching 2.7 GPa [104]. Not to forget, this is positively assisted by the fabrication technique as well as by chemical etching, which results in a smooth profile devoid of surface defects.

It is however only recently that glass-based *active* mechanical components have started to gain some attention. An electrostatic micro-actuator was demonstrated in [105] inside a transparent glass monolith using femtosecond laser processing and wet chemical etching. The device (Figure 1.10b) combines comb arrays with flexures to produce a linear translational motion. Another device was reported in [84] that relies on dielectrophoresis actuation of a micro-mechanical cantilever.

In [106], and shown in Figure 1.11, a similar integration principle was demonstrated, albeit one major difference – the electrostatic actuation is replaced by laser-based remote actuation. In this device, a flexure motion stage is attached to a U-shaped actuator, which when exposed in different regions by a femtosecond laser, undergoes a volume change and generates a push/pull force on the stage.

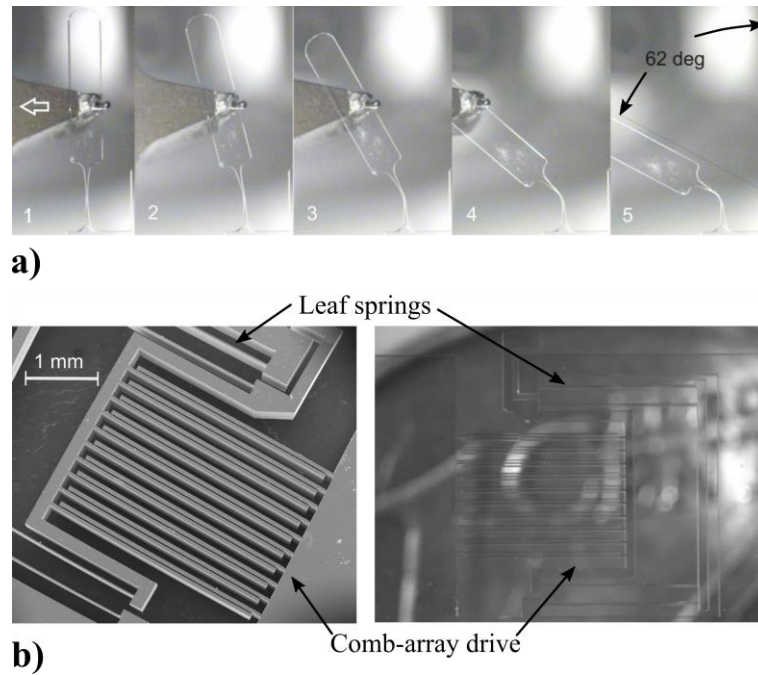


Figure 1.10 – Micromechanical elements fabricated in a glass substrate. a) A fused silica flexure is shown under gradual elastic deformation during a bending experiment [104]. b) SEM and microscope images of an electrostatically actuated transparent glass micro-actuator [105].

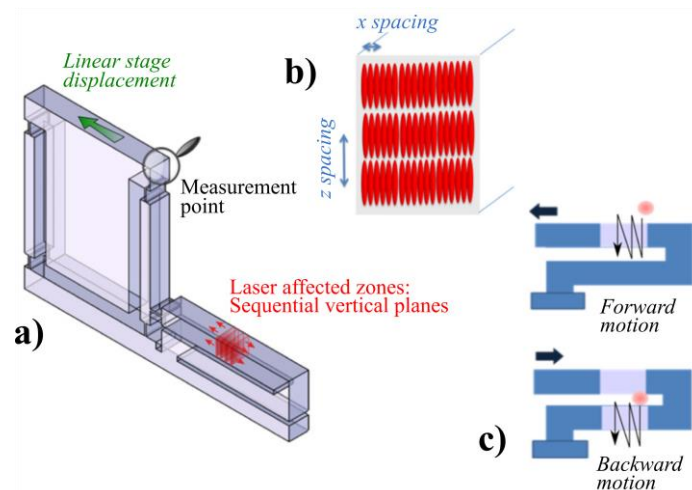


Figure 1.11 – Femtosecond laser-based non-contact repositioning principle [106]. a) Mechanical design: a linear motion stage interfaced with a U-shaped actuator. b) Non-linear absorption of the laser energy induces a volume expansion inside the modified region. c) By varying the location of the modified zone, the actuator can either pull or push on the flexure stage.

The above example also demonstrates that kinematic design of the actuator can offer an alternative to stress-state inversion – one where opposite behaviors can be simply accessed through raw mechanical design. The unique shape of the actuator in this case allows for both forward and backward motions without changing laser parameters.

Before moving further ahead, let us regroup some important conclusions:

- Ultrashort pulse lasers offer unique opportunities for the internal structuring of transparent dielectric materials. For femtosecond laser processing, fused silica offers a rich playing field enabling applications for

embedded photonics, 3D subtractive printing, micromechanics, etc., and a hybrid combination of several functions onto one single substrate.

- The structural modifications written with femtosecond lasers possess some very unique properties – a positive or negative refractive index change depending upon the type of modification, an enhanced etching rate together with a high selectivity up to 1:100 for certain etchants, and a local stress field that can be tailored in magnitude as well as in direction.
- Fused silica flexures fabricated by femtosecond laser processing show superior mechanical performance, and can stably sustain stresses in the GPa range without fracturing. Surface flaws present after fabrication are smoothened and sealed during the etching process thus enhancing their load-bearing capability. This makes them highly attractive for optomechanical systems.

Bearing these points in mind, our goal is to develop new methods for integrating complex optical functions with actuation capabilities inside a single monolith. We approach this problem by taking advantage of the 3D capability of femtosecond laser processing to fabricate non-trivial mechanical elements integrated with flexure-based motion stages, which we actuate using localized stress-state manipulation within the modified region. Therefore, a strong emphasis lies on how to fine-tune the position of optical components using non-linear laser-matter interaction without physically touching them.

1.4 Thesis objectives and outline

Within the realm of femtosecond laser manufactured 3D systems, **this work aims at developing highly integrated optical circuitry in glass, fulfilled by non-contact methods of permanent alignment, and to demonstrate their applications in selected representative examples of free-space optical assemblies.**

More specifically, our goals are:

- A comprehensive design methodology for the necessary kinematics to fulfill basic alignment functions in an optical circuit, such as translation, in-plane, and out-of-plane rotation.
- Proof-of-concept demonstration of elemental units carrying optical functions using femtosecond laser processing both for fabrication as well as alignment.
- Study of the long-term behavior of stressed fused silica under different environmental conditions.
- Proof-of-concept integrated systems for optical packaging of precision instruments.

Beyond this *first introductory* chapter, this thesis manuscript reads as follows:

The *second chapter* encompasses the kinematic design aspect of this thesis. To align any optical circuit, mirror mounts are commonly used to adjust various degrees of freedom (DOFs) such as in-plane rotation, out-of-plane rotation, translation, etc. To achieve the same in glass, various mechanisms fulfilling these functions are introduced. Broadly speaking, we discuss two classes of mechanisms – one where an actuating element is connected to a flexure kinematic, and one where the guiding flexures also serve as actuators. The chapter concludes by introducing a mathematic tool for stiffness estimation of kinematic mechanisms.

The *third chapter* introduces two elemental devices – a remote center of rotation (RCR) mechanism capable of rotating in-plane [107], and a cruciform mechanism capable of rotating out-of-plane, both functions fulfilled under the remote action of a femtosecond laser. As mentioned earlier, volume expansion of the modified zone is a function of various laser parameters. Using the approach introduced in [96], a parameter study is also carried out and subsequently reused in the rest of this thesis. The chapter concludes by experimentally validating an actuator-free compact mechanism, one where the mechanical guidance also serves as an actua-

tor, without any appreciable loss in performance. This demonstration further enriches the applicability of our methods, particularly in constrained spaces where real estate comes at a premium.

The *fourth chapter* introduces novel exposure patterns and characterizes their influence on volume expansion. To harness the maximum potential of repositioning capabilities offered by femtosecond laser exposure, distribution of the modified patterns plays an important role to generate maximum strain. The chapter also showcases how these methods can be used for the optical packaging of high-precision devices. For this demonstration, a glass coupler with a mechanically integrated optical fiber is fabricated for a high-efficiency injection from a laser diode.

The *fifth chapter* discusses progress on a fiber Fabry–Pérot cavity (FFPC) assembled and permanently aligned on a glass substrate. A Fabry–Pérot cavity demands stringent alignment accuracy together with high mechanical stability against environmental disturbances. To meet such requirements is challenging, and often requires bulky, multiple-axis alignment stages. We showcase how such a cavity assembled inside a laser machined fused silica chip – consisting of prealigned trenches for fiber alignment, together with flexure motion stages, can be permanently aligned using femtosecond lasers. We believe the methods developed in this thesis, combined with the underlying material and process advantages, can find applications in such ultra-high-precision optomechanical systems.

The *sixth chapter* addresses a crucial aspect of this thesis – stress relaxation phenomena in fused silica at the micro-scale. The study therewith investigates long-term relaxation dynamics spanning several months, in varied atmospheric conditions, and up to 2 giga-Pascal (GPa) stress levels under static loading conditions. Such experimental data, to the best of our knowledge, are unknown at room temperature in the existing literature and are essential for demonstrating the long-term viability of stress-induced devices and more specifically, their stability upon aging.

The *seventh chapter* offers a brief conclusion of the main results achieved in this thesis, discusses their potential applications, and proposes future research directions.

Chapter 2 Design Methodology

This chapter presents a design overview of the various kinematic mechanisms implemented in this thesis. These mechanisms focus on fulfilling two basic functions in an optical system – rotational and translational motion along a given axis. Although their experimental validation follows in the coming chapters, this chapter provides a general design framework. Briefly, we explore the various design constraints for flexure-based guidance mechanisms, such as physical footprint, complexity, travel range, and vibrational stability. As an important aid in kinematic design, we also present an analytical framework for a quick estimation of the cumulative stiffness of a compound kinematic mechanism. Femtosecond laser-based remote actuation, which was introduced briefly at the end of Chapter 1, is also discussed in broader detail.

2.1 Towards pseudo-monolithic optical assemblies

Our goal is to develop methods such that a free-space bulk optical circuit can be replicated as a compact, pseudo-monolithic assembly, put together on a single substrate of glass. A broader vision is depicted in Figure 2.1.

In Figure 2.1a, a free-space optical system assembled on a breadboard is shown. Apart from the obvious necessities, a basic requirement is the necessary degrees of freedom (DOFs) to align the various optical elements with respect to each other. The initial positioning is often done manually, followed by finer adjustments using in-built positioners present in the kinematic mounts. A relatively monolithic system, such as the one depicted conceptually in Figure 2.1b¹ circumvents most of the assembly requirements of Figure 2.1a; most cavity optics are fabricated into the base substrate at well-defined locations, physical adjusters are replaced by sophisticated laser-actuated adjustment mechanisms, and minimal assembly is needed at input/output ports. Although such a system is difficult to realize due to the complexities associated with the optics: in-volume 3D curvature, surface flatness, optical coatings, input/output connections (electrical or optical), etc., however, a pseudo-monolithic version, one where off-the-shelf optical elements are assembled into a monolithic design template is possible. In such a case, the compact assembly must possess the necessary DOFs, such that tolerances present in the fabrication process can be corrected.

¹ Proposal Y. Bellouard, GigaFemto, ERC-2017-PoC, 2017.

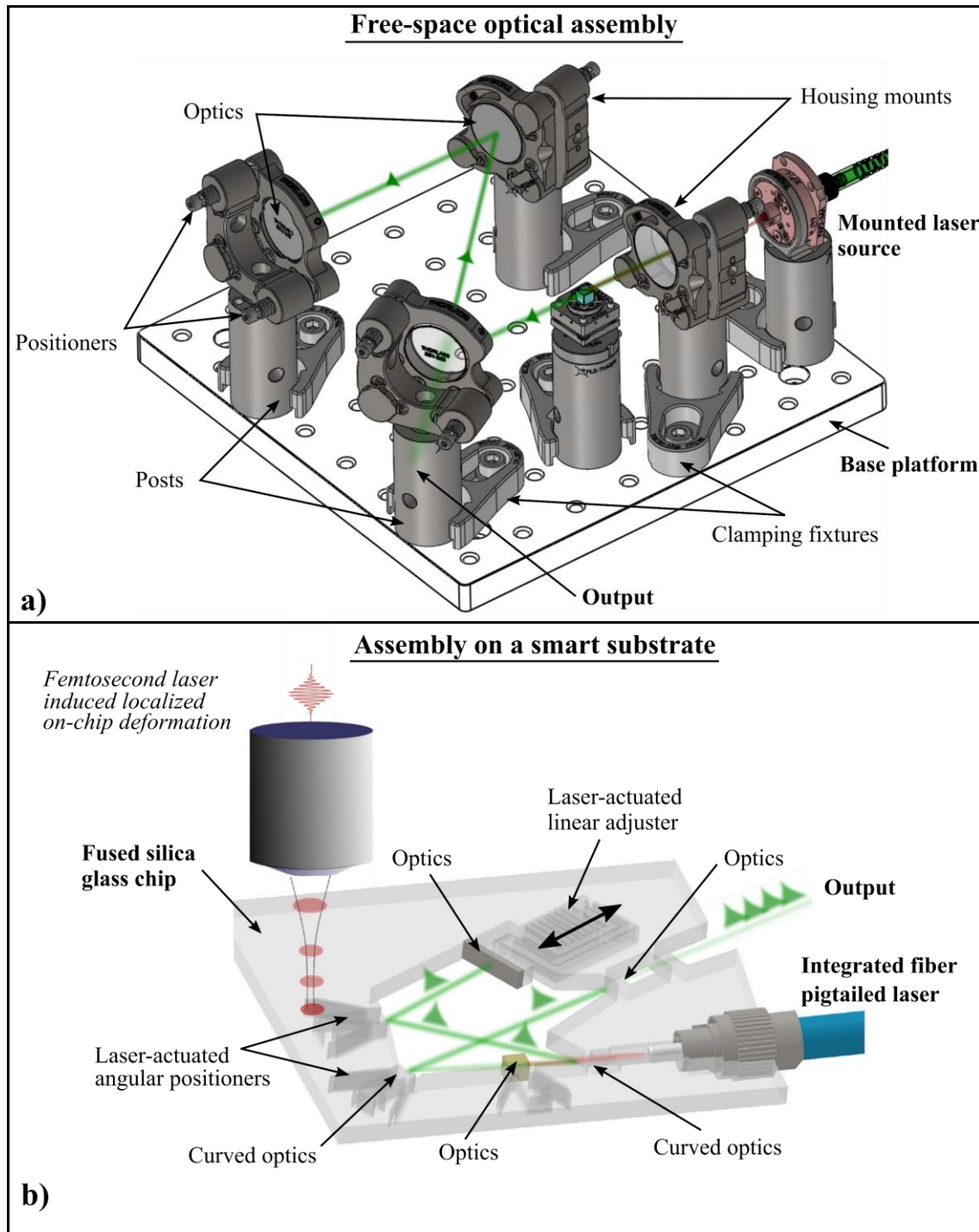


Figure 2.1 – Free-space optical assembly versus assembly on a single substrate.

The actuators present in kinematic mounts can rotate or translate the optical component along one or a set of axes. These optical mounts are themselves attached to a solid base, and once fixed, usually possess two DOFs. In an optical assembly, where multiple such mounts are used, an exceedingly large number of DOFs (in the order of 2^n , where n denotes the number of mounts used) are present, than what is theoretically necessary to fully define the optical path of a light beam. For the sake of discussion, Figure 2.2 shows a few illustrative examples.

In Figure 2.2a, a simple case of a two-mirror resonator is depicted. To align the mirrors parallel to each other, each mirror possesses two rotational DOFs. However, only two DOFs on one mirror or one DOF on each

mirror are sufficient to achieve parallelism between the mirror surfaces. Part of the issue is also related to the difficulty in reconciling pure motions and manufacturing costs. A pure gimbal mount (i.e. without parasitic motion) is complicated and more expensive to manufacture than a simpler mount with parasitic motions, in which, center of rotation of the mount does not coincide with the center of the optical element, thus producing parasitic translational motion. Therefore, to achieve two rotations while compensating the unwanted effect of linear motion coupling, four actuators are needed instead of two. The total DOFs grow rapidly with the increasing number of mirror mounts.

In Figure 2.2b, the schematic of a Z-shaped laser resonator is shown. Assuming a fixed optical pump and gain-crystal position, the cavity consists of sixteen angular DOFs. If coarse misalignments are not present, for accommodating angular misalignments, two DOFs on the out-coupler mirror can uniquely define a well-confined beam near the cavity axis, and make enough round trips to amplify the cavity mode. An additional one-axis translation can be added to fine-tune the cavity length, limiting to three DOFs as the minimum and sufficient requirement for position adjustments.

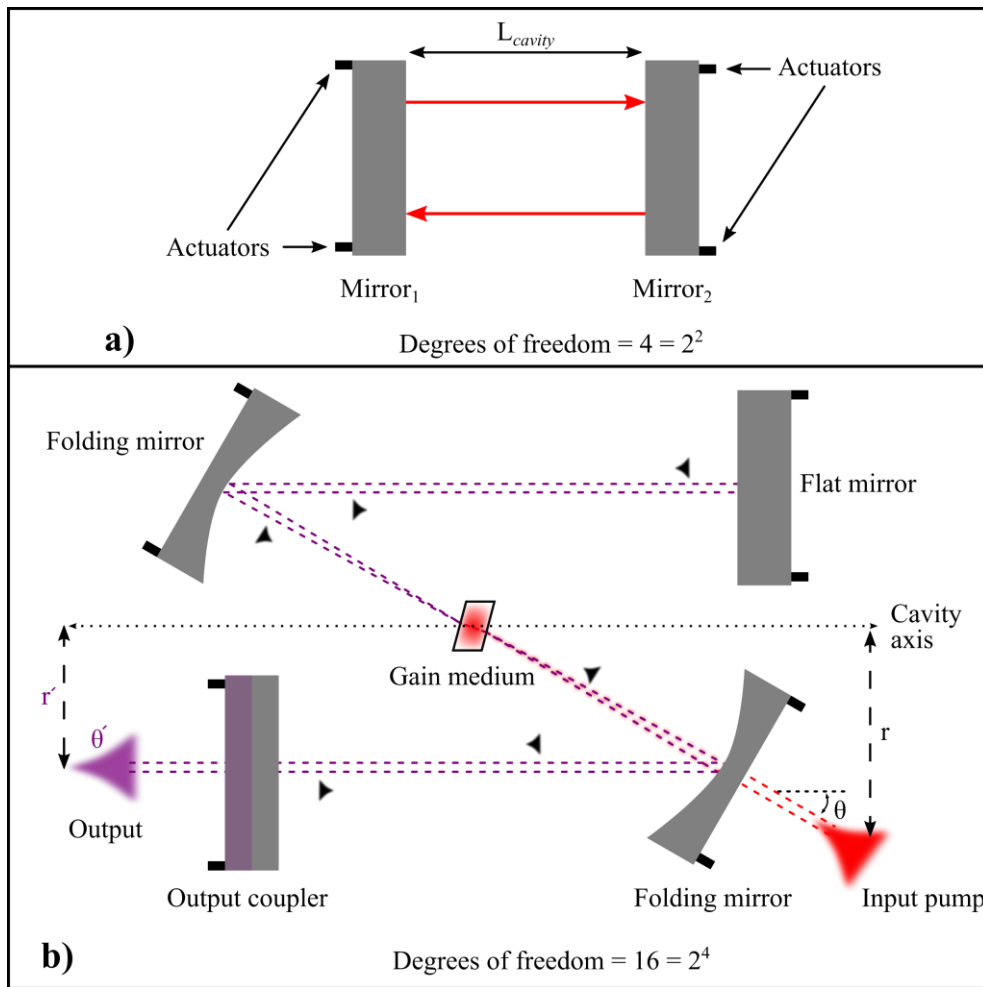


Figure 2.2 – Degree of freedom analysis. a) A two-mirror flat optical resonator. b) A four-mirror folded Z-configuration resonator.

Another advantage of a monolithic design template is that the position of the optical elements – both distance as well as the angle concerning the cavity axis can be known precisely. The output can therefore be fully defined in space using ray-transfer matrices [108]:

$$\begin{bmatrix} r' \\ \theta' \end{bmatrix} = \begin{bmatrix} A & B \\ C & D \end{bmatrix}^n \begin{bmatrix} r \\ \theta \end{bmatrix} \quad (2.1)$$

where n denotes the number of round trips. The ray-transfer matrix is given by multiplying the individual matrices of the optical elements in the form of a matrix product.

In light of the examples discussed above, the minimum requirements of a pseudo-monolithic assembly are evident; precise pre-alignment between optical elements, in-plane, and out-of-plane rotational DOFs to correct for finer misalignments, and a translational DOF to adjust the distance between the optical elements. To progress further, we first discuss the concept of femtosecond laser-based repositioning in broader detail.

2.2 Femtosecond laser-enabled actuation – general concepts

As introduced earlier in Chapter 1, femtosecond laser micromachining combined with wet chemical etching enables the fabrication of arbitrarily shaped structures almost anywhere on the surface or inside the bulk of a transparent dielectric material [74], [83]. The non-linear nature of the absorption process limits the material modification to a very small volume (a few μm^3), thus opening the door to novel applications exploiting a truly three-dimensional design space. The morphological changes that occur within the irradiated volume include a localized change in refractive index, density or volume, and Young's modulus among many others. Below, we elaborate further on the concept of laser-induced volume change – our proposed method for guided fine repositioning.

The basic principle is to utilize the net volume expansion (or contraction for Type I modifications) that occurs during laser exposure. In this process, the material is scanned repeatedly and lines are written next to each other. Depending on the focal parameters, a single line is $\sim 1.5 \mu\text{m}$ wide, $\sim 10 \mu\text{m}$ long along the laser propagation direction, and can have any desired length (L) in the plane of the substrate. The order of magnitude of the volume change depends on several parameters such as pulse energy and deposited energy, but typically varies between 0.01 – 0.05% of the irradiated volume. To further increase the net strain, lines are stacked not just laterally, but also vertically on top of each other with different line-to-line and plane-to-plane separation, resulting in a densely stacked configuration. The cumulative effect is the summation of the volume changes resulting from these individual lines, which can be further oriented along a preferential direction by tuning the laser polarization [98], [99].

To induce a prescribed motion, the laser-irradiated regions can be arranged spatially in certain specific locations. For example, in Figure 2.3 (left), a cantilever is exposed near its top and bottom surfaces resulting in a downward and upward *out-of-plane* motion respectively. The same cantilever when exposed near its sides (shown in the middle) causes a bending motion *in the plane* of the cantilever. Here too, by exposing opposite sides, the orientation of the bending can be controlled. On the extreme right, a U-shaped positioning element is shown. Again, by exposing different regions of the element, a translational motion towards or away from the anchor can be achieved. In Chapter 4, we provide an in-depth analysis of different exposure strategies.

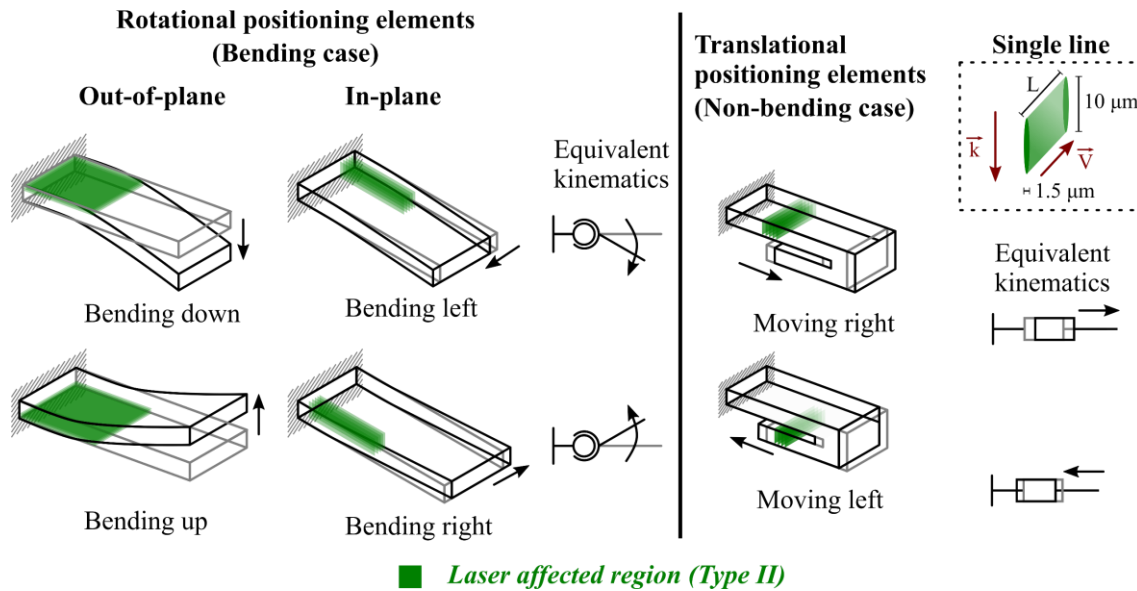


Figure 2.3 – Illustrative examples of various positioning elements actuated by femtosecond laser exposure. On the left: a cantilever beam mimicking a simple pivot. Depending on the exposure conditions, both in-plane and out-of-plane movements can be created. On the right: a U-shaped linear translation element. The initial and final states are drawn in gray and black respectively. Parts of this figure were re-created from [106].

The above example introduces some primitive cases consisting of a single element and in which the effect is observed in the same element that is exposed to the laser. By incorporating advanced mechanical elements such as flexures [109]–[111], complex kinematic chains can be created, in which, the deformation is channeled away from the laser-exposed region and towards the end effector. In this manner, an optical element at that location can be repositioned along its geometrical axes [107].

To design such a kinematic chain, certain important factors need to be kept in mind:

- The laser-exposed region, which we refer to as an ‘actuator’, must remain as flat as possible (perpendicular to the laser propagation direction) during the exposure step. Since the deformation occurs inside the actuator, its surface evolves dynamically; initially flat regions start to bend as the laser-exposure process evolves (see Figure 2.3, left). In this particular case, the exposure starts at a location away from the anchor and gradually moves towards it. Therefore, the region yet to be modified remains flat whereas the rest of the surface gets deformed. In certain cases where this is unavoidable, the exposure patterns need to be adjusted to follow the bending or as we will see later, the deposited energy can be varied to maintain a relatively flat surface.
- In certain cases where the irradiated zone is embedded deep inside the actuator, or laser-written lines are stacked along its entire thickness (Figure 2.3, middle and right), beam diffraction effects are common near the edges of the actuator (note that the effect can be suppressed using beam-shaping techniques [112], albeit at the cost of more sophisticated setup). Therefore, in such cases, the actuator is designed in a manner such that the modified region lies a few hundred micrometers away from the edges.
- One limitation of laser-induced volume change is that the strain is limited to a fraction of the modified volume ($\sim 0.02\%$). Therefore, amplification stages are needed in the kinematic chain to achieve an appreciable deformation (a few milliradians for angular motion or a few micrometers for linear motion) at the end effector. Amplification can be intrinsically provided by the actuator configuration too, as is the case in Figure 2.3 (left and middle) when a bending motion is produced, while a 1:1 relation exists between the laser-induced strain and the motion at the end effector in the case of linear actuation (Figure 2.3, right).
- Lastly, the actuator needs to be optically accessible and void of any barriers that may hamper the laser beam propagation. Furthermore, it needs to have an optically smooth surface, which becomes important

in certain cases where the actuator does not share a common surface with the rest of the substrate. An example of this will be discussed in Section 3.4.2.2. Note that using post-processing techniques such as CO₂ laser-based polishing [113], [114], it is possible to achieve optically smooth surfaces with surface roughnesses down to a few nm R_a .

Bearing these points in mind, we now outline some essential design guidelines for kinematic mechanisms fulfilling basic functions in an optical assembly – rotations and translations along different axes. Afterward, we introduce various such mechanisms, which are then experimentally implemented and validated in later chapters.

2.3 A brief overview of the main design constraints

In this section, we will establish design rules necessary to choose a kinematic mechanism for a given function. For most cases, the desired function is either a rotation, in-plane as well as out-of-plane, or translation along a given axis, both being fundamental requirements of an optical circuit.

2.3.1 Range of motion

The alignment of optical elements requires either a pure translation and/or a rotational motion – both in and out-of-plane. As such, we define the range of motion in terms of linear displacement or angle of rotation achieved at the end effector.

In a design template fabricated using femtosecond laser micromachining, typical angular inaccuracies are in the order of < 1 milliradian (i.e. a deviation of 1 μm across a distance of 1 mm). Similarly, in the worst-case scenario, a positioning inaccuracy of 1 μm can exist. However, major inaccuracies stem from the fabrication tolerances of the added optical elements themselves; lack of perpendicularity between optical faces and sidewalls (in some cases this can extend up to 5 milliradians or even more), size tolerances (errors in thickness of the optical element), etc. In an optical circuit (such as the one depicted in Figure 2.2b), the former is more significant and often needs to be corrected within a fraction of a milliradian. Therefore, the range of motion of the designed mechanisms, at the very least, has to be bigger than these tolerances.

From a design point of view, the actuator has a limited volume and therefore, can only accommodate a finite number of laser-written lines. Furthermore, in each exposure step, part of the actuator is permanently consumed (although complete erasure of the modified zone is possible through annealing [115], [116]), and the range of motion per line gradually reduces as more lines continue to be added. Depending on the type of motion desired, the actual available volume can be only half of the total volume since exposure beyond a certain point will reverse the direction of motion. In the cantilever example of Figure 2.3, exposure in the top half causes a downward motion, which is reversed by exposure in the bottom half. Furthermore, the range of motion is directly affected by the stiffness of the kinematics involved. This manifests itself into a straightforward problem; minimize the cumulative stiffness of the kinematic chain at the point of interest and along the DOF while maximizing it along the degree of constraint (DOC).

Another important factor linked to the range of motion is the maximum allowable stress above which the material would fail. The flexures are designed to always operate below a critical stress level. A basic design principle to avoid stress accumulation in the flexures is to make them highly compliant in comparison to the actuator (i.e., $K_{\text{actuator}} \gg K_{\text{flexure}}$, where K denotes the stiffness).

2.3.2 Dynamics

Another important design consideration has to deal with the different vibration modes of the kinematic mechanism. The elemental flexures need to be appropriately designed to achieve a specific vibration frequency response towards external perturbations such as mechanical noise, sudden impulses, etc. In general,

one cannot do so without compromising other design specifications. For example, for a larger range of motion, a lower stiffness is required along the DOF. While this can be achieved by making the element more flexible, however, in doing so, the stiffness along the DOC changes too, consequently lowering the DOC vibration mode. This practical limitation is a direct consequence of the strong coupling between stiffnesses along different directions.

As an example, let us look at the simplest case of a slender cantilever beam (Figure 2.4), which is repeatedly used throughout this work. The linear stiffnesses along the three translational axes can be written as:

$$k_{F_x, \delta_x} = E \left(\frac{hw}{l} \right); k_{F_y, \delta_y} = E \left(\frac{hw^3}{l^3} \right) = k_{F_x, \delta_x} \left(\frac{w^2}{l^2} \right); \text{ and } k_{F_z, \delta_z} = E \left(\frac{wh^3}{l^3} \right) = k_{F_x, \delta_x} \left(\frac{h^2}{l^2} \right) \quad (2.2)$$

Where h , w , and l denote the cantilever dimensions as shown in the figure below. E , F , and δ denote Young's modulus, applied force, and the observed displacement respectively.

Assuming the desired DOF is along the z -axis, and l , w are fixed, then the translational stiffness (along z -axis) can be reduced by decreasing h . However, due to the inherent coupling between the axes, the stiffness along x -axis is lowered too. This underlines the fundamental non-constraining nature of flexure elements.

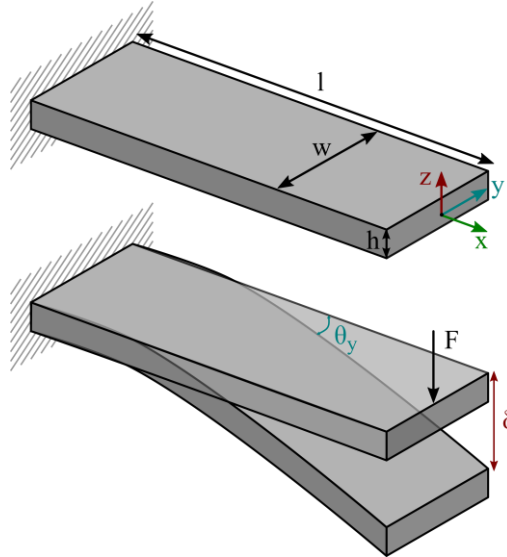


Figure 2.4 – A cantilever beam. Top: freestanding cantilever. Bottom: a cantilever beam with a transverse force at the free end.

For precision systems requiring high mechanical stability, achieving a fundamental vibration mode above a certain critical value is one of the main design constraints. In such cases, a compromise has to be made between the range of motion and their dynamic frequency response. A practical example of this is discussed in Chapter 5.

2.3.3 Real estate

The term ‘real estate’ refers to the physical footprint an object occupies in three-dimensional space. Generally speaking, serial kinematic mechanisms are larger in comparison to their parallel counterparts. When degrees of freedom (DOFs) are required to be stacked vertically or in the presence of multiple DOFs, serial systems tend to scale rapidly in size and mass.

Another important and associated parameter is the overall mass of the mechanism. As we will see later, by optimizing the material distribution in a compliant mechanism, the resonance frequency (Equation 2.3) can be adjusted for a given stiffness. This is critical for applications where stability and precision are important.

$$\omega_0 \propto \sqrt{\frac{k}{m}} \quad (2.3)$$

The size of a kinematic mechanism is especially important when integrating into a multi-component optical assembly. The optical elements can sometimes be densely distributed, and in such cases, the mechanism must fit into very confined spaces without compromising the range of motion.

2.3.4 Fabrication and exposure constraints

The manufacturability plays an obvious role in the design of flexure-based mechanisms. Although femtosecond laser micromachining offers a versatile fabrication tool, for certain mechanisms, the complexity can grow rapidly, therefore hindering their successful implementation. In this work, as we rely on a relatively simple manufacturing platform, a sacrifice has often to be made with respect to the design complexity of the chosen mechanisms. This can be either in their range of motion, mechanical stability, or aspect ratio.

For actuation, we also use femtosecond laser exposure to locally modify the material in certain specific locations. Depending on the type of motion desired at the end effector, these modifications have a well-defined geometric orientation and volumetric distribution. This defines additional design constraints specifically concerning the actuator.

2.3.5 Fatigue

The underlying phenomenon of femtosecond laser-induced actuation is stress; the material is incrementally stressed until the desired motion has been achieved. Afterward, the device remains in that stressed state during its operation. Therefore, during optimization, final static stress becomes one of the main design variables. It should not exceed a certain critical value, typically up to 1 GPa as we will see later on in Chapter 6.

2.4 Taxonomy of mechanisms

In this section, we present various mechanisms that were conceived in this thesis. The goal of these mechanisms is to provide a fine-alignment function in a compact optical circuit. We, therefore, limit ourselves to mechanisms with either rotational or translational DOFs, as they constitute basic building blocks of an optical assembly. Designs producing more complex motion trajectories combining rotation and translation in a compact volume can also be considered based on similar general design principles. In what follows, we further limit the scope of our discussion to design synthesis, followed by experimental validation in the subsequent chapters. Some mechanisms, though not experimentally implemented, are also discussed briefly.

To guide us through the rest of this discussion, the mechanisms are segregated into two categories. In the first part, we focus our attention on guiding mechanisms comprised of monolithic flexure kinematics operated by a separate and distinct element – ‘the actuator’, itself part of the same substrate. In these mechanisms, the actuator is separated from the flexure kinematics and is connected through a deformable interface. The actuator can bend along its designed DOF, and in certain geometries, can be flexible along more than one direction, a choice that can be made during the exposure step (see for instance Figure 2.3, the cantilever can bend in-plane or out-of-plane depending on the writing patterns).

In the second part, we focus on mechanisms that can be actuated without separating the actuator from the guiding mechanism. The remote actuation principle of femtosecond laser exposure makes it possible to use

the guiding flexures as actuators. More specifically, the elemental flexures carry two functions: i) they are partially exposed to create localized volume changes and, ii) as flexures, they guide the motion of the optical element. This approach considerably reduces the overall size of the mechanisms, however, it introduces certain practical difficulties as will be discussed later.

Before moving ahead, it is important to re-emphasize the definition of an actuator. As we will see next, depending on the type of mechanism, it may either refer to a semi-rigid link or to the flexure element itself. In any case, it is the region that is exposed to the laser.

2.4.1 Class A: Actuators coupled to a guidance

Flexure mechanisms, upon application of a force at one or more points, produce a motion that can be either purely translational, purely rotational, or a hybrid combination of the two. Below, we first take a look at mechanisms producing a rotational motion.

- **Examples of actuators coupled with flexures producing rotational motion**

Figure 2.5 outlines some common pure rotation (in-plane) mechanisms. In the first example, a serial combination (fixed on the same base) of two parallelogram mechanisms is shown. Under the application of a force, the mechanism rotates about a remote point O. The second example shows a similar mechanism albeit one difference; the two parallelograms are connected in parallel (fixed on different bases). When actuated, the mechanism rotates about point O, which is located symmetrically unlike before. The last example shows a remote center of compliance (RCC) mechanism. In this mechanism, the force is applied directly below point O, about which the mechanism rotates under actuation.

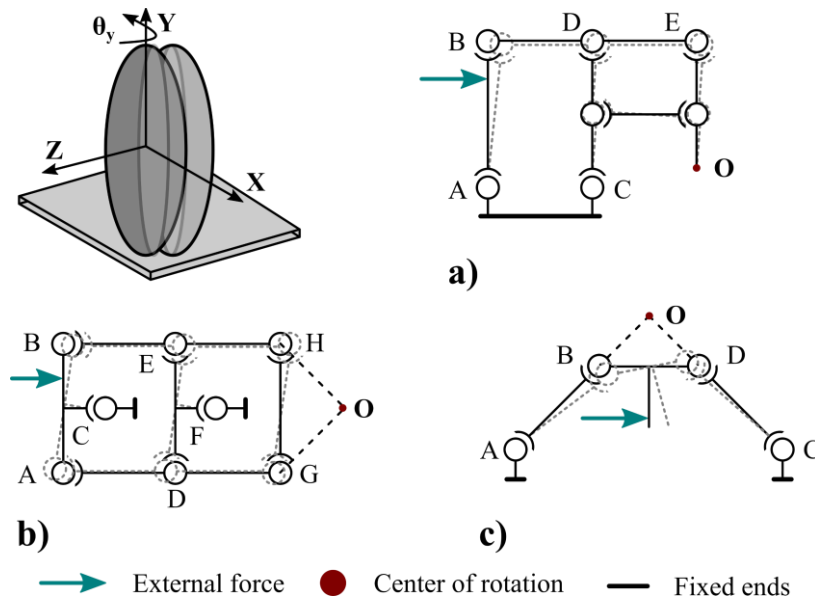


Figure 2.5 – Examples of in-plane rotation mechanisms. a) A simple parallelogram mechanism. b) A symmetric double parallelogram mechanism. c) A remote center of compliance (RCC) mechanism. All mechanisms have a rotational center located outside the mechanism.

The RCC mechanism (Figure 2.5c, alternatively referred to as RCR – remote center of rotation or gimbal mechanism) is further developed, and two different implementations will be discussed in Chapters 3 and 4.

One necessary function for precise optical alignment is to achieve a rotation out of the substrate plane. Considering a Cartesian coordinate system XYZ, and assuming the substrate lies in the XZ plane, a rotation about the X-axis can be achieved by using various types of elemental flexures, like for instance, starting from

the simplest to the more complex ones: torsion bars, cruciform hinge, notch hinge, cartwheel hinge or cross-pivot. These elemental hinges share the same characteristic of having one low-stiffness rotational axis while being significantly stiffer along the remaining axes. The choice between one elemental hinge versus another is dictated by its real estate, precision requirements, the mechanical frequency response (therefore their stiffness matrix), stress concentration, as well as processing time.

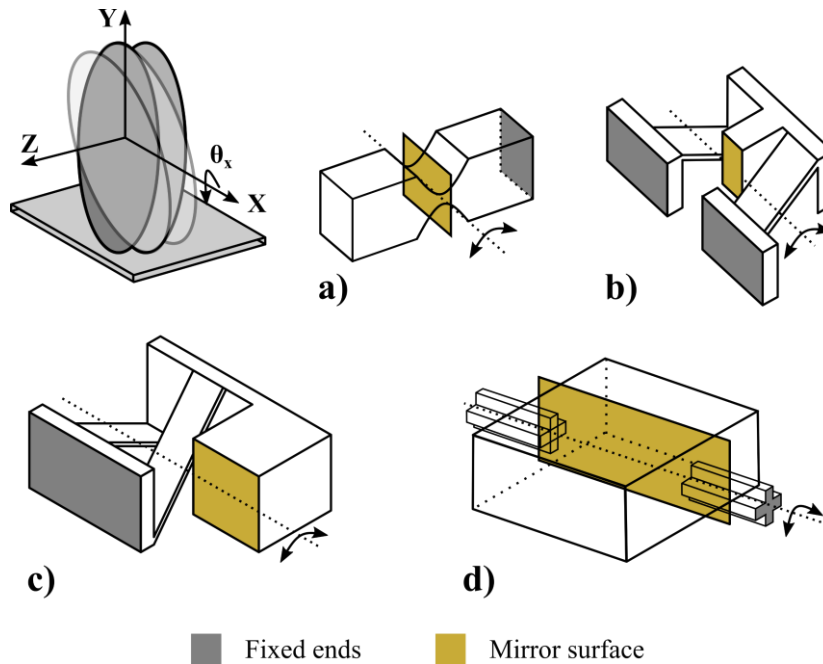


Figure 2.6 – Examples of out-of-plane rotation mechanisms. a) A notch hinge. b,c) Different implementations of a cross-pivot with two leaf springs. d) A cruciform hinge. In practice, the mirror surface needs to be deformed for a) or an opening through the volume is required for d).

The example of Figure 2.6a shows a notch hinge flexure formed by two circular edges. The thin region at its center serves as the flexible element, which can also be replaced by a leaf spring or an elliptic shape (the circular hinge is a special case in which the ratio between the major and minor axes is unity). The examples of Figures 2.6b and Figure 2.6c show different variations of a cross-strip pivot. It consists of two strips, fabricated at an angle to each other, normally orthogonal, with the axis of rotation lying at their intersection. Compared to the notch hinge, it is more compliant and can provide larger deflections. Other variations of this mechanism include the symmetric four-leaf pivot and the cartwheel hinge, both with similar performance characteristics.

The cruciform hinge shown in Figure 2.6d is chosen and validated experimentally. This choice is primarily motivated by its low torsion rigidity, high bending stiffness, as well as its fabrication simplicity, and interfacing with an actuator. In Chapter 3, we will illustrate in more detail one practical implementation based on this design, and later on in Chapter 4, will show a combination of two different rotational mechanisms, one in-plane, and one out-of-plane.

- **Examples of actuators coupled with flexures producing translational motion**

The simplest way to realize a linear motion with pivots is based on parallelogram kinematics with four pivots. There, the end-body moves in translation parallel to a static reference. As a cantilever is somewhat equivalent (in first approximation) to pivots, two elongated cantilevers connected through a rigid body mimic a parallelogram kinematics (Figure 2.7a). This configuration gives a reasonable first approximation of a linear motion for small amplitudes. For higher amplitudes, more complex arrangements are needed, such as a

double compound mechanism (Figure 2.7d). By serially adding a second parallelogram, the parasitic motion present in a simple parallelogram mechanism is compensated. Other such mechanisms include Hoecken's and Watt's linkages, which provide a close to linear motion along a specific path of their motion trajectories [81].

In Figure 2.7e, a representative case of an actuator interfaced with the simple parallelogram mechanism is shown. If the motion stage is free to move (zero-load condition), the design rules are straightforward – longer the actuator, larger is the travel range. In other words, an actuator with a low bending stiffness is required. The actuator stiffness, in this case, varies in a manner analogous to Equation 2.2. Under a non-zero load condition, the bending stiffness of the actuator needs to be larger than the stiffness acting on the mobile stage. If not so, the actuator cannot efficiently apply the required load and will lead to an increase in lost motion. This requires design optimization to achieve appropriate dimensions for the actuator as will be discussed later on.

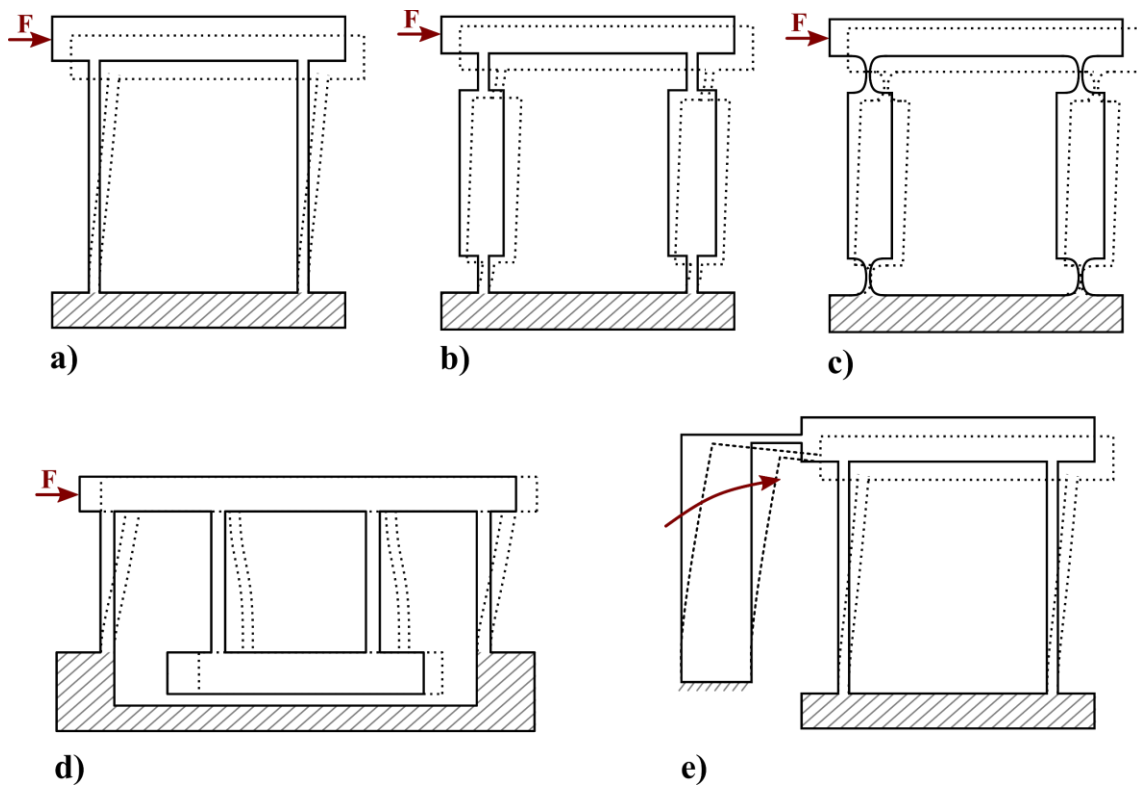


Figure 2.7 – Schematic illustrations of linear translation mechanisms. a) A leaf spring linear guidance. b,c) Two different implementations of the same linear guidance with stiffening bars and using four basic elements – elementary beams and notch hinges respectively. d) A four-bar compensated linear guidance. e) An illustration of an actuator integrated with a simple leaf spring mechanism. The interfacing bar accommodates the bending motion of the actuator with the linear motion of the guidance. In all illustrations, the deformations are exaggerated for visual purposes.

Although the above mechanisms have a similar level of fabrication complexity and therefore can be used interchangeably, the simple parallelogram structure is implemented experimentally. Its parasitic motion can be rightfully neglected as the requirement of motion amplitude is small ($\sim 1 \mu\text{m}$). In Chapters 5 and 6, we will illustrate its use in two cases – a tensile-tester device, and a Fabry P rot resonator.

- **Examples of multi-DOF mechanisms – hybrid mechanisms**

In the preceding examples, the end effector was either rotated or translated along a single axis. To illustrate more complex arrangements, we show a Cardan (universal joint) design where the end effector can effectively rotate along two axes. Here, torsion bars are used as out-of-plane rotation elements, although other types of elements can be used too. As shown in Figure 2.8, the mechanism consists of two concentric rings at-

tached to a pair of orthogonal torsion rods. A mounting hole is provided in the center for inserting the optical element. Although the mechanism can be implemented in any optical system requiring angular alignment along two axes, the original motivation was for a robust fiber-based Fabry P  rot cavity.

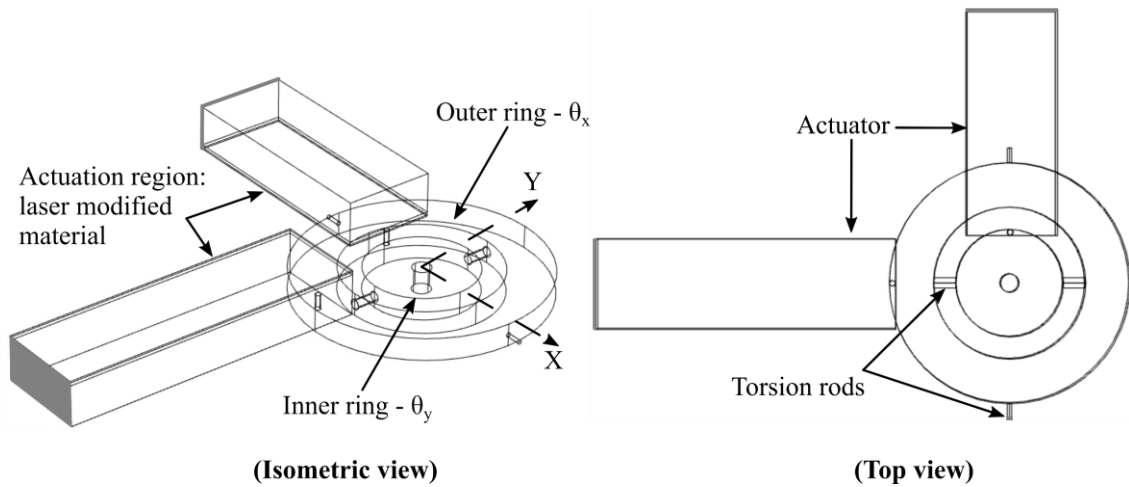


Figure 2.8 – Isometric and top views of a Cardan joint mechanism using torsion rods for two rotations. A mounting hole is provided at the center of rotation for inserting an optical element.

By combining the above mechanism with an XY motion stage, a 4-DOF adjustment is possible as shown in Figure 2.9. Due to their fabrication complexity and coupling between different DOFs, these mechanisms are not experimentally implemented.

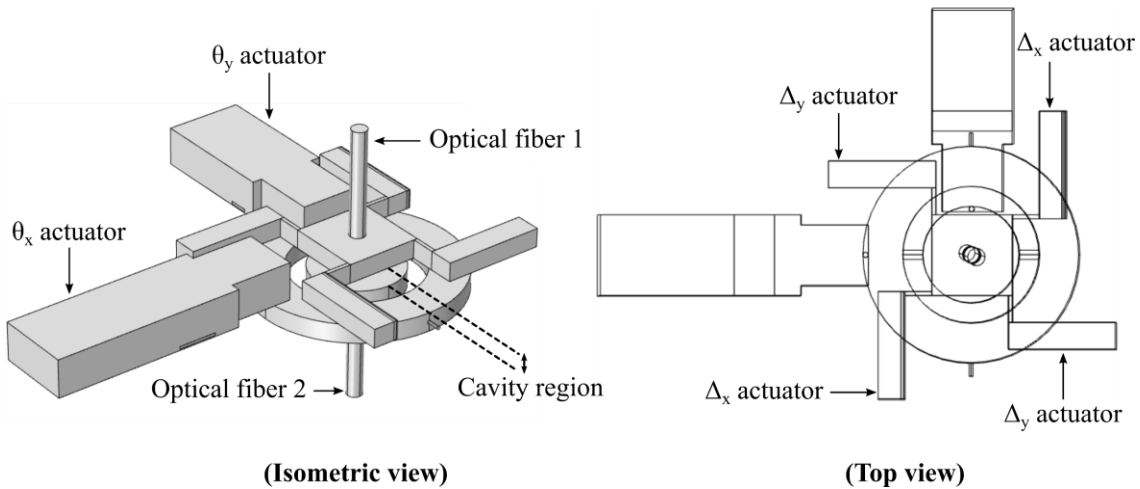


Figure 2.9 – A 4-DOF adjustment mechanism with two rotations and two translations. The mechanism is designed to be fabricated on a single substrate.

2.4.2 Class B: Integrated solution – combined actuating and guiding elements

The notion of using femtosecond lasers to reposition optical elements mainly relies on the ability to induce nanoscopic volume changes within the material. Further, the versatility of the process allows distributing these volume changes almost anywhere in the material. This effectively means that an element in which the deformation occurs can produce a controlled motion along a specified axis while maintaining a high stiffness along other axes where no motion is desired. The main advantage compared to the approach discussed in the previous section is to bypass the need for decoupling the actuator from the guiding element, and in doing so, similar results can be achieved in a reduced real estate.

To build upon this concept, we introduce the example of Figure 2.10. A block of mass (motion stage) is suspended on two thin flexure elements, both fixed to a static base at the other end. By varying the position and orientation of the laser affected region within the flexures, different types of motion can be activated as shown in the figure.

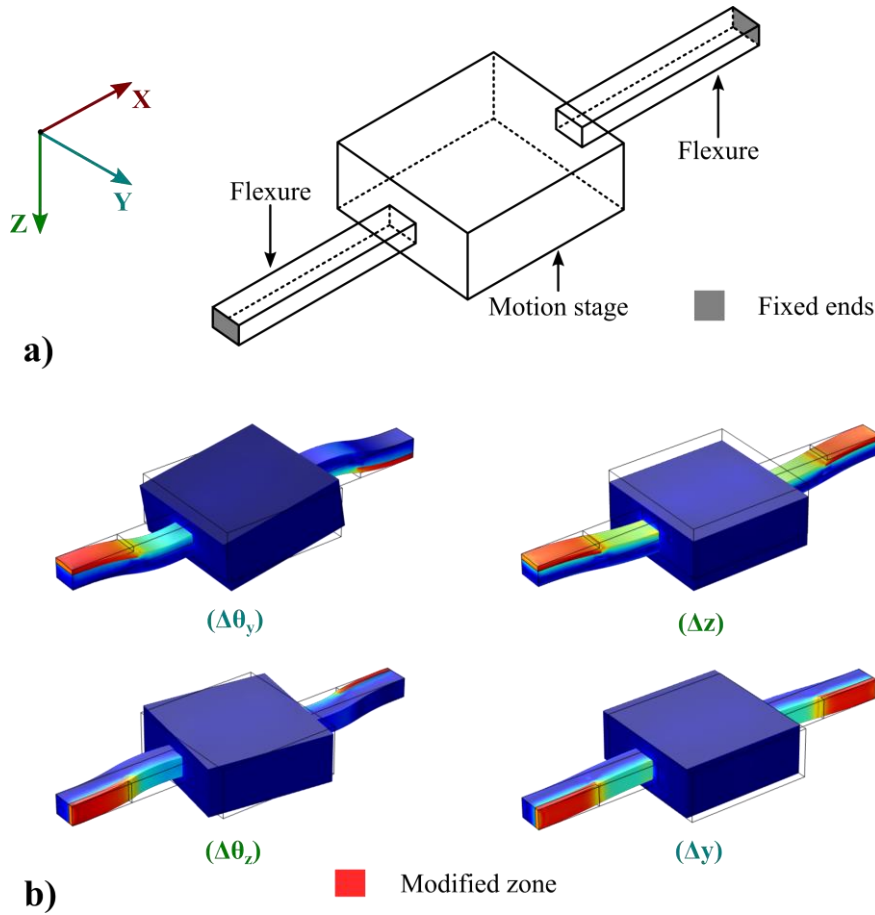


Figure 2.10 – a) A 3D sketch of a flexure-only motion stage. b) Different degrees of freedom. The motion stage can be actuated differently depending on the position of the laser-affected region within the flexures.

The simplicity of the mechanism is visibly evident. Owing to its small size, it can be deployed in very tight spaces, as is usually the constraint in compact optical circuits. Further, it carries low mass, therefore robust and insensitive to common sources of vibrations, and due to the absence of any rigid links, multiple DOFs can be activated as shown above.

Practically speaking, some disadvantages exist too:

- To activate any given DOF optimally, a two-side simultaneous exposure would be required. This requires continuous back and forth travel during laser actuation, thus significantly increasing the time required for the alignment process.
- Since the flexure dimensions primarily define the range of motion, a strong dependence exists between the motion capability of the stage and the modification ability of the process. For example, in Figure 2.10b, a larger $\Delta\theta_y$ demands lower bending stiffness of the flexures along the Z-direction. While this could be achieved by reducing the flexure height (along Z-axis), at the same time, it directly affects the number of laser-affected regions that can be written inside the flexures.

- The flexure volume is limited and also consumed in each actuation. Consequently, this limits the number of DOFs that can be actuated in a practical case. Further, due to the small size of the flexures and their continuously evolving surface shape, maintaining a uniform laser exposure can be challenging.

Nevertheless, in Figure 2.11, an illustrative parameter analysis is presented for the different DOFs. This is for the case of a 1 mm thick substrate, that is typically used in our experiments.

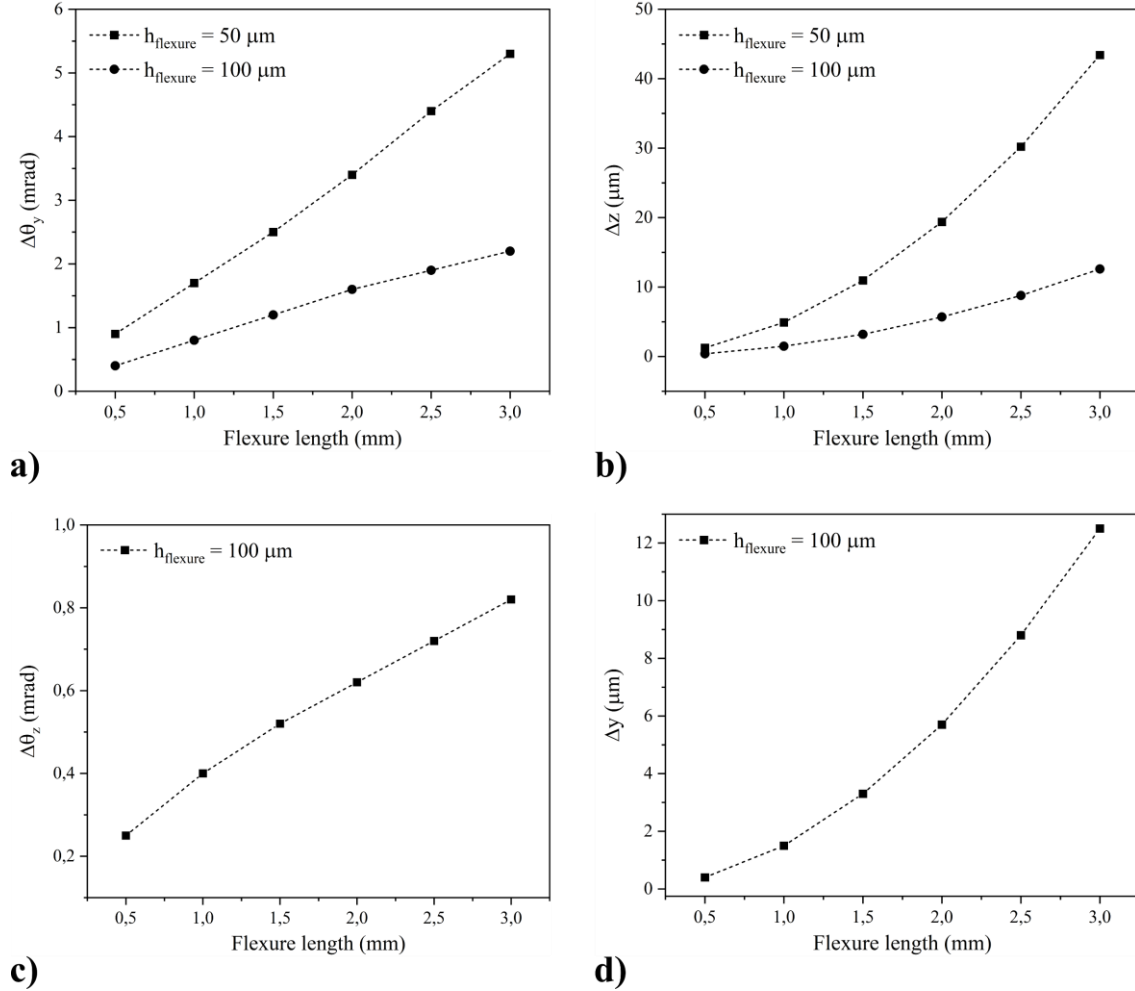


Figure 2.11 – Motion characteristics of the flexure-only stage for a specific set of design parameters. a) Angular rotation about Y-axis. b) Translation along Z-axis. c) Angular rotation about Z-axis. d) Translation along Y-axis. Here, flexure-height denotes the Z-dimension, whereas length and width are oriented along X and Y axes respectively.

Following the exposure strategy of Figure 2.10b, the different DOFs are simulated and plotted above. For a fixed flexure width, the influence of length and height are studied.

2.5 Topology optimization

All of the mechanisms discussed thus far are based on discrete individual elements put together either in a serial or parallel fashion. Starting from established mechanisms, the flexure and actuator parameters are iterated until an optimal geometry that fulfills the desired function is established. In the context of direct-write processes, topology optimization is a promising technique that can find novel solutions unknown to a designer and can also aid the designer's intuition to optimize an existing solution. Starting from a simple geometry with certain load and boundary conditions, an algorithm is used to optimize the elements of the design domain, until an optimal mass distribution satisfying the desired objective and constraints is found. Below

we provide a brief, and by no means exhaustive description of some common topology optimization techniques.

One of the common approaches towards parametrization of the design space in topology optimization problems is the ground structure approach. In this approach, the design space is discretized into a dense grid of nodes that are interconnected using tentative elements. The resulting structure is either a union of all the nodes (full ground structure) or a small subset of them. To solve the optimization problem, the cross-sectional areas of the connecting elements are used as design variables whose values are determined by defining a lower limit approaching zero. As the optimization converges, redundant elements with values equal to or near the lower limit are subsequently removed (white areas), while elements with higher values (black areas) define the optimal topology satisfying the set of imposed constraints. As elements are only removed during the optimization process, the initial grid should be as dense as possible to determine the optimal solution.

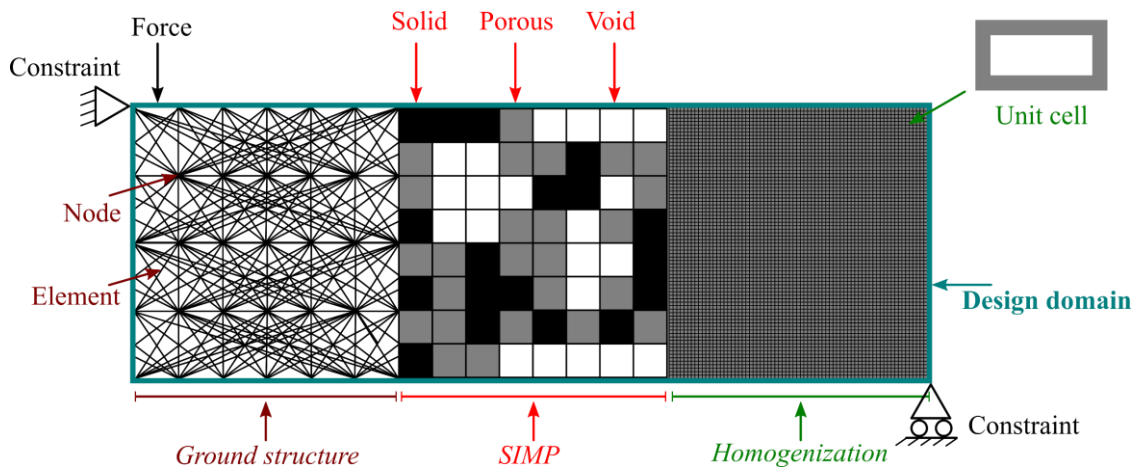


Figure 2.12 – Different topology optimization techniques. a) Ground structure approach. B) Solid isotropic material with penalization (SIMP) method. C) Homogenization method.

Another common and more widely used approach is the solid isotropic material with penalization (SIMP) method. Unlike the ground structure approach, where elements can be either solid or void, SIMP allows for intermediate densities or gray areas. In the optimization problem, the relative densities of the connecting elements are chosen as design variables. As the optimization converges, elements with a relative density approaching the lower limit are considered to be void (white areas), while elements with higher densities define a solid (black areas). The introduction of a continuous relative density function avoids the binary distribution present in the ground structure approach. However, as it is often difficult to interpret the gray areas, the SIMP method applies a penalty factor (by raising the density to a large exponent) to drive intermediate density elements (gray areas) to be either solid or void.

Finally, a similar method to the one described above is called the homogenization method, in which the design domain is discretized into a periodic microstructure of unit cells, that consist of a material and a void. The optimization problem is to identify the optimal distribution of porosity in the design domain. Like before, some regions of the porous structure are identified as voids, while non-porous regions are replaced by a solid structure. For intermediate values, a porous medium is replaced instead.

Irrespective of the chosen method, these techniques often generate very complex solutions that require further interpretation on part of the designer. Specific to our case, further analysis is necessary to translate these complex shapes into manufacturable ones using the two-step process described earlier. For this reason and

given that our manufacturing platform has a limited fabrication capability, these methods are not implemented in this thesis. Nevertheless, it remains an interesting approach for future considerations.

For in-depth details, the reader is referred to [117]–[120]. Some works on the extension of topology optimization techniques for photonic applications exist too and can be found in [121]–[125].

2.6 Analytical description of compliant mechanisms

To conclude this chapter, we present an analytical approach to determine the stiffness of a compliant mechanism. Such a formulation focuses on formulating a mathematical relationship between the applied load(s) and the output deformation of a given mechanism. This helps identify key parameters and understand their influence on the overall stiffness and can be used as a quick tool to redesign the system. In literature, various methods such as finite element method (FEM), pseudo rigid body (PRB) method [126], Castigliano's theorem, etc. can be used to do so. In this analysis, we will instead use a matrix-based approach [110] that relies on the stiffness matrices of the elemental joints.

A single flexure element has a direct relationship between the stiffnesses along different axes and the flexure dimensions. For example, in Figure 2.4 and with the aid of Equation 2.2, it is easy to visualize the influence on stiffness as the different dimensions are scaled up or down. However, in a compound mechanism where a motion stage may be connected to multiple such units, sometimes through both serial and parallel kinematic chains, it is nearly impossible to identify how the stiffness of a single unit will affect the global stiffness of the mechanism at any given point. In such a case, an analytical stiffness model offers a quick tool to cross-check and redesign the mechanism.

For this analysis, we will take the example of the RCC mechanism shown in Figure 2.5c. An actuator is interfaced through a deformable beam and connected via a lever-amplification mechanism, which is facilitated by a circular notch hinge. A kinematic diagram is described below.

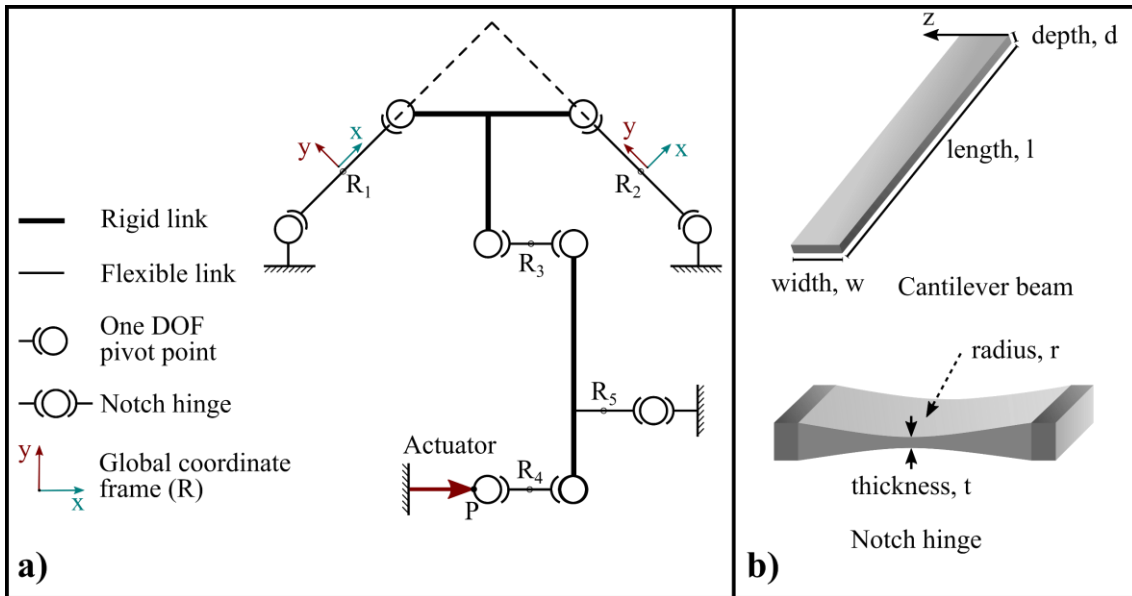


Figure 2.13 – a) A kinematic diagram of the RCC mechanism showing the various flexure elements in their respective coordinate frames. The global coordinate frame R is located at P ; the interface between the actuator and the mechanism. R_x ($x = 1 - 5$) represents the secondary coordinate frame attached to the individual elements. b) A geometric representation of the flexure units. On top, the inclined cantilever beams are shown, and on the bottom, the notch hinge is described.

The primary governing equation linking the applied load to the resulting deformation can be written as:

$$\mathbf{F}_Q^P = \mathbf{K}_Q^P \times \hat{\mathbf{r}}_Q^P \quad (2.4)$$

Here, \mathbf{F}_Q^P denotes a wrench (a six-coordinate vector containing force and moment), \mathbf{K}_Q^P represents the stiffness matrix, and $\hat{\mathbf{r}}_Q^P$ represents the overall deformation of the system at an arbitrary point P, all evaluated in the same coordinate frame Q.

Equation 2.4 can be inverted and re-written as:

$$\hat{\mathbf{r}}_Q^P = (\mathbf{K}_Q^P)^{-1} \times \mathbf{F}_Q^P = \mathbf{C}_Q^P \times \mathbf{F}_Q^P \quad (2.5)$$

Where \mathbf{C}_Q^P represents the compliance of the system.

Under the application of a known load, if the stiffness matrix is known, the resulting deformation can be calculated using Equation 2.5. Similarly, Equation 2.4 can be used to calculate the load required for a given deformation.

For the example of Figure 2.13, we intend to develop the force-deformation relation at point P in a global coordinate frame R centered at P. For the inclined cantilever beams, the local coordinate frames R_1 and R_2 are located at their respective centers of mass with orientation as depicted in the figure. Coordinate frames R_3 , R_4 , and R_5 are located at their respective flexure elements, however, with the same orientation as the global coordinate frame R. By writing the individual stiffness matrices in their local coordinate frames, rotating coordinate frames R_1 and R_2 by 45 degrees, and finally transporting all the matrices to point P, the cumulative stiffness of the system can be determined.

For the cantilever beam at R_1 , the terms of the principal stiffness matrix are given by the von Mises stiffness matrix [127] and can be written as:

$$\begin{aligned} k_{F_x, \delta r_x} &= \frac{Ewd}{l} & k_{M_{x, \delta \theta_x}} &= \frac{1}{3} \left(\frac{wd^3}{l} \right) \left(\frac{E}{2(1+\nu)} \right) \\ k_{F_y, \delta r_y} &= \frac{Ewd^3}{l^3} & k_{M_{y, \delta \theta_y}} &= \frac{E}{12} \left(\frac{dw^3}{l} \right) \\ k_{F_z, \delta r_z} &= \frac{Edw^3}{l^3} & k_{M_{z, \delta \theta_z}} &= \frac{E}{12} \left(\frac{wd^3}{l} \right) \end{aligned} \quad \text{and} \quad (2.6)$$

Here E and ν denote Young's modulus and Poisson's coefficient respectively. The other terms denote the cantilever dimensions as indicated in the figure. Similar diagonal matrices can be constructed for the other flexure elements in their principal coordinate frames, (such matrices are well documented in the literature, and for instance, can be found in [110]).

To transport the stiffness matrices from their local coordinate frames to the global coordinate frame located at P, we use a method common in robotics and screw theory:

$$\mathbf{K}_B^Q = \left(\mathbf{T}_{A \rightarrow B}^{P \rightarrow Q} \right) \mathbf{K}_A^P \left(\mathbf{T}_{A \rightarrow B}^{P \rightarrow Q} \right)^T \quad (2.7)$$

Equation 2.7 represents the transport of a stiffness matrix \mathbf{K}_A^P from point A in coordinate frame P to point B in coordinate frame Q. The transport matrix \mathbf{T} (6×6) contains a spatial vector and a rotation matrix, linking A to B and P to Q respectively, and is given by:

$$\mathbf{T}_{A \rightarrow B}^{P \rightarrow Q} = \begin{bmatrix} \mathbf{Rot}^\theta & 0 \\ \mathbf{QP} \times & \mathbf{Rot}^\theta \end{bmatrix} \quad (2.8)$$

Here, \mathbf{Rot}^θ represents the rotational matrix between the two frames and $\mathbf{QP} \times$ is an operator that contains the vector components from the center of one coordinate frame to another and can be written in matrix form as:

$$\mathbf{QP} \times = \begin{bmatrix} 0 & -z & y \\ z & 0 & -x \\ -y & x & 0 \end{bmatrix} \quad (2.9)$$

Using the above methodology, we can now write down the transport matrices for all the flexures as:

$$\mathbf{T}^{R_1 \rightarrow R} = \begin{bmatrix} \frac{1}{\sqrt{2}} & \frac{1}{\sqrt{2}} & 0 & 0 & 0 & 0 \\ \frac{-1}{\sqrt{2}} & \frac{1}{\sqrt{2}} & 0 & 0 & 0 & 0 \\ 0 & 0 & 1 & 0 & 0 & 0 \\ 0 & 0 & -b & \frac{1}{\sqrt{2}} & \frac{1}{\sqrt{2}} & 0 \\ 0 & 0 & a & \frac{-1}{\sqrt{2}} & \frac{1}{\sqrt{2}} & 0 \\ b & -a & 0 & 0 & 0 & 1 \end{bmatrix}; \mathbf{T}^{R_2 \rightarrow R} = \begin{bmatrix} \frac{1}{\sqrt{2}} & \frac{1}{\sqrt{2}} & 0 & 0 & 0 & 0 \\ \frac{-1}{\sqrt{2}} & \frac{1}{\sqrt{2}} & 0 & 0 & 0 & 0 \\ 0 & 0 & 1 & 0 & 0 & 0 \\ 0 & 0 & -a & \frac{1}{\sqrt{2}} & \frac{1}{\sqrt{2}} & 0 \\ 0 & 0 & b & \frac{-1}{\sqrt{2}} & \frac{1}{\sqrt{2}} & 0 \\ a & -b & 0 & 0 & 0 & 1 \end{bmatrix} \quad (2.10)$$

Here, $\mathbf{r}_1 = -a\mathbf{i} - b\mathbf{j}$ denotes the position vector from R_1 to R as seen in R_1 and $\mathbf{r}_2 = -b\mathbf{i} - a\mathbf{j}$ denotes the corresponding vector from R_2 to R as seen in R_2 , with \mathbf{i} and \mathbf{j} denoting unit vectors in these coordinate frames.

Similarly, for the flexure units at R_3 and R_4 ,

$$\mathbf{T}^{R_3 \rightarrow R} = \begin{bmatrix} 1 & 0 & 0 & 0 & 0 & 0 \\ 0 & 1 & 0 & 0 & 0 & 0 \\ 0 & 0 & 1 & 0 & 0 & 0 \\ 0 & 0 & -L & 1 & 0 & 0 \\ 0 & 0 & \frac{l'}{2} & 0 & 1 & 0 \\ L & \frac{-l'}{2} & 0 & 0 & 0 & 1 \end{bmatrix}; \mathbf{T}^{R_4 \rightarrow R} = \begin{bmatrix} 1 & 0 & 0 & 0 & 0 & 0 \\ 0 & 1 & 0 & 0 & 0 & 0 \\ 0 & 0 & 1 & 0 & 0 & 0 \\ 0 & 0 & 0 & 1 & 0 & 0 \\ 0 & 0 & \frac{l'}{2} & 0 & 1 & 0 \\ 0 & \frac{-l'}{2} & 0 & 0 & 0 & 1 \end{bmatrix} \quad (2.11)$$

Here, L represents the length of the rigid link between R_3 and R_4 and l' denotes the length of the flexure units at R_3 and R_4 .

Lastly, for the notch hinge at R_5 :

$$\mathbf{T}^{R_5 \rightarrow R} = \begin{bmatrix} 1 & 0 & 0 & 0 & 0 & 0 \\ 0 & 1 & 0 & 0 & 0 & 0 \\ 0 & 0 & 1 & 0 & 0 & 0 \\ 0 & 0 & \frac{-L}{1+A} & 1 & 0 & 0 \\ 0 & 0 & r+l' & 0 & 1 & 0 \\ \frac{L}{1+A} & -(r+l') & 0 & 0 & 0 & 1 \end{bmatrix} \quad (2.12)$$

Here, A and r represent the amplification factor of the lever mechanism and the radius of the notch hinge respectively. Although the von Mises stiffness matrix terms are quite complex for a notch hinge, a simplified expression can be obtained under the approximation $\beta = t/2r \ll 1$. This effectively means that the thickness at the center of the notch hinge is much smaller compared to its radius.

Finally, once all the transport matrices are known, using Equation 2.7, the stiffness matrix at point P and in coordinate frame R can be calculated as:

$$\mathbf{K}_R^P = \left\{ \left(\mathbf{K}_A^{-1} + \mathbf{K}_B \right)^{-1} + \mathbf{K}_C^{-1} \right\}^{-1} \quad (2.13)$$

Where the matrices on the right can be calculated as follows:

$$\mathbf{K}_A = \left[\left(\mathbf{T}^{R_1 \rightarrow R} \right) \mathbf{K}_{R_1} \left(\mathbf{T}^{R_1 \rightarrow R} \right)^T + \left(\mathbf{T}^{R_2 \rightarrow R} \right) \mathbf{K}_{R_2} \left(\mathbf{T}^{R_2 \rightarrow R} \right)^T \right]^{-1} + \left[\left(\mathbf{T}^{R_3 \rightarrow R} \right) \mathbf{K}_{R_3} \left(\mathbf{T}^{R_3 \rightarrow R} \right)^T \right]^{-1} \quad (2.14)$$

$$\mathbf{K}_B = \left(\mathbf{T}^{R_5 \rightarrow R} \right) \mathbf{K}_{R_5} \left(\mathbf{T}^{R_5 \rightarrow R} \right)^T \quad (2.15)$$

$$\mathbf{K}_C = \left(\mathbf{T}^{R_4 \rightarrow R} \right) \mathbf{K}_{R_4} \left(\mathbf{T}^{R_4 \rightarrow R} \right)^T \quad (2.16)$$

Here, \mathbf{K}_A denotes the equivalent stiffness of links at R_1 , R_2 , and R_3 at P. Similarly, \mathbf{K}_B and \mathbf{K}_C denote the final stiffnesses of links at R_5 and R_4 at P. Depending on whether the links are in series or parallel, they are added accordingly, i.e., summing stiffnesses for elements parallel to one another, and adding compliances for elements in series.

The above summation results in a very complex expression for the individual stiffnesses along different axes. The \mathbf{K}_{xx} term is however simple, and can be written as:

$$\mathbf{K}_{xx} = E \left(\frac{1}{l} + \frac{2}{l'} + \frac{d^2}{l^3} + \frac{1}{\pi \sqrt{rd}} \right) dw \quad (2.17)$$

To validate the above equation, we plug in the following parameters: $l = 9$ mm, $l' = 1.2$ mm, $d = 0.05$ mm, $w = 1$ mm, and $r = 4.5$ mm. This results in $\mathbf{K}_{xx} = 7 \times 10^6$ N/m. Through FEM simulations, a similar value of 7.15×10^6 N/m is obtained. This is done by applying a force $F_x = 1$ N at point P and measuring the displacement along X-axis.

The method described above is generic and can be applied to arbitrarily complex mechanisms satisfying linear elasticity and usual beam theory conditions.

2.7 Summary

In this chapter, we have introduced the concept of pseudo-monolithic assembly on a single substrate. Although the assembly complexities associated with a bulk free-space design are partly circumvented, fabrication and assembly tolerances are present nevertheless. To correct these errors, the concept of femtosecond laser-based remote actuation was discussed in broader detail. A necessary component of the repositioning principle is the kinematic design. For this, we established a set of design rules within which, various kinematic mechanisms were proposed. As these mechanisms are intended to be integrated into optical circuits, we focussed our attention on mechanisms having rotational and translational degrees of freedom. Finally, we presented an analytical design tool for stiffness estimation of a kinematic mechanism, and its validation when compared to finite element analysis simulations.

With this understanding, we now proceed towards Chapters 3 and 4, which present an experimental implementation of some of the mechanisms introduced here. In Chapter 4, we will demonstrate their integration in an optical circuit.

Chapter 3 One degree of freedom repositioning using femtosecond lasers²

In this chapter, we demonstrate proof-of-concept components that can be repositioned using femtosecond laser exposure. Building upon our knowledge about the events occurring within a laser exposed region, the localized effects on density and volume of the material, our goal is to channel the volume changes away from the focal spot and add a component-level functionality. To do so, we add advanced mechanical elements called flexures, and leverage the volume changes into a controlled motion at the end effector. By varying the laser parameters or the kinematic design of the components, we showcase a bi-directional in-plane and out-of-plane rotational motion. From a pure laser standpoint, a study on optimal exposure parameters is also presented, which then serves as a basis for the rest of the experiments. A preliminary stability analysis is also presented.

3.1 Measurement setup

The small magnitude of the volume changes presents a need for amplification mechanisms to achieve a relatively large output motion. Still, the observed angles are small (in the order of μ -radians) and need to be measured accurately. Although interferometric or microscopic methods could be used postmortem, they suffer from a loss of information as to how the final state of the device was reached. As such, it is necessary to perform in-situ measurements to understand the actuator response when exposed.

To measure the deformation of the laser exposed zone, we use a triangulation scheme as shown in Figure 3.1. A fiber pigtailed laser diode ($\lambda = 980$ nm) is used as a light source. The fiber output is collimated using an aspheric lens and then reduced in diameter using a pair of bi-convex lenses. The resulting beam has a beam diameter of < 1 mm and is thus contained completely within the test-mirror surface (the sample is 1 mm thick). The reflected beam passes through an f - θ lens and is focussed on a position sensing detector (PSD) that measures the actual position of the beam in a plane (within ± 1 μ m), therefore, not only measuring lateral but also vertical motion. The f - θ lens, in addition to amplifying the output displacement, has a flat image plane at the position of the detector, thus ensuring the beam is always focussed in the same plane. By design of the f - θ , the displacement in the image plane is *linearly* proportional to the change in angle of incidence and is given by:

$$\Delta x = f \times \Delta \theta \quad (3.1)$$

Here, $\Delta \theta$ is the change in the in-plane angle of incidence of the incident ray with respect to the optical axis of the lens, f is the focal length of the lens, and Δx is the net displacement observed on the surface of the detector.

Similarly, any change in the out-of-plane angle is given by the displacement along Y direction,

² Part of this chapter has been published in [107].

$$\Delta y = f \times \Delta \phi \quad (3.2)$$

Here, $\Delta \phi$ is the change in the out-of-plane angle of incidence with respect to the optical axis of the lens.

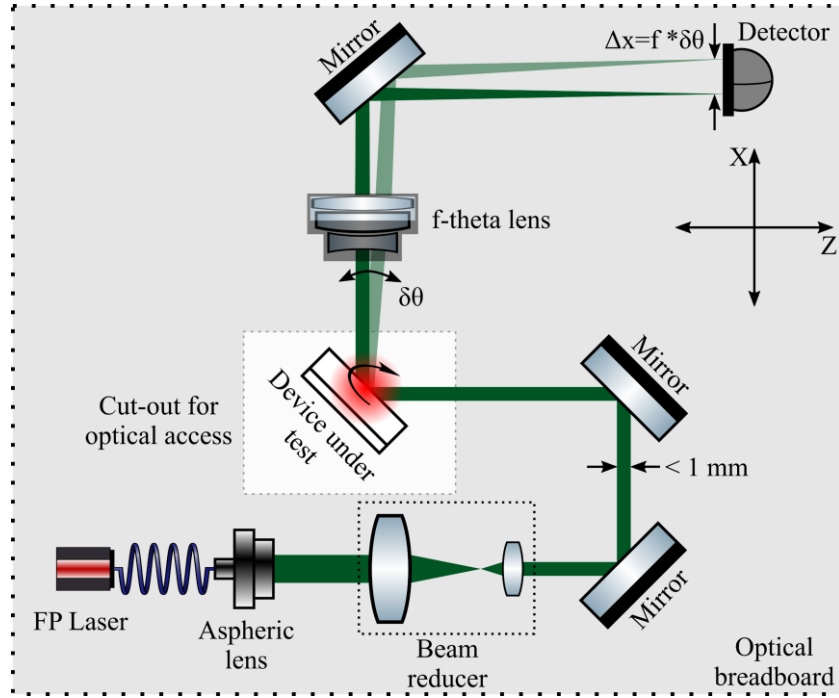


Figure 3.1 – A schematic of the measurement setup. A pigtailed laser diode is collimated and reflected off the mirror surface of the test specimen. The beam is then focussed using an f-theta lens ($f = 254$ mm). At the image plane, a sensor records the position of the focal spot along X and Y directions. The entire setup is mounted on a portable optical breadboard, which is then mounted on positioning stages and under the focus of a femtosecond laser. Parts of this figure were created using the component library developed by Alexander Franzen.

The measurement setup is portable and can be mounted directly on a laser exposure platform to perform the repositioning experiments and measure the deformations dynamically as the exposure process evolves.

3.2 In-plane actuation

3.2.1 Working principle

The proof-of-concept device (Figure 3.2a) is a Remote Center of Rotation (RCR) mechanism. It consists of a mirror element suspended on two thin slender beams or flexures. The thin beams are suspended at 45° from the vertical and fixed to bulk glass on one end. The actuator, located elsewhere, connects to the mirror element through three components; a) a thin bar at the end of the actuator to couple the strain to the rest of the device, b) an amplification mechanism to magnify the strain and c) a thin bar at the top of the amplification mechanism to transfer the strain to the mirror element. The actuator is a wide and long cantilever fixed on one end and free to move on the other end. To reposition the mirror in-plane, the actuator can rotate the mirror in a bi-directional manner, with precise control and in a non-contact manner. As the method is based on non-linear interaction and relies on the volume changes happening within nanometer-sized pores within the modified volume [96], it is capable of providing sub-nanometer linear displacement resolution [106]. Although the displacement within the actuator is linear, it is converted into a rotational motion of the mirror through the implemented kinematics as described in detail in the next section.

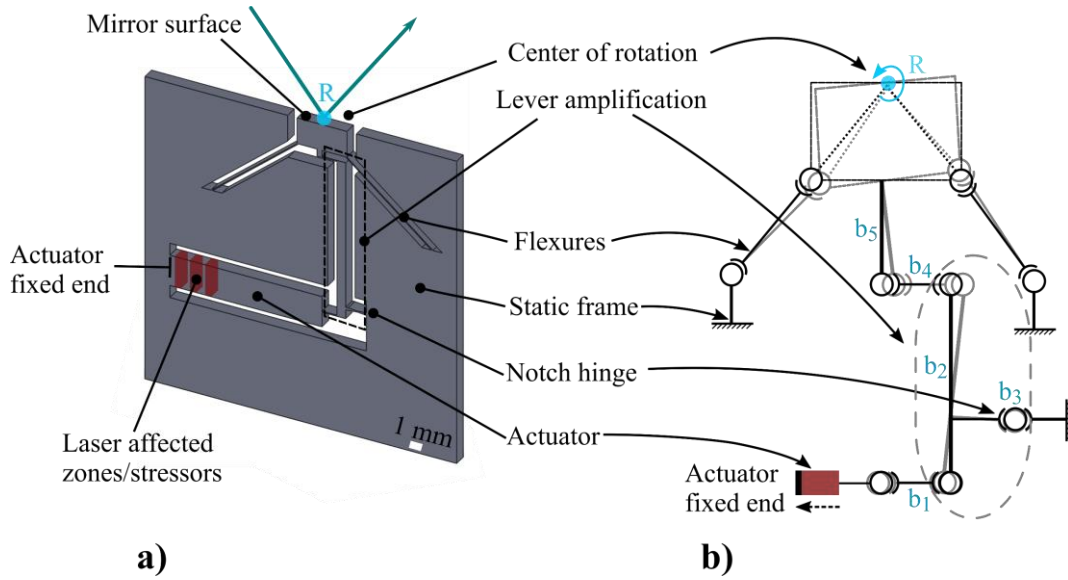


Figure 3.2 – a) A computer-aided design (CAD) of the proof-of-concept gimbal mirror. It consists of three main elements, an actuator, a lever amplification mechanism, and the mirror element suspended on flexures. b) A kinematic diagram of the mechanism is shown on the right. The actuator, shown in red here is constrained at one end and attached to a flexure (b_1) at the other end. A deformed state of the device is drawn underneath to showcase the effect of compression inside the actuator.

3.2.2 Device kinematics

The kinematic design of the gimbal mirror is shown in Figure 3.2b. Each pivot joint represents one degree of freedom. The center of the mirror—denoted here as R , is defined by the intersection of the two thin beams oriented at 45° with respect to the mirror normal. The mirror is supported by a thick arm (b_5) at its center that transfers the force from the actuator. The latter, shown in red here, is exposed in certain specific locations to short pulses to induce a net strain. As one end – the anchoring point of the actuator – is infinitely stiff in comparison to the other end, the volume changes are directed towards the less stiff end, causing a net displacement. A classic lever mechanism (b_2) is employed to amplify this motion. An amplification ratio of 15 is chosen here to get a measurable rotation of the mirror surface. The lever arm is attached to a notch hinge (b_3) capable of bending about its center (thinnest part). Another thin beam (b_4) connects the lever mechanism to the mirror, effectively pulling or pushing on the beam and causing a rotation about R . The two beams (b_1 , b_4) are designed to be loaded in both tension or compression, without any appreciable effect on the overall functioning of the mechanism. For illustrative purposes, a deformed state of the device, corresponding to the situation where shrinkage occurs inside the actuator, is shown in gray.

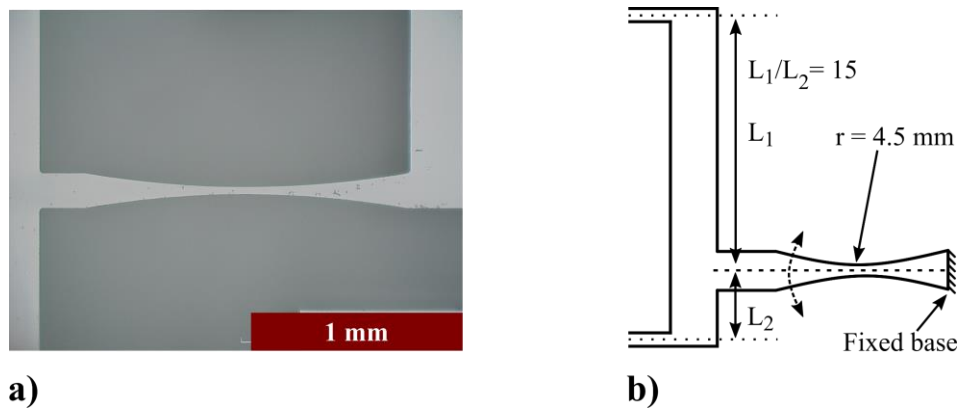


Figure 3.3 – a) An optical micrograph of the notch hinge. b) The crank wheel amplification mechanism. A relatively large amplification ratio is chosen here while optimizing the stiffness acting on the actuator.

3.2.3 Fabrication process

In this work, all the specimens are fabricated using femtosecond laser micro-manufacturing process, though process parameters vary from case to case. Below, we provide a detailed description of this method.

A short-pulse laser (Ytterbium-fiber, Amplitude Systemès) emitting 270 fs pulses at a wavelength of 1030 nm is used as a source. Using a high numerical aperture objective (NA = 0.4), the beam is focussed down to a beam diameter of 1.5 μm . The focusing objective is mounted on a motorized vertical axis while the sample is mounted on precise positioning stages capable of translating along X and Y directions at high speed. A combination of these three axes allows for a three-dimensional control in positioning the focal spot anywhere inside the substrate. A half-wave plate mounted above the objective allows for polarization control whereas a combination of a half-wave plate and a polarizing beam splitter (PBS) is used to modulate the writing power. For this step, pulse energy of 250 nJ and a writing speed of 8 mm/sec is used. The repetition rate of the laser is 750 kHz.

After the laser exposure step, the specimen is etched in a bath of dilute hydrofluoric acid (2.5%) for 24 hours, thereby etching away the laser-affected regions. In this particular case however, the etching step is preceded by a polishing step. The substrate edge containing the mirror face is polished to near optical quality. After each successive grain size, the edge is inspected under a microscope and the process is repeated until a good surface quality is achieved. An example of an etched specimen is shown in Figure 3.4.

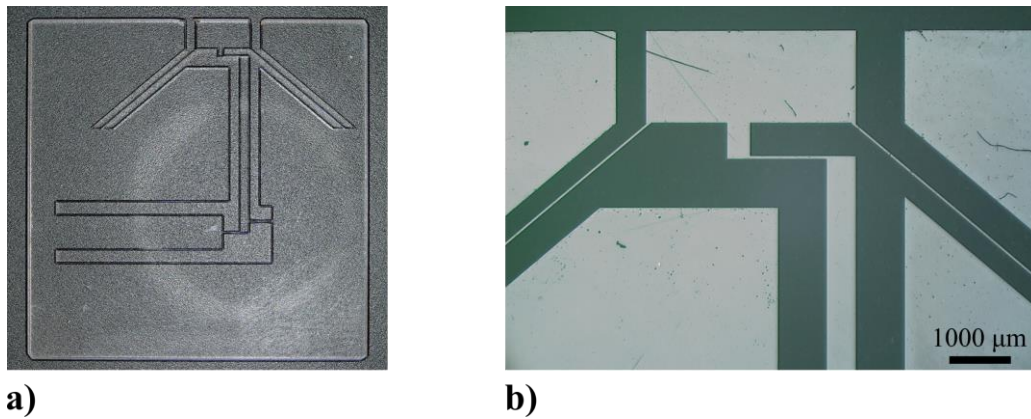


Figure 3.4 – a) A low magnification image of the RCR mechanism. The dark circle in the middle is caused by the ring illumination used for imaging. b) A high magnification image of the mirror area of the device. The width of the 45° flexures is about 50 μm .

3.3 Experiments

After fabrication, the re-exposure of the specimens is carried out on a different laser system. For this, the measurement setup described earlier together with the sample is mounted on a dual-axis motorized stage with high load-bearing capability. As these stages are present on a separate laser system with different beam characteristics, we provide more details below.

3.3.1 Exposure setup

To operate the mechanism, both Type I and type II exposures are required. This requires simultaneous access to two different pulse widths. Later on, we will present mechanisms that bypass this limitation.

The exposure setup uses a ytterbium-based femtosecond source, emitting 300 fs laser pulses with a repetition rate of 120 kHz (changeable to 300 kHz). The seed laser feeds an optical parametric amplifier (OPA), delivering a non-Fourier limited, positively chirped pulse with a temporal width of 550 fs at 850 nm. An external

prism compressor is used to shorten the pulses to 50 fs pulse width. The different pulse width configurations are shown in Figure 3.5.

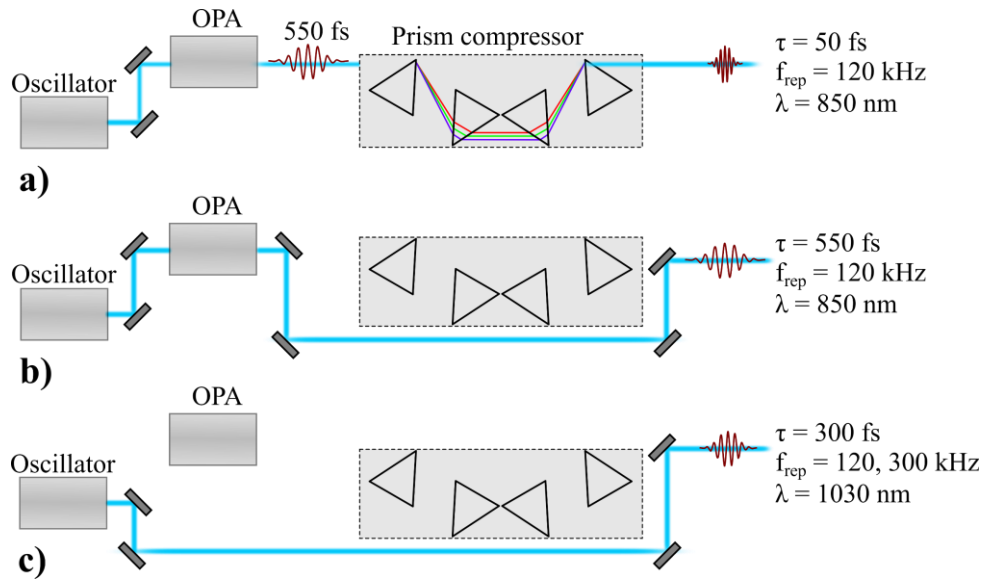


Figure 3.5 – Illustration of the laser system used for post-etching exposures. a) Short pulse configuration: the output of the oscillator is fed into an OPA emitting a positively chirped, non-Fourier limited pulse, which is then compressed into a much shorter 50 fs pulse using a prism compressor. This is used to write Type I modifications. b) Long pulse configuration: the prism compressor is bypassed and the output of the OPA is directly used for experiments (Type II). c) Using a flip mirror, the OPA, as well as the prism compressor are bypassed to directly use the oscillator output at 300 fs (Type II).

3.3.2 Identification of optimal writing parameters using micro-cantilevers

The strain within the modified region is a function of various parameters like pulse energy, spot size, and deposited energy. Similarly, varying the pulse width and/or pulse energy can lead to shrinkage (negative strain or Type I) or expansion of the actuator (positive strain or Type II) [97]. However, the net strain typically varies between 0.01 to 0.05% of the exposed volume, which corresponds to a few hundred nanometers in linear motion within the actuator.

The maximization of strain is important for the efficient use of the actuator volume. It also means less dense exposures are required to achieve the desired motion thus lowering the stress within the exposed volume. From a practical standpoint, size is often a deciding factor and can be considerably reduced by optimizing the writing parameters. To do so, we reuse a technique developed and presented [96] in and explained below.

A series of cantilevers are fabricated on a 250 μm thick sample of fused silica. The cantilevers are 18 mm long and 1 mm wide. After etching, they are exposed near the anchor point by writing a single layer of modification 35 μm below the top surface (the top surface stays pristine). The modified region consists of a series of parallel lines at a lateral spacing of 4 μm . The overall length of the modified zone is 5 mm and contains a total of 1250 lines. The exposure is carried out for all the available pulse widths, i.e., 50 fs, 550 fs, and 300 fs, and only near the top surface, thus forming a bilayer of modified and unmodified material.

For each pulse energy, the deposited energy is gradually increased by reducing the writing speed (Figure 3.6.). Depending on the pulse width, volume expansion is observed for longer pulses while shrinkage occurs for shorter pulses. Hence, the tip of the cantilever bends either up or down depending on the sign of the strain. The bending is further amplified by the length of the cantilever and thus provides an efficient method for characterizing the volume changes.

We use Stoney equation [128] to calculate the stress within the thin laser affected layer at the top of the cantilever. By measuring the bending of the cantilever tip using a white light interferometer, the strain is calculated using:

$$\varepsilon_{laz} = \frac{d_{laz} l_s}{R w_0} \quad ; \quad \frac{1}{R} = \frac{\delta}{L_l (L_c - L_l / 2)} \quad (3.3)$$

Here ε_{laz} denotes the strain within the laser affected layer, d_{laz} is the distance of the exposed region from the neutral line, l_s is the line spacing, w_0 is the width of a single modification, δ is the measured tip deflection, L_l is the length of the exposed region, L_c is the length of the cantilever, and R denotes the radius of curvature of the bimorph region. Equation 3.3 has been validated in earlier texts [102], [129], and is reproduced in the annex.

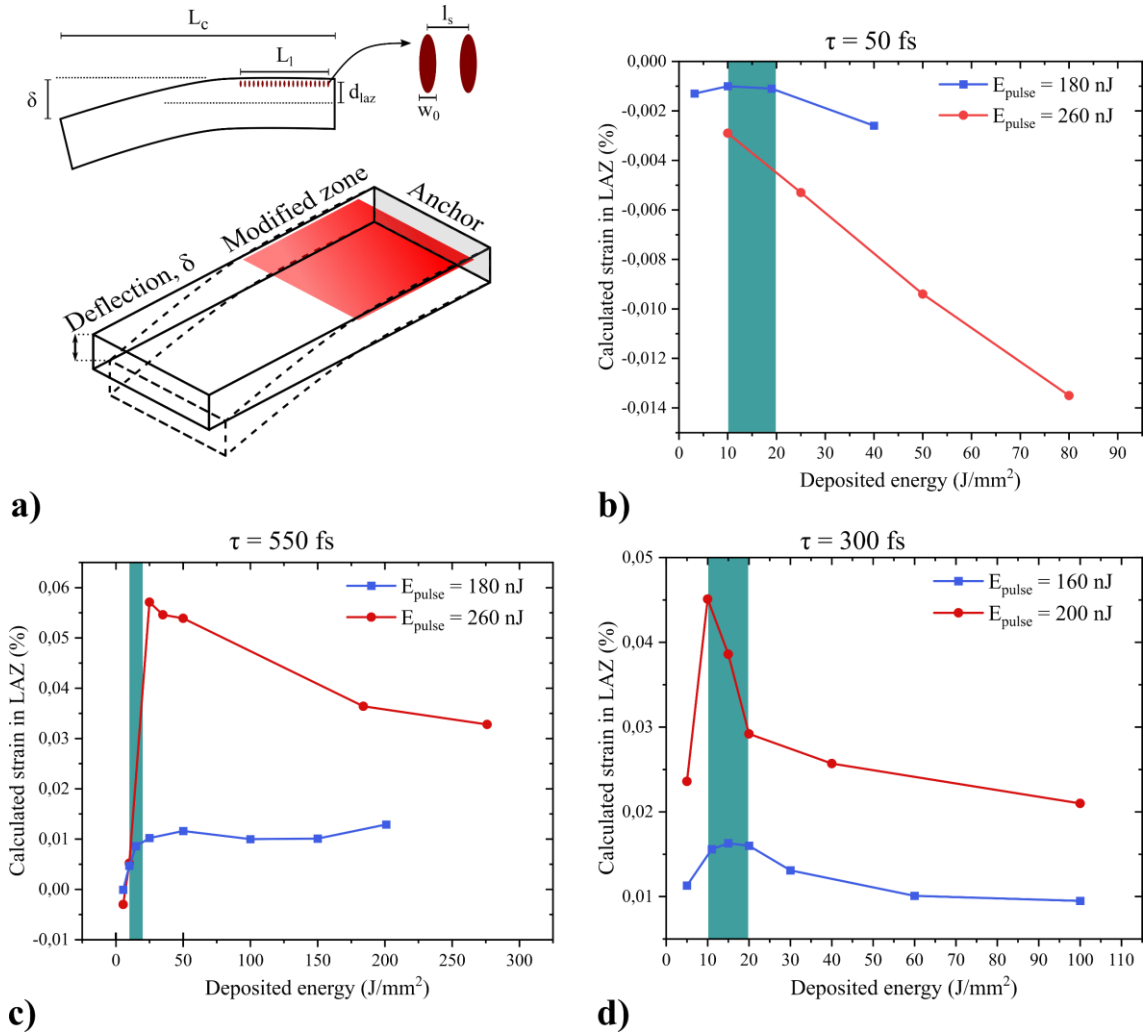


Figure 3.6 – Study to identify the optimal laser exposure parameters. Dependence of strain on deposited energy is studied for each pulse width and different pulse and deposited energies. a) Geometry of the cantilever used for these studies showing the laser affected zone in red. By measuring the tip deflection, the net strain is calculated. b, c, d) Strain in the laser affected zone as a function of deposited energy for $\tau = 50$ fs, 550 fs, and 300 fs respectively. Between (b) and (c,d), the sign of the strain is reversed indicating the transition between Type I to Type II. This is reflected experimentally by the opposite nature of bending between the two cases. The deposited energy typically used for the rest of the experiments in this thesis is also highlighted.

For shorter pulses, we see a monotonic growth in the strain as the deposited energy is increased. The strain is negative and corresponds to densification of the material as expected. For longer pulses, we confirm an al-

ready established trend, where the strain peaks around a fluence of $10 - 20 \text{ J/mm}^2$ before declining sharply [130]. Here, the strain is positive and indicates a volume expansion as is expected for longer pulses. It is also important to note that at higher pulse energies, the strain observed at longer pulse lengths is much larger as compared to that of shorter pulses.

3.3.3 Effect of short pulses (50 fs)

For this experiment, we use the laser configuration depicted in Figure 3.5a. The first exposure is carried out $200 \mu\text{m}$ away from the fixed end of the actuator. A pulse energy of 260 nJ and deposited energy of 20 J/mm^2 are chosen. Although the strain curve for 50 fs pulse width shows a monotonic increase with deposited energy, a moderate value of deposited energy is chosen instead. Unlike the single-layer exposures of the previous section, the exposed volume contains a high density of patterns throughout the thickness of the actuator. This leads to stress buildup within the modified volume and is often accompanied by crack formation as will be discussed in more detail in Chapter 6. To prevent this, the modified zone is written in the form of a trapezium (Figure 3.7a), 1 mm wide at the bottom and $680 \mu\text{m}$ wide at its top surface, and contains approximately 34,000 lines. Such a shape also generates a uniform strain across the thickness of the actuator, therefore minimizing out-of-plane bending. To maintain a uniform deposited energy, a buffer of $500 \mu\text{m}$ is maintained on either side of each written line. This allows enough time for the positioning stages to accelerate to a constant speed before the laser beam is scanned across the actuator.

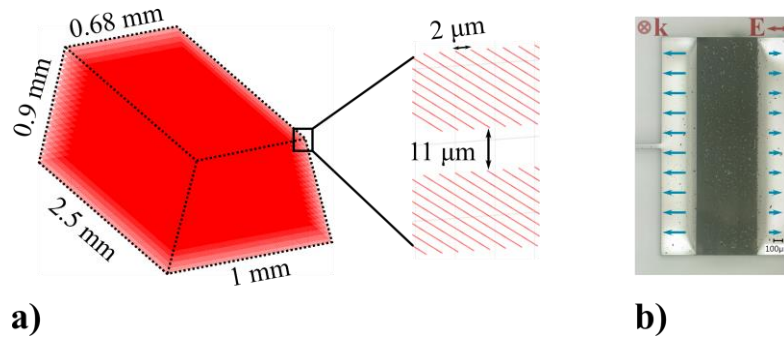


Figure 3.7 – a) A geometrical illustration of the laser affected zones, consisting of equidistant lines within each plane. Similar planes are stacked vertically on top of each other with reducing size to compensate for parasitic bending. b) An optical micrograph of the modified region. The lighter shades on either side are the planes near the bottom surface.

As the material is exposed, the actuator begins to shrink in volume, thus rotating the mirror anti-clockwise. The exposure process is slow, however, the writing time can be considerably reduced by using galvanometric scanners, higher repetition rates, etc. Later on, in Chapter 4, we will present a new kinematic design where the writing time is reduced by an order of magnitude.

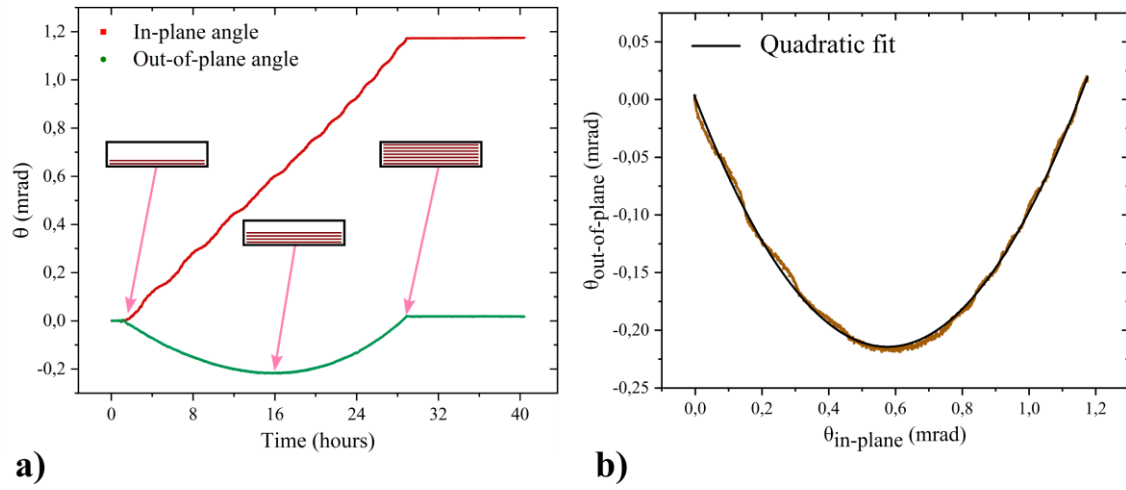


Figure 3.8 – a) Angular rotation of the mirror plotted over time. The angle increases as more planes are added inside the actuator. The parasitic movement increases initially (in magnitude), followed by a return to the initial position. The progression of the writing process is indicated at different stages of the plot. The flat region of the plot is indicative of the end of laser exposure. b) Parasitic out-of-plane movement plotted versus the in-plane movement. At its maximum, it is nearly 18% of the overall in-plane motion. The laser parameters are: 260 nJ pulse energy, 20 J/mm² deposited energy, and 50 fs pulse width.

Along with the in-plane rotation, an out-of-plane parasitic movement is also observed as shown in Figure 3.8. It grows initially as more lines are stacked together and later on, returns to a near-zero level. This effect is attributed to the writing strategy, which follows a sequential approach of bottom-to-top addition of successive planes. As the bottom surface is exposed, it shrinks (or expands depending on the pulse duration) while the top surface remains unaffected. This creates a bimorph-like layered structure of modified and unmodified material causing the actuator to bend down during this sequence. Next, as the laser focus gradually moves up and above the neutral line, the strain in the lower layers is gradually compensated and the bending effect is canceled, leaving only a net contraction (or conversely for longer pulses, an expansion) of the actuator without any out-of-place deflection. To monitor the stability of the mirror in its deformed state, the position of the probe beam is continuously recorded. The observed fluctuations lie within the measurement error of the detector as shown in Figure 3.9.

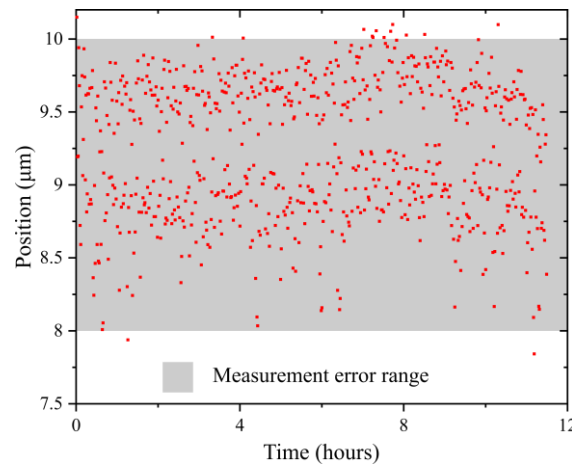


Figure 3.9 – Position variation of the focal spot of the measurement beam after the laser exposure is stopped. The mirror is oriented in its deformed state at a moderate angle of 1.2 milliradians. The observed fluctuations are within the measurement resolution of the detector.

The parasitic bending is strongly influenced by the location of the laser-affected region within the actuator. In other words, depending on where the modified volume is placed within the bulk of the actuator, the parasitic motion can be minimized. To showcase this, we modify the actuator again, this time away from the anchor point and close to its free end ($\sim 200 \mu\text{m}$ away from the free end). Doing so nearly removes the effect of the actuator length, and minimizes the parasitic motion as shown in Figure 3.10.

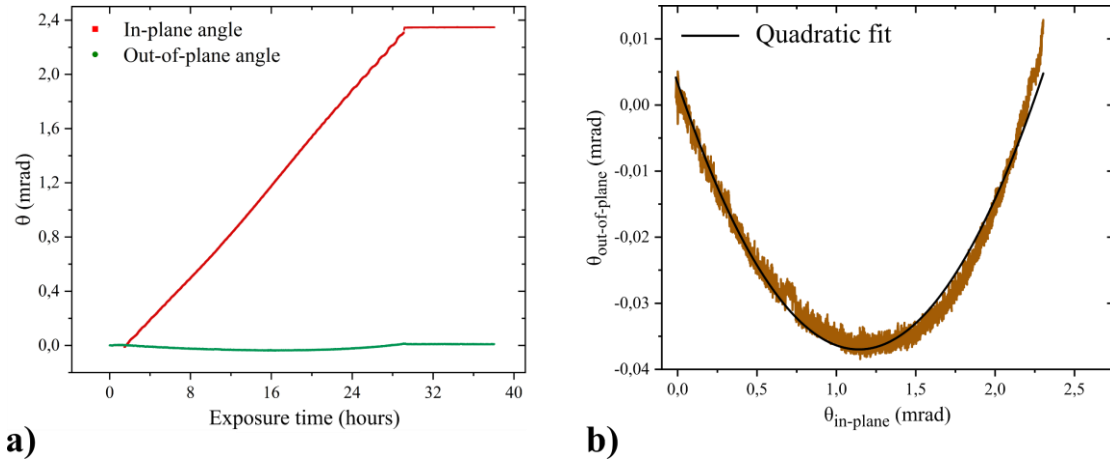


Figure 3.10 – a) Angular rotation of the mirror plotted over time. The parasitic out-of-plane motion is also reduced to less than 2%, an order of magnitude smaller than the previous case. b) Parasitic movement plotted versus the desired in-plane movement. The laser parameters are: 260 nJ pulse energy, 20 J/mm² deposited energy, and 50 fs pulse width.

The current position of the laser exposed zone nearly doubles the angular rotation for the same exposure conditions. This is because nearly all of the strain is transferred to the mobile mirror, as the stiffness of the actuator no longer comes into play. In other words, less strain energy is lost in the actuation bar itself. Besides, the parasitic bending is reduced by nearly an order of magnitude.

3.3.4 Effect of long pulses (300 fs)

To access Type II modifications and the so-called nanogratings, we use the laser configuration depicted in Figure 3.5c. For this exposure, a lower pulse energy of 160 nJ and deposited energy of 8 J/mm² are used. The modified region is placed near the free end of the actuator with the same geometry as earlier.

The angle measurement results (Figure 3.11) show a reversal in orientation of the rotation as compared to earlier experiments with shorter pulse width, thus confirming an overall volume expansion (positive strain) inside the actuator. There is also an offset of nearly 50 μrad between the initial and final out-of-plane angle. This is due to the large in-plane bending angle causing the probe laser beam to move beyond the active area of the sensor.

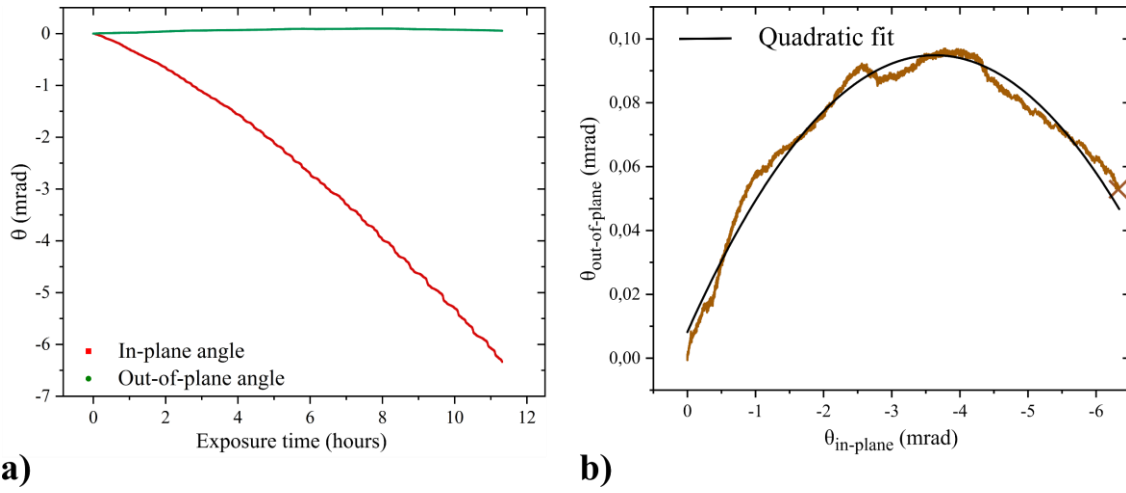


Figure 3.11 – a) Type II modifications resulting in opposite bending direction of the mirror. Even at large bending angles, the parasitic movement stays within 2% of the in-plane movement. b) Parasitic out-of-plane movement plotted versus the in-plane movement. Due to the large bending angle, the beam traveled beyond the measurement area of the detector, indicated by a cross on the plot. The laser parameters are: 160 nJ pulse energy, 8 J/mm² deposited energy, and 300 fs pulse width.

As observed with the cantilever experiments (Figure 3.6), the ratio between the measured values of strain for the deposited energies used is nearly 1:3 between short and long pulses. A similar ratio is obtained in the total deflection angle measurement between the two pulse widths.

The variation of angle with time shows a slightly non-linear behavior which is not present in earlier loading cases. This can be attributed to the increased loading of the pivoting hinge along the axial direction. Under the effect of a transverse load, a hinge becomes less stiff along its bending direction as the load is progressively increased [111]. As a result, it deforms significantly more, causing a larger rotation.

3.3.5 Stability analysis

In this section, we present a stability analysis of the device in its deformed state once the actuator is loaded. Relaxation in glasses is a known phenomenon and therefore poses a valid question: can the mirror hold its final position without any relaxation or deviation over time. In the case of femtosecond laser modified fused silica, stress relaxation is observed depending upon the level of stress and environmental conditions such as temperature and humidity. Although this lies at the core of Chapter 6 and is investigated in much more detail there, it is still interesting to do a preliminary investigation with one of the loaded devices.

To observe this, the device is mounted in a stand-alone configuration under a digital holographic microscope (DHM). The laser beam of the DHM is incident from the top and measurements are carried out in reflection mode. Using a low numerical aperture objective, the beam is partly incident on the deformed mirror and partly on the static base next to it (Figure 3.12a), and holograms are recorded. Based on the recorded pattern, the change in height difference between four arbitrary points on the mirror surface and a fixed point on the base is monitored over time. In Figure 3.12c, the data for four such points are plotted.

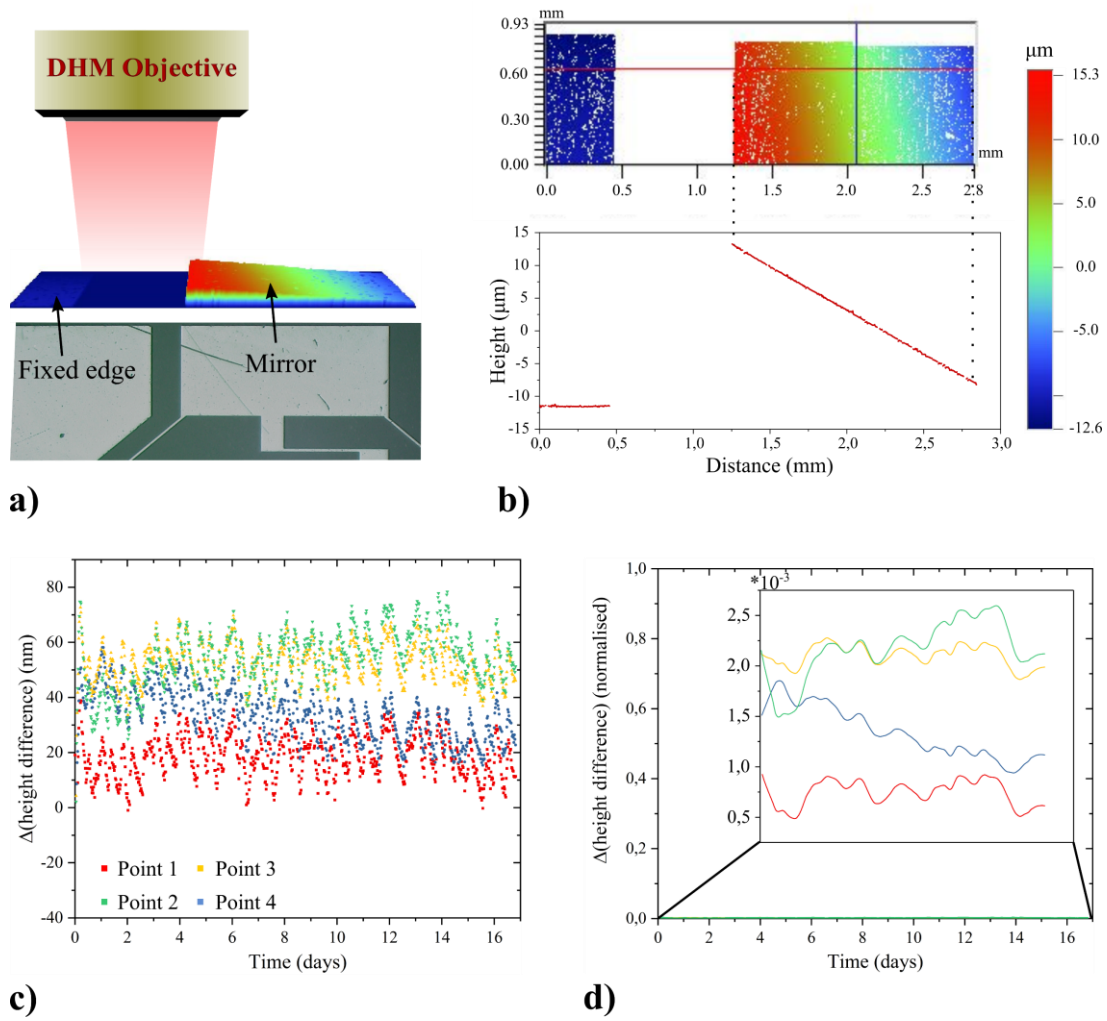


Figure 3.12 – Stability measurements on a mirror rotated by 3.5 milliradians. a) Interferometric measurement technique to observe variation in position between a static base and the test surface. b) A 3D color map of the deformed mirror (top) and a line plot depicting the height profile across it. c) Variation in height difference plotted over time. d) Normalised height variation. The height difference between the mirror and the base is used to normalize the data in (c).

The above experiments do not suggest any departure from the deformed state, i.e., the mirror holds its position for the duration of the measurement. The saw-tooth pattern of Figure 3.12c could be related to the temperature cycle of the DHM laboratory, whose temperature was not precisely controlled. Based on this preliminary investigation, we can conclude that the repositioning does not decay over this time scale. As mentioned earlier, temperature, humidity, and level of internal stress play a crucial role in determining the stability of such stress states. In this proof-of-concept device, the peak stress however does not exceed a few tens of MPa within the flexures.

3.4 Out-of-plane actuation

This section is divided into two parts. In the first part, we follow the same approach used so far, i.e., the actuator where the laser-affected zones are written is separate from the guidance mechanism that channels the volume expansion and guides the end effector. In the second part, we will showcase a more compact mechanism where the flexure encompasses two functions: a) it provides the necessary space for exposing the material, and b) it guides the volume expansion into the desired output motion.

3.4.1 Part 1: Actuator separated from flexures

3.4.1.1 Working principle and motion kinematics

To activate out-of-plane motion, we use a cruciform flexure design (Figure 3.13) that can be loaded in torsion. The axis of rotation is formed by two slender beams fabricated perpendicular to each other. For actuation, the design relies on the cantilever geometry discussed earlier. A similar cantilever is used as an actuator and attached to the cruciform hinge carrying the mirror surface. To accommodate the parasitic errors of the cantilever tip (an upward or downward motion of the cantilever tip is accompanied by a translation along the cantilever length), a flexible joint is used as an interconnect.

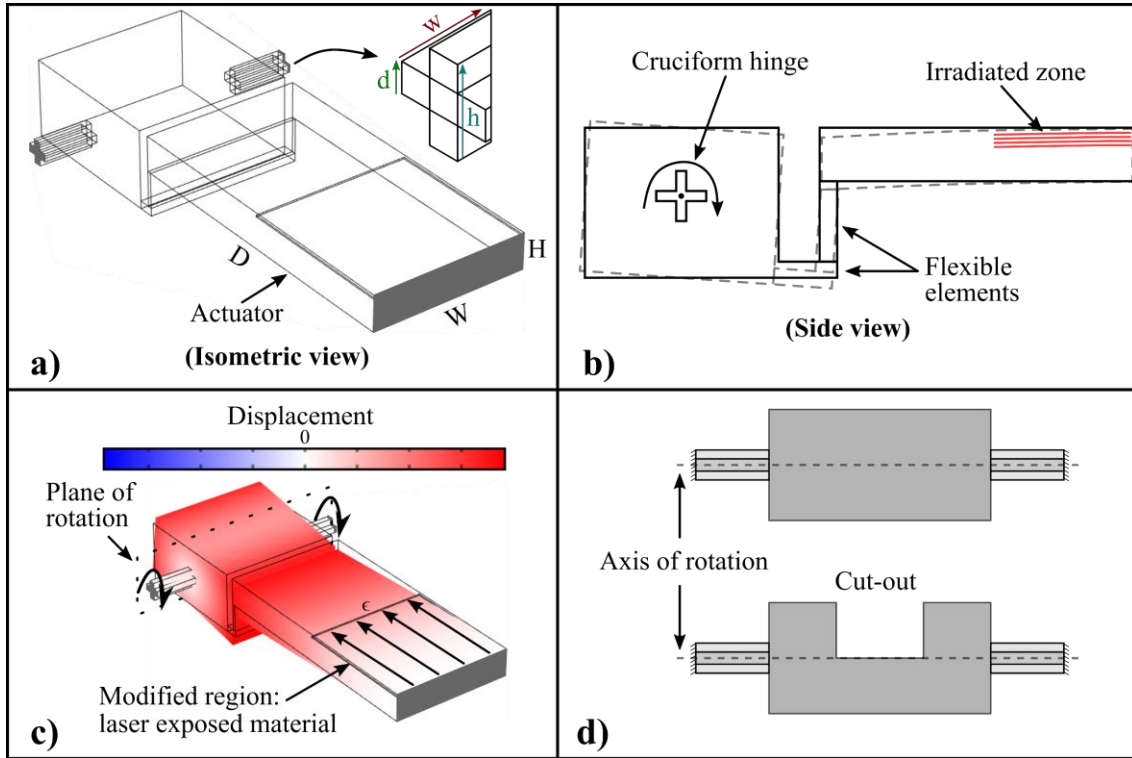


Figure 3.13 – a) An isometric view of the cruciform hinge mechanism. W , D , and H indicate the actuator width, depth, and height respectively. b) Side-view of the mechanism. Laser-affected zones located strategically within the actuator force a bi-directional motion of the tip in an upward or downward direction. The deflection is coupled to the mechanism through two orthogonal deformable elements. c) A deformed state of the device indicating the plane of rotation and relative displacement at various points. d) A possible approach to circumvent the offset between the axis of rotation and the mirror surface. A cut-out can be fabricated to force the coincidence between the two. This is however not implemented in this work.

When actuated, at a point away from the axis such as on the mirror surface, the overall motion includes a translation component too, leading to parasitic motion. This is due to the offset between the axis of rotation and the mirror surface. In Figure 3.13d, a possible solution to overcome this issue is presented.

Unlike the RCR mechanism, bi-directional motion can be achieved while staying in a single regime. This is to say, using a single pulse width, the mechanism can bend upwards as well as downwards. The rotation direction is defined by the location of the modified zone along the thickness of the actuator. For example, if the region near the top surface is modified, the mirror bends clockwise. Similarly, if the region near the bottom surface is modified, the mirror bends anti-clockwise (clockwise and anti-clockwise are defined arbitrarily).

Using an FEM software (Comsol Multiphysics), the stiffness of the elemental flexures is optimized. In such an optimization, our goal is to maximize the achievable angle for a fixed value of strain. Once the flexure dimensions are fixed, the stiffness of the actuator is optimized such that maximum deformation is transferred to the mechanism, thus minimizing lost motion. For this simulation, the ‘initial stress and strain’ module is used by specifying a strain value of 2.2×10^{-3} . The results are shown in Figure 3.14.

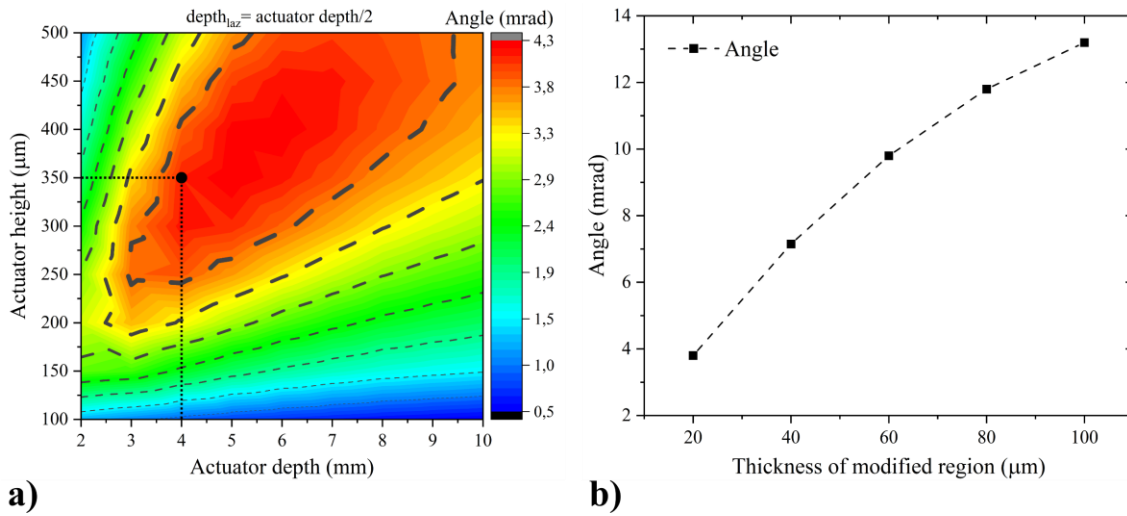


Figure 3.14 – A heat map indicating the angle of rotation as a function of the actuator parameters. b) Angle of rotation as a function of the modified region thickness.

Based on the above analysis, the flexure and actuator parameters are noted in Table 3.1. Although a larger actuator depth can result in a greater angle, however, this is accompanied by lower vibrating modes. As a compromise between stability and range of motion, the dimensions of the actuator are chosen from the bottom-left region of the innermost contour of the heat map. In this region, the fundamental mode is close to 17 kHz, which is reasonably higher than common acoustic vibrations.

Table 3.1 – Optimized actuator and flexure dimensions of the cruciform mechanism (in mm)

W	D	H	w	d	h
2	4	0.35	0.7	0.1	0.3

• Fabrication challenges

Using femtosecond direct-laser writing, the device is fabricated starting from the edge of a $25\text{ mm} \times 25\text{ mm} \times 1\text{ mm}$ substrate of fused silica. The contour is drawn in a manner such that the mirror surface coincides with the edge of the substrate. Near the edges, however, the focal spot is distorted due to the presence of an air dielectric interface. Although this effect is negligible near the top surface, however, deeper into the material, it becomes more significant. Near the bottom surface of the substrate, i.e. at a depth of 1 mm, the effect is more severe and leads to a discontinuity in the machined contour. This can extend up to a length of 100 μm or even more from the edge as shown in Figure 3.15.

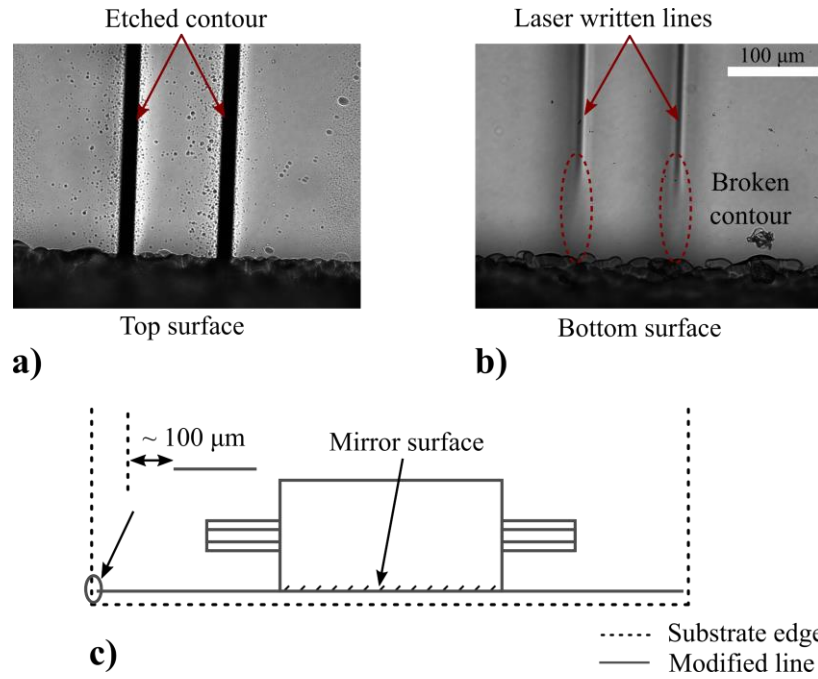


Figure 3.15 – a) Post etching image of a laser machined contour fabricated at the top surface and near the edge. b) An image of the same contour at the bottom surface (at a depth of 1 mm) showing the effect of diffraction near the edge. c) Sketch of the laser contour used for fabrication and to prevent cracks in the flexures.

The non-machined region near the edge can be usually removed by polishing (using abrasive lapping) before the etching step. However, additional stresses due to the physical rubbing lead to small cracks (Figure 3.16) within the hinge which is located close to the polished surface. Since the polishing step precedes the etching step, the presence of bulk glass around the flexures should ideally shield them from the stresses arising during the process. Nevertheless, this is not the case. A possible reason is the high bending stiffness of the cruciform joint, which fractures under bending stress. To solve this, the mirror is fabricated at an offset from the edge and towards the bulk of the substrate. The laser modified line defining the mirror surface is extended towards the edge of the substrate (Figure 3.15c). This forces the clipping effect to occur at the orthogonal edge and away from the flexures, which is then polished away before etching.

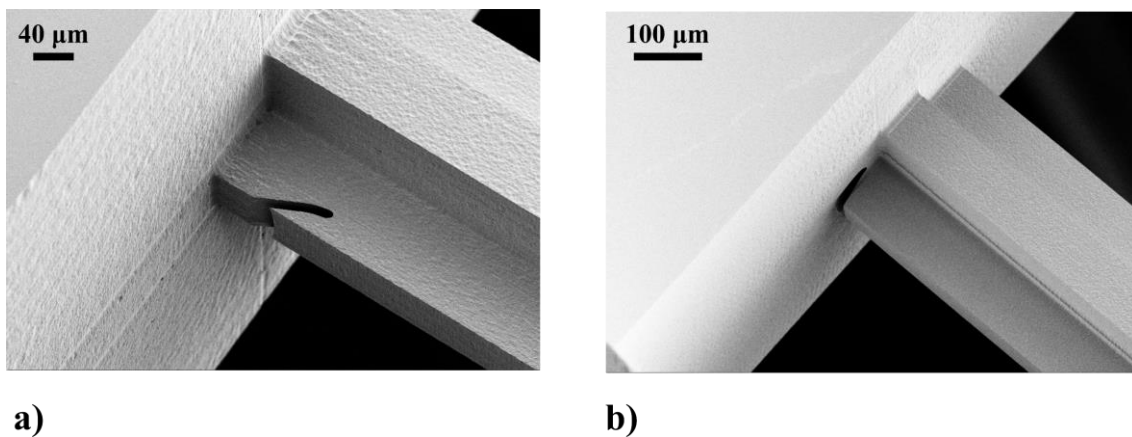


Figure 3.16 – a,b) SEM pictures of cracks initiated during the polishing process.

Post etching, there is some residual roughness (~ 100 nm Ra) on the mirror surface. Since mechanical polishing is not possible at this stage, for the sake of demonstrating the mechanism, we fabricate circular disks out of a 250 μm thick fused silica substrate. The pristine face is gold-coated and glued to the mirror surface.

Note that CO₂ laser-based polishing techniques as demonstrated in [113], [114] could be used to achieve much smaller roughnesses, down to a few nm Ra.

3.4.1.2 Experiment

In the following experiments, a single laser pulse configuration is used and only Type II modifications are written. For the exposures, pulse energy of 220 nJ and deposited energy of 12 J/mm² are used. The laser pulse width is 300 fs and the repetition rate is 120 kHz. To enhance the volume expansion, the polarization is oriented perpendicular to the scanning direction [98].

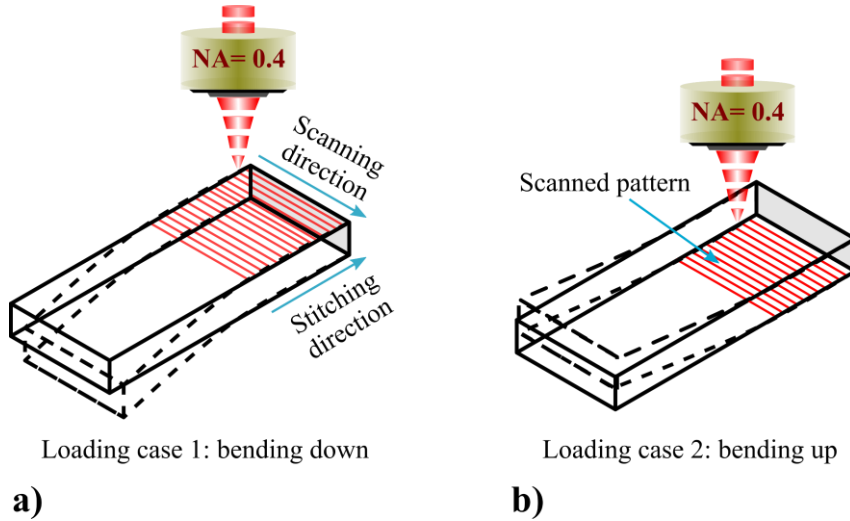


Figure 3.17 – Illustration of the loading scheme. a) Patterns written near the top surface and across the width of the actuator force a downward motion. b) The same patterns written near the bottom surface force an upward movement. In both cases, the exposure starts at a point away from the anchor and moves towards it as indicated by the stitching direction.

- **Unidirectional loading**

In this case, only the bottom surface of the actuator is modified while the top surface stays pristine. The volume expansion within the modified zone creates an upward bending motion. The tip deflection is coupled to the torsion mechanism through two flexures, the first one is connected to the loading bar itself while the second one is connected to the base of the mechanism. Starting 30 μm inside the bottom surface, lines are written across the width of the loading bar as shown in Figure 3.17b. Additional lines are inscribed at a lateral spacing of 5 μm up to a total width of 2 mm. In this manner, a sheet of modified zone (referred to as stressor) containing 400 lines is written (Figure 3.18). Afterward, the focusing objective is moved up by 10 μm and additional stressors are added on top of each other. Between stressors, the writing is paused to distinguish the individual planes from each other. This is indicated by the horizontal region of the staircase plot in Figure 3.19. In total, 5 such stressors are written.

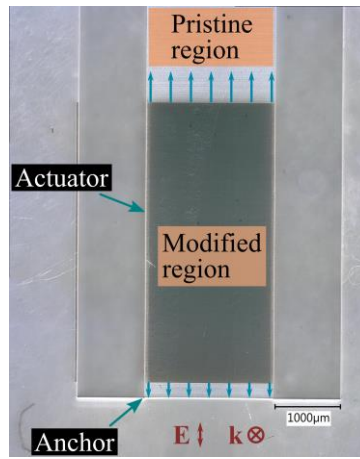


Figure 3.18 – A microscope image of the laser modified area. The modification lines are offset from the nearest edges to prevent the formation of stress concentration points and subsequent crack nucleation. The arrows indicate the direction of volume expansion. The scale bar is 1000 μm .

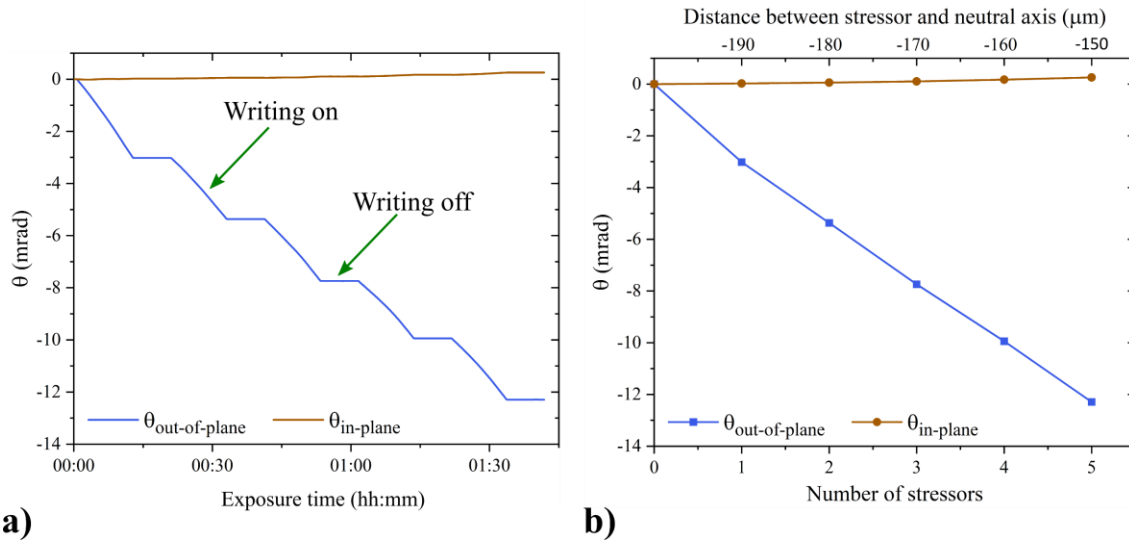


Figure 3.19 – The case of unidirectional loading. a) Angle of rotation plotted versus time. Five planes are written and between planes, the laser is turned off to distinguish them from each other. This is indicated by the stagnant portion of the plot. b) Angle of rotation as a function of the number of stressors (modified planes) and distance between the stressors and the neutral axis. The effective loading time is nearly one hour.

• Bi-directional loading

In this case, both bottom and top surfaces are modified. Logically, the bottom surface is modified first followed by the top surface. A reverse approach would not allow the bottom stressors to be written as the beam would have to be focussed through the top stressors. In a given case, the bottom stressors can be shifted laterally with respect to the top stressors. This is however not efficient in terms of utilization of the actuator volume.

The exposure is started near the bottom surface and gradually moves inwards. After writing four stressors, the focal spot is moved upwards and near the top surface. The region in between is left unmodified. The first stressor (near the top surface) is written at a depth of 60 μm . To generate nearly the same strain between the bottom and top layers, the power is modulated by about 15% across a thickness of 460 μm . The results are plotted in Figure 3.20.

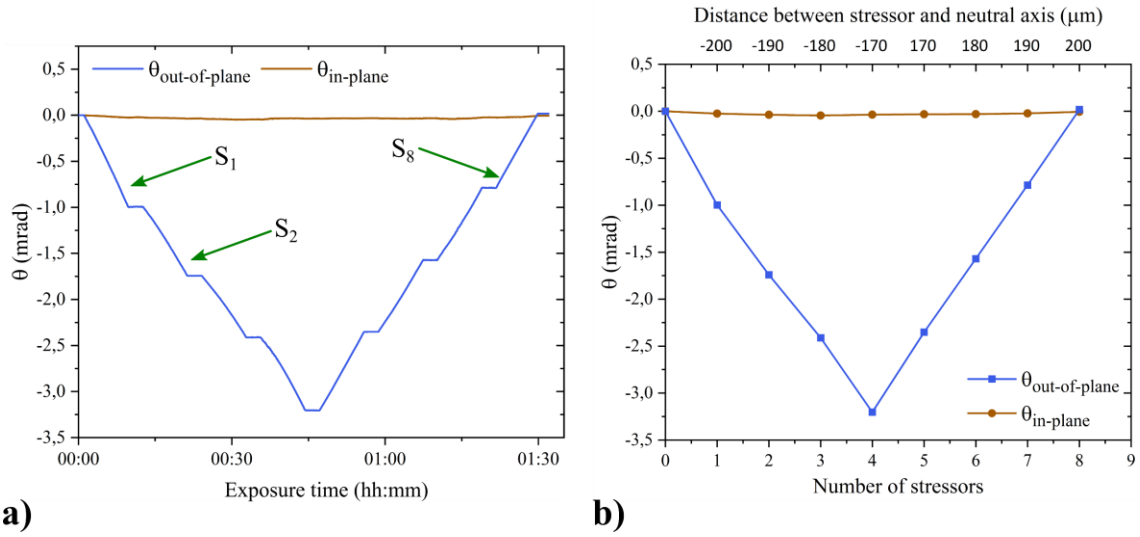


Figure 3.20 – The case of bi-directional loading. a) The downward trend in the plot corresponds to stressors near the bottom surface, followed by stressors near the top surface. In the transition between the bottom to the top surface, the laser power is varied to compensate for parasitic motion. This is indicated by the return to the starting position after the eighth stressor. b) Angle of rotation as a function of the number of stressors and distance between the stressors and the neutral axis. In this case, the stressors are written at the far end of the actuator away from the anchor point resulting in a smaller angle of rotation. In a practical case, this is useful for achieving a finer resolution.

Without modulating the power, the strain in the top stressors is larger causing a residual bending as shown in Figure 3.21. In earlier experiments, we were able to compensate for this by changing the geometry of the patterns. This was done by reducing the width of the stressors while approaching the top surface. Changing the laser power presents an alternate and possibly a simpler way to achieve the same outcome.

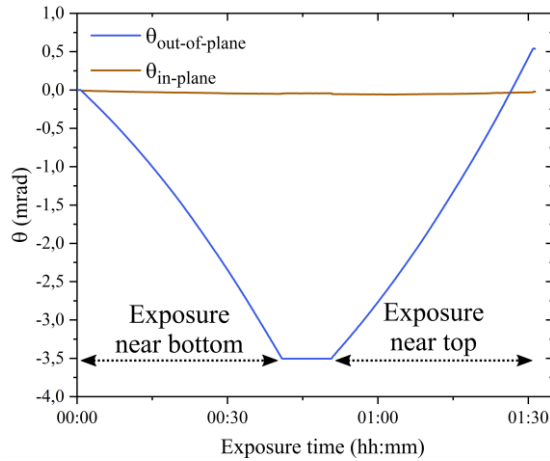


Figure 3.21 – Bi-directional loading without correcting for strain variation across the thickness of the actuator. The strain in the top part of the actuator results in a larger bending angle and overshooting the starting zero position.

• Effect of actuator length

The kinematic design of the device allows for an intrinsic amplification, thanks to the length of the actuator. In a free case, i.e., where no stiffness is acting on the movable end of the actuator, a longer length will always lead to more bending. However, when a non-zero stiffness acts on the movable end, a longer actuator length will not necessarily lead to a larger motion. We demonstrate this for two values of actuator length, 4 mm and 7 mm as shown in Figure 3.22. The actuators are exposed near the top surface and three planes are written in both of them. As expected, a larger angle is observed for the 7 mm case.

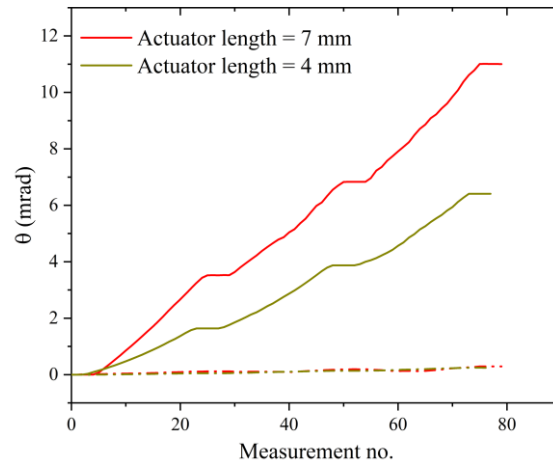


Figure 3.22 – The effect of actuator length on the angle of rotation shows a proportional relationship. In the two cases, the ratio between the angles (1.71) is nearly equal to the ratio of the lengths (1.75).

The bending stiffness of a cantilever varies inversely with its length. As length grows and stiffness reduces, at some point, the stiffness acting on the movable end exceeds the bending stiffness of the cantilever. Beyond this point, the tip deflection starts to decrease and the cantilever starts to buckle along its length. As such, it can no longer effectively apply force on the end-effector. This effect is shown in Figure 3.23.

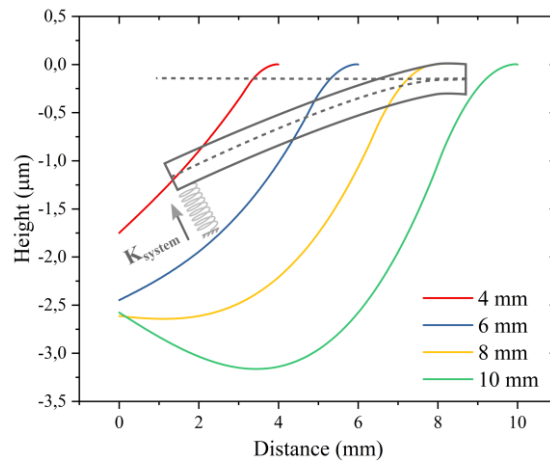


Figure 3.23 – An FEA simulation indicating the effect of increasing actuator length. For shorter lengths, the pristine portion of the actuator is nearly flat. However, for longer lengths, there is an increased bending along the length and a subsequent decrease in the tip deflection.

3.4.2 Part 2: Flexures as actuators

3.4.2.1 Device

A 3D representation of the device is shown in Figure 3.24. It consists of a block of glass in the middle which is gold coated and used as a mirror. On either side, flexures are fabricated symmetrically at a fixed distance from the mirror center. The ends of the flexures are fixed to a static frame surrounding the device.

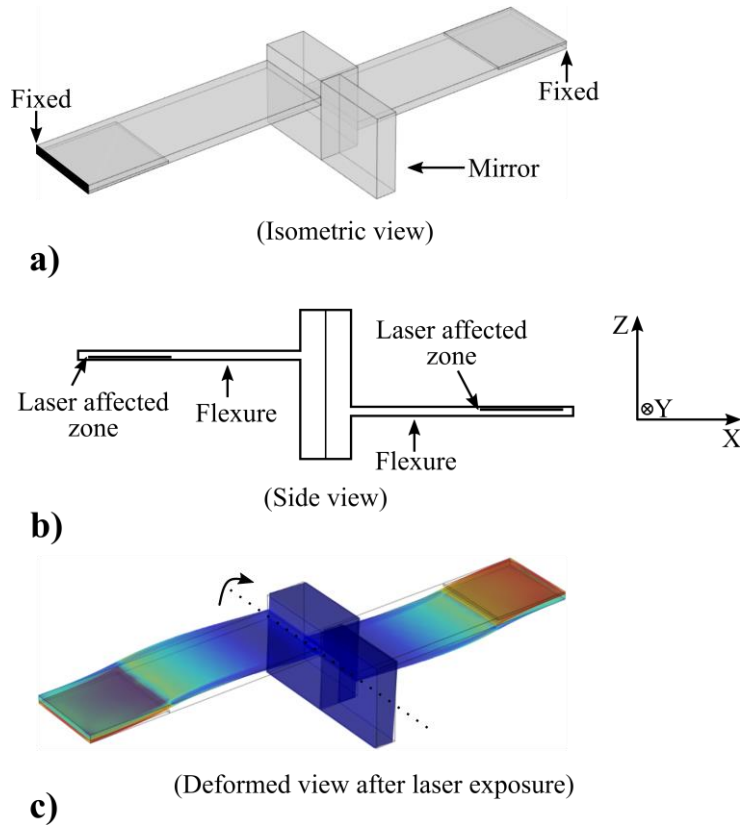


Figure 3.24 – a,b) Isometric and side-views of a flexure-only device. Laser deformation is induced in the flexures to re-orient the mirror. c) A deformed state of the device after laser exposure.

To actuate the device, laser affected zones are written inside the flexures and near their fixed end. Depending on the desired orientation, they are placed accordingly near the bottom or the top surface of the flexures. As is evident from the design, the opposite surfaces of the flexures are actuated. For example, as shown in Figure 3.24c, if the left flexure were to be exposed near its bottom surface, the right flexure would have to be exposed near its top surface. In such a case, the result would be a clockwise rotation of the mirror (when viewed along Y).

3.4.2.2 Experiment

• Exposure challenges

The device is very compact in terms of its real estate (it measures 7 mm in length and 1 mm in width). Furthermore, its small footprint makes it robust to environmental vibrations. However, the lack of a separate actuation mechanism poses some significant challenges during the re-exposure step.

In the devices introduced earlier, the actuator has a pristine surface that allows the femtosecond laser beam to pass through without any appreciable distortion to the beam waist at the focal position. However, in this case, the actuator (left and right flexures) is non-pristine as the surrounding material is removed during the fabrication process. The actuator being bi-functional, must have the following properties, a) it should be able to apply the required force on the mirror and not buckle while doing so, and b) it needs to have a low stiffness to enable the mirror to rotate. However, these conditions dictate opposing requirements on the actuator thickness. While choosing a thickness of 100 μm , two blocks measuring 450 μm in thickness are removed on either surface of the actuator. As such, during the re-exposure step, the femtosecond laser focuses through this rough interface, leading to distortion in the focal plane. This makes uniform exposure challenging as shown in Figure 3.25.

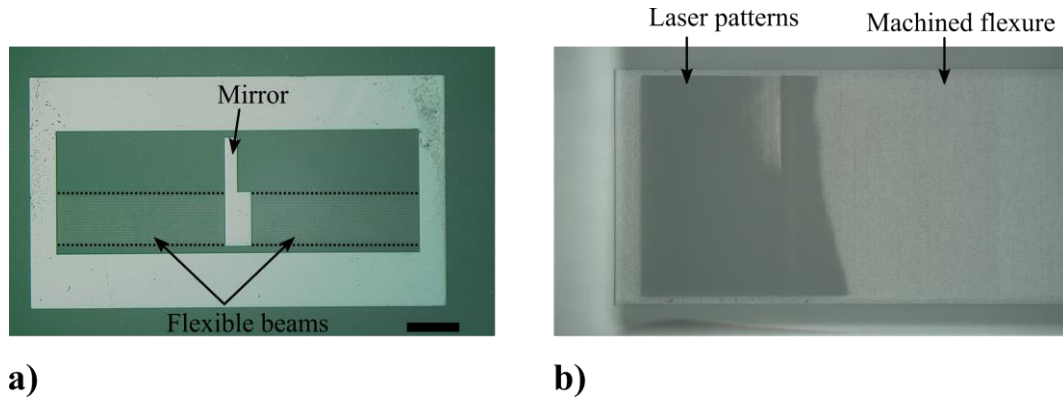


Figure 3.25 – a) An optical micrograph of the fabricated device. The mirror in the middle is suspended on two thin laser-actuated beams on either side. The scale bar is 1 mm. b) Non-uniform laser exposed patterns.

To create a symmetrical loading condition, both flexures need to be exposed simultaneously. If a complete laser affected zone is written inside one flexure, the second flexure no longer presents a flat surface for further exposure. Instead, it deforms into a curved surface making uniform exposure nearly impossible unless the focus is dynamically adjusted at each subsequent writing position. To circumvent this problem, we expose both flexures nearly at the same time. This is done by writing a single modification (a laser exposed line measuring about $1.5 \mu\text{m}$ in width) in one flexure, followed by the same modification in the second flexure. The same unit is then repeated back and forth between the two until the full laser affected zone is stitched. Furthermore, during the movement between one flexure to another, the focal spot needs to be adjusted vertically. As this vertical adjustment lies partially in air and partially in glass, the refractive index compensation needs to be applied carefully to ensure the focal spot stays within the writing volume throughout the process.

• Results

In the re-exposure step, five devices are loaded with increasing number of laser-affected zones. A single laser-affected zone measures $1500 \times 900 \times 10 \mu\text{m}^3$ and contains 750 lines laterally spaced at $2 \mu\text{m}$. For devices loaded with more than one laser-affected zone, the zones are separated vertically by $10 \mu\text{m}$. After loading, the bending angle of the mirror is measured using a confocal microscope. By recording a line profile along the top surface of the mirror, the angle (Figure 3.26) is extracted from the slope of the line. For this measurement, the bulk glass surrounding the mirror is used as a flat reference.

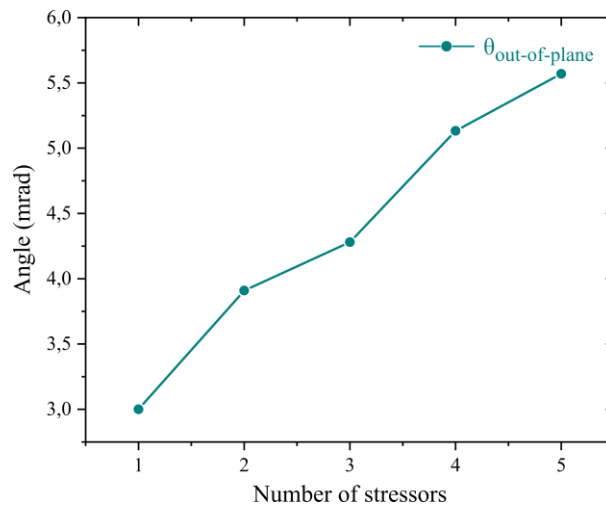


Figure 3.26 – Angle of rotation as a function of the number of stressors. The laser parameters are: 260 nJ pulse energy, 12 J/mm^2 deposited energy, 300 kHz repetition rate, and 300 fs pulse width.

A bending angle of nearly 5.6 milliradians is achieved for a modification thickness of 50 μm . Since the flexures are 100 μm thick, a modification thickness of $> 50 \mu\text{m}$ would result in a reduction in the bending angle. As such, 5.6 milliradians represents the maximum achievable angle in this mechanism for the given laser parameters.

3.5 Summary

In this chapter, we have presented glass-based monolithic flexure devices with integrated functionality. Through an interplay of pulse width, pulse energy, and deposited energy, a bi-directional movement was demonstrated. To leverage maximum output motion, we optimized the writing parameters for different pulse widths. This is particularly important in the context of this work given the small magnitude of the local strain within the modified zone. Later on, we showcased that the dependence on pulse width for achieving a bi-directional movement can be circumvented. From a practical standpoint, it is important to be able to tune the position of an element in either way without the requirement of different pulse width or a different laser altogether. Although this was shown for only one of the two degrees of freedom, a similar design change can also be applied to the in-plane mechanism as will be shown in the next chapter.

A preliminary investigation also revealed that the nature of these modifications is permanent at the current stress levels. At higher levels ($> 1 \text{ GPa}$), stress relaxation can occur, and this is discussed in Chapter 6.

Chapter 4 Femtosecond laser-assisted optical packaging³

In the previous chapter, we introduced the concept of laser-based repositioning. Specifically, we presented one degree-of-freedom mechanisms that were fabricated and later re-adjusted using femtosecond laser exposure. In the current chapter, we will showcase how this can be applied in the context of packaging optical components and devices. The ability to re-adjust elements can relax tight alignment tolerances required during assembly. This is useful for high-precision devices such as interferometers and resonators or in applications related to harsh environment deployment such as in outer space. Other such examples include fiber-pigtailed laser diodes, fiber-coupled integrated photonic devices, fiber-to-chip, and chip-to-chip interfaces, etc. A commonality between these systems is that they demand an extremely precise and stable alignment between their components. While they can be routinely aligned in a laboratory environment, for a fully packaged device, adjustments are often difficult to realize. Before any technology can make its way out of a research environment, it needs to be packaged. This requires integrating the individual device elements, often with different materials and properties, together on a single platform. Not just that, the elements need to be positioned in a specific orientation and the fixation should be invariant in field operation and against external shocks and changes in temperature or humidity.

We begin with an overview of conventional packaging principles for assembling high-precision devices. Afterward, we introduce a novel glass-based bi-directional coupler and its associated kinematics. New alignment patterns are introduced and their geometrical optimization is also studied. Finally, injection from a laser diode into a single-mode fiber is chosen as a test case, and a high-efficiency injection is demonstrated.

4.1 Introduction

Packaging of optical components into a reliable and robust assembly can prove to be a major bottleneck in the commercialization of photonic devices. The micro-assembly of small components with sub-micrometer tolerances requires task-specific and expensive alignment machinery. Therefore, packaging costs, which involve handling of components, actuation, alignment, fixation, etc., can constitute a major portion of the overall production cost depending on the number of individual components. According to some industry estimates, packaging costs can sometimes be as high as 80% of the overall product cost.

In the area of silicon photonics, robust and cost-effective packaging solutions are still a major bottleneck in the commercialization of photonic integrated circuits (PICs) [131]. A key aspect of Si-photonics is the on-chip integration of the light source, which requires efficient and reliable coupling between single-mode fibers (SMF) and nanometer-scale photonic waveguides on a PIC. Although various strategies, such as edge coupling [132], vertical coupling [133], and evanescent coupling [134] have been developed, it remains a formidable challenge nevertheless [131], [135], [136]. Depending on the approach, alignment tolerances are typically in the range of sub- μm to 2.5 μm for 1 dB loss [137]–[139].

³ Part of this chapter has been published in [187].

Direct-write two-photon photopolymerization (2PP) [140], [141], which, combined with its truly three-dimensional capabilities and unprecedented resolution, has enabled 3D printing of beam shaping elements directly onto facets of optical devices [142], [143]. For example, in [142], the authors fabricated microstructures, such as plain lenses, axicon lenses, and phase masks directly on top of optical fibers. In [144], using focussed ion beam (FIB) milling, the authors reported a 67% improvement in coupling efficiency by fabricating a diffractive optical element (DOE) microlens on top of a single-mode fiber. While these methods are arguable very precise, tolerances are nevertheless still present. For example, in 2PP, during the development phase of the resin, a non-uniform shrinkage can occur and lead to misalignment. The use of a resin also poses long-term environmental and temperature-related challenges. Similarly, variation in fiber cladding-core eccentricity (CCE), cladding circularity, etc., can cause misalignments between the guided mode and the fabricated lens. To determine CCE is not straightforward and requires complex approaches such as machine vision [145] for precise measurement.

Laser diode packaging is another classical example of high precision optical packaging. Due to the small size of a laser diode package (a few cm^2 for a typical butterfly package), low-loss coupling between the emitter and a single-mode fiber is challenging. Among the commonly used attachment methods, laser welding is often used for fiber pigtailling. However, post-weld shift (PWS), caused by the shrinkage of the weld after cooling can cause a variation in fiber position and an increase in coupling loss. Passive alignment approaches such as those using silicon etched v-grooves, solder bumps and stops offer high precision in transverse alignment ($\pm 1 \mu\text{m}$), however, due to manufacturing tolerances, an additional alignment step is often required. While relaxing alignment tolerances during assembly, in [146], the authors demonstrated a movable micro-mirror integrated inside the final device package. Similarly, MEMS (micro-electro-mechanical-systems) based positioning systems have also received some attention [147], [148]. Although such systems offer post-assembly correction flexibility, they require additional onboard electronics to dynamically control the actuation. As such, the electronics also become a part of the final device.

In what follows, we will present a glass-based monolithic coupling device fabricated and operated using femtosecond direct laser writing. We will showcase how the device or the actuation principle in general, can be used to correct post-assembly errors in a fully packaged device.

4.2 Coupling device

The device, shown in Figure 4.1, consists of two adjustable mirrors which are positioned to guide the source laser inside the glass chip. The guiding mirrors, fabricated parallel to each other, are positioned such that the incoming beam is shifted laterally. Further downstream from the second mirror, a v-groove is fabricated to hold the fiber and passively align it with the center of the second mirror. To fix the fiber, a mechanical finger, monolithically integrated into the mechanism, clamps the fiber from the top thus forcing it into the v-groove. For the sake of this demonstration, two homemade gold-coated optical flats are glued to the mirror surfaces. However, commercially available mirrors can be integrated too, or by using a laser post-processing step (CO_2 reflow for instance [113], [114]), the surfaces could be smoothened down to sub-nm level without changing the repositioning principle.

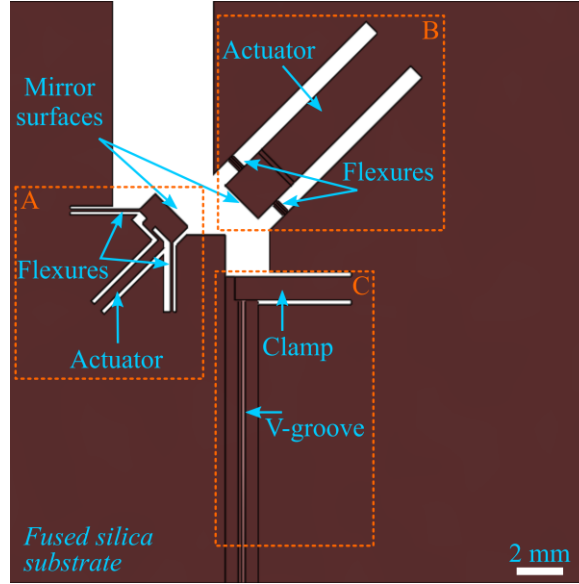


Figure 4.1 – A computer-aided drawing (CAD) of the device showing its main parts. Parts A and B guide the laser diode onto the fiber in addition to providing two degrees of freedom. Part C consists of a v-groove to hold the fiber and a flexible clamp for fixation.

To couple the laser diode into the fiber, the output is first collimated and then refocussed using a long-range objective. The laser beam enters the glass chip at a 45° angle of incidence on the first mirror. The reflected beam is then directed towards the v-groove by the second mirror. By adjusting the position of the focussing objective along the z-direction, the position of the focal spot can be controlled. The schematic of the beam path is shown in Figure 4.2.

To scan the beam in the plane of the fiber end face (XY plane), the mirrors are tilted about their respective axes using femtosecond laser-assisted actuation. The first mirror along the beam propagation direction is a Remote Center of Rotation (RCR) mechanism with its center of rotation lying at M_1 (Figure 4.2). The second mirror is a cruciform mechanism that was introduced in the previous chapter.

For a small tilt angle of $\alpha/2$ and $\beta/2$, the shift of the focal spot can be written as:

$$\begin{aligned}\delta x &= (M_1 M_2 + M_2 O) \times \alpha; \\ \delta y &= (M_2 O) \times \beta\end{aligned}\tag{4.1}$$

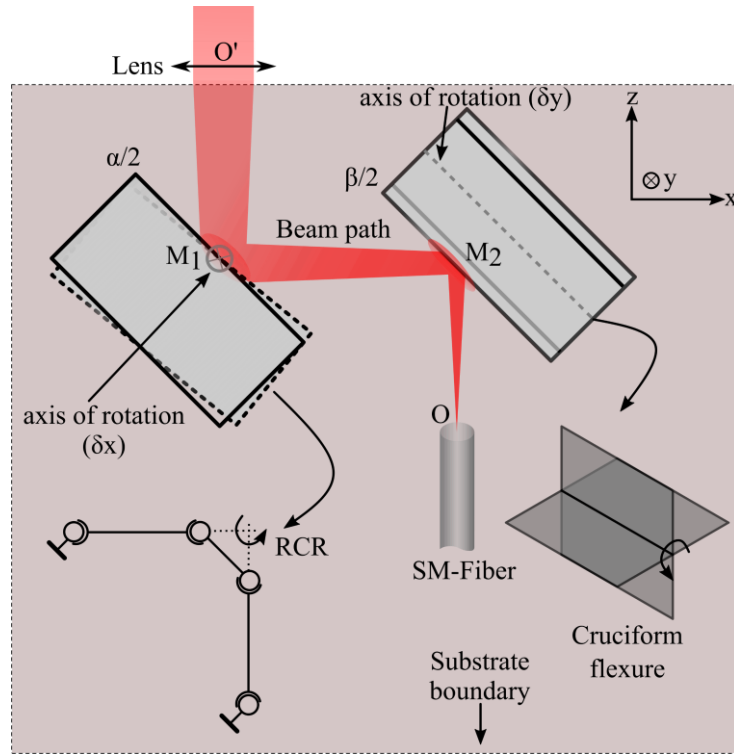


Figure 4.2 – Schematics of the beam path. A collimated laser output is focussed and guided on the end face of the fiber using two micro-machined mirrors. The mirrors are remotely adjusted using a femtosecond laser to scan the fiber face in the x-y plane. The deformed state is drawn underneath each mechanism.

To calculate the theoretical coupling efficiency, we approximate the incoming beam as a gaussian field at the position of the fiber. As the focal spot lies on the end face of the fiber, we assume a zero longitudinal offset (along Z-axis) between the two. Under such an approximation, the situation resembles that of two laterally spaced fibers (Figure 4.3). Using the equation of Marcuse [149], the power transmission coefficient through the fiber can be written as:

$$T = \left(\frac{2w_1w_2}{w_1^2 + w_2^2} \right)^2 \exp \left[\frac{-2(\delta x^2 + \delta y^2)}{w_1^2 + w_2^2} \right] \quad (4.2)$$

Where w_1 and w_2 denote the mode field diameters ($1/e^2$) of the fiber and focusing beam respectively.

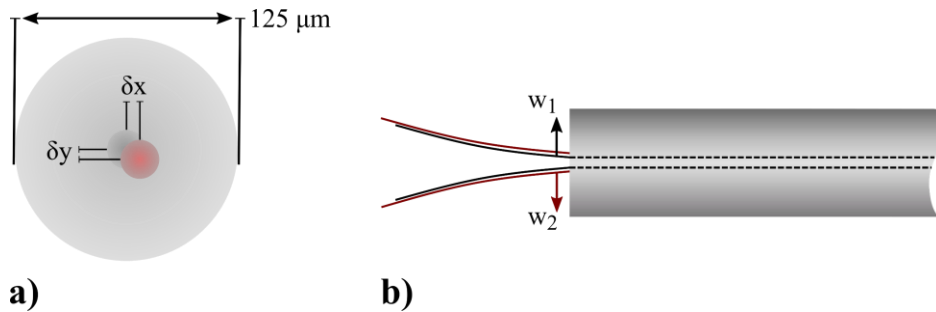


Figure 4.3 – a) A graphical representation of the misalignment between the fiber mode and laser mode and b) their modal diameters indicated by w_1 and w_2 respectively.

The angles α and β can be simply extracted through trigonometric relations from their respective actuator displacements. The relationship between the strain and actuator displacement is given in Equation 3.3. Note that in Equation 4.2 no angular offset is assumed between the two.

Unlike the RCR mechanism of the previous chapter, and to reduce the device footprint, a more compact mechanism is introduced here. In the following section, we will describe its kinematics.

4.2.1 Motion kinematics

To scan the end face of the fiber, two one-degree-of-freedom repositioners are used. The cruciform mechanism discussed in the previous chapter is reused for scanning vertically along the y-direction. For scanning along the x-direction, a new mechanism (Figure 4.4) is designed, which is compact and more robust with an intrinsic amplification arm. It further benefits from a single pulse width bi-directional actuation.

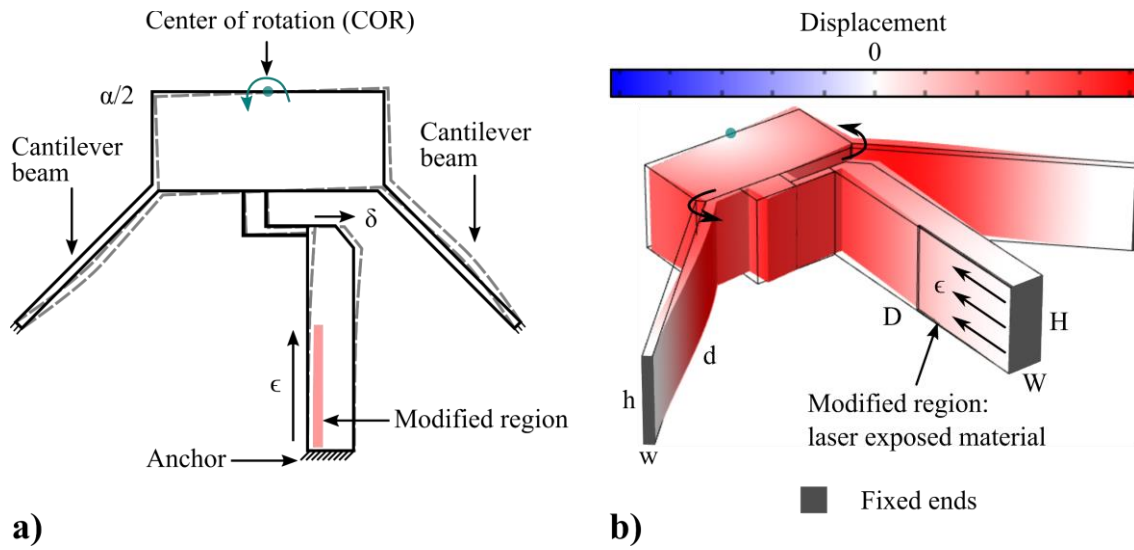


Figure 4.4 – a) A kinematic representation of the RCR mechanism. Laser-written lines are placed in strategic locations in the bulk of the actuator creating a permanent strain (ϵ) in the modified zone and a net displacement (δ) at the tip of the actuator. With the aid of inclined cantilever beams, this linear displacement can drive a rotational movement at the end effector. b) A deformed state of the device showing the relative displacement at various points.

The basic construction is similar to the previous mechanism (section 3.2). Two slender cantilevers inclined at 45° from the vertical define a center of rotation on the mirror surface. To enable motion, the actuator is directly attached to the mirror through a single flexure. For clock-wise rotation, the laser patterns are inscribed near the right side of the actuator and throughout its thickness. This causes volume changes on the sidewall of the actuator and results in an in-plane bending of the free end and a subsequent rotation of the mirror surface. A bi-directional movement can be achieved by simply changing the position of the laser affected zone within the actuator. More specifically, exposure near the left side of the actuator results in a counter-clockwise motion as depicted in Figure 4.4, whereas exposure near the right side results in a clockwise motion (the orientation is defined while looking from the top).

The actuator and flexure dimensions are optimized using Comsol Multiphysics (Figure 4.5). Following a similar argument as in Figure 3.14, the dimensions are noted in Table 4.1.

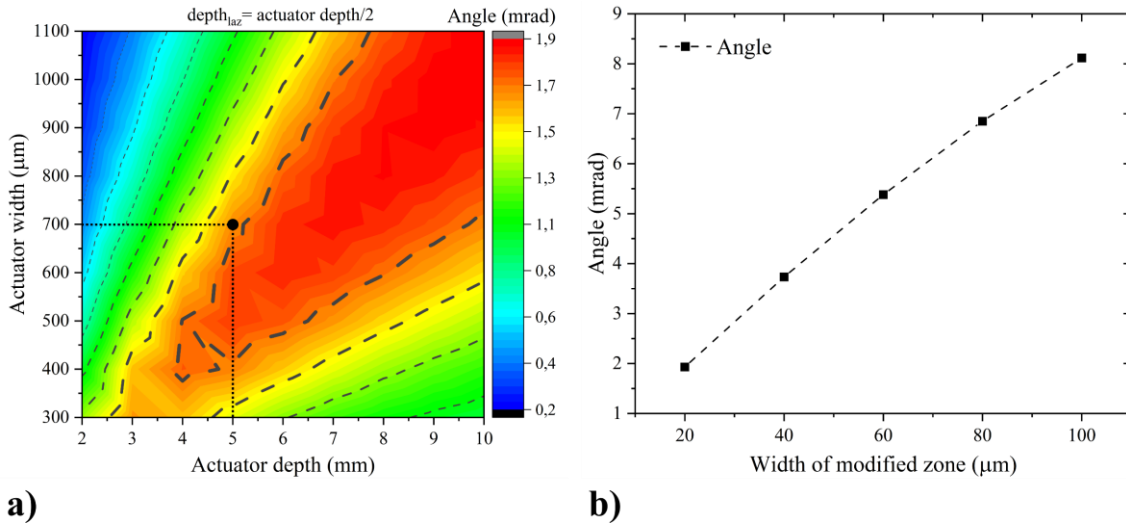


Figure 4.5 – a) A heat map indicating the angle of rotation as a function of the actuator parameters. b) Angle of rotation as a function of the modified width.

Table 4.1 – Actuator and flexure dimensions of the RCC mechanism (in mm)

W	D	H	w	d	h
0.7	5	1	0.1	3	1

To maximize the volume expansion, we introduce three different writing schemes related to the RCC mechanism. The induced strain corresponding to each scheme as well as the parasitic movement is studied. Also, and as we will show in the next section, the exposure time is reduced nearly by an order of magnitude. This is important in the context of aligning an actual system, where the alignment process is carried out manually by an end-user and as such, needs to occur within an experimentally reasonable time frame.

4.3 Volumetric distribution of stressors

The volume increase within the modified zone is not only dependent on laser parameters [130] but also on how the patterns are inscribed and distributed inside the bulk of the material. In the previous chapter, we focussed our attention on laser parameters and their optimization to achieve maximum volume expansion. In the next section, we will explore three different writing schemes and underline the main differences between them. Pertinent to mention, these schemes are only applied to the Remote Center of Rotation (RCR) mechanism. For the cruciform mechanism and as will become evident soon, the conventional writing method is the most efficient already.

4.3.1 Horizontal writing vertical stacking

In our first approach, the sample is translated under the focusing objective, and laser-written lines are stitched laterally, next to one another in one horizontal plane. The spacing between two individual lines is set at 10 μm. In this manner, a sheet of modified zone is created near the bottom surface of the actuator. A single sheet is half the actuator width and extends from the edge until the middle of the actuator.

Afterward, the focusing objective is moved upwards (along Z) and similar planes are stitched through the thickness of the actuator. Two individual planes are separated vertically by 10 μm. A pictorial description is given in Figure 4.6.

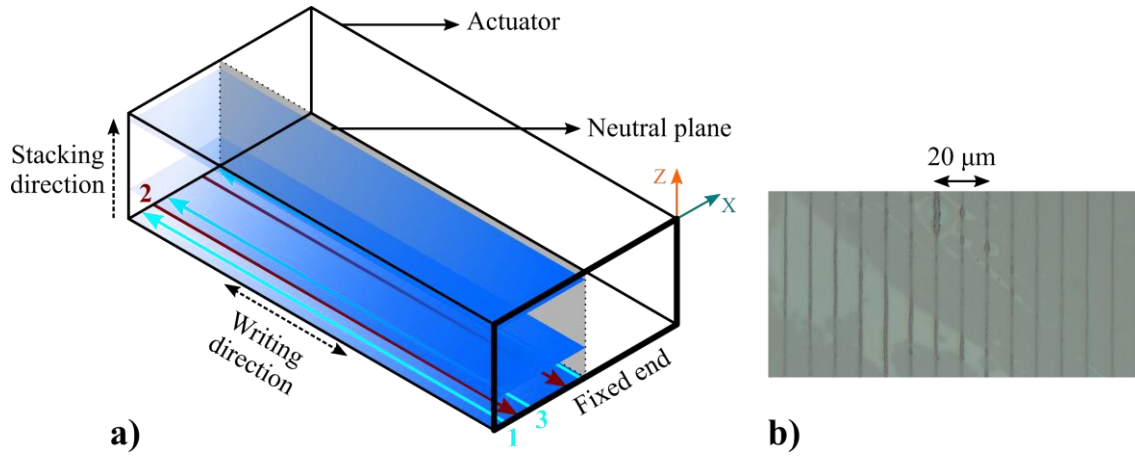


Figure 4.6 – a) Schematic of the first writing method. Starting near the fixed end of the actuator, lines are written along its length in either direction and placed next to each other in one horizontal plane. Afterward, similar planes are stacked on top of each other along the Z-direction. This is continued until the top surface is reached. b) An optical micrograph of the written pattern observed near the top surface. The laser parameters are: 220 nJ pulse energy, 12 J/mm² deposited energy, 300 kHz repetition rate, and 300 fs pulse width. The laser polarization is oriented along the writing direction.

To reduce the writing time, lines are written in both directions – while going away from the anchor and while moving towards it. As soon as the writing process is started, the angle begins to change with the effect being almost instantaneous. Since the writing process is initially confined to the bottom surface, the actuator, much like the actuator discussed in Section 3.3.3, bends up. It continues to do so until the neutral line is reached, beyond which, it starts to bend in the opposite direction and returns towards the starting position. The results are shown in Figure 4.7.

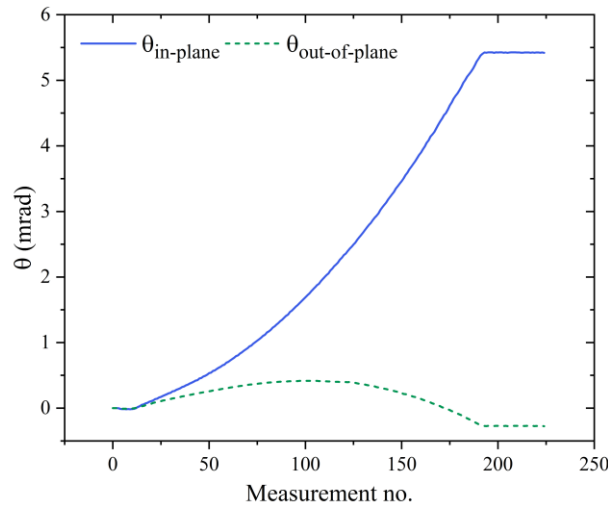


Figure 4.7 – Angular position of the mirror plotted over time. Around $t = 0$, modifications near the lower half of the actuator cause a parasitic bending (indicated by the dashed plot), which is later self-compensated by exposure near the top half. The measurements are recorded every 60 seconds.

4.3.2 Vertical writing horizontal stacking

In this second approach, laser-written lines are stacked vertically on top of each other as shown in Figure 4.8. Starting near the anchor, a single line is inscribed along the sidewall of the actuator. At the end of this line, the focusing objective is moved up and a second line is written while moving towards the anchor. The verti-

cal spacing between the lines is $10\ \mu\text{m}$. More lines are added until the top surface is reached, thus creating a wall of modified zone.

Next, the focal spot is moved downwards near the bottom surface and shifted laterally (along X) by $10\ \mu\text{m}$. Starting from this point, a similar wall is added along the actuator thickness. More walls are added until the neutral axis of the actuator.

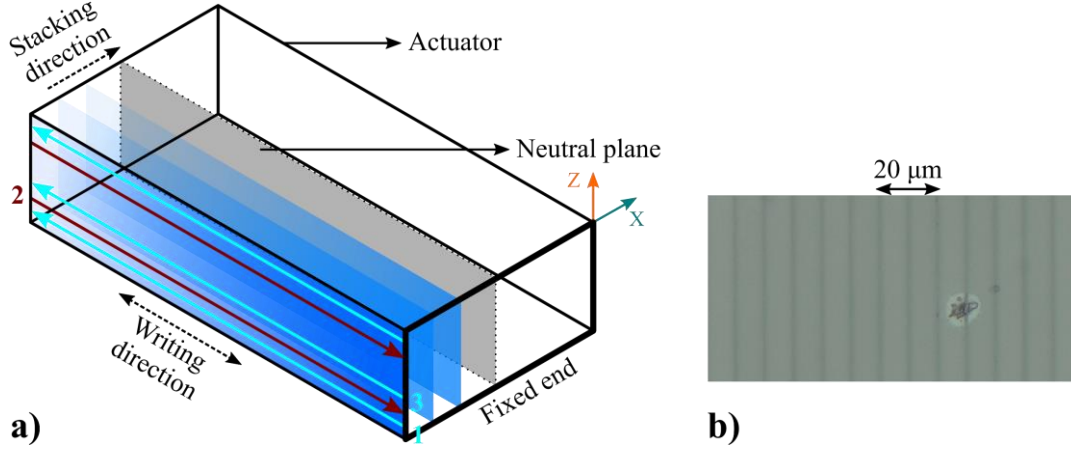


Figure 4.8 – a) Schematic of the second writing method. Starting near the end of the actuator, lines are written along its length in either direction and placed vertically above each other. This is continued until the top surface is reached. Afterward, similar planes are stacked next to each other until the neutral line. b) An optical micrograph of the written pattern as observed near the top surface. The laser parameters are: 220 nJ pulse energy, $12\ \text{J}/\text{mm}^2$ deposited energy, 300 kHz repetition rate, and 300 fs pulse width. The laser polarization is oriented along the writing direction.

Although the overall modified zone looks similar, the net strain is significantly lower. This is due to the interference of the laser beam with already existing patterns. Except for the first plane, the laser beam passes through an interface of modified and unmodified material. The stress field around the existing modifications distorts the focal spot. This lowers the effective dose and causes a reduction in the overall strain as shown in Figure 4.9. For the same size of the modified area, the strain (hence the angle) is reduced by nearly 75%.

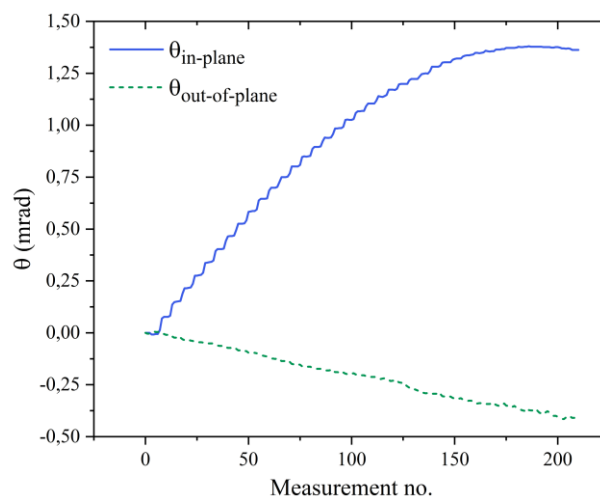


Figure 4.9 – Angular position of the mirror plotted over time. Due to interference from already existing patterns, the overall strain is lower. Besides, the parasitic motion is not self-compensated since the strain is confined mostly in the top half of the actuator. The measurements are recorded every 60 seconds.

By zooming in on the plot (Figure 4.10), it can be seen that the modifications near the lower half of the actuator nearly do not contribute to the overall strain. The angle changes negligibly until the focal point reaches a little above the neutral line. Beyond this, there is a rather fast increment in the observed angle.

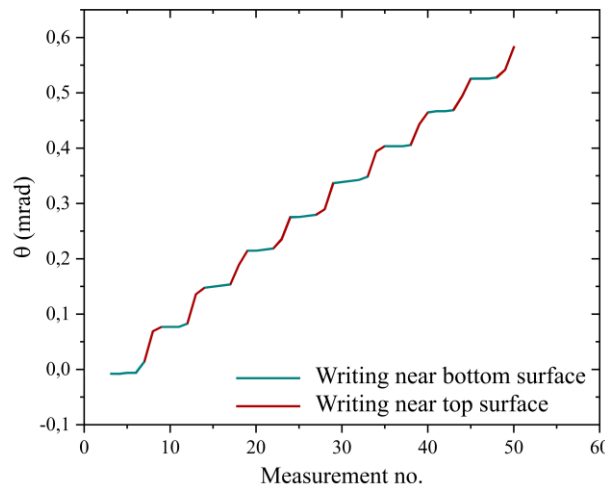


Figure 4.10 – A close-up view of the stairwell pattern of Figure 4.9. After each vertical plane, as the focus is moved downward to write the subsequent plane, the stress field around the already modified region distorts the focal spot. This results in very little or nearly no strain near the bottom half of the actuator (indicated in olive). As the focus gradually moves up, this effect decreases and the strain rapidly increases (indicated in red).

Since most of the strain is confined in the top half of the actuator, a non-zero parasitic (out-of-plane) bending is inevitable. Furthermore, the actuator does not return to its starting position and as such, the effect is somewhat permanent and needs to be compensated separately.

As a possible compensation scheme, patterns could be inscribed on the bottom surface near the anchor. This would force the actuator to bend upwards and return to its starting position. However, doing so could potentially perturb the previously aligned axis, and would thus need iterative adjustments to converge to an optimal position. In such a case, an output metric is necessary to guide the alignment process.

4.3.3 Point writing

Our main objective is to induce strain near the sidewall of the actuator and create a bending motion. So far, we have tested two approaches in which, instead of modifying the conventional top surface, we modified the sidewall of the actuator. In our third approach, a single modification is inscribed through a combined motion of the focusing objective as well as the translation stages holding the sample. This is done as follows:

Starting below the bottom surface of the actuator, the focal spot is translated through the actuator thickness (along Z direction) and above the top surface. The resulting modification is a single line along the thickness and looks like a point when viewed from the top. Next, the objective is moved downward while the laser is off and the sample is shifted laterally along the Y-direction. In this manner, further modifications are added progressively along one straight line. The writing strategy is depicted in Figure 4.11.

Afterward, the sample is translated along X-direction and similar patterns are repeated until a matrix of points is defined on the surface of the actuator. Each point represents a single laser-affected line extending throughout the actuator thickness. All the lines are equally spaced at 10 μm .

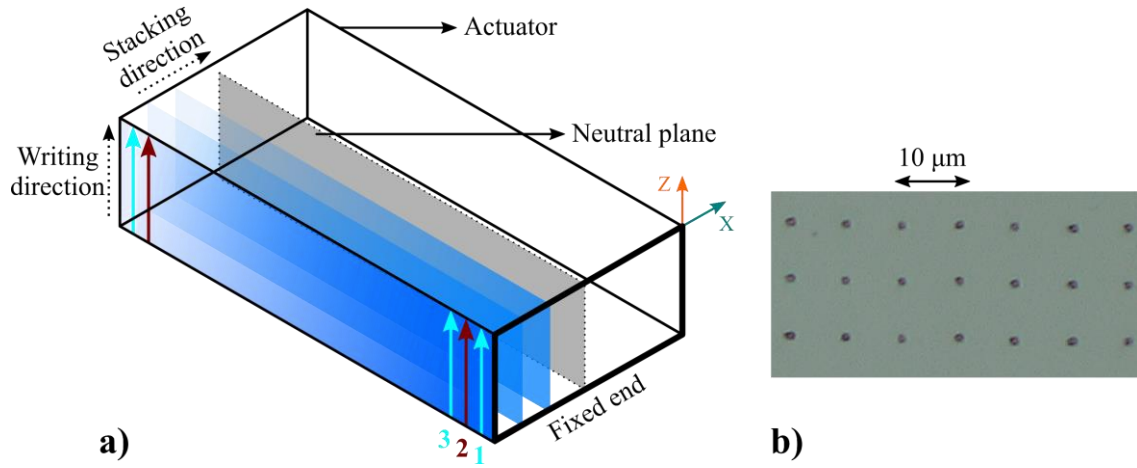


Figure 4.11 – a) Schematic of the third writing method. Starting below the bottom surface of the actuator, lines are written along its thickness by translating the focussing objective. Similar lines are then inscribed next to each other along the length and width of the actuator. b) An optical micrograph of the written pattern as observed near the top surface. The laser parameters are: 220 nJ pulse energy, 12 J/mm² deposited energy, 300 kHz repetition rate, and 300 fs pulse width. The laser polarization is oriented perpendicular to the stacking direction.

Unlike the earlier two approaches, the effective modified volume is considerably lower. Along the length of the actuator, the modifications are discontinuous and consist of alternate regions of affected and non-affected regions. As such, the overall strain is much lower as shown in Figure 4.12.

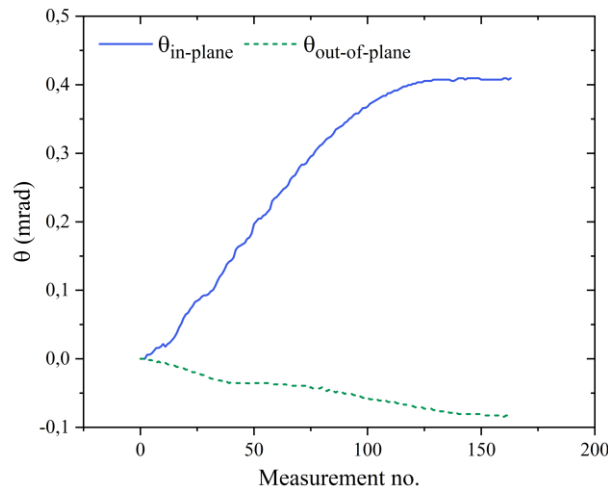


Figure 4.12 – Angular position of the mirror plotted over time. Due to the reduced effective modified volume, the observed strain is significantly smaller. The parasitic bending follows a similar trend to that of Figure 4.9. The measurements are recorded every one minute.

Here too, the presence of previously modified regions affects each subsequent pattern, thus further lowering the strain. Another drawback of this approach is the writing time. As the movement along the length of the actuator is completed in small discontinuous steps, the writing time is considerably larger.

4.4 Monolithic fiber coupler

4.4.1 Fabrication and assembly

The complete device (Figure 4.13) is fabricated in a single step using femtosecond laser micromachining combined with wet chemical etching. This process was already presented in the previous chapter, however, the essential details are presented below.

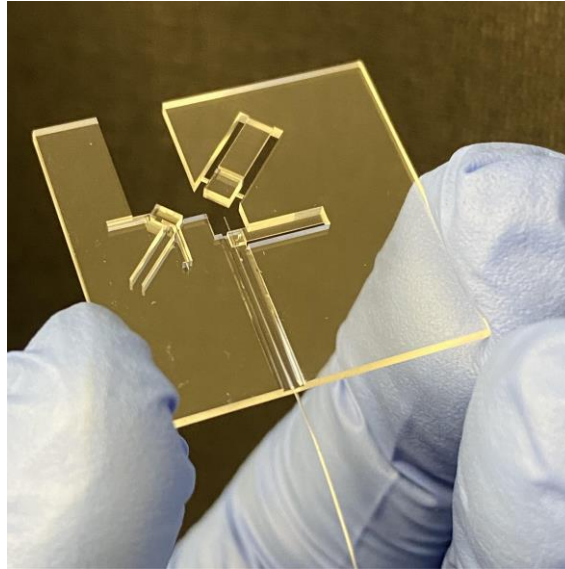


Figure 4.13 – An image of the fully assembled device shown here without the glued mirrors. The optical fiber is clamped inside a v-groove using an elastic element, itself machined within the same substrate (see Figure 4.14).

A short pulse laser delivering 270 fs pulses at a wavelength of 1030 nm is used. To outline the contour, the sample is translated at a speed of 8 mm/s under the focus while maintaining a constant deposited energy of 12 J/mm². The pulse energy is set at 250 nJ. In a subsequent step, the sample is etched in a dilute acid bath (2.5% HF) for nearly 24 hours.

The device consists of multiple structures of varying dimensions. For example, some of the flexures are only 50 µm in thickness. Similarly, the v-groove needs to be just the right size for the clamp to force a contact on the walls of the v-groove. If the v-groove is too deep, the fiber will float and cannot be clamped. If the v-groove is too shallow, there is a risk of stressing the fiber and damaging the cladding. To ensure isotropic etching and a close match between end dimensions and those designed, an etching buffer is added to critical parts during machining. Non-exposed fused silica etches at a rate of approximately 1 µm/hour in a solution of 2.5% HF. Depending on the part, a positive or negative buffer is added. For example, for the flexures, a positive buffer is added while as for the v-groove, a negative buffer is added.

To integrate the fiber, it is fixed on a linear stage and aligned with the long axis of the v-groove. It is then slowly drawn into the v-groove by translating the stage towards the sample. As the fiber arrives near the end of the groove, the clamp (Figure 4.14) is pushed from below and lifted while the fiber is slid under it. The clamp is then released to make contact with the top surface of the cladding thus forming two contact points on the sidewalls of the v-groove. The rest of the fiber is then glued using UV curing glue.

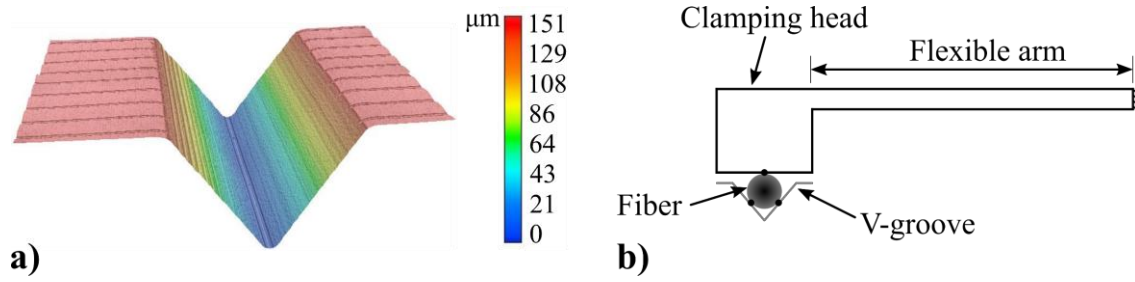


Figure 4.14 – a) A height profile of the laser manufactured v-groove. b) A cross-sectional view of the flexible clamp.

4.4.2 Fiber injection experiment

For this experiment, we use the collimated output of a fiber pigtailed laser diode ($\lambda = 980$ nm). Using a long working distance objective (Mitutoyo, 20X), the beam is focussed and reflected off the adjustable mirrors (Figure 4.15). The glass chip holding the fiber is then coarsely aligned using positioning stages until some power is observed at the output. Next, fine adjustments are done to maximize the output power and thus the coupling efficiency. This step is repeated multiple times to maximize coupling into the fiber mode. Once in its optimal position, the fiber is misaligned by displacing the chip with respect to the focusing lens. The shifts are approximately $3\ \mu\text{m}$ and $4.5\ \mu\text{m}$ along X and Y-directions respectively. This results in a drop in output power, mimicking post-assembly alignment errors in a diode package. To optimize coupling again, a non-contact adjustment is carried out by writing patterns inside both actuators. While writing, the coupled power serves as an assembly function and is monitored simultaneously and maximized along the two axes. In this experiment, the fiber is single-mode (SM-980-G80 from Thorlabs) with an average mode field diameter of $4.5\ \mu\text{m}$ at 980 nm. The focusing objective has a 0.4 NA and a working distance of 20 mm.

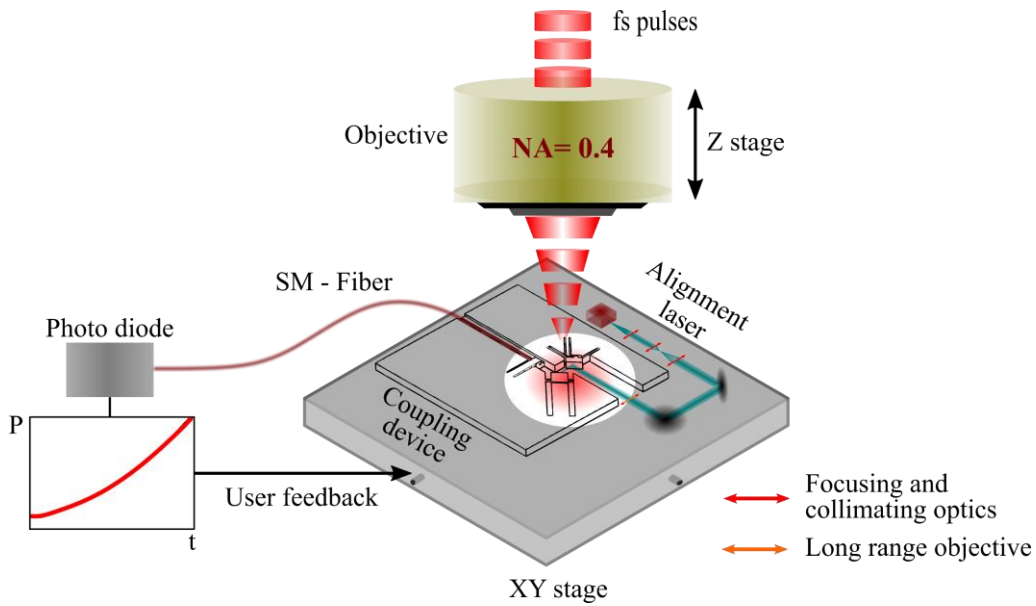


Figure 4.15 – Schematic of the fiber injection experimental platform. The coupling device is positioned on an XY positioning stage and translated under the adjustable focus of a femtosecond laser beam under normal incidence. The laser-induced modifications are written in certain locations to create localized movements within the device thus changing the coupling efficiency between the source laser beam and the fiber. While writing, the coupled power is monitored continuously at the other end of the fiber and used as a performance metric to guide the alignment process. For imaging different parts of the device, an LED is mounted below the XY-stage and optical access is provided through a hole in the breadboard.

The laser-based adjustment is carried in two steps:

Step 1: Starting with the Y-axis alignment, the actuator is modified just below its top surface, resulting in an immediate increase in power indicated by zone 1-a in Figure 4.16. The modification consists of a layer of equidistant lines spaced by 2 μm . After the first layer, the writing is stopped momentarily while the focal spot is moved upwards and near the starting position. The writing is continued through zone 1-b and a second plane is added on top. During this, the power first increases, then saturates, and ultimately decreases as the local maximum is surpassed. This is indicated by point A on the plot. Afterward, the femtosecond laser is switched off (indicated by the black region of the plot) and the focus is moved near the bottom surface. Here, further patterns are written forcing the mirror to rotate in the opposite direction and towards the optimal position. This is shown in zone 1-c of the plot. The process is stopped as soon as the earlier power level (point A) is retrieved. Afterward, the writing is stopped and the XY stage is translated for the X-axis alignment.

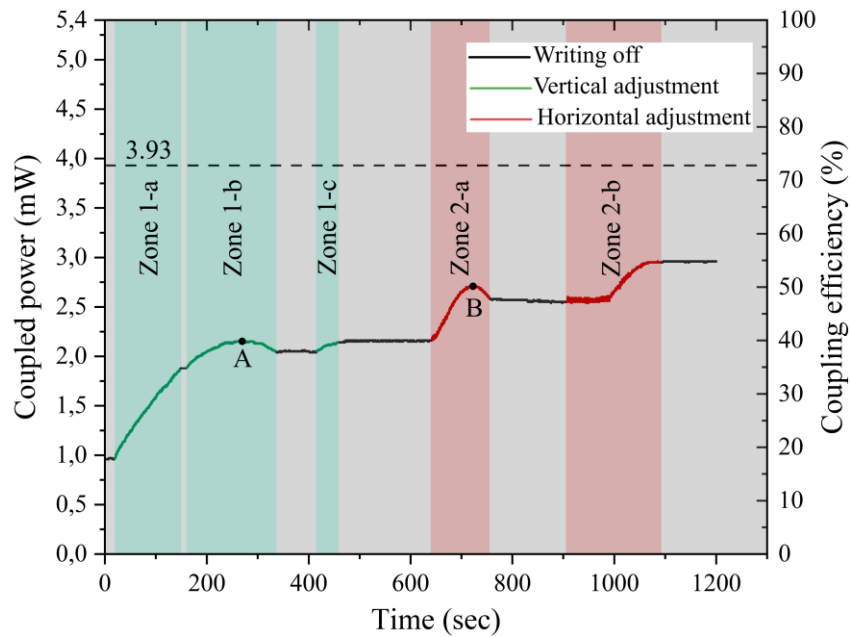
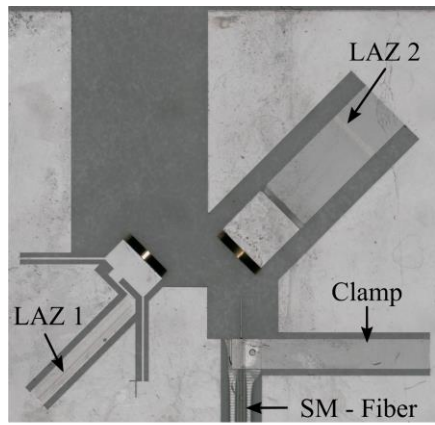
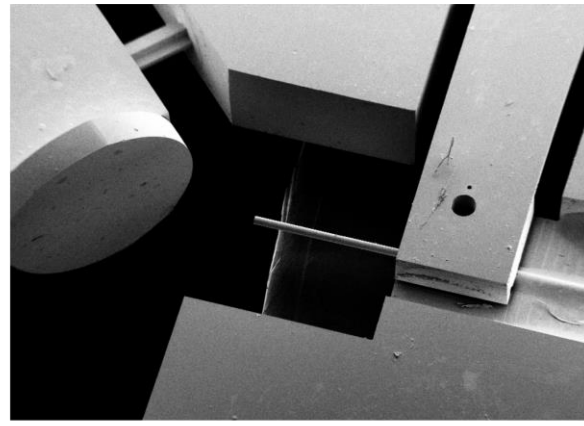


Figure 4.16 – Output power as a function of time. The writing is divided into two zones. In zone-1, vertical adjustment is done until the output power is maximized. This is followed by horizontal adjustment in zone-2. On the right axis, 100% coupling efficiency corresponds to a power level of 5.4 mW measured just after the focussing objective. Note that the writing time is not optimized as the alignment algorithm is implemented manually.

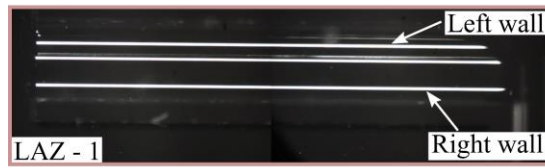
Step 2: In this next step, the actuator of the RCR mechanism is modified for horizontal adjustment. This is done by writing lines along the length of the actuator near its edge. For maximizing strain and minimizing parasitic movement, the patterns discussed in Section 4.3.1 are used. As lines are written in zone 2-a, the coupled power begins to increase further, reaches a maximum (point B), and then decreases. At this point, the writing process is stopped again and the XY stage is translated to modify the opposite wall of the actuator. During this time, the coupled power stays constant as indicated by the black region on the plot. In zone 2-b, further exposure re-orientates the mirror towards the optimal position, resulting in a further increase in power. The alignment is stopped when the power level saturates at a coupling efficiency of 54.8%.



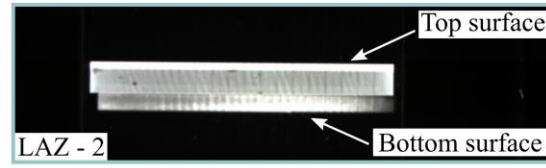
a) LAZ: Laser Affected Zone



b)



c)



d)

Figure 4.17 – Optical image of the device after laser adjustment showing the modified region in the actuators. b) An SEM image of the optical fiber region. c,d) A cross-polarized microscope image revealing the form birefringence within the modified zones.

To validate the coupling, the device is placed on a six-axis precise positioning stage (OptoSigma-DAU-080M-R) and aligned with respect to the free-space laser beam (with the two mirrors and fiber in same positions). The stage has a linear resolution of $0.5 \mu\text{m}$ and an angular resolution of approximately 8 milliradians. After repeated attempts, similar coupling efficiency is achieved.

At this point, we would like to point out two important observations:

- The effective writing time to reposition both axes is just under eleven minutes. One may recall the considerably longer writing time of the RCR mechanism presented in the previous chapter. In a practical scenario, this could be reduced even further by using faster scanning speeds, higher repetition rates, or appropriate beam shaping techniques [112] to write planes instead of lines.
- Although we are correcting for relatively small misalignments in this proof-of-concept experiment, the actual range of motion is significantly larger. This is confirmed by the range of motion capability of the individual positioners as shown in Figures 4.7 and 3.19. At the fiber position, this corresponds to a positioning window whose size is given in Table 4.2. Note that this size is dependent on the working distance of the coupling lens.

Table 4.2 – Size of the positioning window (in micrometers)

Axis	Correction done	Potential range
X	3	45
Y	4.5	15

In addition to laser parameters, the strain within the actuators and consequently their range of motion also depends on the fraction of modified volume. For example, in the result of Figure 4.7, the modified volume is 50% of the overall actuator volume, whereas it's less than 5% in Figure 3.19. Similarly, less than 2% of the

actuator volume was modified in this experiment. Therefore, the actual range of motion is larger than what is corrected here. In addition, by inducing densification [38] in part of the actuator, the range of motion can potentially be doubled. However, a limiting factor in doing so is the peak stress within the flexures or the modified zones.

4.4.3 Loss analysis

In the above experiment, the numerical aperture of the objective was not matched to that of the single-mode fiber. Due to the lack of a better alternative and the mismatch in NA, some losses occur at the interface. Additional losses occur too due to the custom-made mirrors. This is however quantified by mounting the fiber directly in front of the objective (without the mechanism). In this case, the output power is measured at 3.93 mW - a nearly 18% increase in coupling efficiency. The nature of losses due to the mirrors is twofold. On the first mirror, the beam size is slightly larger than the mirror diameter resulting in clipping loss. Also, there is a certain amount of reflection loss on both mirrors. This results in a reduction in optical power at the fiber input. Due to physical constraints, these losses cannot be measured easily on the chip, so we measure them separately. The results are shown in Table 4.3.

Table 4.3 – Budget of measured losses for the different interfaces.

Interface	Clipping loss (%)	Reflection loss (%)
M ₁	6.34 ± 1	5.69 ± 0.8
M ₂	0	5.69 ± 0.8

The summation of these losses ($17.72 \pm 2.6\%$) nearly matches the 18% difference observed earlier. This implies that by discounting the losses induced by the mirrors, the mechanism can compete with commercially available high-resolution fiber positioning stages, and shows potential to even surpass them with some fine refinements.

4.5 Summary and discussion

In this chapter, we have shown how femtosecond lasers can be used for not only fabricating complex three-dimensional devices but also for compact optical packaging. Specifically, we introduced a laser-to-fiber coupling device, in which, coarse alignment was achieved using precisely machined flexural mirrors and v-grooves. A final fine adjustment step was carried out using femtosecond laser exposure and a near-theoretical coupling efficiency was achieved. Furthermore, different exposure strategies were introduced and their effect on net strain was also discussed.

In further refinements, the degrees of freedom can be combined inside a single mount that holds the fiber itself, and which can be actuated using the same principle. Such a system would forego the need for additional optics, be more compact, and can be mounted directly in front of the diode in a butt-coupled configuration. Unlike MEMS-based approaches [146]–[148], [150], [151], this one-time alignment method is permanent and does not require further control to maintain the actuation. Besides, the proposed method offers much more flexibility and precision in comparison to techniques such as laser forming [152], [153] or precision gluing [154], which are very limited in terms of their applicability and nature of obtainable motion.

Laser diode to single-mode fiber coupling is a classic example of high-precision photonics packaging. However, in this case, the gain due to repositioning, which could be better coupling efficiency or less heating due to lower losses, may not be economically justifiable in terms of the additional process cost associated with the repositioning step. On the other hand, in high-power laser systems, the localized heating at interfaces can be a critical issue. It is thus important to minimize losses occurring due to a less precise alignment between the laser and the fiber. Furthermore, in devices such as resonators and laser cavities, a high-precision align-

ment is not a straightforward task for a packaged device. For example, to excite whispering gallery modes of silica microspheres, the fiber taper needs to be positioned within a few hundred nanometers of the resonator [155]. While this can be done in a laboratory using high-resolution 3D translation stages, transitioning outside the laboratory environment often means taking the translation stages too. For such devices, the mechanical strength and thermal stability of fused silica together with the method proposed here offer an alternative flexible packaging principle.

Chapter 5 An all-glass fiber Fabry–Pérot cavity

So far we have shown how laser-induced nanoscopic volume changes can be used for optical repositioning, and in Chapter 4, we showed its application for packaging sensitive optical devices. In these demonstrations, the alignment requirements lie in the sub- μm range at best and therefore are orders of magnitude higher than what is offered by femtosecond laser exposure. To harness and highlight the sub-nm resolution capability, an equally sensitive optical device is required.

This chapter discusses the experimental progress towards a fiber Fabry–Pérot cavity (FFPC) assembled on a glass substrate. The substrate, manufactured using femtosecond laser micromachining, carries essential degrees of freedom (DOFs) to align the cavity fibers and precision grooves for passive alignment. The cavity is formed by concave mirrors fabricated on the fiber end faces, which are glued onto the substrate. The experimental results achieved so far use a piezoelectric scanner to modulate the cavity length.

5.1 Fabry–Pérot resonator

A Fabry–Pérot cavity, named after French physicists Charles Fabry and Alfred Pérot who developed the instrument in 1899 [156], is an optical resonator consisting of two oppositely faced mirrors with high reflectivity and some transmissivity. The working principle of the instrument is as follows: at a fixed wavelength, and for a specific mirror spacing, a steady-state condition is established inside the cavity, under which, specific modes (Figure 5.1) reproduce themselves after one round trip. For an air-spaced cavity, this condition can be mathematically expressed as:

$$\lambda = \frac{2L}{q} \quad (5.1)$$

where L is the distance between the two mirrors or the cavity length, λ is the wavelength in the medium between the mirrors, and q , known as the longitudinal mode number, is an integer. In other words, Equation 5.1 states that a resonance condition is fulfilled only when the cavity length is an integral multiple of the half wavelength. The transmission of a Fabry–Pérot resonator exhibits multiple equispaced resonance frequencies. The separation between two individual frequency lines, known as the free spectral range (FSR), is given by:

$$FSR = \Delta\nu = \frac{c}{\lambda_{q+1}} - \frac{c}{\lambda_q} = \frac{c}{2L} \quad (5.2)$$

where c is the speed of light inside the resonator.

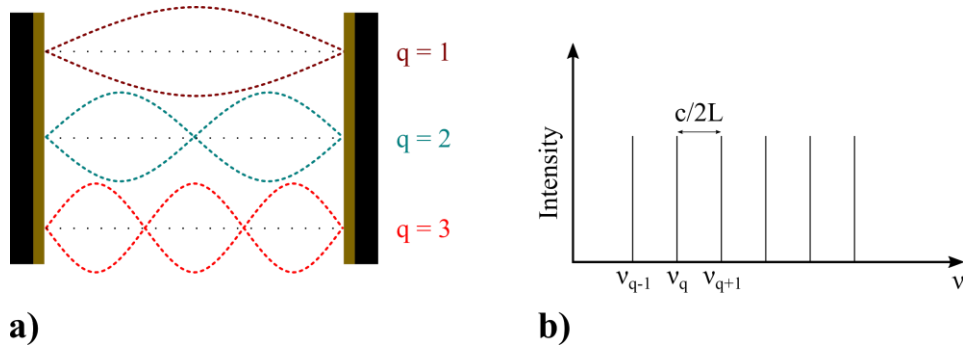


Figure 5.1 – a) A flat mirror Fabry–Pérot cavity with its supported modes $q = 1, 2$, and 3 as examples. b) Typical transmission spectrum depicting different resonant frequencies.

Another term related to the free spectral range is the finesse (\mathcal{F}), which defines the figure of merit of a resonator and is a measure of the average number of round-trips before a photon exits the cavity. Mathematically, it can be expressed as $\mathcal{F} = \Delta\nu_{\text{FSR}}/\Delta\nu_{\text{FWHM}}$, where $\Delta\nu_{\text{FWHM}}$ denotes the full width at half-maximum of the resonances.

If a light of wavelength λ launched into the cavity satisfies Equation 5.1, constructive interference within the cavity causes the intracavity intensity to buildup. For high mirror reflectivities approaching unity, nearly all of the incident intensity is transmitted through the cavity. This phenomenon, although puzzling, occurs due to the constructive interference inside the cavity.

Among their many applications, Fabry–Pérot resonators are excellent length measuring devices. This property manifests itself as a direct consequence of the strict relationship between the cavity resonance and the change in cavity length. In Figure 5.2 [157], the transmission of a high-finesse cavity ($\mathcal{F} > 1.3 \times 10^5$) is shown as a function of the change in cavity length. In this case, a 10 picometer (pm) change in cavity length can have a huge impact on the resonance and result in nearly 80% loss in the transmitted intensity. For low finesse cavities, the situation is more forgiving, and the full-width at half-maximum (FWHM) can be in the sub-nanometer range.

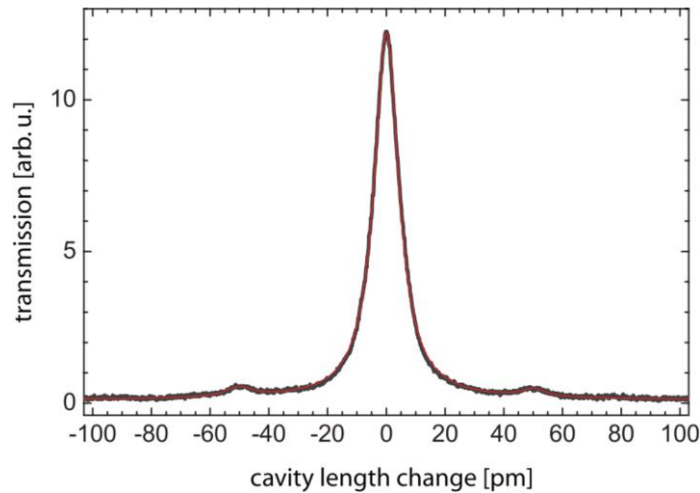


Figure 5.2 – Transmission as a function of the change in cavity length for a Fabry–Pérot cavity [157].

To maintain such precise control and stability of the cavity length is a challenging task and requires bulky and often expensive positioning stages, which are indispensable to cavity alignment. Recently, there has been a push towards miniaturized fiber-coupled cavities, in which the cavity mirrors are fabricated at the fiber

ends using laser ablation [157]–[160]. In [158], a monolithic fiber Fabry–Pérot cavity (FFPC) was demonstrated using off-the-shelf slotted glass ferrules (Figure 5.3), and a piezoelectric element for length control. The use of such ferrules with prealigned markers vastly simplifies the alignment process, and according to the authors, only two degrees of freedom (one rotation, and one translation) were needed for final alignment.

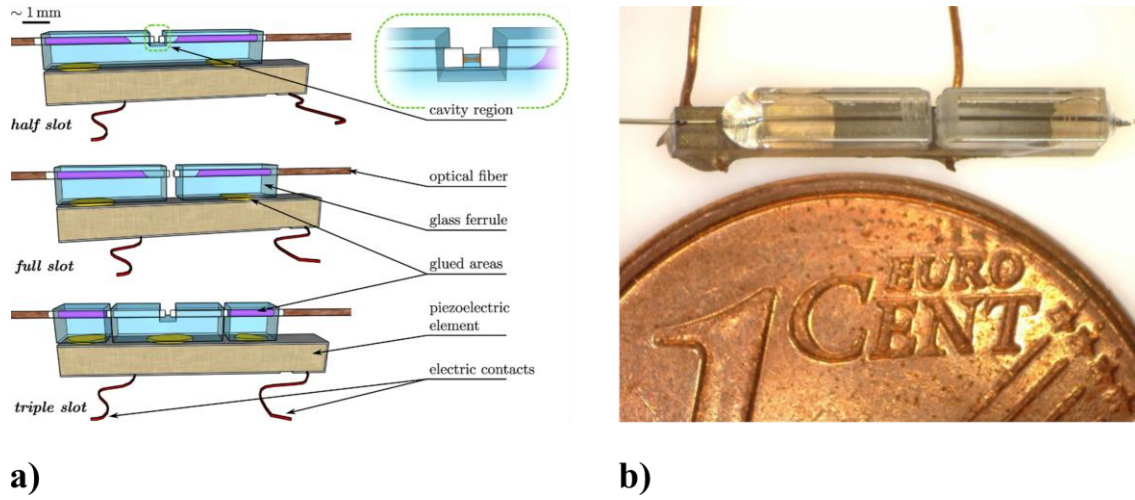


Figure 5.3 – An example of a miniaturized fiber Fabry–Pérot cavity (FFPC) as proposed in [158]. a) Three different configurations of the FFPC. b) A photograph of a full-slot FFPC as depicted in (a).

The sensitivity and alignment precision requirements of an FFPC present an ideal opportunity for the methods presented thus far. By combining the 3D fabrication capabilities offered by femtosecond laser micromachining, excellent thermal and mechanical properties of fused silica, and our non-contact actuation principles, we introduce a pseudo-monolithic, miniaturized, and packaged resonator.

5.2 Design and experiment

5.2.1 Design

Figure 5.4 shows the conceptual design of the device. It consists of the following main parts:

Region A is a modified version of the remote center of rotation (RCC) mechanism introduced previously in Chapter 4. The actuator is connected to the top of the mechanism and provides a rotational degree of freedom (DOF) about Y-axis.

Region B is a linear translation stage to enable adjustment along Z-axis. In an FPC, this DOF is crucial and lies along the cavity axis, thus enabling cavity length control.

Region C consists of two long u-shaped grooves, extending from edge-to-edge of the 25 mm² fused silica substrate. The grooves provide excellent alignment precision and significantly simplify the process. The groove width is ~ 125 μm whereas the depth (~ 100 μm) is chosen to be slightly less than the cladding diameter (~ 125 μm). This makes it easier to clamp the fibers inside the groove as part of the fibers vertically sticks outside the groove.

Region D consists of small through-holes fabricated across the thickness of the substrate. At these points, a UV-curable glue is dispensed to locally fix the fibers once coarse alignment is achieved. The holes allow for a downward movement (along Y) of the glue and also inhibit flow towards the fiber-ends.

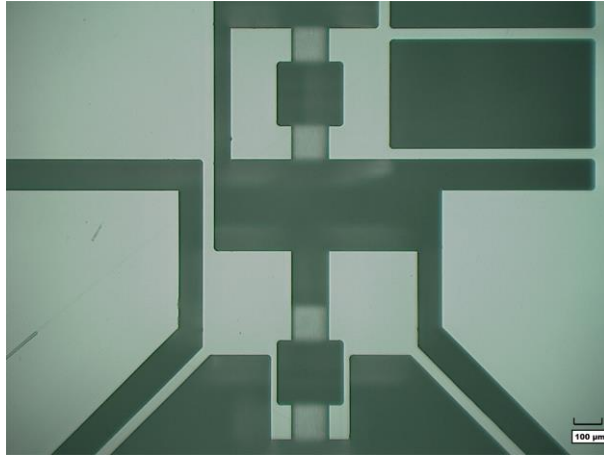


Figure 5.6 – A microscope image showing the cavity region of the device without the optical fibers. The scale bar is 100 micrometers.

5.2.2 Experiment

The experiment concerning the FFPC is preceded by a test run to validate the functioning of the design. As will become clearer later on, the fibers of the FFPC are special. These fibers, provided by our collaborators at the Kastler-Brossel's laboratory (LKB), University of Sorbonne and Ecole Normale Supérieure (ENS) in Paris, are shaped into curved mirrors at their ends and coated with a dielectric layer. More details are mentioned later in the text.

For the test run, we use two single-mode fibers (SMFs). The fibers (SM800-5.6-125 from Thorlabs) have a numerical aperture (NA) between 0.10 - 0.14, and a mode-field diameter (MFD) ranging between 4.7 – 6.9 μm .

- **Fiber preparation and assembly**

The two fibers used in this experiment are produced from a single fiber by cleaving it in the middle. This is to minimize the effect of the cleaving angle on coupling efficiency. To do so, we follow the process described below:

At first, the fiber is stripped in the middle region to remove the polymer coating and expose the cladding underneath. Next, the fiber is marked by writing a single line on the cladding and spanning the length of the stripped region. This is done using femtosecond laser micromachining at low pulse energy, just above the modification threshold. Finally, the fiber is cleaved on the written line. The process is shown in Figure 5.7.

To coarsely align the fibers on the device, an assembly station (Figure 5.8) is built. A laser diode ($\lambda = 980$ nm) is collimated and re-focussed inside the principal fiber, which is mounted on a 6-axis positioning stage. The receiving fiber is mounted on a similar stage, and the fiber output feeds a detector to measure the coupled power in transmission.

Using a fiber rotator, the receiving fiber is rotated to align the two markings with each other. Once aligned, the rotator is locked to prevent any further rotation. In this position, the effect of cleaving angle on the coupling efficiency is minimum. Next, using positioning stages, the fibers are aligned with their respective grooves and finally lowered into them. This step is done carefully to ensure maximum collinearity between the fiber and the groove, and maximum parallelism between the fiber and the substrate. To monitor the alignment, a high-magnification portable imaging microscope is mounted above. The microscope is mounted on a dual-axis translation stage to check the alignment across the entire length of the groove.

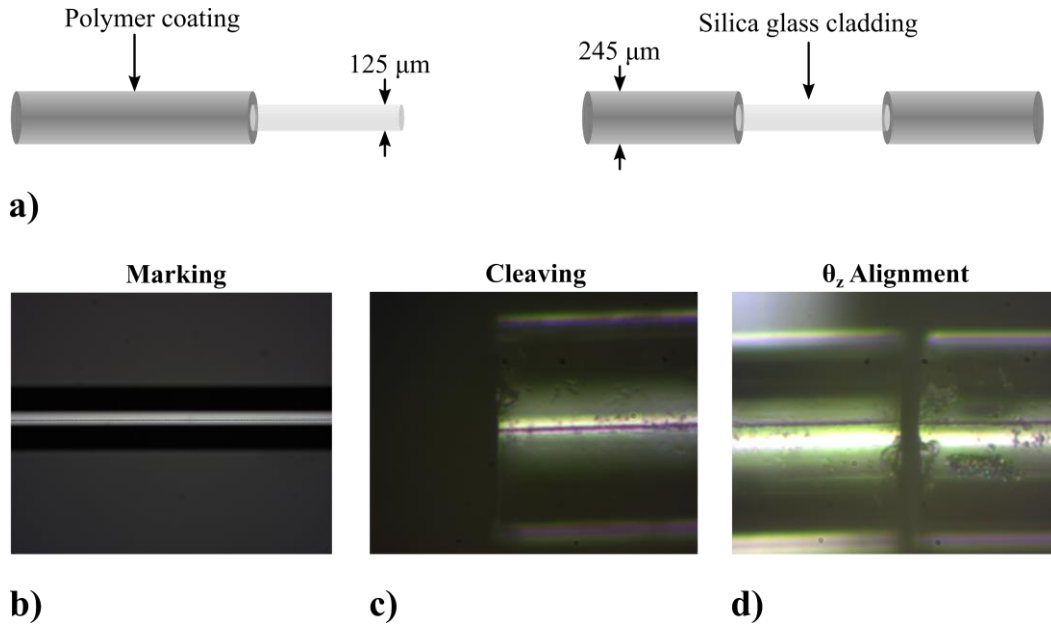


Figure 5.7 – a) A visual representation of fiber stripping. On left: stripped at the end, on right: stripped in the middle. b) Femtosecond laser inscription on a middle-stripped fiber. A single modification measuring $< 2 \mu\text{m}$ in width is written along the stripped region. c,d) A microscope image showing part of the cleaved fiber and final alignment on the pre-existing marker line.

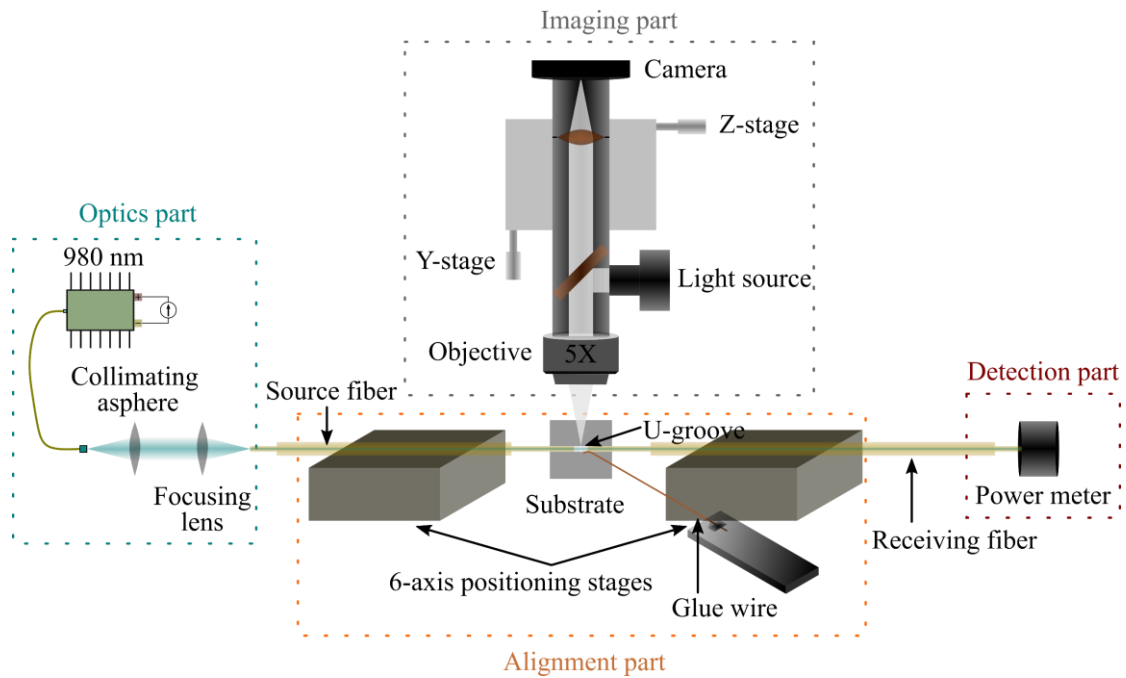


Figure 5.8 – Schematic of the experimental setup to assemble and align the fibers on the device. To monitor the assembly, a portable and high-magnification microscope is mounted vertically.

After coarse adjustment, the fibers are fixed into position with a UV-curable glue. Using a thin copper wire, a small amount of glue is applied to the gluing holes and cured immediately to avoid flow along the fiber. To allow free movement, the fiber of the translation stage is only glued at one point (on the stage), whereas the other end is only glued after the femtosecond laser adjustment. A picture of the assembled device is shown in Figure 5.9.

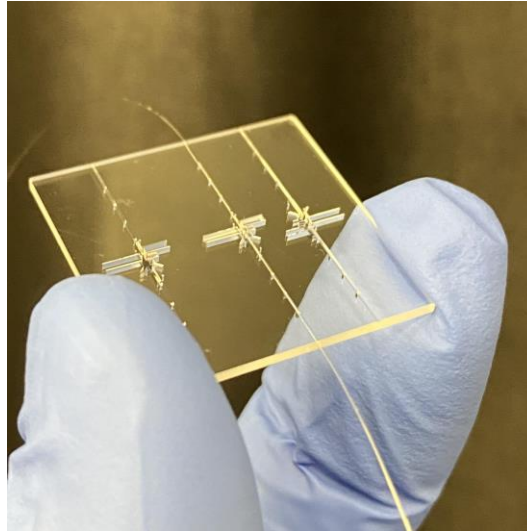


Figure 5.9 – A picture of three micro-machined devices fabricated inside the same substrate. The one in the middle is fitted with fibers.

Figure 5.10 shows a power stability curve of the assembled device.

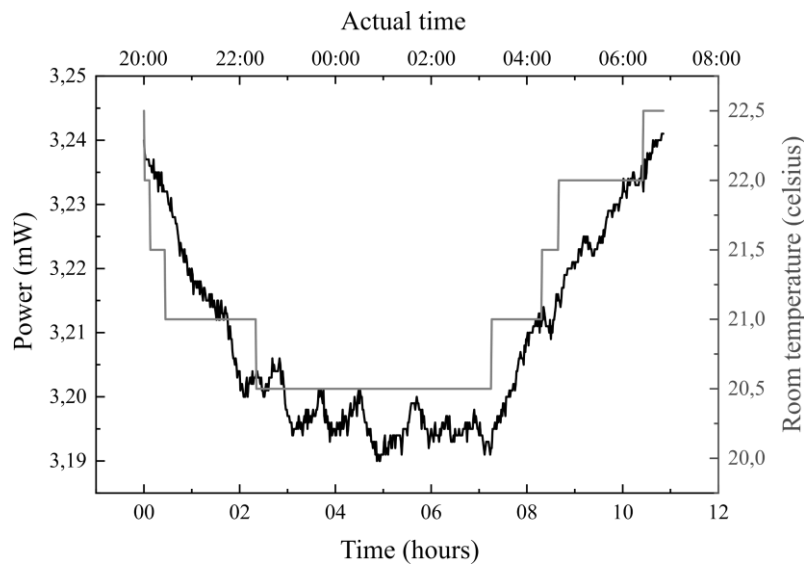


Figure 5.10 – A temperature stability curve showing the coupled power between the fibers as a function of time. During the night, as the temperature drops, a small decrement ($\sim 50 \mu\text{W}$) is observed, which self-recovers as the temperature returns to a stabilized value. The change is likely due to the thermal expansion and shrinkage of the glue, as the temperature inside the laboratory fluctuates.

• Assembly challenges

A v-shaped groove is often a desirable choice for alignment in photonic applications. It provides a single line-of-contact surface on either side, thus constraining lateral movement within the groove. Although we opted for a v-groove design initially (Figure 5.11), this was later changed to the u-groove design of Figure 5.6. During assembly, the slanting shape of the v-groove walls demands exceptional collinearity between the fiber and groove axes. Failing so, a situation similar to the one depicted in Figure 5.11b arises, causing the front end of the fiber to misalign as it is lowered into the groove. On the contrary, the flat walls of the u-groove do not pose any such concern and rather ease the assembly process.

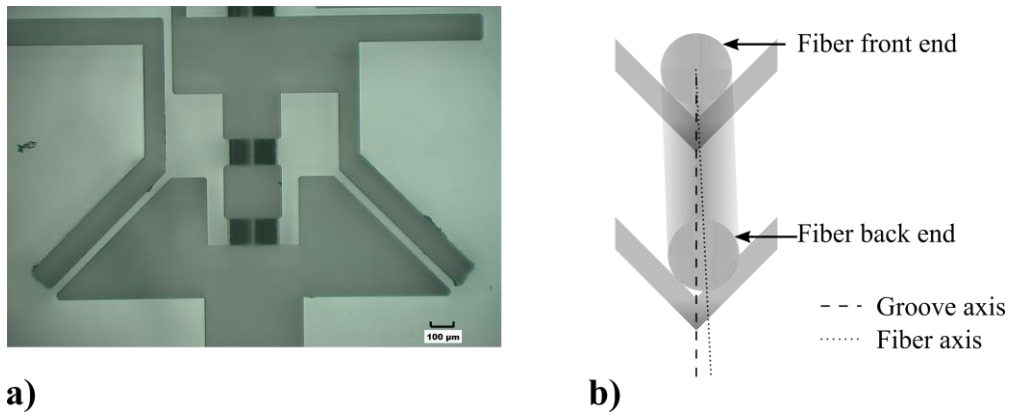


Figure 5.11 – a) An optical micrograph showing the v-groove fabricated using femtosecond laser micromachining. b) A graphical visualization depicting the alignment issues between an optical fiber and the v-groove. If the groove and fiber axis do not coincide, then walls of the v-groove push on the fiber causing misalignment at the other end.

• Results

The final alignment between the fibers is achieved through femtosecond laser exposure of the two actuators, a process similar to the one described in Chapter 4. The essential details however are given here: starting with the angle adjustment (θ_y), the actuator is modified near its sidewall by writing multiple laterally spaced lines across its length, and ultimately stacking similar lines across its thickness. The in-plane separation is set at 2 μm , whereas the interplanar separation is 10 μm . In Figure 5.12, this corresponds to the region marked as A_1 . After saturation and subsequent decrease, the opposite sidewall is modified, resulting in a reverse motion of the mechanism and a further increase in the coupled power (marked as A_2). The overshoot of the coupled power beyond the saturation level is indicative of a parasitic out-of-plane bending working in favor of the alignment. To exploit this further, the actuator is modified near its anchor and just below the top surface, by writing lines across its width, thus forcing a downward motion of the mechanism. This results in a small increment in the coupled power, denoted by B_1 in the plot.

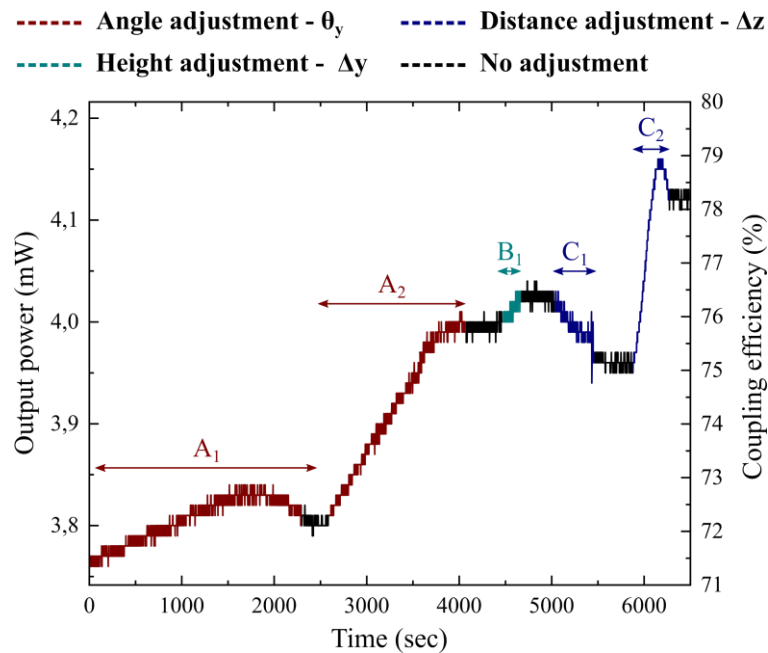


Figure 5.12 – Coupled power plotted versus time. Different stages of the process depicting alignment along various degrees of freedom are shown. A coupling efficiency of 79% is achieved in this experiment.

In a second step, the fiber-to-fiber distance is adjusted by modifying the actuator of the linear translation motion stage. Similar to before, lines are written parallel to one of the sidewalls to reduce the fiber-to-fiber separation. Keep in mind, the choice of the sidewall determines the direction of motion.

As the laser adjustment is started near the bottom surface, unexpectedly, the coupled power starts to decrease (marked as C_1). This is unexpected because a decrease in fiber-to-fiber gap should increase the coupled power instead of decreasing it. At this point, the exposure is stopped, and the focal spot is translated upwards and above the neutral line of the actuator. By resuming the exposure process, the coupled power increases as shown by the region marked as C_2 in the plot.

The unexpected decrease in power can be explained as follows: the power transmission coefficient (T) between two fibers with a lateral offset is given in Equation 4.2. When the writing beam is focussed near the bottom surface (Figure 5.13), the actuator bends along its degree of freedom (DOF, Z-axis), while at the same time, a parasitic motion occurs in the out-of-plane (Y-axis) direction. This introduces a lateral shift between the two fiber cores. However, by moving the focus near the mid-plane of the actuator, parasitic motion is minimized, and primary motion occurs along the DOF, thereby reducing the fiber-to-fiber distance and increasing the coupling efficiency.

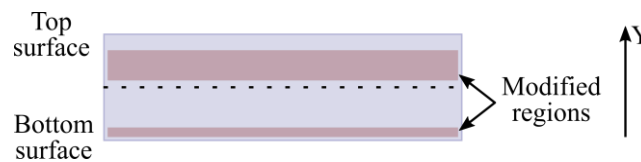


Figure 5.13 – A visual description of the writing process followed for adjustment along Z-axis. Modifications written near the bottom surface cause an upward movement of the actuator and thus induce a parasitic shift. However, by exposing the region near the neutral axis, parasitic effects are minimized and movement mainly occurs along the Z-axis.

In Figure 5.14, microscope images of the device are shown after the laser adjustment.

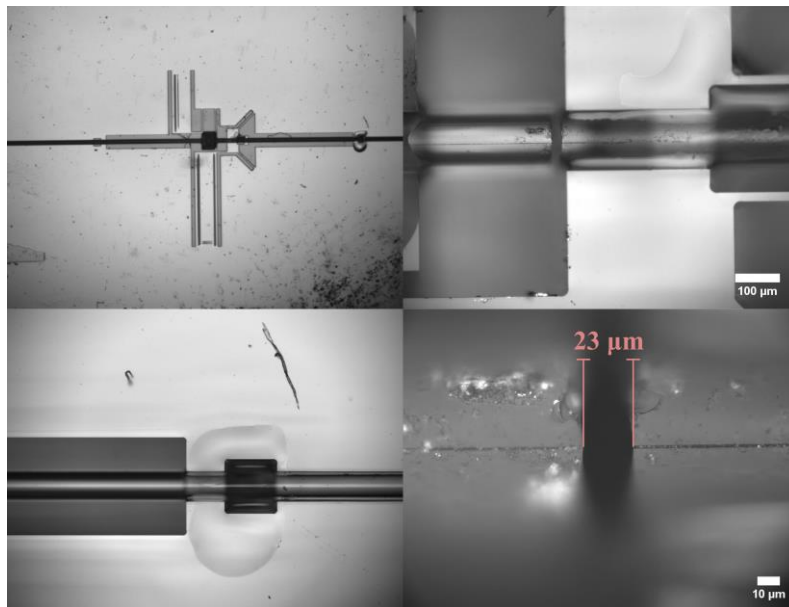


Figure 5.14 – Optical micrographs of the device after laser adjustment. Top left: full device, top-right: a low magnification shot of the cavity region, bottom-left: Gluing hole, bottom-right: a high magnification shot of the cavity region.

5.2.3 Towards a laser-aligned FFPC

- **New design**

As mentioned earlier, a Fabry–Pérot resonator demands stringent alignment accuracy than what is needed for a simple two-fiber case. For a high-finesse cavity, the extremely narrow linewidth (Figure 5.2) requires exceptional stability of the cavity length, with sensitivities reaching down to a few picometers. To progress in this direction, a small design change is necessary. Unlike before, where fiber of the translation stage was partly glued before the laser alignment step, now requires prior fixation at both points. This is because post-alignment fixation will cause a shrinkage in the glue, vary the cavity length, and lead to a non-resonant cavity. However, in the current design, since one glue hole is located outside the motion stage, prior fixation will fully constrain the fiber and inhibit cavity length adjustment. Thus, the translation stage is re-designed as shown in Figure 5.15.

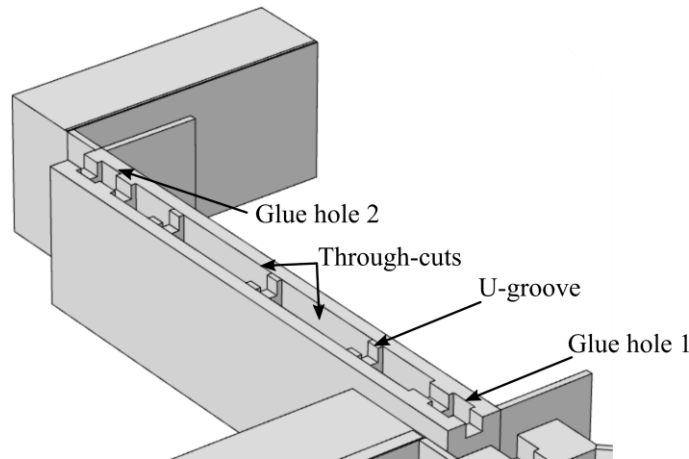


Figure 5.15 – A CAD model of the modified linear motion stage. Two glue holes, extending throughout the thickness of the substrate, are fabricated at the ends of the stage to fix the fiber. Through-cuts are created to remove the additional mass and maintain a high fundamental vibration mode.

In the re-designed motion stage, both glue-holes are located on the stage itself, thus allowing for post-fixation length adjustment. Further, due to additional mass of the stage, resonant frequencies are lowered, and to compensate for this, material is removed from the middle region as shown in the figure. A mode frequency analysis is shown in Figure 5.16.

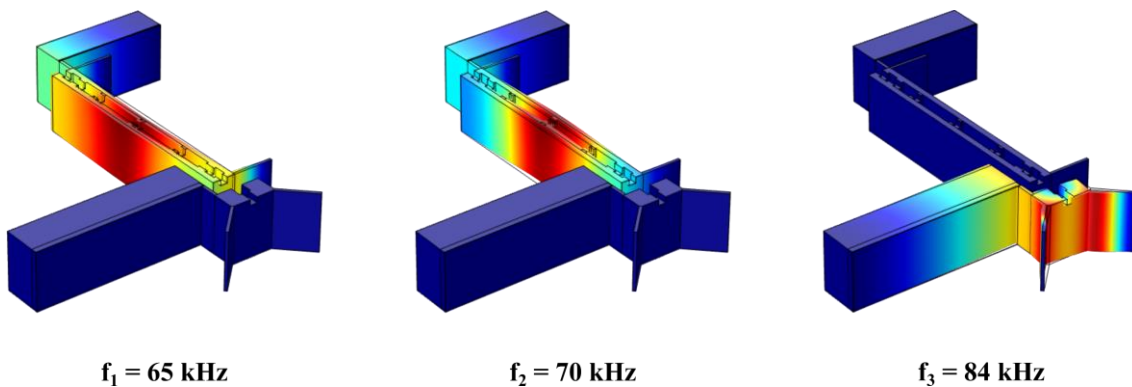


Figure 5.16 – Left-to-right: the first three mechanical resonance modes of the device.

- **Cavity mirrors**

An advantage of the FFPC is that the cavity mirrors are realized directly on the tips of the cavity fibers. A pulsed carbon dioxide (CO₂) laser is focussed on the cleaved ends to locally ablate the material. This results in a thin melt layer with surface tension naturally smoothening the surface. Afterward, a high-performance dielectric coating is applied to the concave depressions, which ultimately act as the cavity mirrors (Figure 5.17). Such a class of FFPCs have very high finesse due to the excellent surface roughness (~ 0.2 nm rms) achieved during the melting process, which is better than most classical super-polishing techniques. More details about the CO₂ laser treatment can be found in [161].

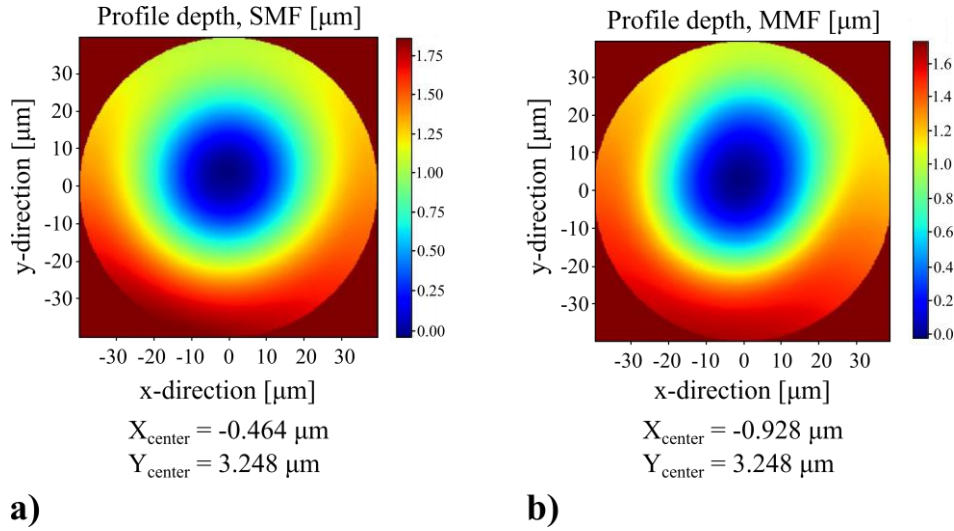


Figure 5.17 – Surface profile of the CO₂ fabricated mirrors [161] a) the single-mode source fiber, and b) the multi-mode receiving fiber. (Courtesy of Romain Long at Laboratoire Kastler Brossel in Paris)

- **Cavity alignment**

The experimental setup shown in Figure 5.8 is slightly modified to align the FFPC. The details are:

Two fiber-pigtailed laser diodes at $\lambda_1 = 1560$ nm and $\lambda_2 = 1310$ nm are used. At the design wavelength (λ_1), the dielectric coating of the cavity mirrors has a transmission of only 30 parts per million (ppm). Under a non-resonant condition (as is the case initially), this results in a near-zero transmission between the two fibers. To monitor the alignment during the initial assembly of the fibers, an alignment laser at a different wavelength (λ_2) is used. At this wavelength, the coating has a transmission of nearly 50%, and therefore the coupling efficiency between the fibers can be used for finer adjustments. The laser output is directly butt-coupled to the principal cavity fiber, which is single-mode (SM), whereas the receiving fiber is multimode (MM). Both fibers are copper-coated, however, near the ends, the coating is removed by etching in a solution of ferric chloride (46%, FeCl₃). To scan the cavity length, a single-axis piezo stage is integrated into one of the positioning stages. Lastly, the receiving MM fiber is mounted on a rotation mount (θ_z) to minimize the cavity birefringence. The modified experimental setup is shown in Figure 5.18.

On the glass substrate, alignment markers are embedded during the fabrication step. These markers are located 100 ± 1 μm from each other and are used to set the initial cavity length by coinciding the fiber end faces on the respective markers. Using the piezo stage, the SM fiber is continuously scanned about its marker in a back and forth motion to modulate the cavity length. The scan length is of the order of one wavelength or less, and the scan frequency is set to a low value of 0.5 Hz. Since the scanning fiber moves back and forth inside the groove, at higher scanning frequencies, we observed a small displacement of the substrate caused by either the friction between the groove walls and the glass cladding or static charging of the fiber surface.

During the scanning, the MM fiber is rotated along its axis to find the optimal θ_z position. Due to rotational asymmetry of the cavity mirrors (different radii of curvature along two principal axes, Figure 5.17) and the fact that a slight decentration is present between the mirror center and the fiber core, a rotation along the Z-axis helps to reduce the cavity birefringence [162]. During this process, the cavity transmission is monitored on an oscilloscope, and the MM fiber is locked in place once an optimal position (minimum intensity of higher-order modes) is found.

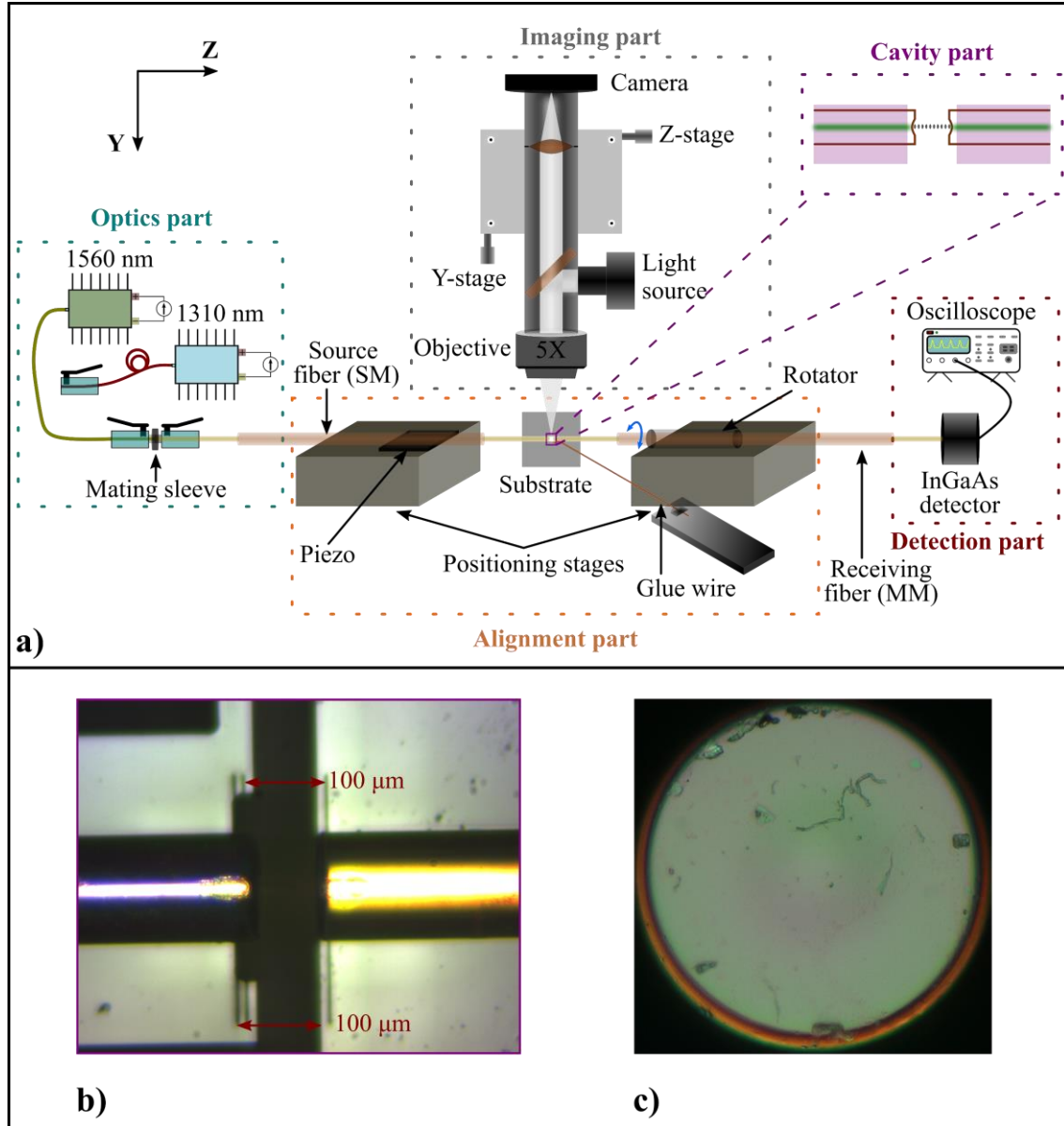


Figure 5.18 – a) Schematic of the re-designed assembly setup for the FFPC. The cavity output is monitored in transmission using an InGaAs photo-detector. b) A snapshot of the cavity during assembly; a pair of markers located precisely 100 μm away from each other are used for coarse positioning. c) A single-mode functionalized optical fiber, 125 μm in diameter processed with a concave mirror at the tip. The marks on the mirror surface occurred during the experiments and should not be attributed to the polishing process.

Next, the fiber is glued at multiple points to permanently secure it on the glass chip. The fixation points are strategically placed such that the fiber can rotate (about Y-axis) when the RCC mechanism is actuated. As the fiber adds additional stiffness to the RCC mechanism, the location of the fixation points is used to control this increment as well as the fundamental vibration mode of the device. Once the MM fiber is fixed, the SM

fiber is scanned to acquire the cavity transmission at two successive resonant cavity lengths, $L_1 = q \lambda/2$ and $L_2 = (q + 1) \lambda/2$. The results are shown in Figure 5.19.

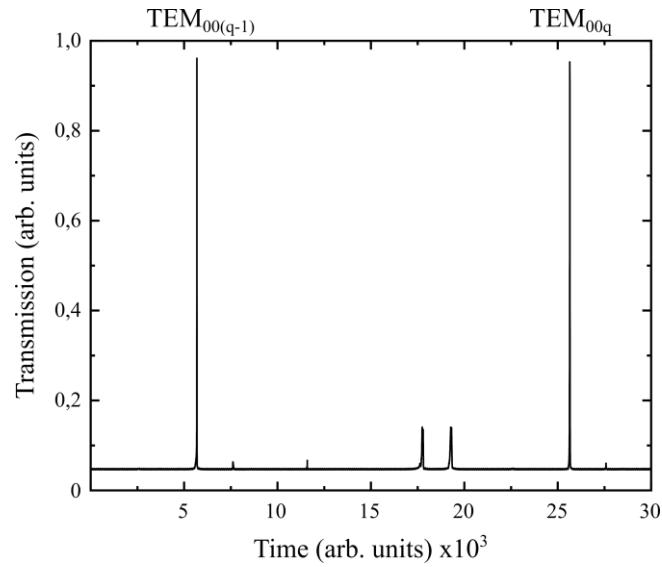


Figure 5.19 – Transmission of the FFPC cavity at 1560 nm. The cavity length is scanned using a one-axis piezo stage. On the X-axis, the time scale is arbitrary since the piezo stage was not calibrated to obtain an accurate voltage-displacement response. However, the distance between the main peaks is expected to be 780 nm.

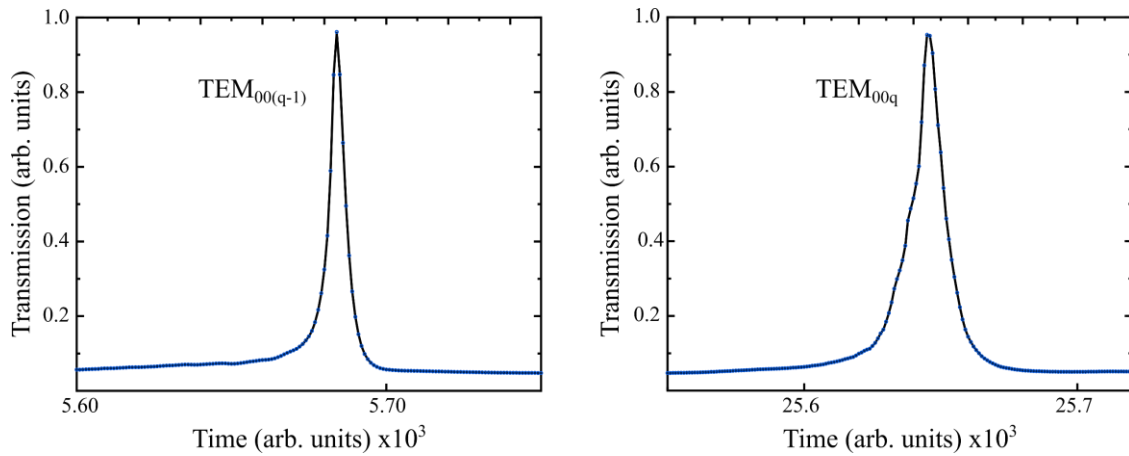


Figure 5.20 – Lineshapes of the two longitudinal modes plotted separately from Figure 5.19.

As can be seen in Figure 5.19, multiple low-intensity peaks appear in the transmission spectrum. This can be attributed to the way the laser is coupled into the cavity. Due to butt-coupling, light oscillating in the cavity has an arbitrary polarization, which can excite modes corresponding to the different orthogonal polarization directions. Although this can explain the smaller peaks, whose intensity is more than 15-times smaller than the primary peak, the source of the other two relatively high-intensity peaks is not known yet.

Due to the unavailability of additional fibers, cavity length modulation experiments using femtosecond laser exposure will be done in the immediate future. At the time of writing this thesis, the fibers were still in preparation.

5.3 Summary

In this chapter, we reported our results on a fiber cavity assembled on a glass substrate with pre-aligned grooves to align the fibers, and precision markers to fix the cavity length. The length modulation experiments of the fiber cavity were preceded by a fiber-to-fiber (both single-mode) alignment case, in which a near theoretical coupling efficiency was demonstrated. The angular position of the fibers was first adjusted, followed by adjusting the longitudinal offset between them. Later on, we demonstrated a resonant Fabry–Pérot cavity by modulating the cavity length using a piezo stage. The glass substrate, with on-chip angular and linear positioners, vastly simplified the alignment process and required single-axis tunability to observe the cavity resonance.

As mentioned in Section 5.1, Fabry–Pérot cavities demand an extremely high degree of alignment accuracy and stability. For this reason, very bulky equipment and elaborate experimental know-how are often required. We believe our methods present a simple approach towards fulfilling these alignment requirements, that too with a high degree of accuracy and in a compact and permanent manner.

Chapter 6 The behavior of fused silica under high stress at room temperature

In what has been presented so far, ultrashort pulses are tightly focussed leading to extreme intensities in the focal volume. This results in structural changes of the irradiated zone and involves either a positive or a negative volume change. Through intricate flexural mechanisms, such local strain is transferred away from the modified region, amplified in magnitude, and results in more complex movements elsewhere in the device.

This naturally raises the question about the long-term stability of these modifications over time, when subjected to different environments. Fused silica like other glasses is known to show temperature and moisture-dependent mechanical strength. It is therefore important to go beyond the preliminary analysis presented at the end of Chapter 3 and investigate this in more detail. The following study is important on two fronts: to understand how fused silica behaves when subjected to GPa levels of stress, and particularly within the realm of this thesis, it attempts to answer a very fundamental question – can an element, repositioned using femto-second laser exposure, stay aligned in its final position when subjected to ambient conditions? In other words, is the nature of this repositioning method permanent or non-permanent, and what role do stress, temperature, and humidity play?

In what follows, we begin with a discussion on glass-water interaction and the role of stress in this reaction. Next, we take a slight detour and discuss the optimization of the writing approach to achieve high stresses while avoiding cracks within the modified zone itself. Afterward, we introduce a unique flexure-based tensile tester, that when exposed to short pulses, can generate stresses above 2 GPa inside a thin test beam. To conclude, we present our results on stress relaxation and propose a possible interpretation.

6.1 Introduction

6.1.1 Water in glass

Although fused silica offers excellent mechanical, thermal, and optical properties, however, like all glasses, it suffers delayed fatigue when exposed to moisture [163], [164]. A minuscule amount of water can have a significant impact on its mechanical properties such as lowering of Young's modulus, density, viscosity, and glass transition temperature [165], [166]. Surface flaws such as micro-cracks (usually present on a machined surface) may act as stress concentration points leading to a reduction in fracture strength [167], [168]. Under the application of a constant load and assisted by the presence of moisture, such cracks can nucleate and result in delayed failure.

Although glass-water interaction has been the subject of many studies [165], [169], [170], a complete explanation is still pending. Particularly at room temperature, very few experimental data are available.

So far, various mechanisms have been proposed to understand the exact nature of this interaction. One of the most widely accepted mechanisms is the one proposed by R. Doremus [171], according to which, silica reacts with water and forms hydroxide. The diffusion of water takes place through the motion of molecular

water while the reaction end-product, hydroxyl, is immobile. At room temperature, the diffusion coefficient of water molecules in glass is extremely small (10^{-19} cm²/s [172] - 10^{-16} cm²/s [173]) and hence, it is difficult to observe the reaction within a normal time frame. However, the reaction can be accelerated at high temperatures, and in the presence of high vapor pressure. Moreover, the volume changes occurring during the reaction make it pressure/stress-sensitive and can be used to further accelerate the reaction.

The presence of stress is known to affect water solubility as well as its diffusion constant [174]. At low temperatures ($< 250^{\circ}\text{C}$), and under compressive stress, water solubility increases while the diffusion coefficient decreases. However, under tensile stress, the trend is reversed. At high temperatures ($> 650^{\circ}\text{C}$), an opposite behavior is observed. For compressive stress, water solubility decreases, and the diffusion coefficient increases while the opposite is true for tensile stress. As such, water diffusion in glass is somewhat anomalous.

In light of the above discussion, it is evident that stress plays a peculiar role in glass. While it is an enabler for various applications as shown thus far, on the other hand, it poses a question on their long-term sustainability, especially under varied conditions of temperature and humidity. Therefore, understanding this further is of fundamental as well as technological importance.

6.2 Stress optimization within stressors

Our goal in this chapter is to study the response of fused silica under high stress. To observe any measurable effect at room temperature, high stresses in the GPa range are needed. Since our approach relies on femto-second laser exposure, extremely dense patterns juxtaposed on each other, are needed. A challenge, therefore, is to avoid cumulative stress buildup within the modified zone [175].

To avoid crosstalk, a proper kinematic design is necessary to confine high stresses only in the region of interest. Logically, the required elements are - an actuator (to write the laser affected zones), flexures (to drive the displacement), and the element to be loaded (test beam). Depending on the nature of stress, the kinematics can be designed to drive the displacement away from the test beam (for tensile stress) or towards it (for compressive stress). A few possible examples are shown in Figure 6.1.

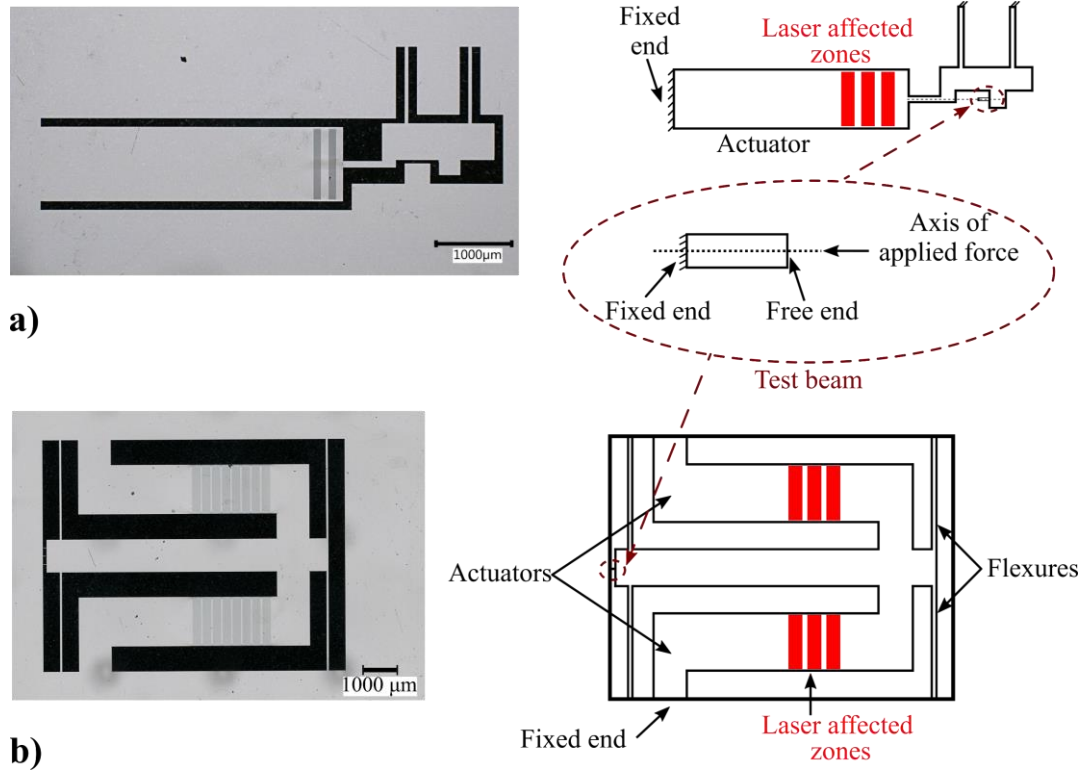


Figure – 6.1 a) Parallelogram flexure mechanism. The mechanism consists of an actuator connected to a linear guidance with two parallel flexure. The test beam is located symmetrically about the axis of the applied force. b) Double parallelogram flexure mechanism. Here, two actuators are required to stress a test beam located on a mobile platform between the actuators. The guidance is driven by four parallel flexures, two on either side of the platform.

The above examples lack an amplification mechanism and strain is transferred one-to-one from the modified zone to the test beam. Therefore for high stresses, multiple laser affected zones need to be stitched together. In fact, in the example shown in Figure 6.1b, the entire volume of the dual-actuators is consumed to generate > 1 GPa stress in the test beam. Due to such dense exposures, we observe cracks initiating within the laser affected zone, thus releasing all of the stress within the test beam. This happens for nearly all geometries of the laser affected zone as well as for different values of pulse energy, deposited energy, line spacing, and inter-plane spacing. A pictorial description is provided in Figures 6.2 and 6.3.

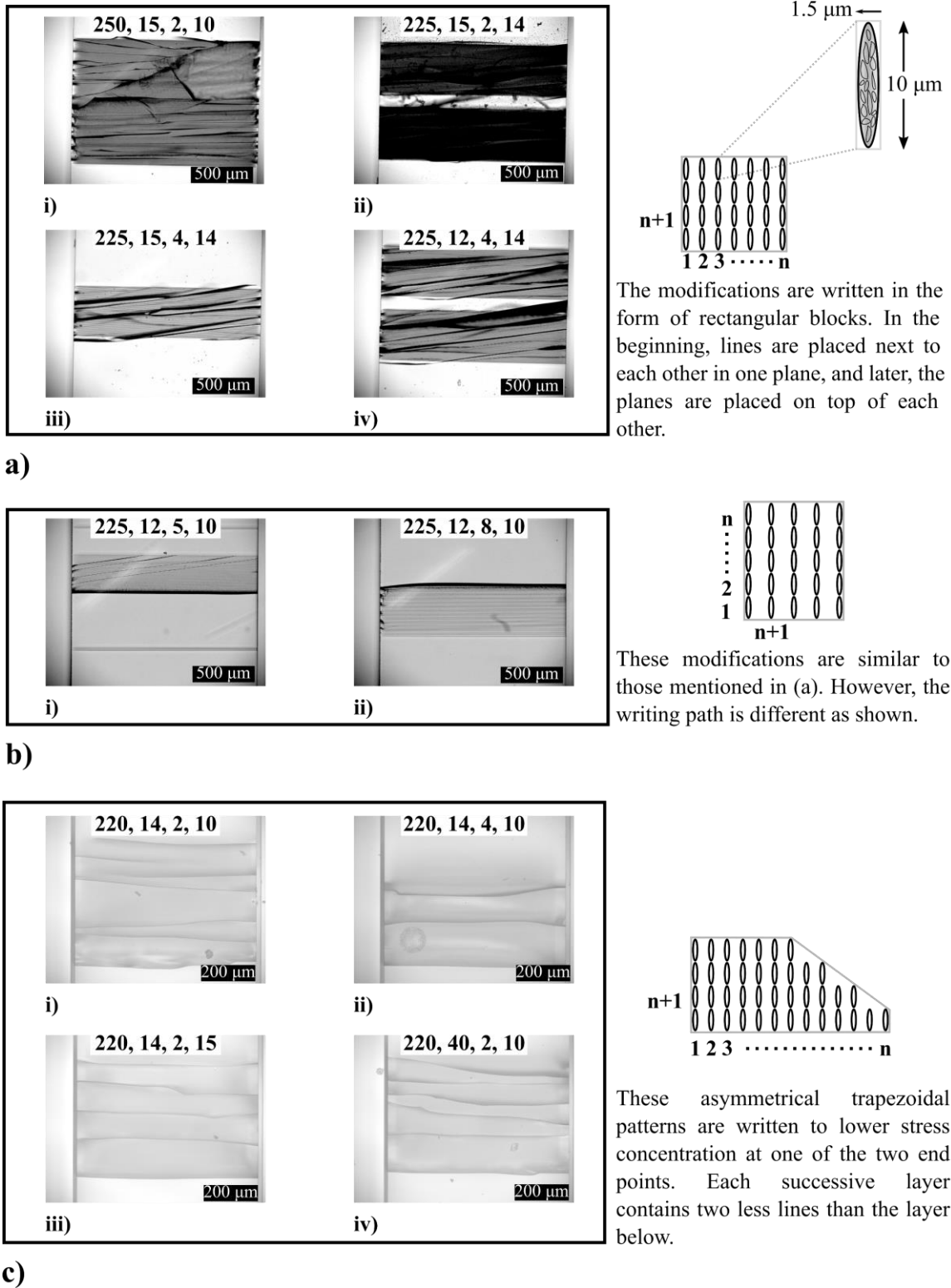


Figure – 6.2 Crack formation within the laser affected zone for various writing configurations. a) Rectangular writing blocks consisting of lines stitched together vertically and horizontally. The writing method is depicted on the right. b) Similar to (a) while following the approach of Section 4.3.2. c) To lower the stress at one end of a written line, each successive plane is shortened resulting in an asymmetrical trapezium shape. One can see the decrease in number of cracks for similar writing geometries, (a) and (c). The numbers on each figure represent the pulse energy (nJ), deposited energy (J/mm^2), line spacing (μm), and inter-plane spacing (μm) in that order.

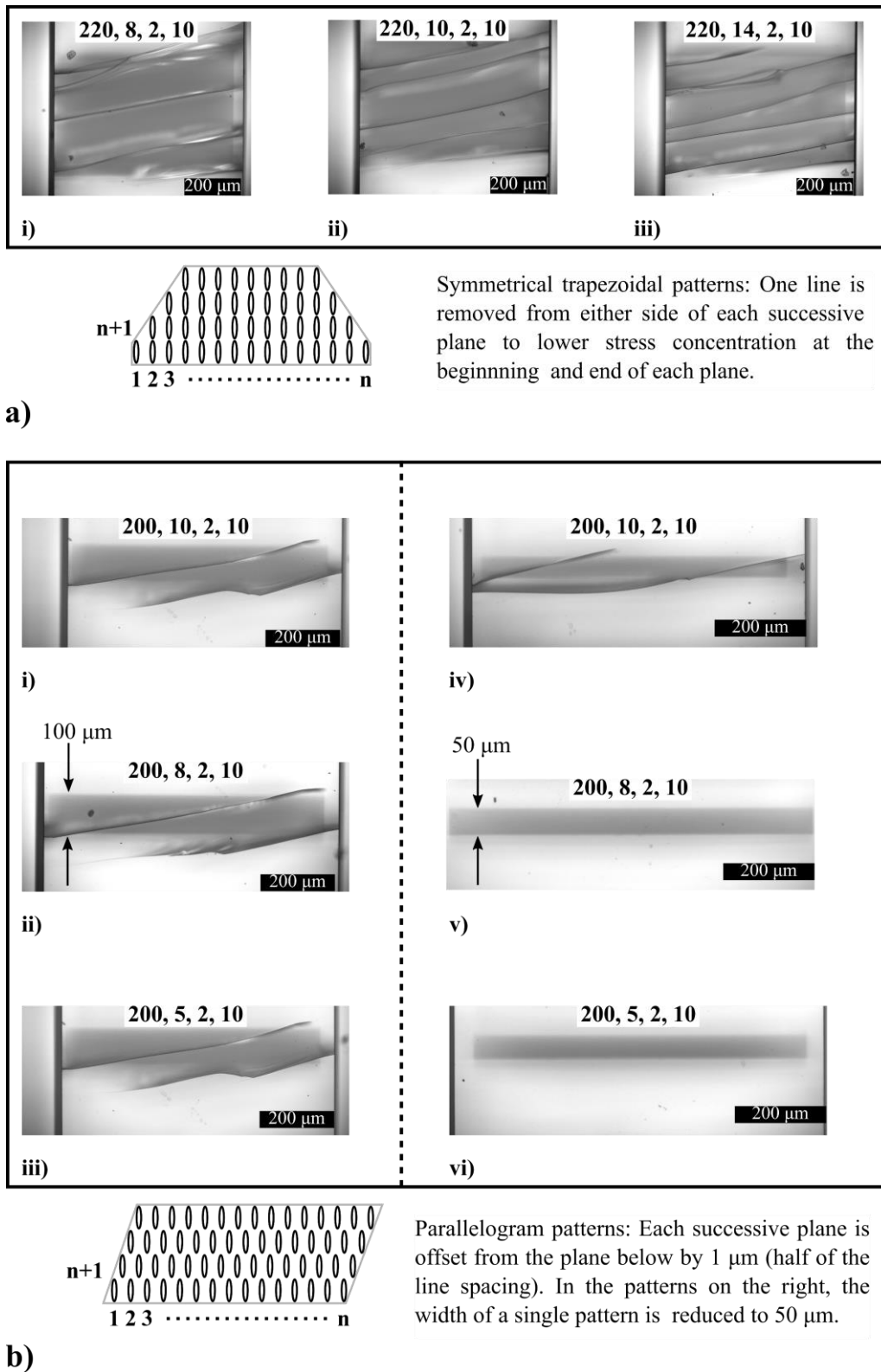


Figure 6.3 – Crack formation within the laser affected zone for various writing configurations. a) Symmetrical trapezium-shaped patterns in which each successive plane is shortened on either side with respect to the plane below. b) To shift every line of a plane from the respective line of the plane below, an offset of 1 μm is added to each plane. On the right, the same patterns are repeated, however, the width of each pattern is reduced by half. The numbers on each figure follow the same nomenclature as before.

In the analysis of Figures 6.2 and 6.3, several parameters were tested to optimize the stress within the modified zone. Although the severity of the failure is reduced gradually, the cracks persist nevertheless. Only in two configurations, Figures 6.3b(v) and b(vi), the modified region is crack-free. However, when the same pattern is repeated, the cracks appear again. Although the cause for these cracks is not known completely, a possible explanation is as follows:

The above patterns are written using a Satsuma laser with a repetition rate of 120 kHz and a pulse width of 300 fs. Due to the short length of the written lines and the slow acceleration of the stages, a uniform writing speed cannot be maintained. This causes non-uniform energy deposition across the modified region, particularly resulting in a high dose at the two ends of a modification. To test this hypothesis, a set of cantilevers are fabricated and re-exposed similarly using the same laser. The length of the modified region is increased progressively as shown in Figure 6.4. With the exception of the first cantilever, all other cantilevers develop cracks until a certain length of the modified zone, beyond which, no cracks are observed.

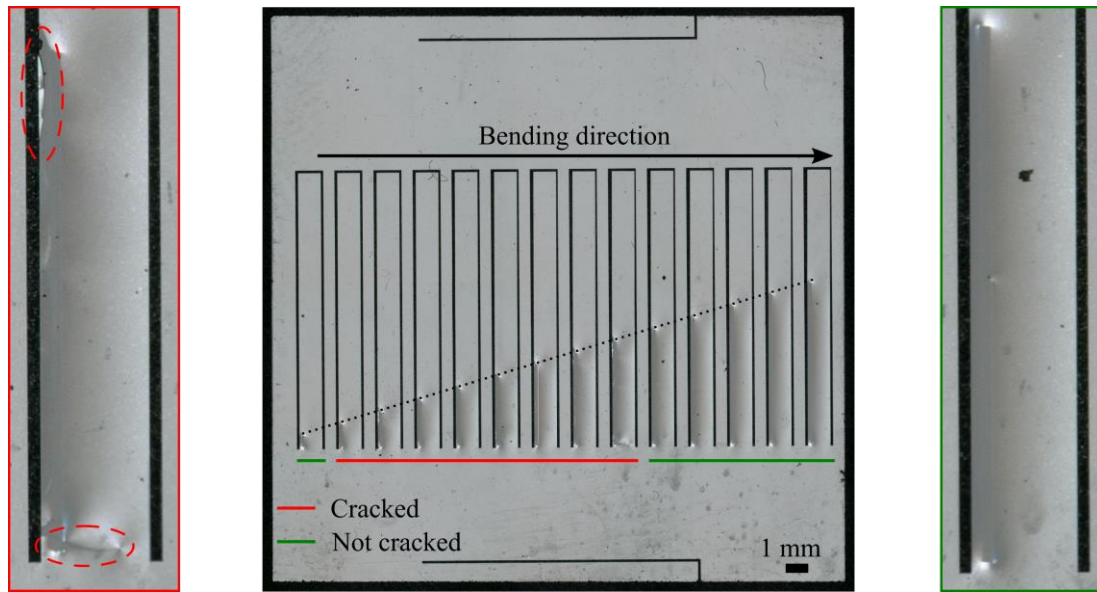


Figure 6.4 – An optical micrograph of a set of cantilevers exposed with an increasing length of the modified zone. The writing parameters are: 220 nJ pulse energy, 12 J/mm² deposited energy, 2 μ m line spacing, and 10 μ m vertical spacing. On left: modified zone cracks highlighted by the ellipses. On right: crack-free modified zone.

After this comprehensive analysis, however, an exact answer is still pending. Based on the above results, a new loading mechanism is designed featuring an intrinsic amplification mechanism and a longer modified zone.

6.3 Device mechanism

The monolithic micro-tensile tester device shown in Figure 6.5 consists of a loading bar for laser inscription. The strain due to the laser exposure causes the loading bar to bend and deflect at its free end. At this end, a flexible interface couples the strain into a guidance, which is driven by two parallel flexure units to produce a nearly linear motion. Normally, such a guidance produces a coupled motion, a displacement along the direction of force as well as a parasitic component in the transverse direction (to account for bending of the flexures). However, for the displacements involved here, the transverse component is negligible and thus, we can assume a uniaxial loading case.

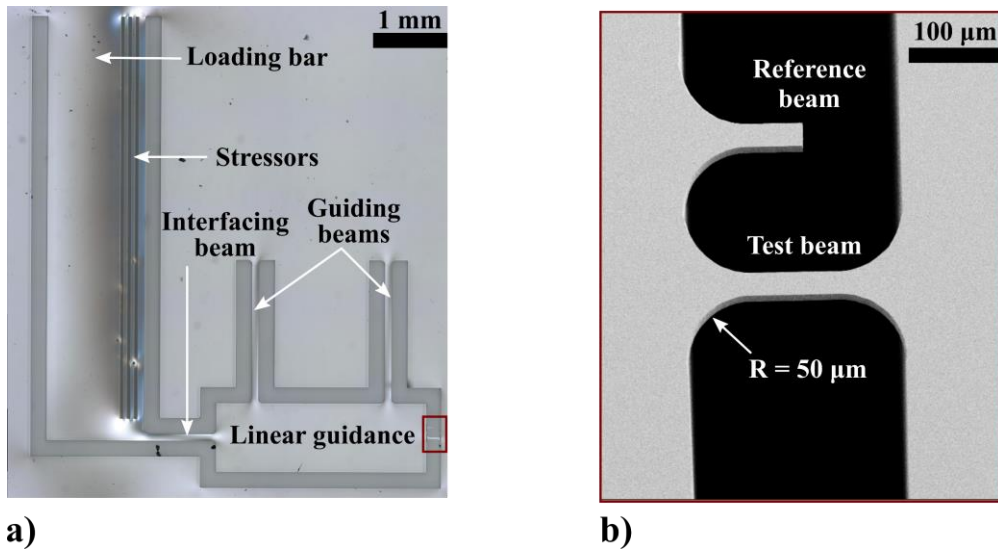


Figure 6.5 – a) An optical image of the loading device fabricated using direct laser writing and wet chemical etching. b) A high magnification image of the test beams and the reference beam. To avoid stress concentration near edges, all corners are radiused as shown.

The test beam is fabricated at the end of the guidance with one end constrained by the bulk glass. The beam is positioned symmetrically with respect to the interfacing bar connecting the loading area to the guidance. This ensures a zero bending moment about the fixed end of the beam and a pure tensile loading mode. For retardance calibration purposes, next to each test beam, a dummy half-beam is fabricated and attached to the guidance on one end while the other end extends roughly to the midpoint of the main beam. Being free on one end, this element does not see any stress and is used as a marker for retardance measurements to focus the probe laser at the same point in each measurement. To prevent stress concentration at sharp boundaries, all corners are radiused at $50\ \mu\text{m}$. The overall design is compact ($7 \times 6\ \text{mm}^2$), monolithic, and fabricated in a single step using femtosecond laser micromachining. An illustrative diagram of the mechanism is shown in Figure 6.6.

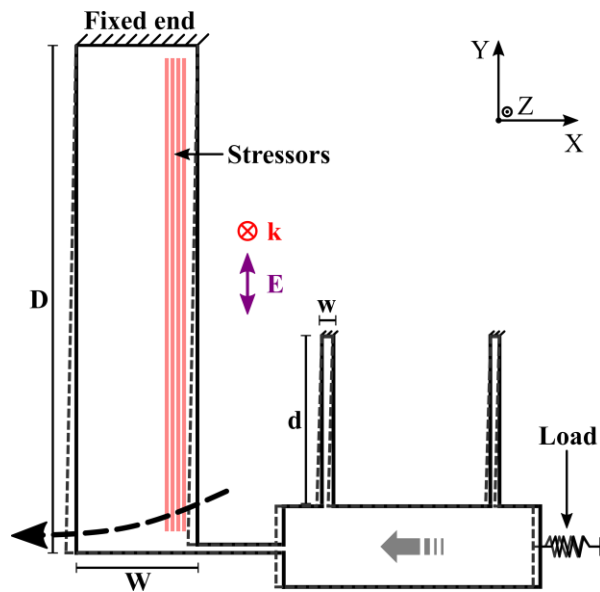


Figure 6.6 – A kinematic diagram of the loading mechanism showing the deformed state (in-dash) underneath. The modifications are written along the length of the loading bar with polarization oriented along the writing direction.

The optimal parameters for the actuator-guidance combination are found using Comsol Multiphysics. To do so, stress in the test-beam is maximised by varying the different parameters. As shown in Figure 6.7, the maximum stress is nearly invariant for different combinations of actuator width and length. However, the parameters noted in Table 6.1 are chosen such that more volume is available to write laser-modified patterns.

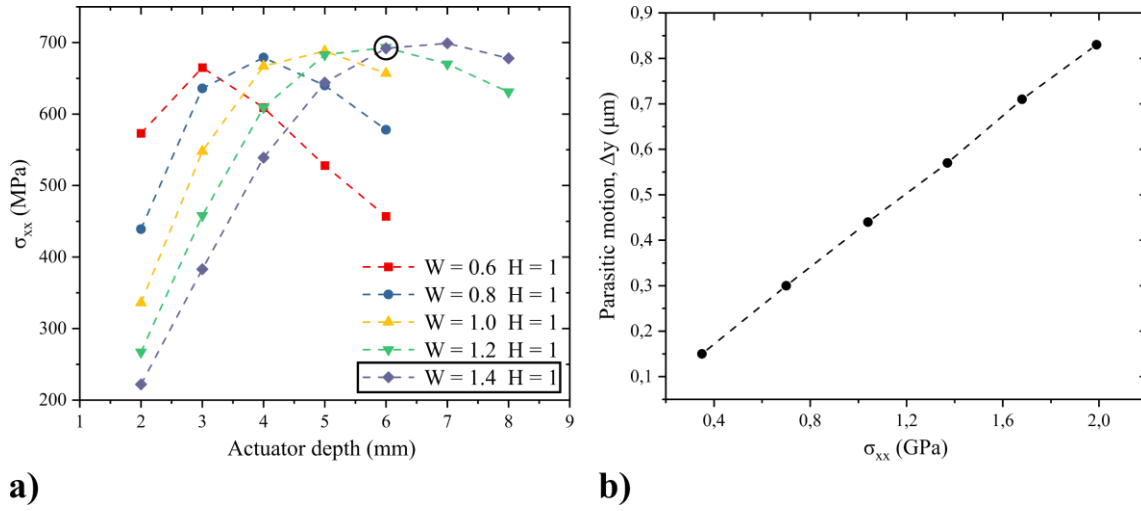


Figure 6.7 – a) Dimensional optimization of the actuator. For various actuator parameters, the tensile stress inside a thin beam attached to the mobile stage is plotted. b) Transverse parasitic motion (along Y) plotted as a function of tensile stress in the beam.

Table 6.1 – Actuator and flexure dimensions of the linear guidance (in mm)

W	D	H	w	d	h
1.4	6	1	0.1	2	1

6.4 Experimental procedure

6.4.1 Fabrication and re-exposure

The devices are fabricated out of a $25 \times 25 \text{ mm}^2$, 1 mm thick silica substrate (synthetic fused silica with low OH content) using femtosecond laser manufacturing process presented earlier. For the fabrication, laser parameters are: 270 fs pulse width, 250 nJ pulse energy, 18 J/mm^2 deposited energy, and 500 kHz repetition rate.

After machining, the samples are slowly etched in a 1.25% solution of hydrofluoric acid for about 40 hours. A slow etching step is used to prevent an aggressive attack on the modified regions and improve surface roughness [104]. This is particularly critical for the surface quality of the test beams and to prevent crack nucleation while loading. On each substrate, six micro-tensile testers are fabricated as shown in Figure 6.8.

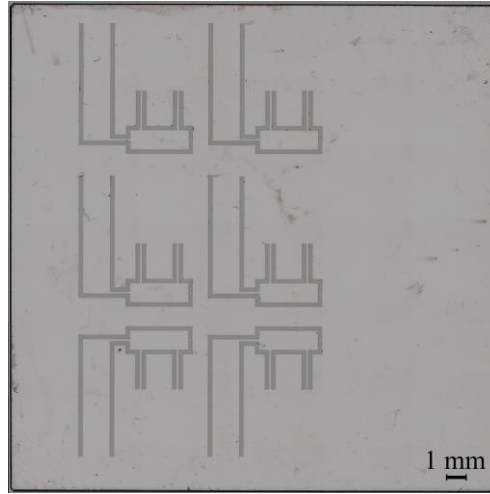


Figure 6.8 – Image of the fused silica substrate consisting of six devices. The devices at the bottom are inverted to push the test beam towards the bulk and avoid any interference from the edge.

After etching, the tensile-testers are re-exposed under the same laser to load the test beams. For this step, the samples are placed inside a sealed miniature environmental chamber with optical access viewports at the top and bottom for laser exposure and subsequent measurements. The chamber has a continuous supply of dry N_2 gas to create a dry atmosphere.

Two different writing strategies are tested for achieving maximum stress in the test beams. The first strategy follows the same approach as mentioned in Section 4.3.2. Laser-affected zones are written along the length of the loading bar and stacked on top of each other. Afterward, similar planes are then stacked next to each other. The resulting stress is plotted in Figure 6.9.

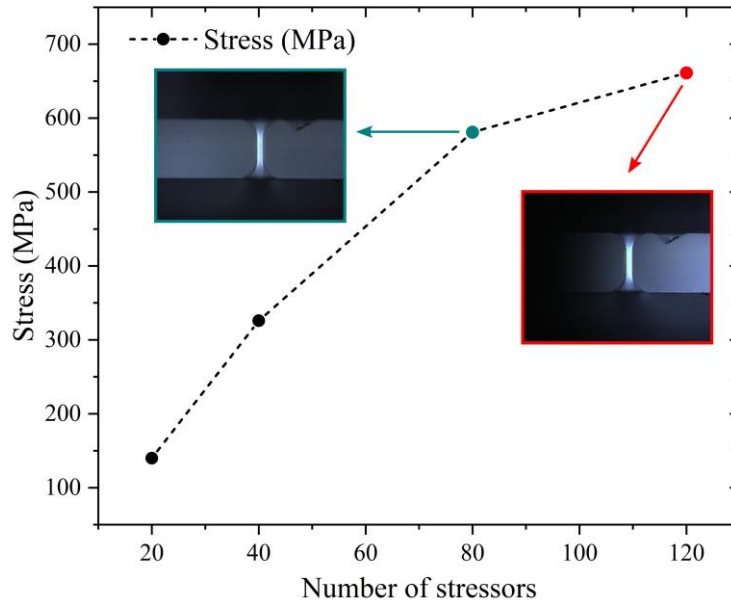


Figure 6.9 – Measured stress as a function of the number of stressors. In this case, a single stressor is defined as a set of lines along the length of the loading bar and stacked vertically on top of each other across its thickness. The width of a single stressor is about $2 \mu m$. The spacing between stressors is $5 \mu m$. Photoelastic images at different stress levels are shown in the inset.

The second strategy follows a hybrid writing approach. Patterns are first written following the approach introduced in Section 4.3.1. However, instead of writing one continuous block of the modified zone, the region

is discretized into smaller blocks that are laterally spaced from each other. The measured stress is plotted in Figure 6.10. In this chapter, a single block is referred to as a stressor from hereon.

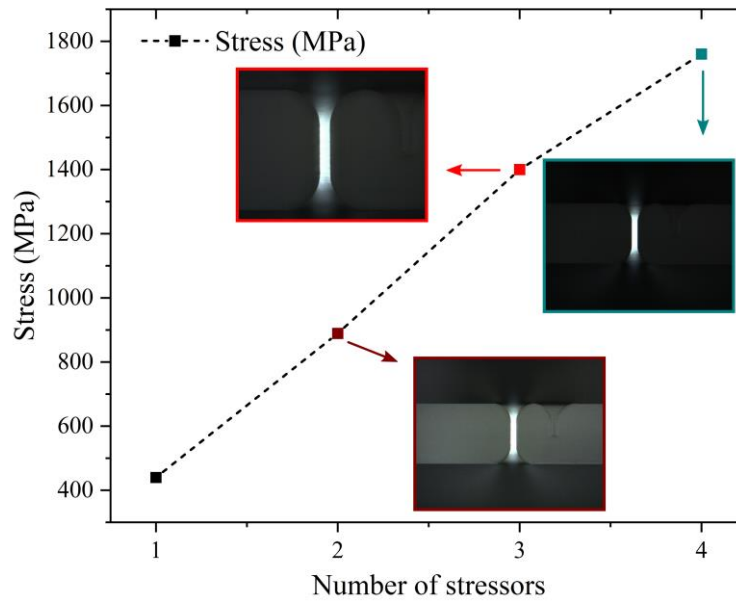


Figure 6.10 – Measured stress as a function of the number of stressors. A single stressor is $50\ \mu\text{m}$ wide and contains 25 lines spaced at $2\ \mu\text{m}$. Photoelastic images at different stages of the loading process are shown in the inset.

Since the measured stress is much larger in this case, these patterns are used in the rest of this chapter. So, we describe them in more detail below.

A single stressor is $50\ \mu\text{m}$ wide and spans the entire length of the actuator. To prevent surface ablation, the stressors are embedded inside the bulk of the loading bars at a depth of $20\ \mu\text{m}$ from the top and bottom surfaces. Within each stressor, the lateral spacing between two individual lines is set at $2\ \mu\text{m}$ and the planes are spaced by $10\ \mu\text{m}$ along the vertical direction (Z-axis). In the region near the edges, the stressors are placed $100\ \mu\text{m}$ away from the nearest edge to prevent stress concentration and possible crack formation. Between two individual stressors, a wide gap of $50\ \mu\text{m}$ is left unmodified. In the re-exposure step, a pulse energy of $220\ \text{nJ}$ and deposited energy of $12\ \text{J}/\text{mm}^2$ is used. The writing speed is $5.9\ \text{mm}/\text{sec}$ and the repetition rate is $500\ \text{kHz}$.

By varying the number of stressors, the overall strain and the resulting stress in the beams can be controlled precisely. Depending on the desired stress level, the loading process can take anywhere between 1 and 4 hours. For example, it takes nearly 30 minutes to write a single stressor and 8 stressors are needed to reach a $2\ \text{GPa}$ stress level.

As we will see later, the test beams have very little thickness (for lower stiffness) and thus are extremely fragile. Therefore, it is important to avoid any out-of-plane bending commonly associated with these exposures. Such bending is caused by non-uniform laser exposure conditions due to spherical aberrations along the thickness of the substrate [176]. To do so, we modulate the power by nearly 25% across a thickness of $1\ \text{mm}$. Without compensating for out-of-plane bending, the guidance together with the loading bar bends down resulting in failure of the test beams as shown in Figure 6.11.

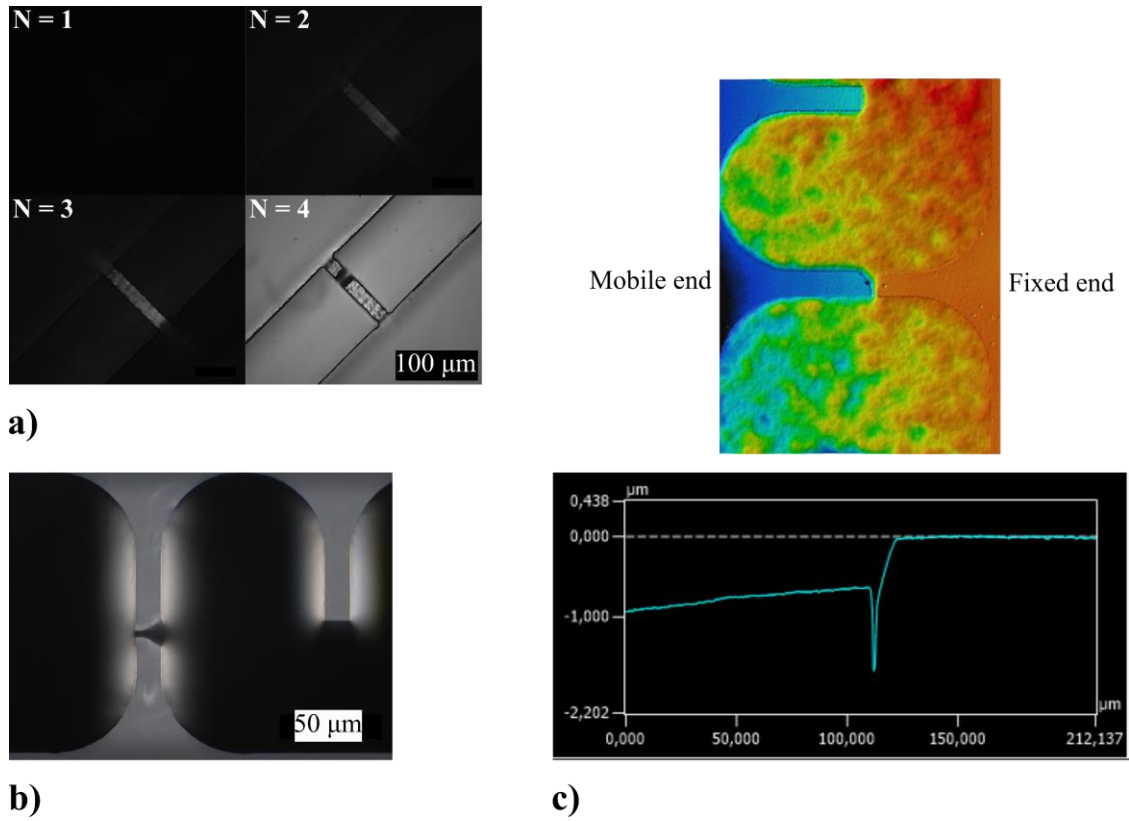


Figure 6.11 – a) Cross polarized images at different stages of the loading process. The numbers denote the number of stressors. At $N = 4$, the test beam breaks due to out-of-plane bending. b) An optical micrograph of a failed test beam due to bending stress caused by parasitic movement of the loading bar. c) A color map of the failed beam showing the height profile along its length.

Finally, to maintain a uniform deposited energy along the length of the stressors, a buffer is added before the beginning and at the end of each line to account for the acceleration/deceleration phases of the translation stages. This buffer gives the stages enough time to attain a constant speed before arriving at the endpoints of each line.

6.4.2 Retardance measurements

The stress within the beams is measured using a non-contact method based on photo-elasticity. Although fused silica is isotropic, it can become birefringent when subjected to external stress and in such a case, the principal optical axis is defined by the direction of applied stress. In our measurements, we observe the retardance of a monochromatic laser beam passing through the stressed region. To do this, we use a highly stable and collimated Helium-Neon laser ($\lambda = 633 \text{ nm}$), which is focussed inside the specimens (test-beam region) placed in a cross-polarized configuration. The stress is then calculated according to the following equation:

$$\sigma_1 - \sigma_2 = \frac{R}{T(C_1 - C_2)} \quad (6.1)$$

Here, R is the measured retardance, T is the thickness of the test beam, $C_1 - C_2 = 3.55 \times 10^{-12} \text{ Pa}^{-1}$ is the stress optic coefficient of fused silica, and σ_1, σ_2 denote the stresses along the axial and transverse directions respectively. In our case, we consider σ_2 negligible due to uniaxial loading.

Figure 6.12 shows a schematic of the experimental setup. The laser output is expanded via a telescope to match the entrance aperture of the focusing objective. The beam is then split using a polarizing beam splitter (PBS) and part of it is incident on a photodiode to monitor power fluctuations of the source. The other half is focussed through an optical window using a long-range objective (Mitutoyo 20X, Japan) with a working distance of 20 mm and a numerical aperture of 0.4. The waist at the focus is approximately $2.5\ \mu\text{m}$ and the Rayleigh range is nearly $30\ \mu\text{m}$ (hence larger than the thickness of the measured beams). The choice of a large working distance objective is necessary to access the beams placed inside the environmental chamber. The chamber (Figure 6.13) is mounted on an XY stage to access the four sample slots. Within each slot, a substrate containing six micro-tensile testers can be fitted.

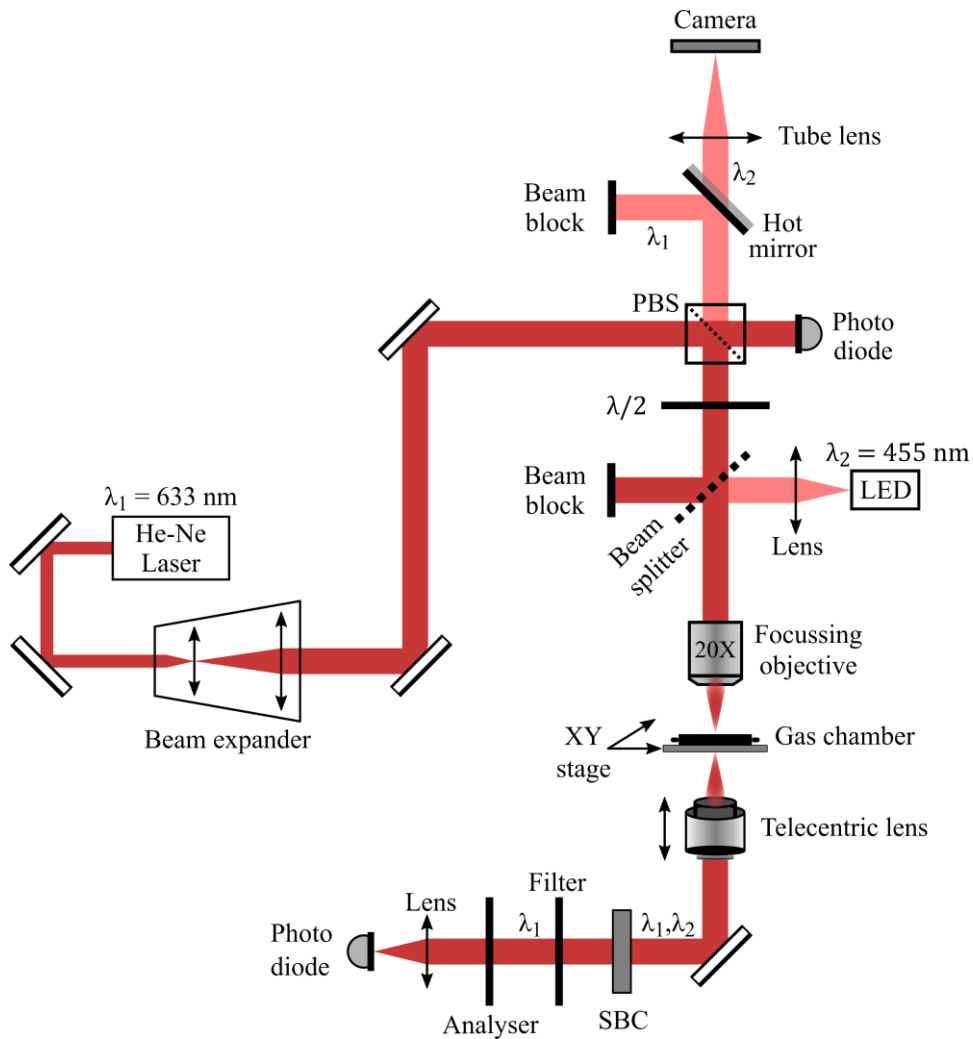


Figure 6.12 – Schematic of the stress measurement setup. A He-Ne laser source ($\lambda_1 = 633\text{ nm}$) is focussed inside the stressed beams located within the chamber. The recollimated beam is passed through a second polarizer oriented in a cross-polarized configuration and focussed onto a photodiode. For retardance measurements, a Soleil Babinet Compensator (SBC) is inserted in a zero retardance configuration. To image the beams, a blue LED ($\lambda_2 = 455\text{ nm}$) is illuminating from the top.

A half-wave plate orients the polarization of the beam at 45° with respect to the principal stress axis in the test beams. After focusing, the beam is recollimated using a telecentric lens and made incident on a variable retarder (Soleil Babinet Compensator, SBC) which is used to quantitatively measure the induced retardance in the optical path. The compensator plate inside the SBC can be set to a variable retardance or be used to measure an unknown retardance. Further downstream from the SBC, an analyzer is placed in a cross-polarized configuration with respect to the polarization axis defined by the half-wave plate. In this way, the

test beams are placed in a cross-polarization configuration. The output is then focussed on an amplified detector to measure the resultant birefringent signal. To precisely focus the He-Ne laser at the center of the beams, an LED ($\lambda = 455 \text{ nm}$) is used for imaging. The LED is focussed using the same objective and the reflected light is focussed on a camera using a tube lens. To prevent the back-reflected laser beam from saturating the camera, a 45° angle of incidence (AOI) mirror is inserted before the camera. The mirror is reflective at 633 nm and transmissive at 455 nm . Similarly, to block the unpolarized LED from contributing to the detector signal, a long-pass filter ($\lambda_{\text{cut-off}} = 600 \text{ nm}$) is inserted after the SBC.

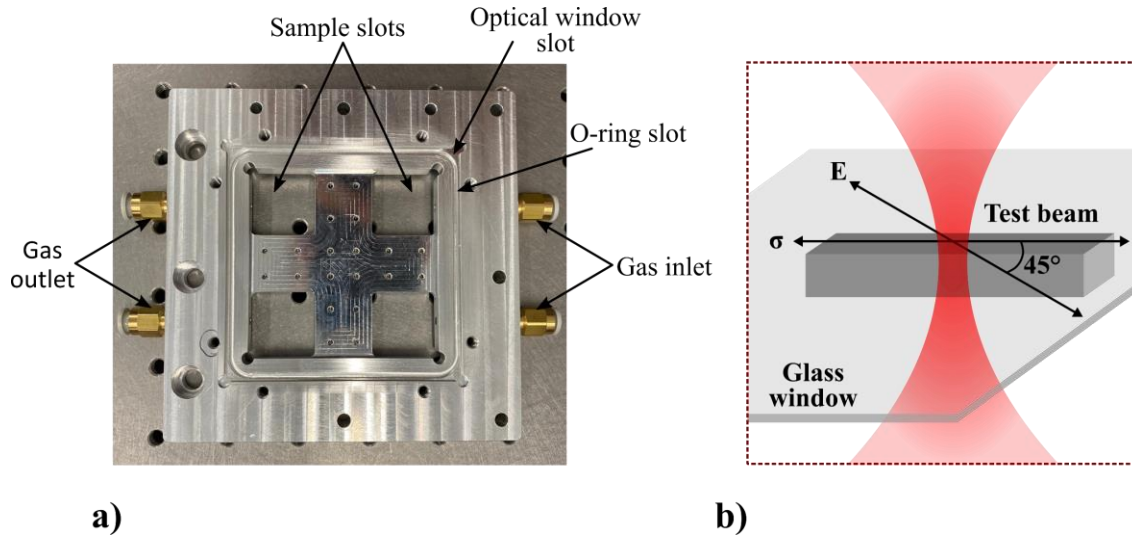


Figure 6.13 – a) The environmental chamber used to maintain dry conditions. The chamber can hold four samples in dedicated slots and optical access is available from both top and bottom. b) An illustrative schematic of the tightly focussed He-Ne laser beam passing through the test beam. The laser polarization (E) is oriented at 45° with respect to the principal stress axis (σ).

6.4.3 Stress measurements over time

The beams are loaded sequentially each time with an increasing stress level. After each loading step, the retardance is measured. A loading step consists of writing a certain number of stressors (depending on the desired stress level) inside the loading region of the tensile tester where each stressor consists of nearly 2500 laser written lines. This sequence is repeated until all the beams (six) on a single substrate are loaded. To minimize alignment errors during positioning of the chamber on the measurement setup, it is fitted with two alignment pins, thus ensuring it sits in almost the same position after each iteration.

For our measurements, we fabricate two sets of samples. In the first set, the thickness of the test beams is relatively large (ranging between $15.9 - 26.4 \mu\text{m}$) and varies substantially between the individual beams. This set contains a total of seven loaded beams. The second set with four beams has a much lower beam thickness (ranging between $5.3 - 8.7 \mu\text{m}$). The thickness of the beams is measured precisely using a confocal microscope (Keyence VK-X1000 Series). The accuracy of this measurement is within 100 nm . The beam dimensions are given in Table 6.2.

Table 6.2 – *Beam dimensions of the loaded specimens.*

Test beam	Width (μm)	Thickness (μm)
A1	22.1	15.9
A2	21.8	13.2
A3	22.3	15.9
A4	22.7	19.1
A5	27.4	24.5
A6	28.6	25.3
A7	26.9	26.4
B1	30.3	5.3
B2	25.0	8.1
B3	24.2	8.7
B4	26.0	8.1

In the first set, the beams are loaded successively after each other and the stress is measured after each loading step. However, in the second set, each beam is loaded and the stress is monitored for a few days before loading the next beam. The stress measurement results are shown in Figure 6.14. To make the plots easier to understand, we plot the data of each set separately.

In what follows, we first report our observations followed by an interpretation.

After loading, the retardance is monitored for three weeks while the samples are inside a dry atmosphere of Nitrogen gas. The N_2 gas is 99.99% pure and contains very low concentrations of O_2 (< 50 ppm) and H_2O (< 30 ppm). During this first period (referred to as the ‘dry phase’ in Figure 6.14), a comparatively fast decay (up to 20 Mpa/day in some cases) is observed immediately after loading followed by a relatively stable stress state. This decay is particularly prominent in beams with more than 1 GPa stress. Around three weeks (indicated by the first dotted line), the N_2 flow is stopped and the samples are exposed to normal laboratory conditions (referred to as ‘wet phase’). In our laboratory, the average temperature is 22°C with a fluctuation of $\pm 1^\circ\text{C}$, while the average humidity is 50% with a fluctuation of $\pm 15\%$. As the samples are exposed to these conditions, a slight increase in stress is observed almost immediately (the next measurement is recorded nearly 17 hours after letting the ambient atmosphere flow inside the chamber). This increase in stress is independent of the number of laser-exposed patterns but rather appears to depend on the thickness (and hence, the overall laser-machined area) of the test beams as shown in Figure 6.15. After this point, further measurements are carried out under normal atmospheric conditions.

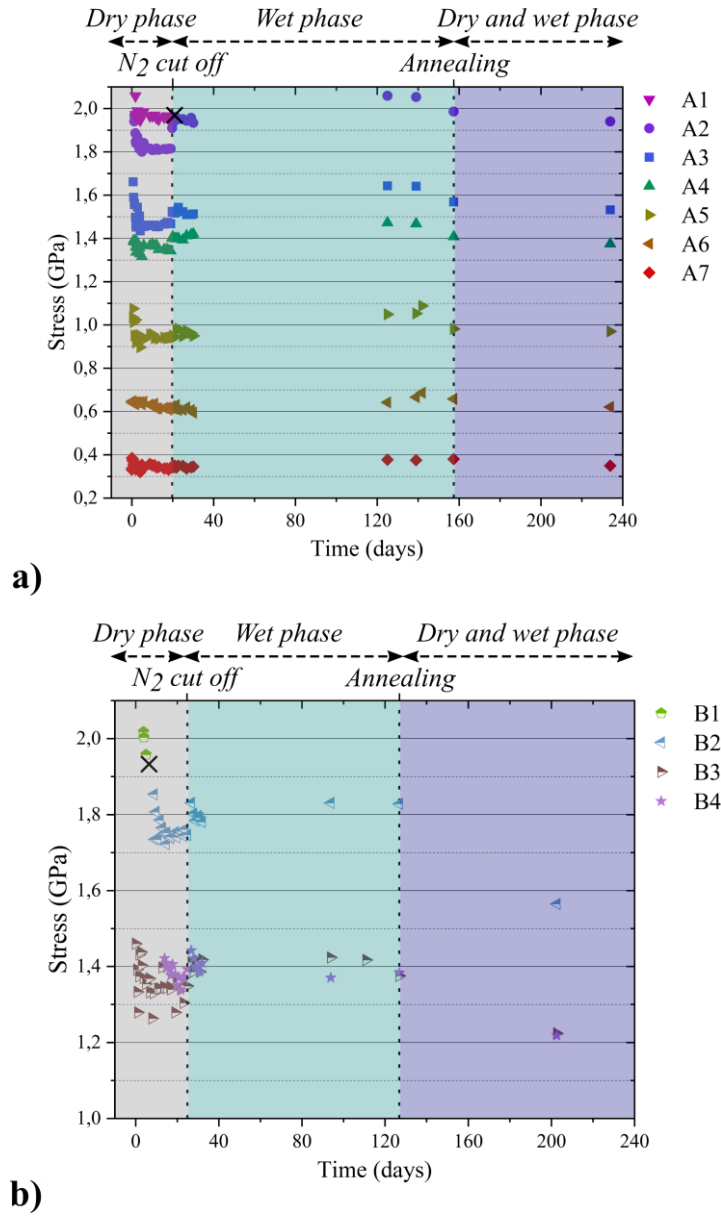


Figure 6.14 – a,b) Prolonged stress measurements on fused silica at room temperature and under dry and moist conditions. The first dotted line indicates the stopping of dry N₂ gas and exposure to ambient environment. The second dotted line marks low-temperature annealing carried out at 300 °C for 30 hours.

The removal of dry conditions is almost immediately followed by failure of the A1 specimen. Note that this specimen has the highest initial stress of more than 2 GPa. However, this failure occurs within the loading bar and not inside the test beam as shown in Figure 6.16.

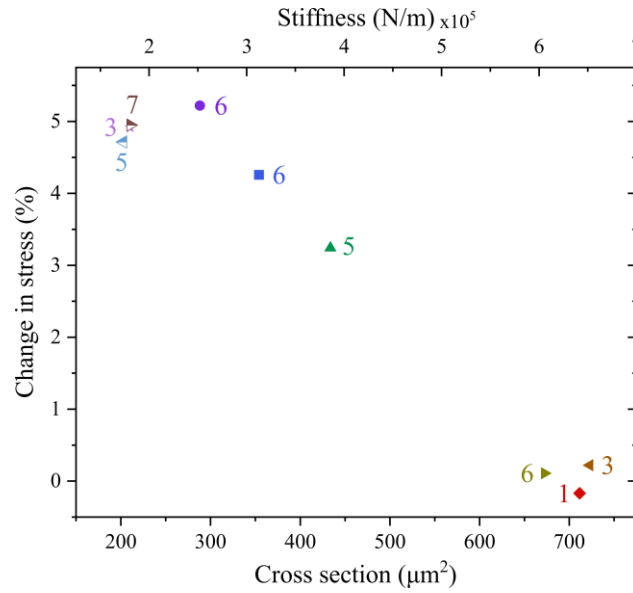


Figure 6.15 – Change in stress plotted against the cross-sectional area and stiffness of the test beams. The numbers beside each data point indicate the number of laser-written stressors.

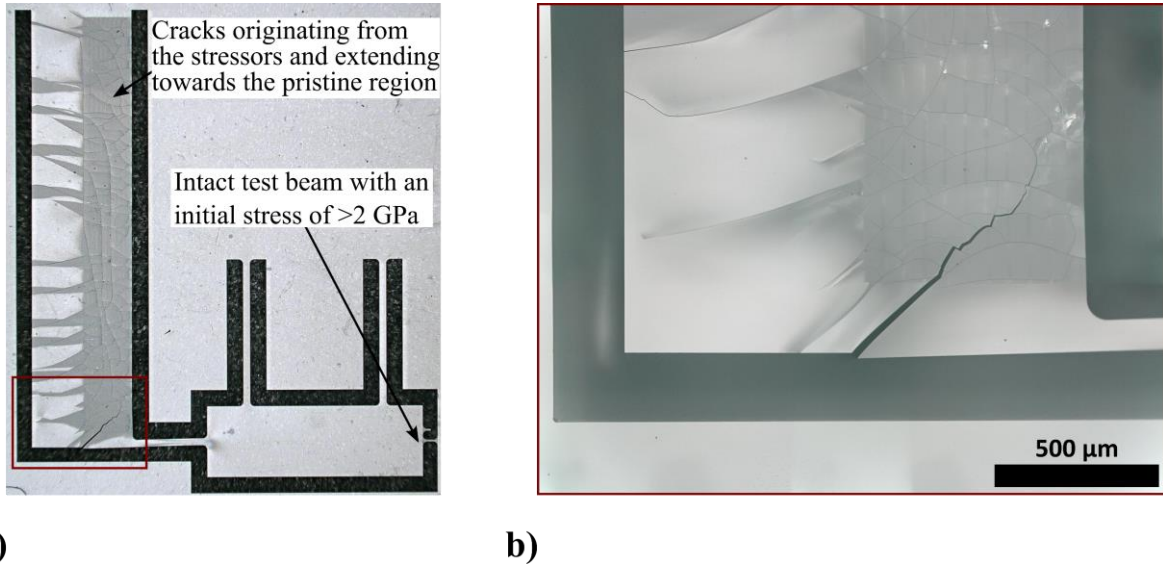


Figure 6.16 – a) An optical micrograph indicating the cracks initiated in the loading bar when exposed to an ambient humid environment. The cracks seem to originate within the modified region (with high stress) and propagate through the pristine material towards the sidewall. b) A high-magnification image of the boxed region indicated in (a).

To understand this increase in stress on exposure to moist conditions, we keep the beams in these conditions and observe them again after a prolonged period spanning almost 12 weeks. During this prolonged exposure to moist conditions, and like before, a further swell in stress is observed. At this point (indicated by the second dotted line in Figure 6.14), the samples are annealed at a low temperature of 300°C for 30 hours, and under a dry atmosphere of N₂ gas. The choice of this temperature is dictated by the fact that high-temperature annealing (above 600°C) is known to affect the volume expansion of laser-modified patterns [100], thus altering the loading conditions. However, at 300°C, no such effect is observed, yet the temperature is sufficiently high to cause desorption on the surface. After annealing, the samples are cooled down slowly at a rate of 1°C/min to avoid the buildup of additional stress due to fast quenching.

After annealing, the samples are put back in the chamber and under a dry atmosphere. During the transfer from the furnace to the environmental chamber, the samples are briefly exposed to the ambient atmosphere. As the transfer time is short (< 10 min, and thus negligible in comparison to the timescale of the dynamics reported above), we do not expect further adsorption to occur. Further measurements reveal a decline in stress in nearly all of the stressed beams. To understand the increase in stress upon exposure to a humid environment and the decay after annealing (while under a dry atmosphere), we re-expose the beams to humid conditions by cutting off the flow of nitrogen and letting atmospheric conditions fill the chamber. Since the stress levels showed an increase on earlier exposure to ambient conditions, we expect a similar trend. The beams are exposed for a longer duration than earlier before additional measurements are carried out. The measured stress however shows an opposite behavior. Unlike earlier, we observe a decay in stress. This is particularly substantial for the beams B2, B3, and B4. In Figure 6.14, this part of the measurement is referred to as ‘dry and wet phase’.

6.4.4 Stressed micro-tensile beam profile

As mentioned earlier, the loading process induces some parasitic bending. Although part of it can be corrected for, however, due to a time delay between modifications written near the bottom and top surfaces, some amount of out-of-plane bending is inevitable.

To measure the magnitude of this effect, a confocal measurement is carried out on the stressed beams and a height profile is recorded along their length and width (XY plane). The results are shown in Figure 6.17. For the first set of samples (thicker beams), the out-of-plane bending is relatively large as compared to the second set (thinner beams). This is true for stress levels above 1 GPa. At lower stress levels, the bending is reduced by more than 50%. On the other hand, the thin beams show low parasitic bending although they are all loaded above 1 GPa. The thickness of the beams directly affects their bending stiffness. Consequently, for similar stresses, one would expect smaller bending for thicker beams and larger bending for thinner beams unlike what is observed here. As such a measurement is not possible immediately after loading, it is unclear whether this difference was present initially (after loading) or appeared after exposure to humid conditions. Quantitatively, the maximum measured out-of-plane deformation is 1% ($2.5\ \mu\text{m}$ across a length of $>250\ \mu\text{m}$). Therefore, it has a negligible effect on the loading case.

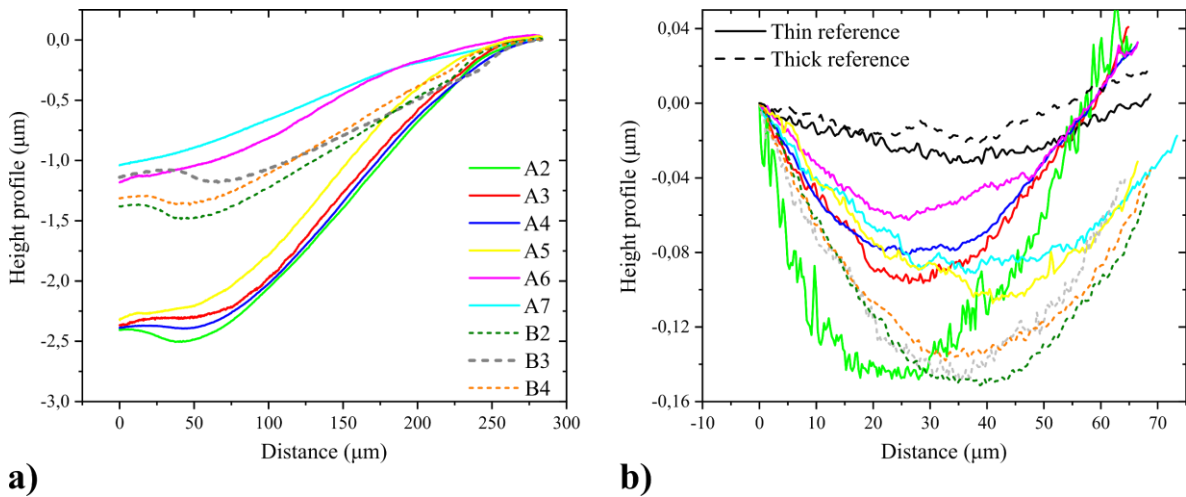


Figure 6.17 – a) Height profile recorded along the length of the loaded beams. For thicker beams, out-of-plane bending increases with increasing stress and nearly doubles for stresses exceeding 1 GPa. For thinner beams, the bending is unexpectedly low. b) Height profile recorded along the width of the beams and near the fixed end. The profile reveals a concave depression similar to a transverse compression expected in a beam when pulled longitudinally. The plot follows the same color mapping as in (a).

A line profile across the width (along Y-axis) of the beams indicates a concave depression near the top surface. As the beams are strained axially, a compression is expected along the transverse direction. According to finite element method (FEM) simulations and assuming a Poisson's ratio of 0.17, the depth of such a depression should be about 40 nm for existing stress levels. However, in some of the beams, the depression is nearly 150 nm deep. Wiederhorn et. al [177] had earlier reported bending of thin silica disks when exposed to water vapor at high temperature and vapor pressure.

6.5 Discussion and interpretation

At low temperature (< 250°C), the reaction of water with silica is believed to be governed by the following reaction:



The rate of this reaction is influenced by temperature, vapor pressure, and stress (the stress can be either residual or externally applied). Even though our measurements are carried out at room temperature conditions, the presence of high stress can accelerate the diffusion process. Roberts and Moulson [169] have previously suggested that the reaction in Equation 6.2 may take place at a detectable rate at room temperature if activated by sufficiently high stress. Furthermore, water diffuses differently depending on whether it is present in vapor form or as liquid water. In liquid form, its concentration in the glass increases rapidly reaching a saturation value. In vapor form, the concentration does not achieve a constant value but builds up with time eventually reaching a steady-state value.

The fabrication of our samples involves a two-step process, femtosecond direct laser writing followed by wet chemical etching in a solution of 1.25% (by volume) hydrofluoric acid. During etching, as there is prolonged contact with liquid water (~ 40 hours), it is plausible to expect a higher water content in the samples post this etching step. At the beginning of our experiment (dry phase), a rather fast relaxation is observed at stresses exceeding 1 GPa. As there is nearly no water present within the chamber, water present within the samples may promote stress relaxation. Fused silica is known to be permeable to helium [178] and hydrogen [179], however, the atomic size of nitrogen makes its penetration impossible. Therefore, the role of Nitrogen in relaxation can be ruled out.

In the micro-tensile tester, the primary stress is tensile in nature and occurs within the test beams. However, as shown in Figure 6.18, moderate compressive stress is also present in the region surrounding the stressors (region S_c). There, as the modified region undergoes expansion, compressive stress builds up in the surrounding pristine material. Similar compressive stress is also present in the flexure beams of the linear guidance, however, its magnitude is negligible in comparison. The presence of compressive stress on the pristine side of the loading bar may aid water solubility on that side (during the wet phase). In comparison, the tensile stress present on the modified side (region S_t) lowers water solubility. As a result, Young's modulus of the pristine region (S_c) reduces leading to a reduction in its stiffness. The adsorption of water causes the replacement of some bridging oxygen atoms, which are replaced by an Si-OH configuration. This leads to a reduction in tensile strength of the pristine region, thus promoting further bending of the loading bar. Since this bending occurs away from the micro-tensile beams, an additional tensile force acts on the beams leading to an increase in the measured stress. As water is present in vapor form, its concentration is expected to grow over time, furthering the stress increase according to this mechanism. This is corroborated by the increase observed during the prolonged exposure to such conditions – the region between the dotted lines in Figure 6.14.

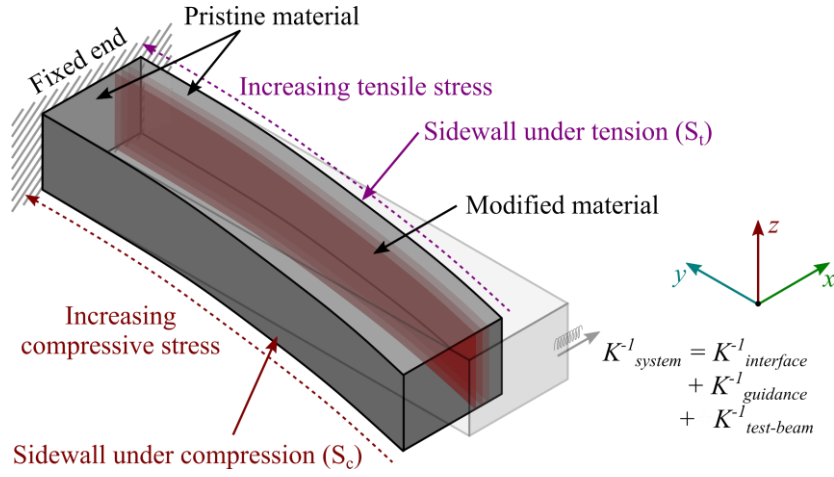


Figure 6.18 – A schematic of the loading bar showing different regions under compressive and tensile stress. The bi-morph-like loading bar consists of three main regions – a pristine region under compression (S_c), stressors, and a pristine region under tension (S_t). At its free end, the stiffness of the system (K_{system}) acts against the bending direction and is primarily dominated by the stiffness of the micro-tensile test beam.

Another event in support of this hypothesis is the failure observed in the A1 specimen. Although the highest magnitude of stress is present within the test beam, yet, on exposure to humid conditions, failure occurs within the loading bar instead. Surprisingly, all failures observed in our specimens (including the ones not reported here) occurred within the loading bar. This suggests that events occurring within the region under compression are dominant over those occurring within the stressed beams. To analyze this further, we follow the analytical model developed in Chapter 2 to quantitatively compare the stiffness of the instrument versus the stiffness of the test beam. As shown in Figure 6.19, the different stiffnesses are represented as springs in this analysis and arranged accordingly depending on whether they are connected in series or parallel. By computing the stiffness matrices of the different elastic elements and projecting their combined stiffness along X-axis at point O, we find out that $(K_{device})_{xx} \sim 6 \times 10^6$ N/m, which is an order of magnitude larger than the average stiffness of the test-beams (that varies between $2 \times 10^5 - 7 \times 10^5$ N/m)

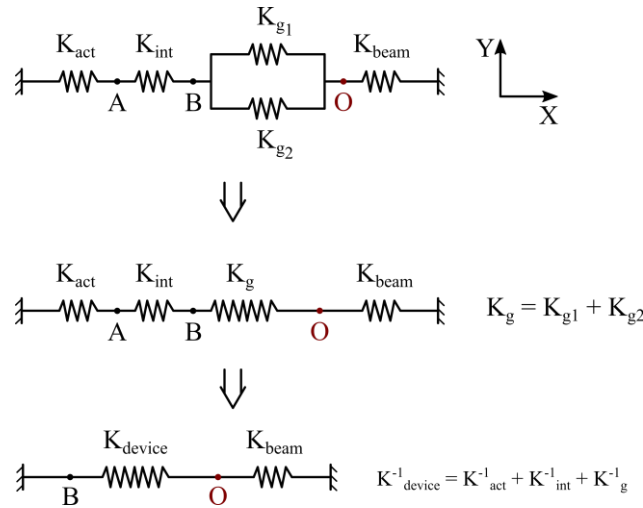


Figure 6.19 – Stiffness model of the tensile tester device. The different stiffnesses are represented as follows: K_{act} – stiffness of the actuator, K_{int} – stiffness of the flexible interface beam, K_{g1} , K_{g2} – stiffnesses of the guidance springs, K_{beam} – stiffness of the test beam, K_g – combined stiffness of the guidance springs, and K_{device} – total stiffness of the tensile tester instrument.

Water penetration in glass is known to increase its volume [166], [177]. If the expansion is constrained to occur, such as on the surface, compressive stresses develop. This further enhances water solubility (at low temperature) leading to additional compressive stresses. In such a case, the resultant outcome would also be an increase in stress in the test beams. Overall, a weakening of the pristine structure surrounding the loading bars or the generation of compressive surface stress will both promote further bending of the loading bar and lead to an increase in measured stress as observed in our experiments (at the start of the wet phase). In either case, such an increase should vary inversely with the cross-sectional area (or the stiffness) of the beams as corroborated by the data in Figure 6.15.

At high temperatures ($> 650^{\circ}\text{C}$) water mostly exists as silanol groups in silica, which are responsible for its volume expansion. At low temperatures ($< 250^{\circ}\text{C}$) water exists both as molecular water as well as in the form of hydroxide. Building upon our hypothesis that water adsorption could be a possible cause for the increase in stress, it is only logical to reverse the process through desorption. To do so, we choose a moderate annealing temperature of 300°C . Ideally, annealing at an elevated temperature would enhance the desorption of molecular water. This would however result in an ambiguity in our measurements due to the change in volume expansion of the stressors [102]. The removal of molecular water, particularly from the pristine part of the loading bar would, through a similar explanation, cause a decrease in the measured stress.

Post annealing, and when the beams are re-exposed to a humid environment (dry and wet phase), there is a rather small decrease in stress in nearly all of the loaded specimens. Of interest, however, are specimens B2, B3, and B4, which show a much larger decrease in the measured stress. The specimens B3 and B4 decay nearly by the same amount (11.1% and 11.9% respectively), whereas B2, with a higher stress level, decays by a larger amount (14.4%). On further inspection, these relaxed beams reveal formation of point-like defects in the stressed beams. These defects appear on the bottom surface of the beams, which is laser-exposed during the fabrication step, and thus has greater surface roughness than the pristine top surface. Furthermore, as shown in Figure 6.20a, the defects appear to be concentrated near the central part of the beam (with high stress) and almost disappear near the low-stress ends. It is though unclear how they are responsible for stress relaxation.

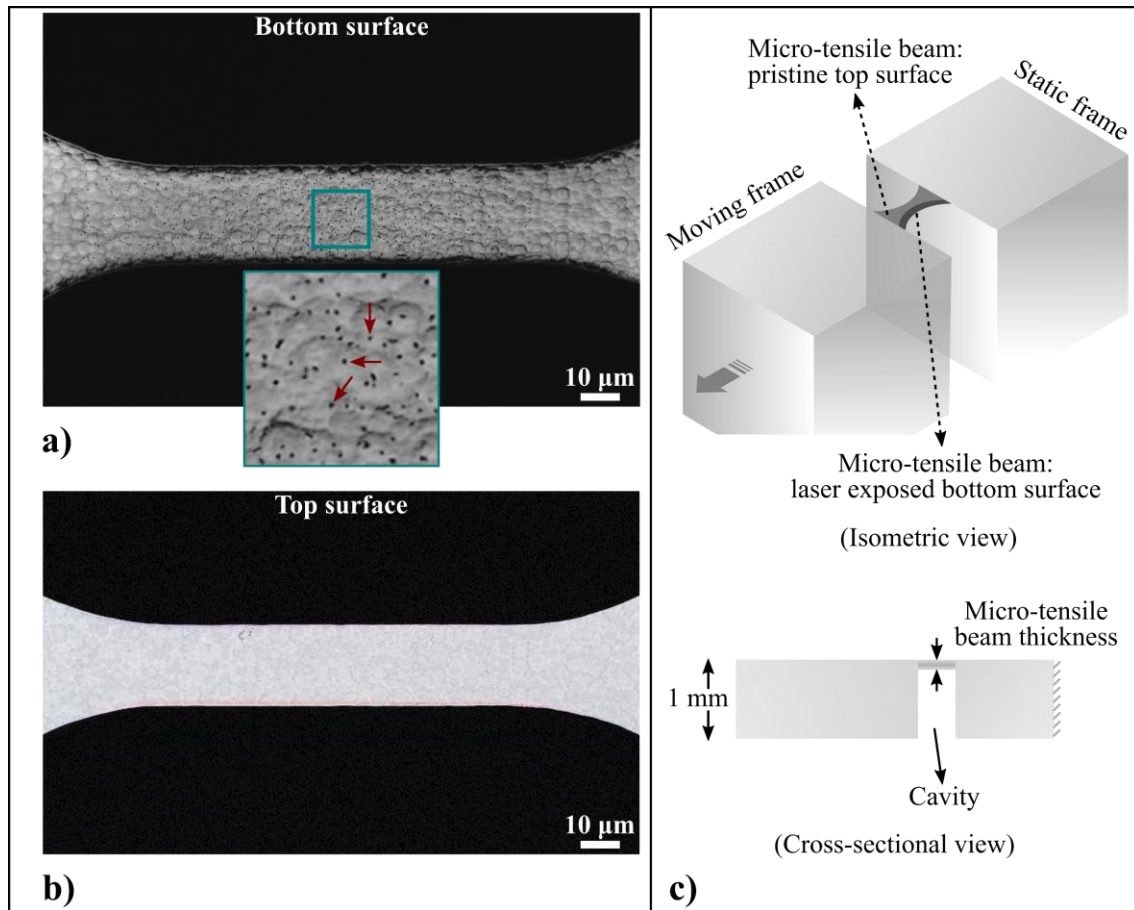


Figure 6.20 – a) An optical image showing point-like defects observed on the laser-machined bottom surface of one of the beams with highest stress relaxation. In the magnified inset, arrows are shown indicating some of the defects. The defects are concentrated in the middle part of the beam with high stress and disappear towards the low-stress ends. b) Optical image of the pristine top surface of the same beam. c) A 3D illustration highlighting the micro-tensile beam position within the tensile tester. On the bottom surface of the beam, material is removed during fabrication resulting in a cavity.

To validate our hypothesis that water intake during the etching step could be responsible for the relaxation observed initially, we fabricate a new sample with two tensile testers. After etching, this sample is annealed at 800°C for 300 hours to remove any water that might have penetrated the sample during the etching step of the fabrication process. After annealing, the sample is placed within the chamber with a flow of dry N₂ gas and loaded as before. The stress measurement results are shown in Figure 6.21.

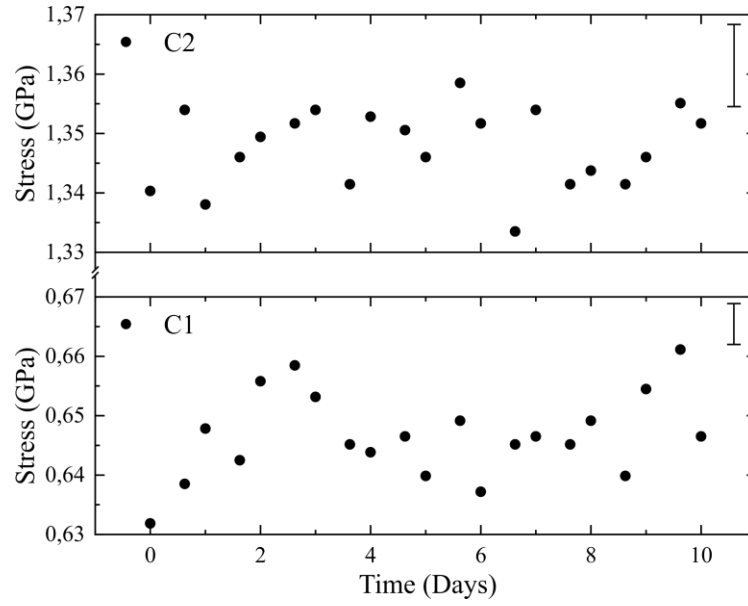


Figure 6.21 – Stress versus time measurements of an annealed sample. Post etching (1.25% HF) and before stress loading using femtosecond laser exposure, the sample is annealed at 800 °C for 300 hours to remove any water that might penetrate the sample during the 40-hour etching process. The measurements show a stable stress state unlike the fast initial decay observed for non-annealed samples. The error bars are analytical and do not include other sources of error such as uncertainties in the angle between σ and E , variation in measurement position over time, etc.

6.6 Summary

In what precedes, we have employed an innovative combination of methods to study the behavior of fused silica when subjected to a constant uniaxial tensile stress at room temperature and under various conditions of humidity. We have shown how flexure-based micro-devices together with photoelasticity measurements can be used to explore the mechanical behavior of glass at time-and-length scales that remain experimentally inaccessible otherwise [180]–[183].

Our measurements reveal that static tensile stress up to 1 GPa applied to the micro test-beam is stable in magnitude under a dry atmosphere as measured over a period exceeding a year. Above this critical level, and measured up to 2 GPa, we notice an initial relaxation of a few percent while maintaining the structural integrity of the test beams. The mechanism responsible for this observed relaxation is related to the instrument design, where a beam acting as the actuator is loaded in bending. We further show that this relaxation appears to be directly related to the manufacturing technique used to prepare the specimens, and can be efficiently suppressed via thermal annealing. In such samples that are subjected to high-temperature annealing before laser exposure, a stable stress level is observed for stresses below as well as above 1 GPa.

Chapter 7 Epilogue

This chapter abridges the important contributions of this thesis, discusses possible pathways for future research, and provides a brief insight into the current ongoing work. Overall, this work broaches a new regime of optical devices - monolithically or pseudo-monolithically fabricated in glass using femtosecond laser micromachining (FLM), merged with remote actuation principles based on material modification through non-linear absorption.

7.1 Summary

Broadly speaking, the work presented thus far can be categorized into three different genres – mechanical, optical, and materials. Below, we summarize these aspects separately.

- **Mechanical**

Flexures are somewhat ubiquitous in precision and micro-engineering. Unlike their mechanical counterparts, mobility is a direct consequence of material elasticity and deformation that occurs at the molecular level. As a result, joint-less, hysteresis-free ensembles can be realized, whose motion is insensitive to friction, wear, and assembly inaccuracies. Therefore, in most applications that require high precision, flexures and flexure-based motion stages play a pivotal role and are sometimes the only bearing choice that can deliver the requirements.

At the micro-scale, fabrication of flexures is challenging, especially for those with complex three-dimensional shapes. FLM not only allows for such miniaturization and shape versatility but has also ushered in totally novel possibilities – glass as a mechanical component in 3D manufacturing.

For the most part, the mechanical aspect of this work is captured in Chapter 2, although some parts are scattered through the rest of the thesis. In this chapter, we introduced several glass-based flexure mechanisms with various degrees of freedom (DOFs). Such mechanisms, designed for integration into optical circuits, can fulfill various functions, such as translation along a given axis, rotation about one or two axes, or a combination of both. The list therewith is by no means exhaustive and only describes some possible representative solutions. We also proposed some design rules necessary for any kinematic design.

As a technology, FLM offers a lot of design flexibility, not only in fabrication but also in motion actuation. The kinematic mechanisms proposed in this thesis do not require interfacing of an external actuator, but rather can be actuated remotely using the same laser. This allows further miniaturization by leveraging the flexure units themselves as actuators, as introduced in Section 2.4.2.

An analytical framework was also introduced to evaluate and optimize the performance of an assembly of flexures. Although most design optimization in this thesis is done through finite element method (FEM) simulations in Comsol Multiphysics, such a tool can discretize the influence of each parameter on the performance of the whole system and is useful for rapid optimization.

The experimental validation of the proposed mechanisms is distributed through the rest of the chapters. In Chapter 3, we demonstrated the remote center of rotation (RCC) mechanism that was bi-directionally actuated using two different pulse widths (Type I and Type II modifications). This was further improved in Chapter 4 where bi-directional motion was demonstrated using a single pulse width. Travel ranges up to 12 milliradians for out-of-plane and > 5 milliradians for in-plane rotation were demonstrated. Similarly, a linear guidance motion stage was also designed that was later deployed in a Fabry–Pérot (FP) cavity to tune the cavity length. In Chapter 6, we showcased its application as a micro-tensile tester to generate unprecedented stress levels in fused silica glass.

- **Optical**

Flexure-based guidance mechanisms have a high motion accuracy but often a small range of motion. To measure this experimentally is challenging. Although the problem can be simplified by observing the final state of the device, it provides very little insight into the actual motion path. In Chapter 3 (for example in Figure 3.8), although the final state of the device suggests that no motion has occurred along the degree of constraint (DOC), the experiments indicate otherwise. As such, the deformation needs to be measured in real-time to fully understand the behavior of a mechanism when actuated. To do so, a compact and portable experimental setup was built capable of measuring small angles with a resolution of $2\ \mu$ -radians. The setup relies on the flat focal plane property of an f-theta lens and allows in-situ monitoring during laser exposure.

In the context of non-contact actuation using femtosecond laser exposure, the range of motion not only depends on the kinematic design, but also on laser parameters such as pulse energy, pulse width, and deposited energy. An in-depth parameter study was presented in Chapter 3, which formed the basis for the rest of the experiments presented in this thesis.

In Chapter 4, we demonstrated a *system-level* integration of flexure kinematics by coupling a laser diode into a single-mode fiber using non-contact actuation methods. By combining two DOFs in a single substrate, and assisted by precision v-grooves, we showcased how femtosecond laser micromachining and non-contact actuation can be applied for the packaging of optical circuits.

At the end of Chapter 4, we discussed the potential applications of our methods. These methods, which can potentially provide a resolution in the sub-nanometer range, may not be economically viable in certain cases. For instance, in the example of fiber-coupled laser diode discussed there, the cost associated with laser-based repositioning may outweigh the gain achieved in terms of coupling efficiency. On the contrary, packaging alignment-sensitive optical devices, such as resonators or laser cavities, is not a straightforward task, and such devices can benefit if fabricated from a single monolith and later aligned using non-contact positioning.

In Chapter 5, we reported our progress towards a fully packaged fiber Fabry–Pérot (FFP) resonator. For the FFP cavity, an experimental setup was built to align the cavity fibers inside the glass chip. Later on, we demonstrated on-chip alignment of the cavity fibers using a piezoelectric scanner to tune the cavity length. Using the laser manufactured substrate, the alignment process was simplified thanks to pre-aligned grooves, which provided a high-precision pick-and-place alignment between the fibers.

- **Materials**

The materials aspect of this work is reported in Chapter 6. As a material, glass is the material of choice for numerous applications and its excellent properties have even pushed it at the forefront of largescale eternal data storage. Logically, a lot of effort has already been invested to understand its behavior in various conditions of temperature, stress, and humidity. A considerable amount of knowledge also exists regarding its permeation to different gases and response to a wide array of chemical agents.

However, in the currently available literature, very little is known regarding its behavior at room temperature. Most existing data are extrapolated from the measurements carried out at higher temperatures, vapor pressures, and stresses. The aging behavior of glass is almost immeasurable under normal conditions and possibly explains the lack of information therewith.

Besides its fundamental importance, understanding the stress relaxation phenomenon in glass, and fused silica in particular, are of crucial importance to this thesis. A substantial effort was devoted in this direction, and rigorous measurements were done and experimental data was collected over nearly eight months. A micro-tensile tester was used to produce controllable stress states in a micro-scale glass beam, and experimental data were obtained through retardance measurements. When stressed, fused silica's isotropic nature gives way to anisotropy in the stressed region, which can be probed using photoelasticity. To isolate stress-based effects, the experiments were performed in well-controlled conditions of temperature and humidity, and a mini environmental chamber was built for the same. Our results indicated a two-stage relaxation behavior – in dry conditions: a rapid relaxation followed by a stable plateau for stresses above 1 GPa and almost no relaxation for stresses below 1 GPa; in wet conditions: an immediate increase in stress upon exposure to a humid environment. Two types of annealing experiments were also done; the first experiments suggested that the increase in stress due to water adsorption can be reversed through prolonged heating at 300°C, while the second set of experiments indicated that the dry-phase relaxation can be suppressed by annealing the samples after etching and before loading. Overall, our measurements suggest that a critical stress level exists (~ 1 GPa) below which no relaxation seems to occur. At the same time, above this level and up to 2 GPa, although an initial relaxation does occur, the micro-scale beams can withstand such stresses in the presence or absence of humidity and do not show signs of failure. This is true even for observations carried out more than a year after initial loading.

7.2 Outlook

Some key pathways to improve upon the current work are:

- **Optimization of the writing process**

The non-contact repositioning methods rely on nanoscopic volume changes that happen inside the voxels written by the laser. To achieve a larger range of motion, as is often desired for most applications, multiple such voxels (hundreds and sometimes several thousand) are juxtaposed together. A considerable amount of time is consumed in this process, not just in writing the voxels but also in moving from one writing location to another. This can be further investigated and new exposure strategies can be explored to shrink the writing time. A major obstacle in the current method is the inertia of the motion stages used to translate the sample, which are limited in both speed and acceleration. Galvanometric f- θ scan lenses can help overcome this barrier, and the focal spot can instead be scanned on a stationary sample. Modern scanners can scan at very high speeds with frequencies extending up to tens of kilohertz (kHz). This can potentially reduce the writing time down to a few seconds, and further the promise of these methods for industrial use.

The cracking of the laser-affected zone was investigated in Chapter 6, although a conclusion could not be reached. Although preliminary experiments suggest that longer zones appeared to be more stable in general and were subsequently used in the experiments, exploring the role of pulse-width and repetition rate can provide more insight into the problem.

- **Feedback assisted automated alignment**

In all repositioning experiments reported in this thesis, the alignment algorithm is implemented manually. In other words, the complete process is user-controlled, and patterns are written by monitoring an output metric such as power. However, there is potential for more work here. A computer-regulated local search algorithm

can be implemented, in which, the objective function drives the alignment process. A challenging problem in such an implementation may be: in the two-fiber repositioning example shown in Chapter 5, a decrease in the output signal (power) points to two possibilities – either a local maximum has been crossed and the system needs to reverse back to it or a parasitic motion has caused such a decrease. This is especially evident in Figure 5.12 (region C_1), where the decrease in coupling efficiency is caused by a parasitic motion. In this case, a search algorithm will suggest inscribing near the opposite sidewall, which will however lead to a further decrease by pushing the fibers away from each other. Therefore, an intelligent distinction needs to be made in such an implementation. Furthermore, in the case of multiple local maxima, as shown in Figure 7.1, a simple hill-climbing algorithm may converge on a local maximum instead of the global maximum. In such a case, random-search methods such as simulated annealing and stochastic hill climbing can be implemented.

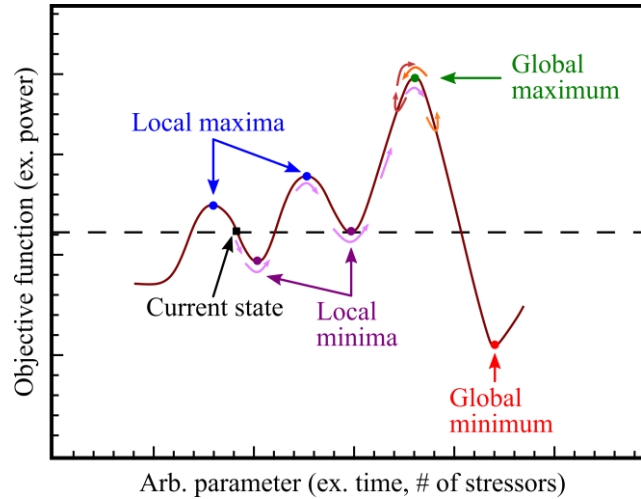


Figure 7.1 – An illustration of a local search algorithm to find the maximum of a given function.

- **Inhibition of water adsorption through surface coatings**

The stress relaxation study has revealed some interesting phenomena while opening a plethora of new questions at the same time. It will be interesting to experimentally observe the effect of a water-resistant coating (silicon carbide (SiC), Teflon, Mylar, etc.) to inhibit the surface adsorption of molecular water. Furthermore, the stress levels achievable with the micro-tensile tester can provide further insight into the role of stress during chemical etching. It has been experimentally shown before that an optimal deposited energy exists for the fastest etching rate, strongly suggesting that stress-induced effects play a role in the process. The micro-tensile tester facilitates such a study and because of its compact size, multiple specimens can be tested at the same time.

- **Implementation of topology optimization techniques**

Although not implemented in this work, topology optimization is a powerful tool for the synthesis of optimal compliant mechanisms fulfilling a given function. One can, for instance, benefit from the works of topology optimization (TopOpt, <https://www.topopt.mek.dtu.dk>) group at Denmark Technical University and their open-source software for shape optimization of compliant mechanisms. Their software code [184]–[186] can be used to further optimize the material distribution of various mechanisms reported in this thesis. Furthermore, an inverse design approach can also be implemented, in which topology optimization techniques can be used to design photonic systems [124].

Annex A: Bimorph strain validation

Here, we reproduce some of the previous work carried out in our research group. In these works, Equation 3.3 was validated in the case of the laser-exposed bimorph element. A comparison was made between analytical values as calculated using the Stoney equation and those predicted using FEM simulations and experimental data.

In Figure A.1 [102], Equation 3.3 is applied in the case where the size of the laser-affected region is comparable to the size of the cantilever. In Figure A.2 [129], the equation is slightly modified and applied to the case of a smaller laser-affected region. In this case, the strain differs by nearly 18% when compared to what is predicted by Equation 3.3.

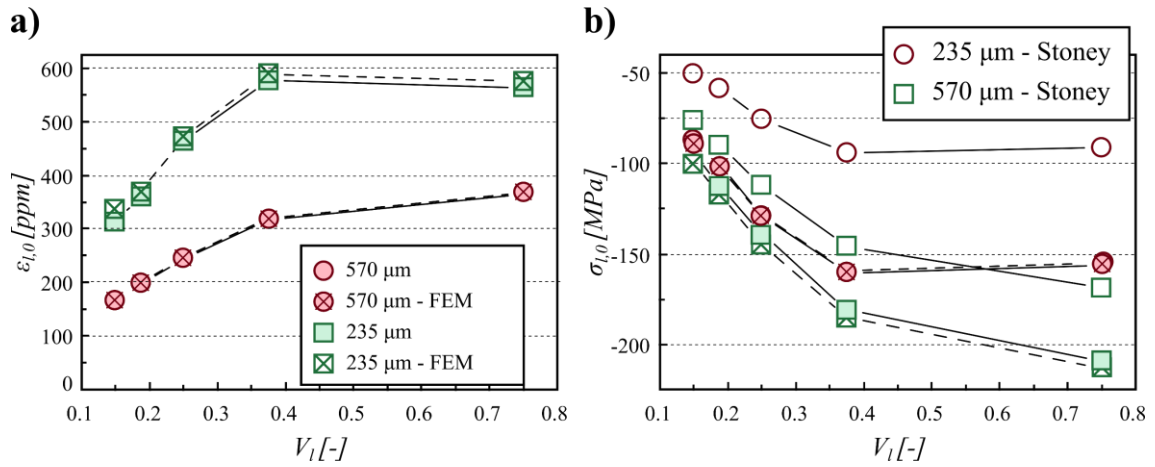


Figure A.1 – A comparison between FEM simulation and analytical estimation (Equation 3.3) on the a) average strain and b) average stress [102]. In (b), a comparison is also made with the Stoney equation.

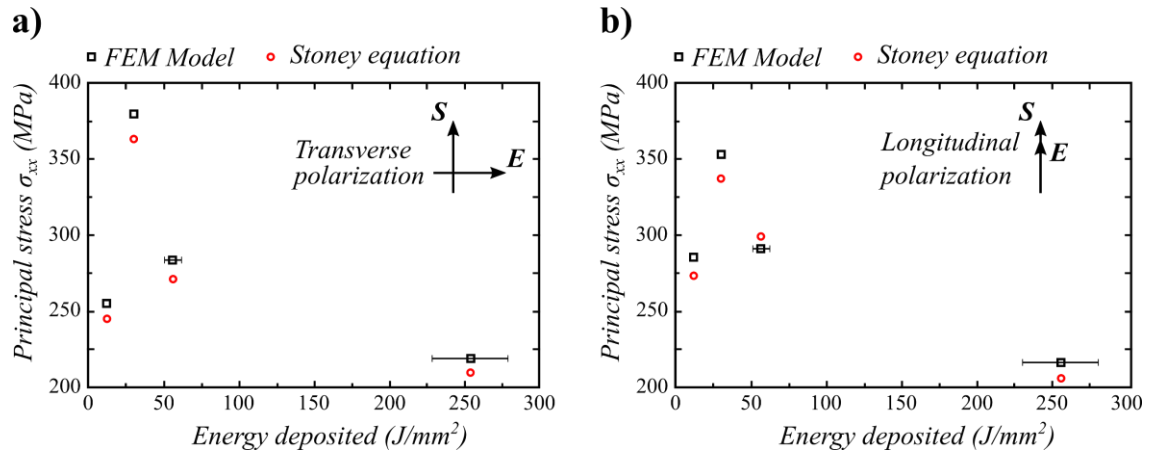


Figure A.2 – A comparison between FEM simulations and discrete model using Stoney equation for stress as a function of deposited energy in the case of a) polarization perpendicular to writing direction, and b) polarization parallel to writing direction [129].

Bibliography

- [1] DiamondSA, “Method for centering an optical fiber in an optical fiber end piece and an optical fiber end piece produced according to this method,” European patent, EP0058172B1, 1985.
- [2] M. Graf, “Active alignment process reduces fiber-core offsets,” *Laser Focus World*, 1996.
- [3] R. Matthey, L. Stauffer, G. Mileti, P. Giaccari, A. Pollini, and L. Balet, “Assembly Technique for Miniaturized Optical Devices: Towards Space Qualification,” in *Proc. SPIE 10564, International Conference on Space Optics — ICSO 2012*, 2017, vol. 10564, pp. 105643D1-105643D6.
- [4] M. Leers *et al.*, “Highly precise and robust packaging of optical components,” 2012.
- [5] M. Chwalla *et al.*, “Design and construction of an optical test bed for LISA imaging systems and tilt-to-length coupling,” *Class. Quantum Gravity*, vol. 33, no. 24, pp. 245015–245029, 2016.
- [6] E. J. Elliffe *et al.*, “Hydroxide-catalysis bonding for stable optical systems for space,” *Class. Quantum Gravity*, vol. 22, pp. S257–S267, 2005.
- [7] D.-H. Gwo, “Ultra Precision and Reliable Bonding Method,” U.S. patent 6,284,085 B1, 2001.
- [8] C. J. Killow *et al.*, “Construction of rugged, ultrastable optical assemblies with optical component alignment at the few microradian level,” *Appl. Opt.*, vol. 52, no. 2, pp. 177–181, 2013.
- [9] D. I. Robertson, E. D. Fitzsimons, C. J. Killow, M. Perreux-Loyd, and H. Ward, “Automated precision alignment of optical components for hydroxide catalysis bonding,” *Opt. Express*, vol. 26, no. 22, pp. 28323–28334, 2018.
- [10] S. Ressel *et al.*, “Ultrastable assembly and integration technology for ground- and space-based optical systems,” *Appl. Opt.*, vol. 49, no. 22, pp. 4296–4303, 2010.
- [11] S. Kulkarni *et al.*, “Ultrastable optical components using adjustable commercial mirror mounts anchored in a ULE spacer,” *Appl. Opt.*, vol. 59, no. 23, 2020.
- [12] J. Magee, K. G. Watkins, and W. M. Steen, “Advances in laser forming,” *J. Laser Appl.*, vol. 10, pp. 235–246, 1998.
- [13] G. Folkersma, G. Römer, D. Brouwer, and B. Huis in ’t Veld, “In-plane laser forming for high precision alignment,” *Opt. Eng.*, vol. 53, no. 12, pp. 126105–126116, 2014.
- [14] Y. Shi, H. Shen, Z. Yao, and J. Hu, “Temperature gradient mechanism in laser forming of thin plates,” *Opt. Laser Technol.*, vol. 39, no. 4, pp. 858–863, 2007.
- [15] R. Zou *et al.*, “Adaptive laser shock micro-forming for MEMS device applications,” *Opt. Express*, vol. 25, no. 4, pp. 3875–3883, 2017.
- [16] Z. Shen, C. Gu, H. Liu, and X. Wang, “An experimental study of overlapping laser shock micro-adjustment using a pulsed Nd:YAG laser,” *Opt. Laser Technol.*, vol. 54, pp. 110–119, 2013.
- [17] M. Dirscherl, G. Esser, and M. Schmidt, “Ultrashort Pulse Laser Bending,” *J. Laser Micro/Nanoengineering*, vol. 1, no. 1, pp. 54–60, 2006.
- [18] P. Bechtold, S. Roth, and M. Schmidt, “Analysis and application of micro shockwave adjustment using ultrashort laser pulses,” *ICALEO*, vol. 1124, 2009.
- [19] D. L. Baughman, “An overview of peen forming technology,” *Proc. 2nd Int. Conf. Shot Peen.*

Chicago, USA, pp. 28–33, 1984.

- [20] T. H. Maiman, “Stimulated Optical Radiation in Ruby,” *Nature*, vol. 187, pp. 493–494, 1960.
- [21] D. Strickland and G. Mourou, “Compression of amplified chirped optical pulses,” *Opt. Commun.*, vol. 56, no. 3, pp. 219–221, 1985.
- [22] R. Srinivasan, E. Sutcliffe, and B. Braren, “Ablation and etching of polymethylmethacrylate by very short (160 fs) ultraviolet (308 nm) laser pulses,” *Appl. Phys. Lett.*, vol. 51, pp. 1285–1287, 1987.
- [23] S. Küper and M. Stuke, “Femtosecond uv Excimer Laser Ablation,” *Appl. Phys. B*, vol. 44, pp. 199–204, 1987.
- [24] D. Du, X. Liu, G. Korn, J. Squier, and G. Morou, “Laser-induced breakdown by impact ionization in SiO₂ with pulse widths from 7 ns to 150 fs,” *Appl. Phys. Lett.*, vol. 64, pp. 3071–3073, 1994.
- [25] B. C. Stuart, M. D. Feit, A. M. Rubenchik, B. W. Shore, and M. D. Perry, “Laser-induced Damage in Dielectrics with Nanosecond to Subpicosecond Pulses,” *Phys. Rev. Lett.*, vol. 74, no. 12, pp. 2248–2251, 1995.
- [26] B. N. Chichkov, C. Momma, S. Nolte, F. von Alvensleben, and A. Tünnermann, “Femtosecond, picosecond and nanosecond laser ablation of solids,” *Appl. Phys. A*, vol. 63, pp. 109–115, 1996.
- [27] C. B. Schaffer, J. F. García, and E. Mazur, “Bulk heating of transparent materials using a high-repetition-rate femtosecond laser,” *Appl. Phys. A Mater. Sci. Process.*, 2003.
- [28] S. Eaton *et al.*, “Heat accumulation effects in femtosecond laser-written waveguides with variable repetition rate,” *Opt. Express*, vol. 13, no. 12, pp. 4708–4716, 2005.
- [29] C. Corbari, A. Champion, M. Gecevičius, M. Beresna, Y. Bellouard, and P. G. Kazansky, “Femtosecond versus picosecond laser machining of nano-gratings and micro-channels in silica glass,” *Opt. Express*, vol. 21, no. 4, pp. 3946–3958, 2013.
- [30] C. Hnatovsky *et al.*, “Pulse duration dependence of femtosecond-laser-fabricated nanogratings in fused silica,” *Appl. Phys. Lett.*, vol. 87, no. 1, pp. 014104–014106, 2005.
- [31] R. Taylor, C. Hnatovsky, and E. Simova, “Applications of femtosecond laser induced self-organized planar nanocracks inside fused silica glass,” *Laser Photonics Rev.*, vol. 2, no. 1–2, pp. 26–46, 2008.
- [32] K. M. Davis, K. Miura, N. Sugimoto, and K. Hirao, “Writing waveguides in glass with a femtosecond laser,” *Opt. Lett.*, vol. 21, pp. 1729–1731, 1996.
- [33] K. Miura, J. Qiu, H. Inouye, T. Mitsuyu, and K. Hirao, “Photowritten optical waveguides in various glasses with ultrashort pulse laser,” *Appl. Phys. Lett.*, vol. 71, pp. 3329–3331, 1997.
- [34] H.-B. Sun, S. Juodkazis, M. Watanabe, S. Matsuo, H. Misawa, and J. Nishii, “Generation and Recombination of Defects in Vitreous Silica Induced by Irradiation with a Near-Infrared Femtosecond Laser,” *J. Phys. Chem. B*, vol. 104, pp. 3450–3455, 2000.
- [35] Y. Bellouard, E. Barthel, A. A. Said, M. Dugan, and P. Bado, “Scanning thermal microscopy and Raman analysis of bulk fused silica exposed to low-energy femtosecond laser pulses,” *Opt. Express*, vol. 16, no. 24, pp. 19520–19534, 2008.
- [36] Y. Bellouard, J. Dugan, A. A. Said, and P. Bado, “Thermal conductivity contrast measurement of Fused Silica exposed to low-energy femtosecond laser pulses,” *Appl. Phys. Lett.*, vol. 89, pp. 161911–161913, 2006.
- [37] J. W. Chan, T. Huser, S. Risbud, and D. M. Krol, “Structural changes in fused silica after exposure to focused femtosecond laser pulses,” *Opt. Lett.*, vol. 26, no. 21, pp. 1726–1728, 2001.

- [38] Y. Bellouard, T. Colomb, C. Depeursinge, M. Dugan, A. A. Said, and P. Bado, “Nanoindentation and birefringence measurements on fused silica specimen exposed to low-energy femtosecond pulses,” *Opt. Express*, vol. 14, no. 18, pp. 8360–8366, 2006.
- [39] Y. Sikorski, A. A. Said, P. Bado, R. Maynard, C. Florea, and K. A. Winick, “Optical waveguide amplifier in Nd-doped glass written with near-IR femtosecond laser pulses,” *Electron. Lett.*, vol. 36, no. 3, pp. 226–227, 2000.
- [40] K. Minoshima, A. M. Kowalewicz, I. Hartl, E. P. Ippen, and J. G. Fujimoto, “Photonic device fabrication in glass by use of nonlinear materials processing with a femtosecond laser oscillator,” *Opt. Lett.*, vol. 26, no. 19, pp. 1516–1518, 2001.
- [41] P. Bado, A. A. Said, M. Dugan, T. S. Sosnowski, and S. Wright, “Dramatic Improvements in Waveguide Manufacturing with Femtosecond Lasers,” *Proc. 18th Annu. Natl. Fiber Opt. Eng. Conf.*, vol. 2, pp. 1153–1158, 2002.
- [42] G. Cerullo *et al.*, “Femtosecond micromachining of symmetric waveguides at 1.5 micron by astigmatic beam focusing,” *Opt. Lett.*, vol. 27, no. 21, pp. 1938–1940, 2002.
- [43] S. Nolte, M. Will, J. Burghoff, and A. Tuennermann, “Femtosecond waveguide writing: a new avenue to three-dimensional integrated,” *Appl. Phys. A*, vol. 77, pp. 109–111, 2003.
- [44] R. Osellame *et al.*, “Optical waveguide writing with a diode-pumped femtosecond oscillator,” *Opt. Lett.*, vol. 29, no. 16, pp. 1900–1902, 2004.
- [45] M. Ams, G. D. Marshall, D. J. Spence, and M. J. Withford, “Slit beam shaping method for femtosecond laser direct-write fabrication of symmetric waveguides in bulk glasses,” *Opt. Express*, vol. 13, no. 15, pp. 5676–5681, 2005.
- [46] R. R. Thomson *et al.*, “Ultrafast-laser inscription of a three dimensional fan-out device for multicore fiber coupling applications,” *Opt. Express*, vol. 15, no. 18, pp. 11691–11697, 2007.
- [47] R. R. Thomson *et al.*, “Active waveguide fabrication in erbium- doped oxyfluoride silicate glass using femtosecond pulses,” *Appl. Phys. Lett.*, vol. 87, pp. 121102–121104, 2005.
- [48] A. A. Said, M. A. Dugan, T. Sosnowski, and P. Bado, “Waveguide fabrication methods and devices,” United States Patent, US 7,294,454 B1, 2007.
- [49] R. R. Thomson, T. A. Birks, A. K. Kar, and J. Bland-Hawthorn, “Ultrafast laser inscription of an integrated photonic lantern,” *Opt. Express*, vol. 19, no. 6, pp. 5698–5705, 2011.
- [50] T. A. Birks, I. Gris-Sánchez, S. Yerolatsitis, S. G. Leon-Saval, and R. R. Thomson, “The photonic lantern,” *Adv. Opt. Photonics*, vol. 7, pp. 107–167, 2015.
- [51] G. D. Marshall *et al.*, “Laser written waveguide photonic quantum circuits,” *Opt. Express*, vol. 17, no. 15, pp. 12546–12554, 2009.
- [52] L. Sansoni *et al.*, “Polarization Entangled State Measurement on a Chip,” *Phys. Rev. Lett.*, vol. 105, no. 20, pp. 200503–200506, 2010.
- [53] G. Corrielli *et al.*, “Rotated waveplates in integrated waveguide optics,” *Nat. Commun.*, vol. 5, 2014.
- [54] R. Heilmann, R. Keil, M. Gräfe, S. Nolte, and A. Szameit, “Ultraprecise phase manipulation in integrated photonic quantum circuits with generalized directional couplers,” *Appl. Phys. Lett.*, vol. 105, pp. 061111–061115, 2014.
- [55] T. Meany *et al.*, “Laser written circuits for quantum photonics,” *Laser Photonics Rev.*, vol. 9, no. 4, pp. 363–384, 2015.
- [56] C. A. Antón *et al.*, “Interfacing scalable photonic platforms: solid-state based multi-photon

interference in a reconfigurable glass chip,” *Optica*, vol. 6, no. 12, pp. 1471–1477, 2019.

- [57] Y. Bellouard, A. Said, M. Dugan, and P. Bado, “Monolithic Three-Dimensional Integration of Micro-Fluidic Channels and Optical Waveguides in Fused Silica,” *MRS Proc.*, vol. 782, p. A3.2, 2003.
- [58] A. A. Said *et al.*, “Manufacturing by laser direct-write of three-dimensional devices containing optical and microfluidic networks,” *Proc. SPIE - Int. Soc. Opt. Eng.*, vol. 5339, pp. 194–204, 2004.
- [59] R. M. Vazquez, R. Osellame, D. Nolli, and C. Dongre, “Integration of femtosecond laser written optical waveguides in a lab-on-chip,” *Lab Chip*, vol. 9, pp. 91–96, 2009.
- [60] R. Osellame *et al.*, “Integrated optical sensing in a lab-on-chip by femtosecond laser written waveguides,” *Conf. Lasers Electro-Optics 2008 Conf. Quantum Electron. Laser Sci.*, pp. 1–2, 2008.
- [61] F. Madani-Grasset and Y. Bellouard, “Femtosecond laser micromachining of fused silica molds,” *Opt. Express*, vol. 18, no. 21, pp. 21826–21840, 2010.
- [62] Y. Bellouard *et al.*, “The Femtoprint Project,” *J. Laser Micro/Nanoengineering*, vol. 7, no. 1, pp. 1–10, 2012.
- [63] L. Borasi *et al.*, “3D metal freeform micromanufacturing,” *J. Manuf. Process.*, vol. 68, pp. 867–876, 2021.
- [64] L. Sudrie, M. Franco, B. Prade, and A. Mysyrowicz, “Study of damage in fused silica induced by ultra-short IR laser pulses,” *Opt. Commun.*, vol. 191, no. 3–6, pp. 333–339, 2001.
- [65] P. G. Kazansky, H. Inouye, T. Mitsuyu, K. Miura, J. Qiu, and K. Hirao, “Anomalous Anisotropic Light Scattering in Ge-Doped Silica Glass,” *Phys. Rev. Lett.*, vol. 82, no. 10, pp. 2199–2202, 1999.
- [66] J. D. Mills, P. G. Kazansky, E. Bricchi, and J. J. Baumberg, “Embedded anisotropic microreflectors by femtosecond-laser nanomachining,” *Appl. Phys. Lett.*, vol. 81, no. 2, pp. 196–198, 2002.
- [67] Y. Shimotsuma, P. G. Kazansky, J. Qiu, and K. Hirao, “Self-Organized Nanogratings in Glass Irradiated by Ultrashort Light Pulses,” *Phys. Rev. Lett.*, vol. 91, no. 24, pp. 247405–24708, 2003.
- [68] E. Bricchi, B. G. Klappauf, and P. G. Kazansky, “Form birefringence and negative index change created by femtosecond direct writing in transparent materials,” *Opt. Lett.*, vol. 29, no. 1, pp. 119–121, 2004.
- [69] E. N. Glezer *et al.*, “Three-dimensional optical storage inside transparent materials,” *Opt. Lett.*, vol. 21, no. 24, pp. 2023–2025, 1996.
- [70] E. N. Glezer and E. Mazur, “Ultrafast-laser driven micro-explosions in transparent materials,” *Appl. Phys. Lett.*, vol. 71, pp. 882–884, 1997.
- [71] J. Zhang, M. Gecevičius, M. Beresna, and P. G. Kazansky, “Seemingly Unlimited Lifetime Data Storage in Nanostructured Glass,” *Phys. Rev. Lett.*, vol. 112, pp. 033901–033905, 2014.
- [72] Y. Kondo, J. Qiu, T. Mitsuyu, K. Hirao, and T. Yoko, “Three-Dimensional Microdrilling of Glass by Multiphoton Process and Chemical Etching,” *Japanese J. Appl. Phys. Three-Dimensional*, vol. 38, pp. L1146–L1148, 1999.
- [73] A. Marcinkevičius *et al.*, “Femtosecond laser-assisted three-dimensional microfabrication in silica,” *Opt. Lett.*, vol. 26, no. 5, pp. 277–279, 2001.
- [74] Y. Bellouard, A. Said, M. Dugan, and P. Bado, “Fabrication of high-aspect ratio , micro-fluidic channels and tunnels using femtosecond laser pulses and chemical etching,” *Opt. Express*, vol. 12, no. 10, pp. 2120–2129, 2004.
- [75] C. Hnatovsky *et al.*, “Fabrication of microchannels in glass using focused femtosecond laser radiation

and selective chemical etching,” *Appl. Phys. A*, vol. 84, pp. 47–61, 2006.

- [76] S. Kiyama, S. Matsuo, S. Hashimoto, and Y. Morihira, “Examination of Etching Agent and Etching Mechanism on Femtosecond Laser Microfabrication of Channels Inside Vitreous Silica Substrates,” *J. Phys. Chem. C*, vol. 113, pp. 11560–11566, 2009.
- [77] M. Hermans, J. Gottmann, and F. Riedel, “Selective , Laser-Induced Etching of Fused Silica at High Scan-Speeds Using KOH,” *J. Laser Micro/Nanoengineering*, vol. 9, no. 2, pp. 126–131, 2014.
- [78] E. Casamenti, S. Pollonghini, and Y. Bellouard, “Few pulses femtosecond laser exposure for high efficiency 3D glass micromachining,” *Opt. Express*, 2021, [Online]. Available: <https://doi.org/10.1364/OE.435163>.
- [79] C. Hnatovsky, R. S. Taylor, E. Simova, V. R. Bhardwaj, D. M. Rayner, and P. B. Corkum, “Polarization-selective etching in femtosecond laser-assisted microfluidic channel fabrication in fused silica,” *Opt. Lett.*, vol. 30, no. 14, pp. 1867–1869, 2005.
- [80] Y. Cheng *et al.*, “Three-dimensional micro-optical components embedded in photosensitive glass by a femtosecond laser,” *Opt. Lett.*, vol. 28, no. 13, pp. 1144–1146, 2003.
- [81] V. Tielen and Y. Bellouard, “Three-Dimensional Glass Monolithic Micro-Flexure Fabricated by Femtosecond Laser Exposure and Chemical Etching,” *Micromachines*, vol. 5, pp. 697–710, 2014.
- [82] A. Schaap, T. Rohrlack, and Y. Bellouard, “Optical classification of algae species with a glass lab-on-a-chip,” *Lab Chip*, vol. 12, pp. 1527–1532, 2012.
- [83] Y. Bellouard, A. A. Said, and P. Bado, “Integrating optics and micro-mechanics in a single substrate: a step toward monolithic integration in fused silica,” *Opt. Express*, vol. 13, no. 17, pp. 6635–6644, 2005.
- [84] T. Yang and Y. Bellouard, “Monolithic transparent 3D dielectrophoretic micro-actuator fabricated by femtosecond laser,” *J. Micromech. Microeng.*, vol. 25, pp. 105009–105016, 2015.
- [85] M. Zanaty *et al.*, “Programmable Multistable Mechanisms for Safe Surgical Puncturing,” *J. Med. Device.*, vol. 13, pp. 021002–021011, 2019.
- [86] M. Lancry, B. Poumellec, J. Canning, K. Cook, J.-C. Poulin, and F. Brisset, “Ultrafast nanoporous silica formation driven by femtosecond laser irradiation,” *Laser Photonics Rev.*, vol. 7, no. 6, pp. 953–962, 2013.
- [87] W. Yang, E. Bricchi, P. G. Kazansky, J. Bovatsek, and A. Y. Arai, “Self-assembled periodic sub-wavelength structures by femtosecond laser direct writing,” *Opt. Express*, vol. 14, no. 21, pp. 10117–10124, 2006.
- [88] E. Bricchi, J. D. Mills, P. G. Kazansky, B. G. Klappauf, and J. J. Baumberg, “Birefringent Fresnel zone plates in silica fabricated by femtosecond laser machining,” *Opt. Lett.*, vol. 27, no. 24, pp. 2200–2202, 2002.
- [89] W. Watanabe, D. Kuroda, K. Itoh, and J. Nishii, “Fabrication of Fresnel zone plate embedded in silica glass by femtosecond laser pulses,” *Opt. Express*, vol. 10, no. 19, pp. 978–983, 2002.
- [90] M. Beresna and P. G. Kazansky, “Polarization diffraction grating produced by femtosecond laser nanostructuring in glass,” *Opt. Lett.*, vol. 35, no. 10, pp. 1662–1664, 2010.
- [91] H. Zhang, S. M. Eaton, J. Li, and P. R. Herman, “Femtosecond laser direct writing of multiwavelength Bragg grating waveguides in glass,” *Opt. Lett.*, vol. 31, no. 23, pp. 3495–3497, 2006.
- [92] M. Beresna, M. Gecevičius, P. G. Kazansky, and T. Gertus, “Radially polarized optical vortex converter created by femtosecond laser nanostructuring of glass,” *Appl. Phys. Lett.*, vol. 98, no. 20,

pp. 201101–201103, 2011.

- [93] J. Zhang, A. Čerkauskaitė, R. Drevinskas, A. Patel, and M. Beresna, “Eternal 5D data storage by ultrafast laser writing in glass,” *Proc. SPIE 9736, Laser-based Micro- Nanoprocessing X*, 97360U, 2016.
- [94] B. McMillen, C. Athanasiou, and Y. Bellouard, “Femtosecond laser direct-write waveplates based on stress-induced birefringence,” *Opt. Express*, vol. 24, no. 24, pp. 27239–27252, 2016.
- [95] G. D. Marshall, M. Ams, and M. J. Withford, “Direct laser written waveguide – Bragg gratings in bulk fused silica,” *Opt. Lett.*, vol. 31, no. 18, pp. 2690–2691, 2006.
- [96] A. Champion and Y. Bellouard, “Direct volume variation measurements in fused silica specimens exposed to femtosecond laser,” *Opt. Mater. Express*, vol. 2, no. 6, pp. 789–798, 2012.
- [97] Y. Bellouard *et al.*, “Stress-state manipulation in fused silica via femtosecond laser irradiation,” *Optica*, vol. 3, no. 12, pp. 1285–1293, 2016.
- [98] A. Champion, M. Beresna, P. Kazansky, and Y. Bellouard, “Stress distribution around femtosecond laser affected zones : effect of nanogratings orientation,” *Opt. Express*, vol. 21, no. 21, pp. 24942–24951, 2013.
- [99] B. McMillen and Y. Bellouard, “On the anisotropy of stress-distribution induced in glasses and crystals by non-ablative femtosecond laser exposure,” *Opt. Express*, vol. 23, no. 1, pp. 86–100, 2015.
- [100] P. Vlugter, E. Block, and Y. Bellouard, “Local tuning of fused silica thermal expansion coefficient using femtosecond laser,” *Phys. Rev. Mater.*, vol. 3, no. 5, pp. 053802–053809, 2019.
- [101] P. Vlugter and Y. Bellouard, “Elastic properties of self-organized nanogratings produced by femtosecond laser exposure of fused silica,” *Phys. Rev. Mater.*, vol. 4, pp. 023607–023613, 2020.
- [102] P. Vlugter, “Investigation of femtosecond laser-tuned thermomechanical properties of fused silica,” Ph.D. Thesis, N 7967 EPFL, 2020.
- [103] Y. Bellouard, “Conception de dispositifs en alliage à mémoire de forme en microtechnique,” Ph.D. Thesis, N 2308 EPFL, 2000.
- [104] Y. Bellouard, “On the bending strength of fused silica flexures fabricated by ultrafast lasers [Invited],” *Opt. Mater. Express*, vol. 1, pp. 816–831, 2011.
- [105] B. Lenssen and Y. Bellouard, “Optically transparent glass micro-actuator fabricated by femtosecond laser exposure and chemical etching,” *Appl. Phys. Lett.*, vol. 101, pp. 103503–103506, 2012.
- [106] Y. Bellouard, “Non-contact sub-nanometer optical repositioning using femtosecond lasers,” *Opt. Express*, vol. 23, no. 22, pp. 29258–29267, 2015.
- [107] S. I. Nazir and Y. Bellouard, “A Monolithic Gimbal Micro-Mirror Fabricated and Remotely Tuned with a Femtosecond Laser,” *Micromachines*, vol. 10, no. 9, pp. 611–627, 2019.
- [108] H. Kogelnik and T. Li, “Laser Beams and Resonators,” *Appl. Opt.*, vol. 5, no. 10, pp. 1550–1567, 1966.
- [109] S. Henein, *Conception des guidages flexibles*. Presses Polytechniques et Universitaires Romandes, Lausanne, Switzerland, 2001.
- [110] Y. Bellouard, *Microrobotics Methods and Applications*. Boca Raton, FL: CRC Press, 2010.
- [111] S. T. Smith, *Flexures: Elements of Elastic Mechanisms*, 1st ed. London, UK: Gordon and Breach Science Publishers, 2000.

- [112] P. S. Salter and M. J. Booth, "Focussing over the edge: adaptive subsurface laser fabrication up to the sample face," *Opt. Express*, vol. 20, no. 18, pp. 19978–19989, 2012.
- [113] K. M. Nowak, H. J. Baker, and D. R. Hall, "Efficient laser polishing of silica micro-optic components," *Appl. Opt.*, vol. 45, no. 1, pp. 162–171, 2006.
- [114] J. Drs, T. Kishi, and Y. Bellouard, "Laser-assisted morphing of complex three dimensional objects," *Opt. Express*, vol. 23, no. 13, pp. 17355–17366, 2015.
- [115] Y. Wang, M. Cavillon, N. Ollier, B. Poumellec, and M. Lancry, "An Overview of the Thermal Erasure Mechanisms of Femtosecond Laser-Induced Nanogratings in Silica Glass," *Phys. Status Solidi A*, vol. 218, p. 2100023 (15), 2021.
- [116] R. S. Taylor, C. Hnatovsky, E. Simova, P. P. Rajeev, D. M. Rayner, and P. B. Corkum, "Femtosecond laser erasing and rewriting of self-organized planar nanocracks in fused silica glass," *Opt. Lett.*, vol. 32, no. 19, pp. 2888–2890, 2007.
- [117] O. Sigmund, "On the Design of Compliant Mechanisms Using Topology Optimization," *J. Struct. Mech.*, vol. 25, no. 4, pp. 493–524, 1997.
- [118] M. I. Frecker, G. K. Ananthasuresh, S. Njshiwaki, N. Kikuchi, and S. Kota, "Topological Synthesis of Compliant Mechanisms Using Multi-Criteria Optimization," *Trans. ASME*, vol. 119, pp. 238–245, 1997.
- [119] S. R. Deepak, M. Dinesh, D. K. Sahu, and G. K. Ananthasuresh, "A Comparative Study of the Formulations and Benchmark Problems for the Topology Optimization of Compliant," *J. Mech. Robot.*, vol. 1, pp. 011003–011010, 2009.
- [120] O. Sigmund and K. Maute, "Topology optimization approaches A comparative review," *Struct. Multidisc. Optim.*, vol. 48, pp. 1031–1055, 2013.
- [121] M. P. Bendsøe, E. Lund, N. Olhoff, and O. Sigmund, "Topology optimization – broadening the areas of application," *Control Cybern.*, vol. 34, no. 1, pp. 7–35, 2005.
- [122] J. S. Jensen and O. Sigmund, "Topology optimization for nano-photonics," *Laser Photonics Rev.*, vol. 5, no. 2, pp. 308–321, 2011.
- [123] Y. Tsuji, K. Hirayama, S. Member, T. Nomura, K. Sato, and S. Nishiwaki, "Design of Optical Circuit Devices Based on Topology Optimization," *IEEE Photonics Technol. Lett.*, vol. 18, no. 7, pp. 850–852, 2006.
- [124] R. E. Christiansen and O. Sigmund, "Inverse design in photonics by topology optimization: tutorial," *J. Opt. Soc. Am. B*, vol. 38, no. 2, pp. 496–509, 2021.
- [125] F. Wang, R. E. Christiansen, J. Mørk, and O. Sigmund, "Maximizing the quality factor to mode volume ratio for ultra-small photonic crystal cavities," *Appl. Phys. Lett.*, vol. 113, pp. 241101–241105, 2018.
- [126] Y.-Q. Yu, L. L. Howell, C. Lusk, Y. Yue, and M.-G. He, "Dynamic Modeling of Compliant Mechanisms Based on the Pseudo-Rigid-Body Model," *Trans. ASME*, vol. 127, pp. 760–765, 2005.
- [127] R. V. Mises, "Motorrechnung, ein neues Hilfsmittel der Mechanik," *Z. angew. Math. Mech.*, vol. 4, pp. 155–181, 1924.
- [128] G. G. Stoney, "The tension of metallic films deposited by electrolysis," *Proc. R. Soc. London*, vol. A82, pp. 172–175, 1909.
- [129] A. Champion, "Local effective volume changes in fused silica induced by femtosecond laser irradiation," Ph.D. Thesis, Eindhoven University of Technology, 2015.

- [130] S. Rajesh and Y. Bellouard, "Towards fast femtosecond laser micromachining of fused silica: The effect of deposited energy.," *Opt. Express*, vol. 18, no. 20, pp. 21490–21497, 2010.
- [131] L. Carroll *et al.*, "Photonic Packaging : Transforming Silicon Photonic Integrated Circuits into Photonic Devices," *Appl. Sci.*, vol. 6, no. 12, pp. 426–446, 2016.
- [132] J. H. Song, H. N. J. Fernando, B. Roycroft, B. Corbett, and F. H. Peters, "Practical Design of Lensed Fibers for Semiconductor Laser Packaging Using Laser Welding Technique," *J. Light. Technol.*, vol. 27, no. 11, pp. 1533–1539, 2009.
- [133] D. Taillaert *et al.*, "An Out-of-Plane Grating Coupler for Efficient Butt-Coupling Between Compact Planar Waveguides and Single-Mode Fibers," *IEEE J. Quantum Electron.*, vol. 38, no. 7, pp. 949–955, 2002.
- [134] J. R. Kim and A. Siahmakoun, "Evanescent coupling to silicon waveguides using surface plasmon polaritons," *Appl. Opt.*, vol. 59, no. 13, pp. D64–D68, 2020.
- [135] R. Marchetti, L. C. L. Carroll, K. Gradkowski, and P. Minzioni, "Coupling strategies for silicon photonics integrated chips [Invited]," *Photonics Res.*, vol. 7, no. 2, pp. 201–239, 2019.
- [136] P. De Dobbelaere *et al.*, "Packaging of Silicon Photonics Systems," in *Proc. Opt. Fiber Commun Conf.*, 2014, pp. 1–3.
- [137] S. J. McNab, N. M., and Y. A. Vlasov, "Ultra-low loss photonic integrated circuit with membrane-type photonic crystal waveguides," *Opt. Express*, vol. 11, no. 22, pp. 2927–2939, 2003.
- [138] L. Carroll, D. Gerace, I. Cristiani, S. Menezo, and L. C. Andreani, "Broad parameter optimization of polarization- diversity 2D grating couplers for silicon photonics," *Opt. Express*, vol. 21, no. 18, pp. 21556–21568, 2013.
- [139] R. Dangel *et al.*, "Polymer waveguides for electro-optical integration in data centers and high-performance computers," *Opt. Express*, vol. 23, no. 4, pp. 4736–4750, 2015.
- [140] S. Maruo, O. Nakamura, and S. Kawata, "Three-dimensional microfabrication with two-photon-absorbed photopolymerization," *Opt. Lett.*, vol. 22, no. 2, pp. 132–134, 1997.
- [141] S. Kawata, H. Sun, T. Tanaka, and K. Takada, "Finer features for functional microdevices," *Nature*, no. 412, pp. 697–698, 2001.
- [142] G. Cojoc *et al.*, "Optical micro-structures fabricated on top of optical fibers by means of two-photon photopolymerization," *Microelectron. Eng.*, vol. 87, no. 5–8, pp. 876–879, 2010.
- [143] M. Malinauskas *et al.*, "Femtosecond laser polymerization of hybrid / integrated micro-optical elements and their characterization," *J. Opt.*, vol. 12, no. 12, p. 124010, 2010.
- [144] F. Schiappelli, R. Kumar, M. Prasciolu, D. Cojoc, and S. Cabrini, "Efficient fiber-to-waveguide coupling by a lens on the end of the optical fiber fabricated by focused ion beam milling," *Microelectron. Eng.*, vol. 73–74, pp. 397–404, 2004, doi: 10.1016/j.mee.2004.02.077.
- [145] C. Andrei and P. John Mark, "Automatic inspection method for contactlessly measuring an offset of a central feature of an object," EP0757226A2, 1997.
- [146] M. J. Daneman, O. Solgaard, N. C. Tien, K. Y. Lau, and R. S. Muller, "Laser-to-Fiber Coupling Module Using a Micromachined Alignment Mirror," *IEEE Photonics Technol. Lett.*, vol. 8, no. 3, pp. 396–398, 1996.
- [147] M. Tichem, B. Karpuschewski, and P. M. Sarro, "Self-adjustment of Micro-mechatronic Systems," *Ann. CIRP*, vol. 52, no. 1, pp. 17–20, 2003.
- [148] V. A. Henneken, W. P. Sassen, W. van der Vlist, W. H. A. Wien, M. Tichem, and P. M. Sarro, "Two-

Dimensional Fiber Positioning and Clamping Device for Product-Internal Microassembly,” *J. Microelectromechanical Syst.*, vol. 17, no. 3, pp. 724–734, 2008.

- [149] D. Marcuse, “Loss Analysis of Single-Mode Fiber Splices,” *Bell Syst. Tech. J.*, vol. 56, no. 5, pp. 703–718, 1977.
- [150] K. Ishikawa, J. Zhang, A. Tuantranont, V. M. Bright, and Y. Lee, “An integrated micro-optical system for VCSEL-to-fiber active alignment,” *Sensors Actuators A Phys.*, vol. 103, no. 1–2, pp. 109–115, 2003.
- [151] O. Solgaard, M. Daneman, N. C. Tien, A. Friedberger, R. S. Muller, and K. Y. Lau, “Optoelectronic Packaging Using Silicon Surface-Micromachined Alignment Mirrors,” *IEEE Photonics Technol. Lett.*, vol. 7, no. 1, pp. 41–43, 1995.
- [152] K. G. P. Folkersma, D. M. Brouwer, G. R. B. E. Römer, and J. L. Herder, “Robust precision alignment algorithm for micro tube laser forming,” *Precis. Eng.*, vol. 46, pp. 301–308, 2016.
- [153] G. Folkersma, G.-W. Römer, D. Brouwer, and B. Huis in ’t Veld, “In-plane laser forming for high precision alignment,” *Opt. Eng.*, vol. 53, pp. 126105–126116, 2014.
- [154] M. H. M. Van Gastel, P. C. J. N. Rosielle, and M. Steinbuch, “A Concept for Accurate Edge-Coupled Multi-Fiber Photonic Interconnects,” *J. Light. Technol.*, vol. 37, no. 4, pp. 1374–1380, 2019.
- [155] M. Cai, O. Painter, and K. J. Vahala, “Observation of Critical Coupling in a Fiber Taper to a Silica-Microsphere Whispering-Gallery Mode System,” *Phys. Rev. Lett.*, vol. 85, no. 1, pp. 74–77, 2000.
- [156] C. Fabry and A. Pérot, “Théorie et applications d’une nouvelle méthode de spectroscopie interférentielle,” *Ann. Chim. Phys.*, vol. 16, no. 7, pp. 115–144, 1899.
- [157] D. Hunger, T. Steinmetz, Y. Colombe, C. Deutsch, T. W. Hänsch, and J. Reichel, “A fiber Fabry–Perot cavity with high finesse,” *New J. Phys.*, vol. 12, p. 065038, 2010.
- [158] C. Saavedra, D. Pandey, W. Alt, H. Pfeifer, and D. Meschede, “Tunable fiber Fabry–Perot cavities with high passive stability,” *Opt. Express*, vol. 29, no. 2, pp. 974–982, 2021.
- [159] K. Ott *et al.*, “Millimeter-long Fiber Fabry–Perot cavities,” *Opt. Express*, vol. 24, no. 9, pp. 9839–9853, 2016.
- [160] T. Steinmetz, Y. Colombe, D. Hunger, T. W. Hänsch, A. Balocchi, and R. J. Warburton, “Stable fiber-based Fabry–Pérot cavity,” *Appl. Phys. Lett.*, vol. 89, pp. 111110–111112, 2006.
- [161] D. Hunger, C. Deutsch, R. J. Barbour, R. J. Warburton, and J. Reichel, “Laser micro-fabrication of concave, low-roughness features in silica,” *AIP Adv.*, vol. 2, p. 012119 (6), 2012.
- [162] M. Uphoff, M. Brekenfeld, G. Rempe, and S. Ritter, “Frequency splitting of polarization eigenmodes in microscopic Fabry–Perot cavities,” *New J. Phys.*, vol. 17, pp. 013053–013063, 2015.
- [163] S. M. Wiederhorn, “A Chemical Interpretation of Static Fatigue,” *J. Am. Ceram. Soc.*, vol. 5, no. 2, pp. 81–85, 1972.
- [164] S. M. Wiederhorn, S. W. Freiman, E. R. Fuller JR, and C. J. Simmons, “Effects of water and other dielectrics on crack growth,” *J. Mater. Sci.*, vol. 17, pp. 3460–3478, 1982.
- [165] M. Tomozawa, “Water in Glass,” *J. Non. Cryst. Solids*, vol. 73, pp. 197–204, 1985.
- [166] J. F. Shackelford, J. S. Masaryk, and R. M. Fulrath, “Water Content, Fictive Temperature, and Density Relations for Fused Silica,” *J. Am. Ceram. Soc.*, vol. 53, pp. 417–417, 1970.
- [167] S. M. Wiederhorn, T. Fett, G. Rizzi, and M. J. Hoffmann, “The effect of water penetration on crack growth in silica glass,” *Eng. Fract. Mech.*, vol. 100, pp. 3–16, 2013.

- [168] S. M. Wiederhorn, T. Fett, G. Rizzi, S. Fu, M. J. Hoffmann, and J. G. J., "Effect of Water Penetration on the Strength and Toughness of Silica Glass," *J. Am. Ceram. Soc.*, vol. 94, no. 1, pp. S196–S203, 2011.
- [169] A. J. Moulson and J. P. Roberts, "Water in silica glass," *Trans. Faraday Soc.*, vol. 57, pp. 1208–1216, 1961.
- [170] M. Tomozawa, K. M. Davis, J. H. Seaman, and E. M. Aaldenberg, "The origin of anomalous water diffusion in silica glasses at low temperatures," *J. Am. Ceram. Soc.*, vol. 100, pp. 4548–4561, 2017.
- [171] R. H. Doremus, "Diffusion of water in silica glass," *J. Mater. Res.*, vol. 10, no. 9, pp. 2379–2389, 1995.
- [172] M. Tomozawa and W.-T. Han, "Water Entry into Silica Glass During Slow Crack Growth," *J. Am. Ceram. Soc.*, vol. 74, no. 10, pp. 2573–2576, 1991.
- [173] A. Zouine, O. Dersch, G. Walter, and F. Rauch, "Diffusivity and solubility of water in silica glass in the temperature range 23-200 degrees C," *Phys. Chem. Glas.*, vol. 48, no. 2, pp. 85–91, 2007.
- [174] A. Agarwal, M. Tomozawa, and W. A. Lanford, "Effect of stress on water diffusion in silica glass at various temperatures," *J. Non. Cryst. Solids*, vol. 167, pp. 139–148, 1994.
- [175] Q. Sun, T. Lee, M. Beresna, and G. Brambilla, "Control of Laser Induced Cumulative Stress for Efficient Processing of Fused Silica," *Sci. Rep.*, vol. 10, p. 3819, 2020.
- [176] C. E. Athanasiou and Y. Bellouard, "A Monolithic Micro-Tensile Tester for Investigating Silicon Dioxide Polymorph Micromechanics, Fabricated and Operated Using a Femtosecond Laser," *Micromachines*, vol. 9, pp. 1365–1386, 2015.
- [177] S. M. Wiederhorn, F. Yi, D. Lavan, L. J. Richter, T. Fett, and J. H. Michael, "Volume Expansion Caused by Water Penetration into Silica Glass," *J. Am. Ceram. Soc.*, vol. 98, no. 1, pp. 78–87, 2015.
- [178] W. A. Rogers, R. S. Buritz, and D. Alpert, "Diffusion Coefficient, Solubility, and Permeability for Helium in Glass," *J. Appl. Phys.*, vol. 25, pp. 868–875, 1954.
- [179] V. Lou, R. Sato, and M. Tomozawa, "Hydrogen diffusion in fused silica at high temperatures," *J. Non. Cryst. Solids*, vol. 315, pp. 13–19, 2003.
- [180] M. A. Haque and M. T. A. Saif, "In-situ tensile testing of nano-scale specimens in SEM and TEM," *Exp. Mech.*, vol. 42, pp. 123–128, 2002.
- [181] S. Jaddi, J. P. Raskin, and T. Pardoën, "On-chip environmentally assisted cracking in thin freestanding - SiO₂ films," *J. Mater. Res.*, vol. 36, pp. 2479–2494, 2021.
- [182] M. Coulombier, G. Guisbiers, M.-S. Colla, R. Vayrette, J.-P. Raskin, and T. Pardoën, "On-chip stress relaxation testing method for freestanding thin film materials," *Rev. Sci. Instrum.*, vol. 83, no. 10, p. 105004(9), 2012.
- [183] Y. Ganesan, Y. Lu, C. Peng, H. Lu, R. Ballarini, and J. Lou, "Development and Application of a Novel Microfabricated Device for the In Situ Tensile Testing of 1-D Nanomaterials," *J. Microelectromechanical Syst.*, vol. 19, no. 3, pp. 675–682, 2010.
- [184] E. Andreassen, A. Clausen, M. Schevenels, B. S. Lazarov, and O. Sigmund, "Efficient topology optimization in MATLAB using 88 lines of code," *Struct. Multidisc. Optim.*, vol. 43, pp. 1–16, 2011.
- [185] O. Sigmund, "A 99 line topology optimization code written in Matlab," *Struct. Multidisc. Optim.*, vol. 21, pp. 120–127, 2001.
- [186] R. E. Christiansen and O. Sigmund, "Compact 200 line MATLAB code for inverse design in photonics by topology optimization: tutorial," *J. Opt. Soc. Am. B*, vol. 38, no. 2, pp. 510–520, 2021.

- [187] S. I. Nazir and Y. Bellouard, “Contactless Optical Packaging Concept for Laser to Fiber Coupling,” *IEEE Trans. Components, Packag. Manuf. Technol.*, 2021.

Curriculum Vitae

Saood Ibni Nazir

Born on June 13th, 1991

saoodnaz@gmail.com

Education

2017 - 2021	Ph.D. candidate in Galatea Laboratory Institute of Microengineering, School of Engineering École Polytechnique Fédérale de Lausanne (EPFL), Switzerland
2014 - 2016	Master of Science in Physics Department of Physics Indian Institute of Technology (IIT), Kharagpur, India
2011 - 2014	Bachelor of Science in Physics Department of Physics Indian Institute of Technology (IIT), Kharagpur, India

Journal articles

Saood I. Nazir and Yves Bellouard, “A Monolithic Gimbal Micro-Mirror Fabricated and Remotely Tuned with a Femtosecond Laser,” *Micromachines*, 10, 611 (2019).

Saood I. Nazir and Yves Bellouard, “Contactless Optical Packaging Concept for Laser to Fiber Coupling,” *IEEE Transactions on Components, Packaging and Manufacturing Technology*, 11, 6, (2021).

Saood I. Nazir, Christos E. Athanasiou, and Yves Bellouard, “On the uniaxial static stress relaxation in fused silica at room temperature”, *Journal of Non-Crystalline Solids: X* (2021). (under review).

Conferences

Saood I. Nazir and Yves Bellouard, “A monolithic gimbal micro-mirror fabricated and remotely tuned with a femtosecond laser”, LPM, Scotland, United Kingdom, 2018. (Oral presentation)

Saood I. Nazir and Yves Bellouard, “A monolithic gimbal micro-mirror fabricated and remotely tuned with a femtosecond laser”, Laser-frontiers, Sao Paulo, Brazil, 2018. (Poster presentation)

Saood I. Nazir and Yves Bellouard, “Non-contact fine positioning of optical components and circuits using femtosecond lasers”, Photonics West (2020), San Francisco. (Oral presentation, Third best presentation award)

Antoine Delgoffe, Saood I. Nazir, Sargis Hakobyan, Clemens Hoenninger, and Yves Bellouard, “Miniature GHz repetition rate femtosecond solid-state laser cavity in a glass substrate”, Photonics West (2022), San Francisco. (Oral presentation, accepted)

